Octet baryon structure observables from lattice QCD

Dissertation

zur Erlangung des Doktorgrades
der Naturwissenschaften (Dr. rer. nat.)
der Fakultät für Physik
der Universität Regensburg

vorgelegt von

Simon Weishäupl

aus Gräfelfing

im Jahr 2023

Promotionsgesuch eingereicht am: 25. Januar 2023
Die Arbeit wurde angeleitet von: Prof. Dr. Gunnar S. Bali

Prüfungsausschuss:

Vorsitzender:	Prof. Dr. Jörg Wunderlich
1. Gutachter:	Prof. Dr. Gunnar S. Bali
2. Gutachter:	Prof. Dr. Taushif Ahmed
weiterer Prüfer:	Prof. Dr. Andrea Donarini

Datum Promotionskolloquium: 21.07.2023

ABSTRACT

In the Standard Model of particle physics quarks and gluons are bound by the fundamental strong force and form particles generally denoted as hadrons. The associated quantum field theory is called Quantum Chromodynamics (QCD). The three lightest quark flavours which exist in Nature are called up, down and strange and are the constituents of, e.g., octet baryons with protons and neutrons being the most prominent examples. How physical properties like the mass or spin of hadrons arise from the quarks and gluons bound by the strong interaction is subject of many experiments and theoretical investigations. In this thesis we employ the framework of lattice QCD, which, at the moment, is the only systematic non-perturbative approach allowing us to investigate structure observables of the octet baryons from first principles. Within this framework QCD is formulated in a well defined way on a four dimensional spacetime lattice and simulations are performed using Monte Carlo techniques.

In our simulations we employ ensembles of gauge field configurations with $N_f = 2 + 1$ sea quark flavours of non-perturbatively improved Wilson fermions at six distinct values of the lattice spacing in the range $a \approx (0.039 - 0.098)$ fm, generated by the Coordinated Lattice Simulations (CLS) effort. The pion mass M_π ranges from around 430 MeV down to a near physical value of 130 MeV and the linear spatial lattice extent L varies from $6.5\,M_\pi^{-1}$ to $3.0\,M_\pi^{-1}$, where $LM_\pi \geq 4$ for the majority of the ensembles. Within this work we analyse a large set of high statistics gauge ensembles along three distinct quark mass trajectories. This allows us to investigate all systematic effects associated with unphysical quark masses, finite volumes and finite lattice spacings by performing a controlled extrapolation of all observables to the physical mass point (or chiral limit), infinite volume and continuum limits.

Chiral perturbation theory (ChPT) often serves as a key instrument in investigations of baryon structure observables. So far, in contrast to SU(2) ChPT, very few lattice QCD studies of SU(3) ChPT exist. In the first part of this thesis a consistent and simultaneous analysis of several observables within the framework of SU(3) ChPT is presented and we determine the leading order mesonic (B_0 and F_0) and baryonic (m_0, F and D) SU(3) ChPT low energy constants (LECs). To this end we employ only the subset of gauge ensembles lying on the quark mass trajectory where exact SU(3) flavour symmetry, i.e., $m_u = m_d = m_s$, holds. The mesonic LECs are determined by a combined analysis of the pseudoscalar mass and decay constant as functions of the quark mass. We find the SU(3) chiral condensate $\Sigma_0 = F_0^2 B_0$ and pion decay constant F_0 to be smaller than their SU(2) counterparts while the Gell-Mann–Oakes–Renner parameters $B_0 \approx B$ are similar. The baryonic LECs are obtained by a simultaneous analysis of the octet baryon mass and the axial charges for the nucleon and the sigma baryon. We found that a consistent description of the pion mass and volume dependence of the axial charges and the octet baryon mass was possible with the same set of LECs and in particular we found consistent results for F and D compared with other lattice determinations.

While there is a long history of lattice calculations of the nucleon (i.e., proton or neutron) charges, the charges for the other octet baryons are not very well determined. In the second part of this thesis we present results for the vector, axial, scalar and tensor

isovector charges of the nucleon, sigma and cascade octet baryons in the infinite volume, continuum limit at physical quark masses. This analysis became feasible employing a stochastic approach which allows for a efficient computation of three-point correlation functions for the whole baryon octet. Additional sources of systematic uncertainties associated with the contributions of excited states to the ground state matrix elements and renormalization factors are carefully taken into account. Phenomenological predictions often rely on SU(3) flavour symmetry arguments. The validity of these assumptions can be tested in lattice QCD calculations where we find moderate symmetry breaking effects for the axial charges at the physical quark mass point, while no significant effects are found for the other charges within current uncertainties. Using the conserved vector current relation and the result for the scalar charge of the sigma baryon, we also predict the difference between the up and down quark masses. Further we compute the QCD contributions to baryon isospin mass splittings and evaluate the isospin breaking effects on the pion baryon σ terms.

Publications

This thesis is based on the publications [SW1, SW2]. Further results obtained within this work led to contributions in [SW3–SW8] and additional contributions have been made to [SW9] and [SW10].

[SW1] RQCD collaboration, G. S. Bali, S. Collins, W. Söldner and S. Weishäupl, *Leading order mesonic and baryonic SU(3) low energy constants from $N_f = 3$ lattice QCD*, *Phys. Rev. D* **105** (2022) 054516, [2201.05591].

[SW2] RQCD collaboration, G. S. Bali, S. Collins, S. Heybrock, M. Löffler, R. Rödl, W. Söldner and S. Weishäupl, *Octet baryon isovector charges from $N_f = 2 + 1$ lattice QCD, submitted to Phys. Rev. D*, [2305.04717].

[SW3] RQCD collaboration, G. S. Bali, L. Barca, S. Collins, M. Gruber, M. Löffler, A. Schäfer, W. Söldner, S. Weishäupl and T. Wurm, *Nucleon axial structure from lattice QCD*, *J. High Energy Phys.* **05** (2020) 126, [1911.13150].

[SW4] RQCD collaboration, M. Löffler, P. Wein, T. Wurm, S. Weishäupl, D. Jenkins, R. Rödl, A. Schäfer and L. Walter, *Mellin moments of spin dependent and independent PDFs of the pion and rho meson*, *Phys. Rev. D* **105** (2022) 014505, [2108.07544].

[SW5] RQCD collaboration, G. S. Bali, S. Collins, P. Georg, D. Jenkins, P. Korcyl, A. Schäfer, E. E. Scholz, S. Simeth, W. Söldner and S. Weishäupl, *Scale setting and the light baryon spectrum in $N_f = 2 + 1$ QCD with Wilson fermions, J. High Energy Phys.* **05** (11, 2023) 035, [2211.03744].

[SW6] G. S. Bali, S. Collins, P. Korcyl, R. Rödl, S. Weishäupl and T. Wurm, *Hyperon couplings from $N_f = 2 + 1$ lattice QCD*, *Proc. Sci.* **LATTICE2019** (2019) 099, [1907.13454].

[SW7] P. L. J. Petrak, G. S. Bali, S. Collins, J. Heitger, D. Jenkins, S. Weishäupl and T. Wurm, *Towards the determination of sigma terms for the baryon octet on $N_\mathrm{f} = 2 + 1$ CLS ensembles*, *Proc. Sci.* **LATTICE2021** (2022) 072, [2112.00586].

[SW8] P. L. J. Petrak, G. S. Bali, S. Collins, J. Heitger, D. Jenkins and S. Weishäupl, *Sigma terms of the baryon octet in $N_\mathrm{f} = 2 + 1$ QCD with Wilson quarks*, *Proc. Sci.* **LATTICE2022** (2023) 112, [2301.03871].

[SW9] T. Auge, G. S. Bali, M. Klettke, B. Ludäscher, W. Söldner, S. Weishäupl and T. Wettig, *Provenance for lattice QCD workflows*, Companion Proceedings of the ACM Web Conference 2023, [2303.12640].

[SW10] M. Padmanath, S. Collins, D. Mohler, S. Piemonte, S. Prelovsek, A. Schäfer and S. Weishäupl, *Identifying spin and parity of charmonia in flight with lattice QCD*, *Phys. Rev. D* **99** (2019) 014513, [1811.04116].

CONTENTS

1 | INTRODUCTION

The Standard Model (SM) of particle physics was developed in the 1970s and incorporates three out of the four fundamental interactions: the electromagnetic, weak and strong force. It has proven to be very successful in describing and predicting a wide range of phenomena and represents an experimentally well tested theory. Up to now only very few experiments have shown tension with the predictions from the SM. Despite its great success, there are still open questions such as including gravity, the existence of dark matter or the matter-antimatter asymmetry, which the SM falls short to explain. In its current form the SM predicts two kinds of fundamental (fermionic) particles called quarks and leptons, which are the building blocks of all visible matter in the universe. Additionally, it encapsulates the Higgs boson, as well as the gauge bosons that mediate the three fundamental interactions. See Fig. 1.1 for a classification of the elementary particles.

In the SM quarks come in six different flavours (up, down, charm, strange, top and bottom) and they interact via the strong force which is mediated through gauge bosons called gluons. Since quarks (and gluons) carry so-called colour charges, the quantum field theory associated to the strong (or colour) force is called Quantum Chromodynamics (QCD)[1]. Because of an important property of QCD called confinement, free 'coloured' particles cannot be observed in Nature and quarks and gluons are bound inside hadrons, forming colour-neutral objects. Hadrons can be further grouped into mesons and baryons. In the quark model [1, 2], mesons are formed by $(q\bar{q})$ states built up of a valence quark q and antiquark $\bar{q}$ while baryons are composed of three valence quarks (qqq). In reality they also contain gluons and sea quarks and there are also more exotic bound states such as tetraquarks or pentaquarks.

---

[1]"chróma" ($\chi\rho\acute{\omega}\mu\alpha$) is the Greek word for colour. In analogy to Quantum Electrodynamics (QED) which describes the theory of the electric charge, the name Quantum Chromodynamics is associated with the theory of the colour charge.
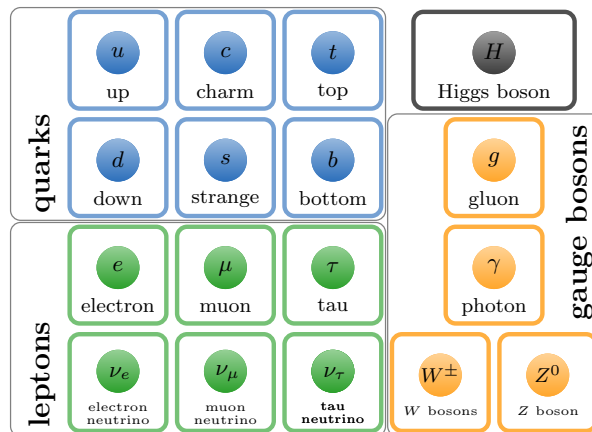

Figure 1.1: The Standard Model of particle physics.

The three lightest quark flavours are called up (u), down (d) and strange (s) and are the constituents of the spin-1/2 octet baryons derived from SU(3) flavour symmetry, as shown in Fig. 1.2. Protons and neutrons, which are the two lightest baryons and commonly denoted as nucleons, are the building blocks of almost all visible matter in the universe. Under more extreme conditions like, e.g., inside neutron stars, so-called hyperons are expected to play an important role too [3]. Generally, all baryons which include at least one strange quark but none of the heavier quark flavours (c, t, b) as valence quarks are denoted as hyperons. Furthermore, hyperons are distinguished according to their strangeness S and are are called lambda (Λ, $S = -1$), sigma (Σ, $S = -1$), cascade (Ξ, $S = -2$) and omega (Ω, $S = -3$) baryons. Compared to the quark masses of $m_u \approx 2\,\mathrm{MeV}$, $m_d \approx 5\,\mathrm{MeV}$ and $m_s \approx 96\,\mathrm{MeV}$ the masses of the octet baryons (e.g., $m_p \approx 938.3\,\mathrm{MeV}$) are much larger than the sum of the masses of their valence quark constituents. These differences in the masses already suggest that gluons and sea quarks have a significant impact on the properties of hadrons. Interestingly, the pions, which are mesons build up from two up and/or down valence (anti)quarks, have masses of only $m_\pi \approx 140\,\mathrm{MeV}$ and hence are much lighter than one naively would have expected when comparing them to the nucleon masses.
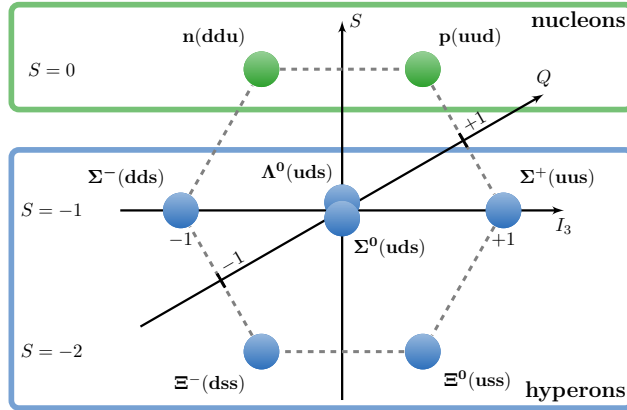
Figure 1.2: The spin-1/2 baryon octet where S, I_3 and $Q = (1 + S)/2 + I_3$ label strangeness, isospin and charge, respectively. According to their strangeness, the baryons can further be classified as nucleons (green) or hyperons (blue).

At present, deriving the properties of hadrons analytically from the fundamental theory of the strong interaction (QCD) poses a significant challenge. Therefore, it is subject of many experiments and theoretical investigations to understand how physical properties of hadrons, such as the mass or spin of a baryon, arise from the quarks and gluons bound by fundamental interactions. For instance, in the planned PANDA experiment [4] at FAIR[2] numerous baryon and antibaryon pairs will be created through proton-antiproton collisions and the experiment allows for high precision studies of the strong interaction and aspects of baryon structure. In the initial phase of the PANDA experiment results will be obtained in particular in the hyperon sector, where experimental knowledge is rather limited so far. As mentioned above, hyperon-hyperon interactions, which are expected to be present in, e.g., the interior of neutron stars, provide an interesting area of research.

In this thesis we will employ the framework of lattice QCD allowing us to investigate

---

[2]The acronyms stand for:
- $\overline{\mathrm{P}}$ANDA = antiProton ANihilation at DArmstadt
- FAIR = Facility for Antiproton and Ion Research

structure observables of the octet baryons from first principles. Within this framework QCD is formulated in a well defined way on a four dimensional spacetime lattice and numerical simulations can be performed using Monte Carlo techniques. Over the last decades, the field of lattice QCD has made great progress, enabling precise calculations of various properties of hadrons and the strong interaction. The work presented in this thesis is a first step in a long-term effort to obtain predictions from lattice QCD for form factors and baryon interactions which can be directly compared to experimental results, e.g., obtained from the PANDA experiment.

A charge of a baryon parameterizes the strength of the interaction of the baryon with a particle that couples to this particular charge. For instance, the isovector axial charge of the nucleon g_A^N, which is very precisely measured in experiment, $\lambda = g_A^N/g_V^N = 1.2754(13)$ [5], determines the β-decay rate of the neutron. In addition, this charge is also related to the individual quark spin contributions in the decomposition of the nucleon spin [6, 7], which can also be determined from lattice QCD calculations [8–12]. Since no scalar or tensor couplings contribute to tree-level SM processes, these isovector charges cannot be measured directly in experiment. However, such interactions may hint at new physics and it is important to constrain new interactions (once discovered) using lattice QCD input, see, e.g., Ref. [13] for a detailed discussion.

Within this work we determine the vector, axial, scalar and tensor isovector charges of the light octet baryons. Despite a long history of lattice calculations of the nucleon charges, see Ref. [14] for a current review, only very few investigations of the axial charges of the baryon octet exist to date [15–19] and only one of these includes the scalar and tensor charges [19]. Determining the precise values of these charges helps in understanding the internal structure and dynamics of the octet baryons in terms of their constituent quarks and their interactions. The results of the charges further allows us to predict the difference between the up and down quark masses, the QCD contributions to baryon isospin mass splittings and isospin differences of pion baryon σ terms. The latter quantity encodes the contribution to the mass of a baryon due to the non-zero up and down quark masses.

Assuming SU(3) flavour symmetry, the charges for the whole baryon octet in a given channel only depend on two independent parameters. For the proton and the isovector axial charge, this relation reads $g_A = F_A + D_A$, where in the massless limit F_A and D_A correspond to the chiral perturbation theory (ChPT) low energy constants (LECs) F and D, respectively. Phenomenological predictions often rely on SU(3) flavour symmetry arguments which are not known *a priori* to hold, in particular at the physical point. Employing lattice QCD simulations, we are able to test the validity of these assumptions. So far, SU(3) flavour symmetry breaking effects have been explored only relatively little in lattice calculations and in this work we establish the size of these corrections in the axial, scalar and the tensor channel.

In the investigation of observables related to baryon structure, or, in general, in the description and understanding of a multitude of hadronic processes, ChPT often serves as a key instrument. Again, it is *a priori* not known whether a ChPT expansion is applicable in a certain quark mass range and in particular at the physical quark mass point. In lattice QCD calculations the quark masses are not fixed but can be varied making a systematic investigation of the precision and validity of a ChPT expansion possible. In contrast to SU(2) ChPT, there exist not many comprehensive lattice QCD studies employing SU(3) ChPT. Here we will present a consistent and simultaneous analysis of several observables within the framework of SU(3) ChPT and determine the leading order mesonic (B_0 and F_0) and baryonic (m_0, F and D) SU(3) ChPT LECs.

This thesis is organized as follows: In chapter 2, we introduce the framework of lattice QCD starting from the continuum formulation of QCD, introducing the lattice

discretization approach and giving an overview over the gauge ensembles analysed in this work. In the last section of this chapter we will introduce the generic workflow of lattice QCD calculations that is applicable to this work.

Then, Chapter 3 gives details about the measurement and analysis methods applied. The computational methods used to obtain two- and three-point correlation functions and the excited state analysis performed to extract the ground state matrix elements of interest are described. Further, details are given on the non-perturbative renormalization and order a improvement, before discussing the systematic effects in our lattice QCD calculations and explaining the infinite volume, continuum limit and quark mass extrapolation strategy.

In chapter 4, first results from an analysis of the leading order mesonic (B_0 and F_0) and baryonic (m_0, F and D) SU(3) ChPT LECs on the subset of gauge ensembles which incorporate exact SU(3) flavour symmetry are presented. The mesonic LECs are determined by a combined analysis of the pseudoscalar mass and decay constant as functions of the quark mass while the baryonic LECs are obtained by a simultaneous analysis of the octet baryon mass and the axial charges for the nucleon and the sigma baryon.

In chapter 5, the results of the vector, axial, scalar and tensor isovector charges of the nucleon, sigma and cascade octet baryons in the continuum, infinite volume limit at physical quark masses are presented. Subsequently, we discuss SU(3) symmetry breaking effects, determine the up and down quark mass difference from the scalar charge of the sigma baryon, split isospin breaking effects on the baryon masses into QCD and QED contributions and determine isospin breaking corrections to the pion baryon σ terms. Finally, in chapter 6, we will summarize the main results before we conclude.

Several Appendices provide further details: Appendix A sets the stage by introducing general conventions and definitions used throughout this thesis. Then, Appendix B outlines the statistical concepts and methods applied within the data analysis part. Appendix C gives further details of the three-point function measurements, including a direct comparison between the sequential source and the stochastic method. Appendix D compiles various data tables giving details about all gauge ensembles analysed and the results used in the final analyses. Additional figures are provided in Appendix E and, for completeness, ChPT expressions that were not used in the final analysis are collected in Appendix F.

2 | LATTICE QUANTUM CHROMODYNAMICS

As part of the Standard Model of particle physics Quantum Chromodynamics [20], or in short QCD, is accepted to be the quantum field theory describing the strong interactions between quarks and gluons. It is a non-Abelian gauge theory with a SU(3) gauge group and fermions in the fundamental representation. The quarks carry colour charges and interact via the strong force mediated by gauge bosons called gluons. The gluons also carry colour charges and hence are themselves interacting strongly. This gives rise to some specific features which makes QCD inherently harder to analyse than, e.g., QED. One important property of QCD is that its strong coupling constant $\alpha_s(\mu) = g^2(\mu)/4\pi$ is a function of the energy scale μ. At high energies the coupling becomes very small and quarks and gluons interact only very weakly (asymptotic freedom [21, 22]). In this region perturbation theory can safely be applied. At low momentum transfer (large distances) the coupling becomes very strong and perturbative methods fail to describe the interactions. At low energies the non-perturbative method of lattice QCD provides a very powerful tool to investigate the strong interactions from first principles.

In the following the key concepts of the lattice QCD discretization are introduced starting from the continuum formulation of QCD. Then the generation of gauge field configurations is outlined and details about the gauge ensembles analysed in this thesis are given. Having a set of suitable gauge ensembles available completes the first part of the lattice QCD workflow factorization as introduced in the last section.

This chapter is based on standard text books and introductory articles [23–25], all suggested for further reading. Parts of this chapter are taken in similar or verbatim form from [26]. General definitions and conventions applied in the following sections are given in Appendix A.

2.1 Continuum QCD

QCD is a non-Abelian gauge theory with a SU(3) gauge group and fermions in the fundamental representation. The form of the QCD Lagrangian is determined by imposing a local SU(3) invariance of the Lagrangian as well as renormalizability. The latter restricts the Lagrangian to only contain terms with mass dimension up to four. These requirements yield the Lagrangian

$$\mathcal{L}_{\mathrm{QCD}} = -\frac{1}{4} F_{\mu\nu}^a(x) F_a^{\mu\nu}(x) + \sum_{f=u,d,s,\ldots} \bar{\psi}^f(x) \left(i D_\mu \gamma^\mu - m_f \right) \psi^f(x), \qquad (2.1)$$

at least if we exclude a term $\propto \epsilon_{\mu\nu\rho\sigma} F_{\mu\nu}^a F_a^{\rho\sigma}$, $\epsilon_{\mu\nu\rho\sigma}$ being the totally anti-symmetric tensor, which would violate the symmetry of charge and parity (CP-violation). The first term in Eq. (2.1) is the kinetic term for the gluons, whereas the second term describes the fermionic part, thus the interactions of quarks and gluons and the quark masses m_f. The quark fields $\psi_{\alpha,k}^f$ are Dirac spinors and come in N_f different flavours $f = u, d, s, \ldots$. Since quarks are in the fundamental representation of the SU(3) (colour) group, the colour

index runs over $k = 1, 2, 3$. Antiquarks, denoted by $\bar{\psi}^f_{\alpha,k}$, transform in the conjugate representation and the mass of the quarks is given by the parameter m_f and is flavour-dependent. The γ-matrices γ_μ live in the Dirac space and mix the components of the spinor fields. To ensure gauge invariance for the kinetic term containing derivatives, the covariant derivative D_μ is defined by

$$D_\mu = \partial_\mu - igA^a_\mu(x)t^a, \tag{2.2}$$

where the parameter g gives the coupling of the fermions to the gauge bosons. Gauge bosons (gluons for QCD) are introduced as vector fields $A_\mu(x) = \sum_a A^a_\mu(x)t^a$ with Lorentz index $\mu = 1, \ldots, 4$ and colour index $a = 1, \ldots, 8$. Here t^a are the generators of the gauge group. These fulfill

$$\left[t^a, t^b \right] = if^{abc}t^c, \tag{2.3}$$

where the structure constants f^{abc} are totally antisymmetric and the fields A_μ are elements of the Lie-algebra su(3). Since in general, $N^2 - 1$ real parameters are needed to describe a SU(N) matrix, the adjoint colour index runs up to 8. We require the fermionic part of the Lagrangian to be invariant under local SU(3) transformations of the fermion fields $\psi(x)$. Suppressing the flavour index f, the fermion fields have to transform as

$$\psi(x) \rightarrow \psi'(x) = V(x)\psi(x), \tag{2.4}$$
$$\bar{\psi}(x) \rightarrow \bar{\psi}'(x) = \bar{\psi}(x)V^\dagger(x) \tag{2.5}$$

with $V(x) = e^{i\omega^a(x)t^a} \in \text{SU}(3)$. This leads to the gauge transformation law of the gluon field as

$$A_\mu(x) \rightarrow A'_\mu(x) = V(x) \left(A_\mu(x) + \frac{i}{g}\partial_\mu \right) V^\dagger(x), \tag{2.6}$$

which implies that $D_\mu(x)\psi(x)$ transforms in the same way as $\psi(x)$. Imposing invariance of the fermionic part of the Lagrangian under local SU(3) transformations therefore requires to introduce gauge fields $A_\mu(x)$ transforming as stated above.

For QCD the field strength tensor $F^a_{\mu\nu}$, which only contains the gluon fields, is given by

$$F^a_{\mu\nu} = \partial_\mu A^a_\nu - \partial_\nu A^a_\mu + gf^{abc}A^b_\mu A^c_\nu, \tag{2.7}$$

i.e., $F_{\mu\nu} = \frac{i}{g}[D_\mu, D_\nu]$, see Eqs. (2.2) and (2.3). The first term in the QCD Lagrangian Eq. (2.1) is built from the contraction of two field strength tensors and therefore is invariant under gauge transformations Eq. (2.6) and describes the dynamics of gluons. In Eq. (2.7) the last term only arises for non-Abelian gauge groups and yields cubic and quartic terms of the fields A_μ in the Lagrangian (2.1) leading to a nontrivial interacting field theory. An important consequence of these additional terms, resulting in self-interactions of the gluons, is asymptotic freedom at high energy scales and (colour) confinement at hadronic scales. Due to confinement, quarks and gluons are, at low energies, bound into colour neutral hadrons and free "coloured" particles cannot be observed in Nature. This has not yet been proven analytically but is confirmed by lattice QCD simulations.

In addition to the local SU(3) invariance discussed above, the QCD Lagrangian for N_f mass degenerate quark flavours is invariant under a global SU(N_f) (vector) flavour symmetry and in the limit of massless quarks (spontaneously broken [27]) SU(N_f) chiral symmetry holds. Further the QCD Lagrangian respects the discrete symmetries parity, charge conjugation and time-reversal and only depends on $N_f + 1$ free parameters, the quark masses m_f and the coupling g. The classical equations of motion for QCD can be derived from this Lagrangian, that serves as a starting point for discretizing QCD on a spacetime lattice.

2.2 QCD on the lattice

Already in 1974 Wilson [28] introduced the formulation of lattice QCD providing a very powerful non-perturbative method which can be used to study the low energy regime of QCD from first principles. In this framework QCD is discretized on a finite four dimensional hypercubic lattice with lattice spacing a which serves as a regulator of the ultraviolet divergences. The quark fields are placed on the sites of the lattice, whereas the gluon fields are link variables connecting two neighboring sites. The theory is well defined and leads itself to numerical simulations enabling the calculation of expectation values by employing Monte Carlo techniques including importance sampling.

We will briefly introduce the framework of lattice QCD starting with the path integral formalism and the lattice discretization. Moreover, we discuss the lattice discretizations of the fermion and gauge action giving further details about the action employed within this thesis.

2.2.1 Path integral formalism

One possibility to quantize a field theory is the path integral formalism proposed by Feynman [29], which is also well suited for the lattice QCD formalism. Applying this approach, the expectation value of an observable O can be expressed by an integral over all field configurations ψ, $\bar{\psi}$ and A_μ as

$$\langle O \rangle = \frac{1}{Z} \int D\psi D\bar{\psi} DA_\mu \; O[\psi, \bar{\psi}, A_\mu] \exp(-S[\psi, \bar{\psi}, A_\mu]), \tag{2.8}$$

where the quark fields ψ and $\bar{\psi}$ are Grassmann valued[1] to incorporate Fermi-Dirac statistics. The partition function Z is defined as

$$Z = \int D\psi D\bar{\psi} DA_\mu \; \exp(-S[\psi, \bar{\psi}, A_\mu]) \tag{2.9}$$

and the Euclidean action S is given by integrating the Lagrangian $\mathcal{L}_{\mathrm{QCD}}$ in Eq. (2.1) over spacetime and performing a Wick-rotation, i.e., going to imaginary time $t \to i\tau$. As a consequence, Minkowski space is transformed into Euclidean space, leading to the Euclidean action

$$S[\psi, \bar{\psi}, A_\mu] = \int \mathrm{d}^4 x \; \frac{1}{4} F^a_{\mu\nu} F^a_{\mu\nu} + \sum_f \bar{\psi}^f \left(\gamma_\mu D_\mu + m_f \right) \psi^f, \tag{2.10}$$

where now the matrices γ_μ satisfy the Clifford algebra in the Euclidean metric $\{\gamma_\mu, \gamma_\nu\} = 2\delta_{\mu\nu}\mathbb{1}$. The integral contains a real valued weight factor $\exp(-S)$, enabling a stochastic estimation via Monte Carlo methods. This would not be possible having an oscillating complex exponential (a so-called sign problem).

As before, the first term of the action in Eq. (2.10) describes the gauge part whereas the second term corresponds to the fermionic part including the interactions between quarks and gluons. When discretizing the action on the lattice it is convenient to separate the gauge and the fermion parts as

$$S[\psi, \bar{\psi}, U] = S_G[U] + S_F[\psi, \bar{\psi}, U]. \tag{2.11}$$

The lattice action is not uniquely constrained by the continuum action and we will discuss the particular choices for the fermion and the gauge action employed within this thesis in the following. Note that on the lattice the gluon fields are represented by the variables U which will be introduced in the next section.

---

[1]i.e., anticommuting as for example $\{\psi^f_{\alpha,k}, \psi^{f'}_{\alpha',k'}\} = 0$
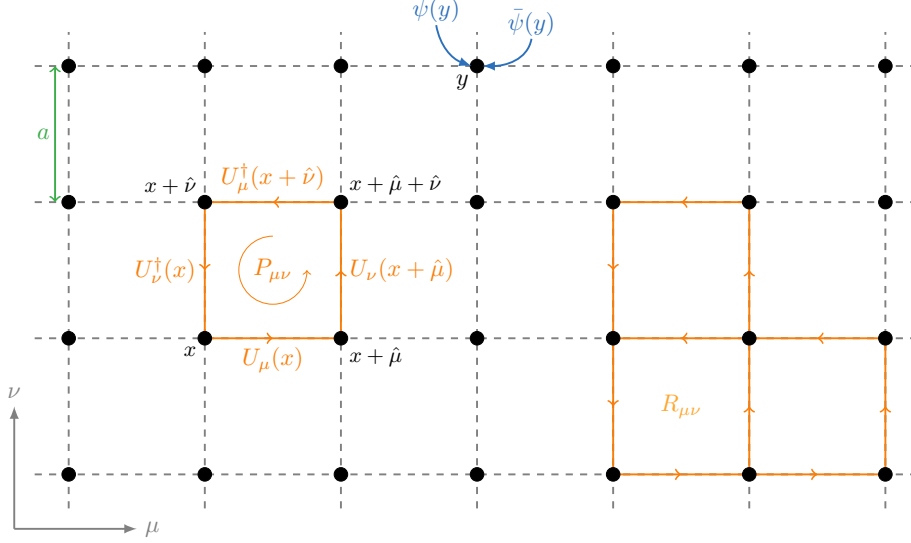
Figure 2.1: Sketch of the μ-ν-plane of a lattice with lattice spacing a. The fermion fields (blue) are sitting on the sites, whereas two neighboring sites are connected by link variables U_μ. A counter clockwise oriented plaquette $P_{\mu\nu}$ built from four link variables and the rectangular 1×2 and 2×1 loops $R_{\mu\nu}$ are depicted in orange.

2.2.2 Lattice discretization

The integral in Eq. (2.8) is still not well defined since it requires integration over infinitely many gauge field variables. To solve this problem one can discretize the Euclidean spacetime on a finite four dimensional hypercubic lattice given by a set of points (sites), separated by the lattice spacing a. This lattice can be denoted as

$$
\begin{aligned}
\Lambda = \{ x = an; \ n = (n_0, n_1, n_2, n_3) \ | \\
n_0 = 0, 1, \ldots, N_t - 1; \ n_1, n_2, n_3 = 0, 1, , \ldots, N_s - 1 \},
\end{aligned}
\tag{2.12}
$$

with $V = a^3 N_s^3$ being the spatial volume and aN_t the Euclidean time extend of the lattice. In principle, the lattice spacing a does not have to be the same in all directions, so one can construct anisotropic lattices with different lattice spacings in different directions. In addition, there are different boundary conditions which can also be chosen independently for different directions of the lattice. Popular choices include, e.g., (anti-)periodic, open or Schrödinger functional boundary conditions. Within this thesis, isotropic lattices are employed and details on the boundary conditions are discussed in section 2.3.2 below. The ultraviolet and the infrared cutoff, introduced by the lattice spacing and the finite lattice extend, respectively, have to be removed to obtain physical results by taking the continuum limit ($a \to 0$) and the infinite volume limit ($V \to \infty$, $aN_t \to \infty$).

When discretizing QCD, the quark fields $\psi(x)$ and $\bar{\psi}(x)$ are put on the sites x of the lattice. Further, the gluon fields, represented by the group valued variables

$$
U_\mu(x) = \mathcal{P} \exp \left(i \int_x^{x+\hat{\mu}} \mathrm{d}x' A_\mu(x') \right) \in \mathrm{SU}(3),
\tag{2.13}
$$

introduced further below, live on the links connecting two neighboring sites x and $x + \hat{\mu}$. Here the algebra valued gauge fields A_μ have been rescaled as $A_\mu \to \frac{1}{g} A_\mu$, $\hat{\mu}$ is a vector with length $|\hat{\mu}| = a$ in direction μ and $\mathcal{P}$ stands for the path ordered product. Figure 2.1 shows a schematic representation of the lattice.

The lattice version of the action should preserve the same local rotational SU(3) invariance as the continuum action, hence one imposes the same transformation properties for the fermion fields as in Eqs. (2.4) and (2.5) with a group element $V(x) \in$ SU(3). In the free fermion action, i.e., with $A_\mu = 0$, the derivative can be discretized in a symmetric derivative form as

$$\partial_\mu \psi(x) \to \frac{\psi(x + \hat{\mu}) - \psi(x - \hat{\mu})}{2a} + O(a^2). \tag{2.14}$$

However, this derivative is not invariant under local transformations of the fermion fields and one has to introduce gauge fields with transformation properties

$$U_\mu(x) \to V(x) U_\mu(x) V^\dagger(x + \hat{\mu}) \tag{2.15}$$

in order to preserve gauge invariance. Furthermore the orientation of the fields are related by

$$U_{-\mu}(x) \equiv U_\mu^\dagger(x - \hat{\mu}). \tag{2.16}$$

The link variables U_μ also exist in the continuum theory. They are the so-called gauge transporters

$$G(x, y) = \mathcal{P} \exp\left(i \int_\mathcal{C} A \cdot \mathrm{d}s \right), \tag{2.17}$$

where $\mathcal{C}$ is a curve between points x and y. The gauge transporter $G(x, x + \hat{\mu})$ has the same transformation properties (2.15) as the link variable $U_\mu(x)$. On the lattice the group valued link variables U_μ as given in Eq. (2.13) are now the new fundamental variables.

2.2.3 Fermion action

Having introduced the gluon fields U_μ as link variables we will now discuss the fermion action. Including link variables, terms like $\bar{\psi}(x) U_\mu(x) \psi(x + \hat{\mu})$ are gauge invariant and the simplest form of the discretized and gauge invariant fermion action for a single quark flavour reads

$$S_F[\psi, \bar{\psi}, U] = a^4 \sum_{x \in \Lambda} \bar{\psi}(x) \left[\gamma_\mu \left(\nabla_\mu + \nabla_\mu^* \right) + m \right] \psi(x). \tag{2.18}$$

The discretized forward and backward covariant derivatives ∇_μ and ∇_μ^* are given by

$$\nabla_\mu \psi(x) = \frac{U_\mu(x) \psi(x + \hat{\mu}) - \psi(x)}{2a}, \tag{2.19}$$

$$\nabla_\mu^* \psi(x) = \frac{\psi(x) - U_\mu^\dagger(x - \hat{\mu}) \psi(x - \hat{\mu})}{2a} \tag{2.20}$$

and the integral over Euclidean spacetime has been replaced by a sum over all lattice sites

$$\int \mathrm{d}^4 x \to a^4 \sum_{x \in \Lambda}. \tag{2.21}$$

Performing the continuum limit $a \to 0$, this so-called naive fermion action indeed yields the continuum form of the fermion action. However, this action suffers from the fermion doubling problem, meaning that it will effectively describe sixteen fermion species instead of one. The doubling problem can be solved by adding to the fermion action a further

irrelevant term of dimension five, called the Wilson term, in such a way to provide an infinite mass to the fifteen unwanted species in the continuum limit.

Within this thesis we employ the Clover-Wilson fermion action for the three lightest quark flavours $f \in \{u, d, s\}$ given by [28, 30]

$$S_F^W[\psi, \bar{\psi}, U] = a^4 \sum_f \sum_{x \in \Lambda} \bar{\psi}^f(x) D(U, m_f) \psi^f(x), \tag{2.22}$$

where the Dirac operator for a single flavour reads

$$D(U, m_f) = \left[\gamma_\mu \left(\nabla_\mu + \nabla_\mu^* \right) - a\Delta - a\frac{c_{SW}}{4} \sigma_{\mu\nu} \hat{F}^{\mu\nu}(x) + m_f \right]. \tag{2.23}$$

The second term with $\Delta = \nabla_\mu^* \nabla_\mu$ is the Wilson term removing the "doublers". In the third term $\hat{F}^{\mu\nu}$ is the lattice discretization of the field strength tensor, see, e.g., Ref. [31]. Following Symanzik's improvement programme [32–34], this so-called clover term[2] is added to remove the discretization effects of order a. A non-perturbative determination of the clover coefficient c_{SW} [35] can effectively remove completely the leading order discretization effects from the fermion action which leaves us with $O(a^2)$ discretization effects only.

One finds that the Wilson term explicitly breaks chiral symmetry on the lattice, i.e.,

$$\gamma_5 D + D\gamma_5 = 0 \tag{2.24}$$

is violated also in the massless limit for the Dirac operator (2.23). In fact, Nielsen and Ninomiya [36–38] showed that it is not possible to construct a fermion action which is ultralocal, free of doublers and invariant under chiral symmetry. However the Dirac operator (2.23) fulfills the property

$$\gamma_5 D = D^\dagger \gamma_5, \tag{2.25}$$

known as γ_5-hermiticity, which implies that the eigenvalues of the Dirac operator come in complex conjugate pairs. Therefore it is ensured that the fermion determinant is real which enables numerical simulations as will be discussed later.

Note again, the discretized lattice action is not unique and there exists a variety of (Symanzik improved) fermion actions having different properties in the literature.

2.2.4 Gauge action

Having a suitable lattice discretization of the fermion action one also needs to construct a gauge invariant gluon action on the lattice. One way to build a gauge invariant object on the lattice from gluon fields is to take the trace over the ordered product of link variables along a closed loop, called Wilson loop. The simplest Wilson loops are the 1×1 plaquette $P_{\mu\nu}$ constructed by the product of four link variables in a plane

$$P_{\mu\nu}(x) = U_\mu(x) U_\nu(x + \hat{\mu}) U_\mu^\dagger(x + \hat{\nu}) U_\nu^\dagger(x) \tag{2.26}$$

and the planar rectangular loop $R_{\mu\nu}$ (of length six), which in the 2×1 case is given by

$$R_{\mu\nu}(x) = U_\mu(x) U_\mu(x + \hat{\mu}) U_\nu(x + 2\hat{\mu}) U_\mu^\dagger(x + \hat{\mu} + \hat{\nu}) U_\mu^\dagger(x + \hat{\nu}) U_\nu^\dagger(x), \tag{2.27}$$

---

[2]The 'clover term' was first introduced by Sheikholeslami and Wohlert in 1985 [30], where the name stems from the fact that the field strength tensor $\hat{F}^{\mu\nu}$ can be expressed in terms of sums over four adjacent plaquettes which are associated with forming a clover leaf.

see Fig. 2.1 for a graphical illustration. The traces of these loops, being gauge invariant quantities, can be used to construct the gauge action for the gluons. The first formulation was proposed by Wilson [28] and is given by

$$S_G^W[U] = \frac{\beta}{6} \sum_P \text{Re Tr} \left[\mathbb{1} - P_{\mu\nu}(x) \right], \tag{2.28}$$

where $\beta = 6/g^2$ and one sums over all plaquettes P of the lattice. It can be shown, that this action reproduces, in the naive continuum limit $a \to 0$, the continuum gauge action. The Wilson gauge action has lattice cutoff effects of $O(a^2)$ as we have for our fermion action. However, there are various approaches to construct improved actions to accelerate the convergence of the limit $a \to 0$.

In this thesis we employ the tree-level Lüscher-Weisz gauge action [39]

$$S_G^{LW}[U] = \frac{\beta}{6} \left(c_0 \sum_P \text{Re Tr} \left[\mathbb{1} - P_{\mu\nu}(x) \right] + c_1 \sum_R \text{Re Tr} \left[\mathbb{1} - R_{\mu\nu}(x) \right] \right). \tag{2.29}$$

The coefficients c_k, for which the normalization $c_0 + 8c_1 = 1$ must hold, can be chosen such that the leading order discretization effects cancel in the linear combinations of the sums over all plaquettes and all rectangular loops on the lattice. For the action used in the simulations $c_0 = 5/3$ and $c_1 = -1/12$ [40]. This leaves us with $\mathcal{O}(\alpha_s a^2)$ discretization effects. Note that for $c_1 = 0$ we again obtain the Wilson gauge action from Eq. (2.28).

Again, many different lattice actions can be written down that reproduce the correct continuum limit of QCD, so that the lattice action provided here is not unique. A review of lattice actions employed in the current literature can be found in Appendix A.1 of the 2019 Flavour Lattice Averaging Group (FLAG) review [41].

2.3 Lattice QCD simulations

So far we quantized QCD via the Feynmann path integral formalism and constructed an appropriate action (discretized on a finite Euclidean spacetime lattice) summarized by

$$S[\psi, \bar{\psi}, U] = S_G^{LW}[U] + S_F^W[\psi, \bar{\psi}, U], \tag{2.30}$$

see Eqs. (2.22) and (2.29) for the fermion and gauge action, respectively, where in the following we will drop the superscripts again. In order to obtain physical results one needs to compute expectation values of gauge invariant observables by computing integrals like

$$\langle O[\psi, \bar{\psi}, U] \rangle = \frac{1}{Z} \int D\psi D\bar{\psi} DU \; O[\psi, \bar{\psi}, U] \exp(-S[\psi, \bar{\psi}, U]), \tag{2.31}$$

with Z defined such that $\langle \mathbb{1} \rangle = \mathbb{1}$ (cf. Eq. (2.9)).

The next section first very briefly outlines the key concepts used in lattice QCD simulations [42] and then gives an overview over the gauge ensembles analysed in this work. For more details on lattice QCD simulations see Refs. [24, 43]. Section 2.3.2 has already been published in similar or verbatim form in Ref. [SW2].

2.3.1 Generation of gauge ensembles

As already mentioned above, the quark fields ψ and $\bar{\psi}$ have Grassmannian nature, making a numerical evaluation on classical computers unfeasible. However, the fermion action is a bilinear functional in the quark fields ($S_F[\psi, \bar{\psi}, U] = \bar{\psi} D[U] \psi$), which enables us to integrate them out analytically. The Gaussian integral over the Grassmann variables in

the partition function Z yields the so-called fermion determinant of the Dirac operator $\det(D[U])$ and one finds that expectation values can be computed as

$$\langle O[U]\rangle = \int DU\, P[U]\; O[D^{-1}[U], U],\tag{2.32}$$

where

$$P[U] = \frac{1}{Z}\prod_f \det(D_f[U])\exp(-S_G[U])\tag{2.33}$$

can be interpreted as a probability distribution and $D^{-1}[U]$ denotes the inverse of the Dirac operator, i.e., the quark propagator. All quark field dependence is gone and one is left with an integration over only the link variables U_μ where the integration measure is given by

$$DU = \prod_{x\in\Lambda}\prod_\mu \mathrm{d}U_\mu(x).\tag{2.34}$$

Note that when introducing so-called pseudo-fermion fields ϕ the fermion determinant for two mass-degenerate quark flavours can be evaluated as

$$\det(D_f[U])^2 \propto \int D\phi D\phi^\dagger \exp\left(-\phi^\dagger (D_f[U]D_f[U]^\dagger)^{-1}\phi\right).\tag{2.35}$$

The pseudo-fermion fields ϕ have the same number of degrees of freedom as the fermion fields ψ but are Gaussian distributed random variables instead of Grassmann numbers. This approach will be used in the Hybrid Monte Carlo (HMC) algorithm [44] applied for the generation of gauge ensembles, see discussion below.

Trying to compute the integral in Eq. (2.32) through, e.g., numerical quadrature, is again unfeasible or even impossible and the method of choice is to use a stochastic approach to evaluate the path integral. In a typical lattice QCD simulation one therefore generates an ensemble of gauge field configurations distributed according to the probability distribution Eq. (2.33) using Markov chain Monte Carlo methods.[3] Because of the factor $e^{-S[U]}$, which can be interpreted as a Boltzmann weight factor, the contributions from many configurations will be negligible due to exponential suppression. Thus uniform sampling would be inefficient and one tries to only sample configurations giving the largest contributions to the path integral using importance sampling. To achieve this the Metropolis [46] or the more favored HMC algorithm can be used. The latter is a combination of the Molecular Dynamics algorithm with a Metropolis accept-reject step. Applying such algorithms, the phase-space is traversed by generating a set of configurations where the new configuration is constructed from the previous one. Sets of successive configurations created in this way are called Markov chains. Note that this approach can only be used if the gauge action $S_G[U]$ as well as the fermion determinant $\det(D[U])$ are real and positive. The gauge configurations actually used in this thesis are generated with the openQCD code [47, 48]. The HMC simulations are stabilized by introducing a twisted mass term for the degenerate $N_f = 2$ light quarks [48] and the strange quark is included via an improved rational HMC (RHMC) algorithm [49]. For further details see references above. The modifications of the target action are corrected for by applying the appropriate reweighting, see Refs. [50–52] for further details.

---

[3]Recently the 'master field' approach [45] is investigated where an ensemble of Markov chain Monte Carlo configurations is replaced by one single very large gauge field configuration.

Having an ensemble of N gauge field configurations, the expectation value Eq. (2.32) can be estimated by

$$\langle O \rangle = \frac{1}{N} \sum_{i=1}^{N} O(D^{-1}[U_i], U_i) + O(1/\sqrt{N}),$$ (2.36)

with a statistical error proportional to $O(1/\sqrt{N})$. More details on error estimation is given in Appendix B.

To save computer time earlier lattice QCD studies often were performed in the 'quenched approximation', i.e., setting $\det(D[U]) = \mathbb{1}$ and effectively neglecting sea quark contributions. Today's state-of-the-art lattice simulations include $N_f = 2 + 1$ or $N_f = 2 + 1 + 1$ dynamical sea quarks for the three, respectively four, lightest quark flavors $f \in \{u, d, s, c\}$. Typically simulations are performed with the up and down quarks being mass degenerate (isospin symmetry, $N_f = 2$) and the masses of the heavier (strange and charm) quarks tuned to match their physical values. However, there exist also simulations away from the isospin symmetric point with different masses for the up and down quarks and including QED effects, see, e.g., Ref. [53].

2.3.2 Overview of analysed gauge ensembles

In this thesis we employ gauge ensembles generated with $N_f = 2 + 1$ flavours of non-perturbatively $O(a)$ improved Wilson fermions and the Lüscher-Weisz gauge action. The ensembles were mostly produced within the Coordinated Lattice Simulations (CLS) [50] effort. Either periodic or open boundary conditions in time [54] are imposed, where the latter choice is necessary for ensembles with $a < 0.06$ fm in order to avoid freezing of the topological charge and thus to ensure ergodicity [55].
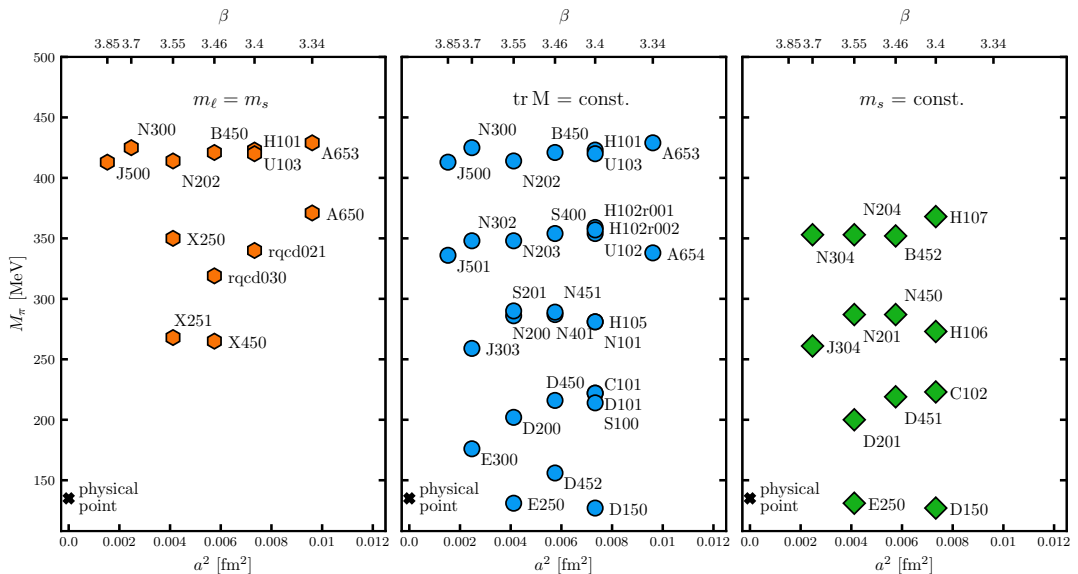
Figure 2.2: Parameter landscape of the ensembles listed in table D.1. The ensembles are grouped according to the three quark mass trajectories (see the text and Fig. 2.3): (left) the symmetric line ($m_\ell = m_s$), (middle) the Tr $M = $ const. line and (right) the $m_s = $ const. line.

In total 47 ensembles were analysed spanning six lattice spacings a in the range 0.039 fm $\lesssim a \lesssim 0.098$ fm, with pion masses between 430 MeV and 130 MeV (below the physical pion mass), as shown in Fig. 2.2. The lattice spatial extent L is kept sufficiently large, where $LM_\pi \geq 4$ for the majority of the ensembles. A limited number of smaller volumes are employed to enable finite volume effects to be investigated, with the spatial

extent varying across all the ensembles in the range $3.0 \leq LM_\pi \leq 6.5$. Further details are given in Table D.1. The ensembles lie along three trajectories in the quark mass plane, as displayed in Fig. 2.3:

- the symmetric line: the light and strange quark masses are degenerate ($m_\ell = m_s$) and SU(3) flavour symmetry is exact.

- The $\mathrm{Tr}\, M = \mathrm{const.}$ line: starting at the $m_\ell = m_s$ flavour symmetric point, the trajectory approaches the physical point holding the trace of the quark mass matrix ($2m_\ell + m_s$, i.e., the flavour average quark mass) approximately constant such that $2M_K^2 + M_\pi^2$ is close to its physical value.

- The $m_s = \mathrm{const.}$ line: the renormalized strange quark mass is kept near to its physical value [56].

The latter two trajectories intersect close to the physical point, whereas the symmetric line is interesting, in particular, for extrapolations to the SU(3) chiral limit.
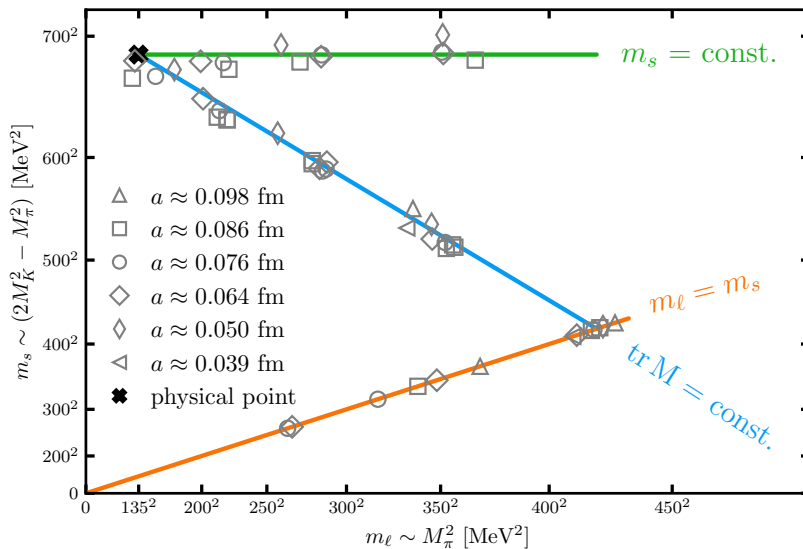
Figure 2.3: Position of the ensembles in the quark mass plane. The $\mathrm{Tr}\, M = \mathrm{const.}$ line (indicated as a blue line) and $m_s = \mathrm{const.}$ line (green line) intersect close to the physical point (black cross). The symmetric line (orange line), which approaches the SU(3) chiral limit, crosses the $\mathrm{Tr}\, M = \mathrm{const.}$ line around $M_\pi = 411\,\mathrm{MeV}$.

2.4 Lattice QCD workflow

In the preceding sections the framework of the lattice QCD discretization and the generation of gauge field ensembles have been discussed. Within this section we will introduce a somewhat higher level aspect of lattice QCD calculations, namely the general workflow of a full lattice QCD calculation, following Ref. [SW9]. We will find that everything discussed so far completes the first part of the lattice QCD workflow while the remaining parts are subject to chapter 3.

The goal of a typical lattice QCD calculation, and in particular the focus of this thesis, is to obtain results of physical observables which then can be compared to experimental findings or used as input to other theoretical calculations. Ideally, such calculations should lead to high precision results. Nowadays, state-of-the-art lattice calculations involve large amounts of data, typically of the order of PetaBytes (PB), making a proper data and workflow management more and more essential.

Figure 2.4: Illustration of the generic lattice QCD workflow factorized into three parts [57] (gray boxes): generation, measurements and analysis. For simplicity further details within the three sub-workflows are omitted. The input (simulation and measurement) parameters are in general included in the metadata and are available in the subsequent workflows.

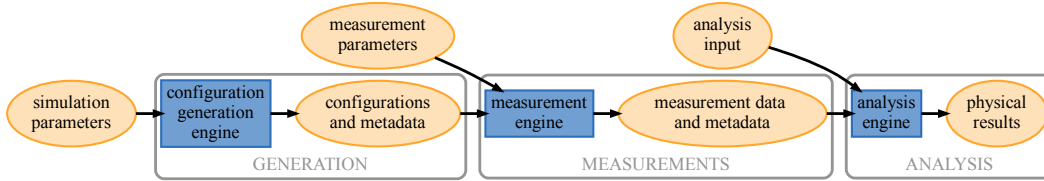Lattice QCD calculations, in their most general form, factorize into three parts [57] commonly referred to as generation, measurements and analysis. Figure 2.4 illustrates the generic workflow that is applicable to the work presented in this thesis. The first (generation) part of the workflow consists of the generation of gauge field ensembles (c.f. section 2.3). Note that this step was not carried out as part of this thesis and all gauge ensembles were already available for further analysis. In the second (measurements) part, correlation functions are computed on the gauge configurations. Within this project two- and three-point correlation function measurements, as described in section 3.2, were carried out. This part (along with the generation part) is computationally intensive and has to be performed on supercomputers such as, e.g., JUWELS [58] or JURECA Booster [59]. In total, approximately 1 PB of gauge configurations were analysed and nearly 2 PB of stochastic three-point correlation function data (see section 3.3) were generated as part of this thesis. In the third (analysis) part, performing a statistical analysis, physical observables are extracted from the correlation functions and extrapolated to the continuum, infinite volume and (chiral or physical) quark mass limits. The physical results we are primarily interested in within this thesis are the baryon charges as defined in section 3.1 which we extrapolate to the physical point. The large number of analysed ensembles covering a wide range of the parameter space allows us to investigate the systematic effects associated with the calculations, as further explained in section 3.6. In the end, the statistical and systematic uncertainties should be fully assessed in order to perform a reliable comparison with experiment.

As a large amount of data is generated at different stages of the workflow described above, it is crucial to maintain the reproducibility and reusability of these datasets. To this end, Ref. [SW9] presents an initial step towards applying provenance workflow modeling to lattice QCD calculations. For further details and in particular a brief introduction to workflow provenance see Ref. [SW9].

3 | MEASUREMENT AND ANALYSIS METHODS

Before presenting the results from the analysis of the leading order SU(3) LECs in chapter 4 and the octet baryon isovector charges in chapter 5 this chapter will review the main technical aspects of the associated measurement and analysis methods.

First the octet baryon charges and some related quantities of interest are defined in section 3.1. Then, in section 3.2, details about the calculation of two- and three-point correlation functions will be given. These correlation functions are the fundamental building blocks of the subsequent analysis and enable one to extract physical results such as masses or matrix elements from lattice QCD calculations. In terms of the lattice QCD workflow factorization, defined in section 2.4 above, see in particular Fig. 2.4, the measurements of correlation functions constitutes the second part. A computationally efficient stochastic approach for calculating baryon three-point functions is described in section 3.3. While the stochastic estimation of baryon three-point functions was already implemented in the course of Ref. [60] (recommended for further details), the results obtained within this thesis are the first substantial results employing this method.

In the subsequent sections, we lay the foundations for part three of the lattice QCD workflow, i.e., the analysis of physical observables extracted from correlation functions. Section 3.4 provides details on the extraction of the ground state matrix elements of interest from the correlation functions and the problem of excited state contaminations. All relevant renormalization factors needed to match the matrix elements to the continuum $\overline{\text{MS}}$ (modified minimal subtraction) scheme and improvement coefficients to ensure leading $O(a^2)$ discretization effects are collected in section 3.5. Then, in section 3.6 the systematic effects associated with the final results of the baryon charges obtained from lattice QCD calculations are discussed. Finally, section 3.7 outlines the strategy for the interpolation/extrapolation of the baryon charges to the physical point in the continuum and infinite volume limit. Within this extrapolation strategy all sources of systematic uncertainty associated with simulating at unphysical quark mass, finite volume and finite lattice spacing are carefully investigated.

Parts of this chapter are based on Ref. [24] or are taken in similar or verbatim form from [26] and [SW2]. General definitions and conventions can be found in Appendix A while some of the basic statistical concepts and methods applied within the data analysis part are described in Appendix B.

3.1 Octet baryon charges

All light baryons (i.e., baryons without charm or bottom quarks)[1] with strangeness $S < 0$, i.e., with a net difference between the numbers of strange (s) antiquarks and quarks are usually called hyperons (and antihyperons for $S > 0$). The spin-1/2 baryon octet,

---

[1]Note that hadrons including top quarks do not exist since the hadronization time is much longer then the mean lifetime of the top quark decaying via the weak force.

depicted in Fig. 1.2, contains the nucleons $N \in \{p, n\}$, besides the $S = -1$ hyperons Λ^0 and $\Sigma \in \{\Sigma^+, \Sigma^0, \Sigma^-\}$ and the $S = -2$ hyperons $\Xi \in \{\Xi^0, \Xi^-\}$ (cascades). Within this thesis isospin symmetry $m_\ell = m_u = m_d$ is assumed, where m_ℓ corresponds to the average mass of the physical up (u) and down (d) quarks. In this case, the baryon masses within isomultiplets are degenerate and simple relations exist between matrix elements that differ in terms of the isospin I_3 of the baryons and of the local operator (current).

Baryon charges $g_J^{B'B}$ are obtained from matrix elements of the form

$$\langle B'(p', s')|\bar{u}\Gamma_J d|B(p, s)\rangle = g_J^{B'B}\bar{u}_{B'}(p', s')\Gamma_J u_B(p, s) \tag{3.1}$$

at zero four-momentum transfer $q^2 = (p' - p)^2 = 0$. Above, $u_B(p, s)$ denotes the Dirac spinor of a baryon B with four momentum p and spin s. We restrict ourselves to $\Delta I_3 = 1$ transitions within the baryon octet. In this case $p' = p$, since in isosymmetric QCD $m_{B'} = m_B$, and it is sufficient to set $\mathbf{p} = \mathbf{0}$. Rather than using the above $I_3 = 1$ currents $\bar{u}\Gamma_J d$ (where the vector and axial currents couple to the W^- boson), it is convenient to define $I_3 = 0$ isovector currents,

$$\mathcal{O}_J(x) = \bar{u}(x)\Gamma_J u(x) - \bar{d}(x)\Gamma_J d(x), \tag{3.2}$$

and the corresponding charges g_J^B,

$$\langle B(p, s)|\mathcal{O}_J|B(p, s)\rangle = g_J^B \bar{u}_B(p, s)\Gamma_J u_B(p, s), \tag{3.3}$$

which, in the case of isospin symmetry, are trivially related to the $g_J^{B'B}$:

$$g_J^N := g_J^p = g_J^{pn}, \tag{3.4}$$

$$g_J^\Sigma := g_J^{\Sigma^+} = -\sqrt{2}\, g_J^{\Sigma^+\Sigma^0}, \tag{3.5}$$

$$g_J^\Xi := g_J^{\Xi^0} = -g_J^{\Xi^0\Xi^-}. \tag{3.6}$$

Note that we do not include the Λ baryon here since in this case the isovector combination trivially gives zero. We consider vector (V), axialvector (A), scalar (S) and tensor (T) operators which are defined through the Dirac matrices (see, e.g., Appendix A.2) $\Gamma_J = \gamma_4, \gamma_i\gamma_5, \mathbb{1}, \sigma_{ij}$ for $J \in \{V, A, S, T\}$, where $i, j \in \{1, 2, 3\}$ and $i < j$.

The axial charges in the $m_s = m_\ell = 0$ chiral limit are important parameters in SU(3) ChPT and enter the expansion of every baryonic quantity. These couplings can be decomposed into two LECs F and D which appear in the first order meson-baryon Lagrangian for three light quark flavours (see, e.g., Ref. [61]):

$$g_A^N = F + D, \quad g_A^\Sigma = 2F, \quad g_A^\Xi = F - D. \tag{3.7}$$

Due to group theoretical constraints, see, e.g., Refs. [62, 63], such a decomposition also holds for $m_s = m_\ell > 0$, for the axial as well as for the other charges. We define for $m = m_s = m_\ell$

$$g_J^N(m) = F_J(m) + D_J(m), \tag{3.8}$$

$$g_J^\Sigma(m) = 2F_J(m), \tag{3.9}$$

$$g_J^\Xi(m) = F_J(m) - D_J(m), \tag{3.10}$$

where $F = F_A(0)$ and $D = D_A(0)$.

3.2 Correlation functions

The octet baryon charges defined in the previous section are extracted from two- and three-point correlation functions of the form

$$C_{2\text{pt}}^B(t) = \mathcal{P}_+^{\alpha\beta} \sum_{\mathbf{x}} \langle \mathcal{B}_\alpha(\mathbf{x}, t)\, \bar{\mathcal{B}}_\beta(\mathbf{0}, 0) \rangle, \tag{3.11}$$

$$C_{3\text{pt}}^B(t, \tau; \mathcal{O}_J) = \mathcal{P}^{\alpha\beta} \sum_{\mathbf{x},\mathbf{y}} \langle \mathcal{B}_\alpha(\mathbf{x}, t) \mathcal{O}_J(\mathbf{y}, \tau) \bar{\mathcal{B}}_\beta(\mathbf{0}, 0) \rangle. \tag{3.12}$$

Here $\mathcal{B}$ and $\mathcal{P}$ denote the appropriate interpolators and projection operators which are discussed in the following in more detail.

On the lattice baryon states with the quantum numbers of interest are created (annihilated) using suitable interpolators $\bar{\mathcal{B}}$ ($\mathcal{B}$). A generic form of a baryon interpolator is given by

$$\mathcal{B}_\alpha(x) = \epsilon_{abc} \Gamma^1_{\alpha,\alpha'} \psi^{f_1}_{\alpha',a}(x) \left(\psi^{f_2}_{\beta,b}(x) \Gamma^2_{\beta,\gamma} \psi^{f_3}_{\gamma,c}(x) \right), \tag{3.13}$$

with quark fields ψ and (Γ^1, Γ^2) being suitable combinations of γ-matrices. For simplicity, in the following we will denote a quark field ψ^f with flavour $f \in \{u, d, s\}$ by its flavour as, e.g., $\psi^u = u$. Common choices for the Γ-matrices are $(\Gamma^1, \Gamma^2) = (\mathbb{1}, C\gamma_5)$ and $(\Gamma^1, \Gamma^2) = (\mathbb{1}, C\gamma_j)$ for spin-1/2 octet and spin-3/2 decuplet baryons, respectively, where C denotes the charge conjugation matrix. Within this thesis we are only interested in spin-1/2 octet baryon states for the nucleon, Σ and Ξ, where we employ the interpolators corresponding to the proton, Σ^+ and Ξ^0, respectively,

$$N_\alpha = \epsilon^{abc} u^a_\alpha \left(u^{bT} C\gamma_5 d^c \right), \tag{3.14}$$

$$\Sigma_\alpha = \epsilon^{abc} u^a_\alpha \left(s^{bT} C\gamma_5 u^c \right), \tag{3.15}$$

$$\Xi_\alpha = \epsilon^{abc} s^a_\alpha \left(s^{bT} C\gamma_5 u^c \right). \tag{3.16}$$

These interpolators are constructed from spatially extended quark fields in order to increase the overlap with the ground state of interest and minimize contributions to the correlation functions from excited states. Wuppertal (Gauss) smearing [64] is employed on the quark fields

$$\psi^{(n)}(x) = \frac{1}{1 + 6\delta} \left(\psi^{(n-1)}(x) + \delta \sum_{i=\pm 1}^{\pm 3} U_i(x) \psi^{(n-1)}(x + a\hat{i}) \right), \tag{3.17}$$

where we set $\delta = 0.25$. The number of smearing iterations (n) is varied with the aim of ensuring that ground state dominance sets in for moderate time separations. The root mean squared quark smearing radius r_{sm}^2 is defined by

$$r_{\text{sm}}^2 = \sum_{n_1,n_2,n_3=-N_s/2}^{N_s/2-1} \psi^\dagger(\mathbf{n}a)\mathbf{n}^2 a^2 \psi(\mathbf{n}a), \qquad \sum_{n_1,n_2,n_3=-N_s/2}^{N_s/2-1} \psi^\dagger(\mathbf{n}a)\psi(\mathbf{n}a) = 1, \tag{3.18}$$

where the light quark smearing radii range from about 0.6 fm (for $M_\pi \approx 430$ MeV) up to about 0.8 fm (for $M_\pi \approx 130$ MeV). See section E.1 (in particular Table 15) of Ref. [52] for further details including the smearing radii for the strange quarks. In order to illustrate the effect of fixed smearing radii, Fig. 3.1 shows as an example the effective mass of the nucleon and the Ξ which in lattice units is defined as

$$am_{\text{eff}}^B(t + a/2) = \log \left(\frac{C_{2\text{pt}}^B(t)}{C_{2\text{pt}}^B(t + a)} \right). \tag{3.19}$$
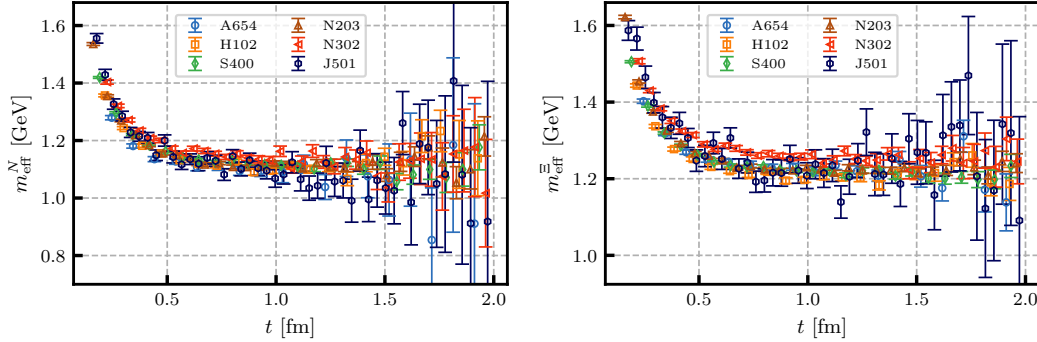
Figure 3.1: Effective masses (see Eq. (3.19)) in physical units of the nucleon (left) and Ξ (right) determined on ensembles with $M_\pi \approx 340\,\mathrm{MeV}$ and $M_K \approx 450\,\mathrm{MeV}$ and lattice spacings ranging from $a = 0.098\,\mathrm{fm}$ (ensemble A654) down to $a = 0.039\,\mathrm{fm}$ (ensemble J501).

This demonstrates that, when keeping for similar pion and kaon masses the smearing radii fixed in physical units, the ground state dominates the two-point functions at similar physical times across different lattice spacings. An alternative quark field smearing method is, e.g., Jacobi smearing [65].

In addition to the quark fields, the gauge links $U_i(x)$ in Eq. (3.17) are APE-smeared [66] via

$$U_i^{(n)}(x) = P_{\mathrm{SU}(3)}\left(\alpha U_i^{(n-1)}(x) + \sum_{j \neq i} S_{ij}^{(n-1)}(x)\right), \tag{3.20}$$

where $i, j \in \{1, 2, 3\}$, $P_{\mathrm{SU}(3)}$ projects into the SU(3) group, the weight factor α is set to $\alpha = 2.5$ and we apply $n = 25$ iterations. The sum in Eq. (3.20) sums all four spatial "staples" adjacent to $U_i^{(n)}(x)$ where

$$\begin{aligned} S_{ij}^{(n)}(x) &= U_j^{(n)}(x)U_i^{(n)}(x + a\hat{j})U_j^{\dagger(n)}(x + a\hat{i}) \\ &\quad + U_j^{\dagger(n)}(x - a\hat{j})U_i^{(n)}(x - a\hat{j})U_j^{(n)}(x - a\hat{j} + a\hat{i}). \end{aligned} \tag{3.21}$$

Other popular algorithms to reduce the short distance fluctuations of the gauge field configurations are HYP [67] or stout [68] smearing. Smeared gauge fields are only used for the construction of interpolators and smeared quark fields. The computations for propagating quarks are performed on the unsmeared gauge configurations, thereby not modifying the fermionic action.

Having constructed the appropriate interpolators for the analysis, the two- and three-point functions from Eqs. (3.11) and (3.12) are constructed for the three baryons $B \in \{N, \Sigma, \Xi\}$ and the isovector current combination $\mathcal{O}_J = \bar{u}\Gamma_J u - \bar{d}\Gamma_J d$ for $J \in \{V, A, S, T\}$. Without loss of generality, we place the source space-time position at the origin $(\mathbf{0}, 0)$ and the sink at $(\mathbf{x}, t)$ such that the source-sink separation in time equals t. The current is inserted at $(\mathbf{y}, \tau)$ with $0 \leq \tau \leq t$.[2] The annihilation interpolators are projected onto zero-momentum via the sums over the spatial sink position, while momentum conservation (and the sum over $\mathbf{y}$ for the current) means the source is also at rest. We ensure positive parity via the projection operator $\mathcal{P}_+ = \frac{1}{2}(\mathbb{1} + \gamma_4)$. For the three-point functions, $\mathcal{P} = \mathcal{P}_+$ for $J = V, S$ and $\mathcal{P} = i\gamma_i\gamma_5\mathcal{P}_+$ for $J = A, T$. The latter corresponds to taking the difference of the polarizations (in the i direction).

Computing the integrals over the Grassmann valued quark fields ψ, i.e., evaluating the expectation value $\langle\cdot\rangle$ over the fermion fields, the expectation values of correlation functions

---

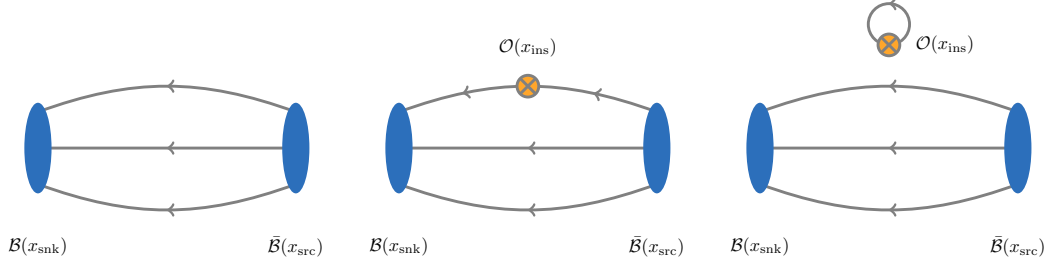[2]In practice only data with $2a \leq \tau \leq t - 2a$ is analysed.

Figure 3.2: Quark-line diagrams of the two-point (left) and connected three-point (middle) correlation functions where $x_{\mathrm{src}} = (\mathbf{0}, 0)$, $x_{\mathrm{ins}} = (\mathbf{y}, \tau)$ and $x_{\mathrm{snk}} = (\mathbf{x}, t)$. The disconnected quark-line diagrams for the three-point functions (left) cancel when forming the isovector flavour combination of the current.

are related to quark propagators using Wick's theorem. Performing these so called Wick contractions for the two- and three-point correlation functions leads to the connected quark-line diagrams displayed in Fig. 3.2. Note that, there are no disconnected quark-line diagrams for the three-point functions as these cancel when forming the isovector flavour combination of the current.

For the example of a nucleon two-point correlation function the Wick contractions yield

$$C_{\mathrm{2pt}}^{N}(t) = \mathcal{P}_{+}^{\alpha\bar{\alpha}} \sum_{\mathbf{x}} \langle N_{\alpha}(\mathbf{x}, t) \, \bar{N}_{\bar{\alpha}}(\mathbf{0}, 0) \rangle$$

$$= \mathcal{P}_{+}^{\alpha\bar{\alpha}} \sum_{\mathbf{x}} \epsilon^{abc} \epsilon^{\bar{a}\bar{b}\bar{c}} (C\gamma_{5})_{\beta\gamma} (C\gamma_{5})_{\bar{\gamma}\bar{\beta}} \langle \, u_{\alpha}^{a}(x) \, u_{\beta}^{b}(x) \, d_{\gamma}^{c}(x) \, \bar{d}_{\bar{\gamma}}^{\bar{c}}(0) \, \bar{u}_{\bar{\beta}}^{\bar{b}}(0) \, \bar{u}_{\bar{\alpha}}^{\bar{a}}(0) \, \rangle$$

$$= \mathcal{P}_{+}^{\alpha\bar{\alpha}} \sum_{\mathbf{x}} \epsilon^{abc} \epsilon^{\bar{a}\bar{b}\bar{c}} (C\gamma_{5})_{\beta\gamma} (C\gamma_{5})_{\bar{\gamma}\bar{\beta}}$$

$$\times D_{\gamma\bar{\gamma}}^{c\bar{c}}(x, 0) \left(U_{\beta\bar{\beta}}^{b\bar{b}}(x, 0) U_{\alpha\bar{\alpha}}^{a\bar{a}}(x, 0) - U_{\alpha\bar{\beta}}^{a\bar{b}}(x, 0) U_{\beta\bar{\alpha}}^{b\bar{a}}(x, 0) \right). \quad (3.22)$$

In the last line $U(x, y)$ and $D(x, y)$ denotes the quark propagator $\left[D^{-1}(x, y)\right]_{f}$ (i.e., the inverse of the Dirac operator D_{f}) describing a quark propagating from point y to x with flavour $f = u$ and $f = d$, respectively. Similar expressions including one additional propagator are obtained for the three-point functions $C_{\mathrm{3pt}}^{B}(t, \tau; \mathcal{O}_{J})$.

The two-point functions are constructed in the standard way using point-to-all propagators $G_{f}(x, x_{0})$ describing the propagation from a fixed space-time point x_{0} to all other points x. To obtain the point-to-all propagator one has to solve the equation

$$\sum_{x} D_{f}(y, x) G_{f}(x, x_{0}) = S(y, x_{0}), \quad (3.23)$$

where $S(y, x_{0})$ is a smeared (see Eq. (3.17)) point-source $\delta(y - x_{0})\delta_{\alpha,\alpha_{0}}\delta_{a,a_{0}}$. In total, 12 inversions have to be performed, one for each combination of the spin (α_{0}) and colour (a_{0}) index, to obtain the point-to-all propagator.

In Fig. 3.2 the quark-line diagram for the connected three-point function contains an all-to-all quark propagator which connects the current insertion at time τ with the baryon sink at time t. The all-to-all propagator is computationally too expensive to evaluate exactly. One commonly used approach avoids directly calculating the propagator by constructing a sequential source [69] which depends on the baryon sink interpolator (including its temporal position and momentum). The sequential propagator $\Sigma_{f}(x, x_{0})$ is obtained by again solving an equation of the form

$$D_{f}(y, x) \Sigma_{f}(x, x_{0}) = S_{\mathrm{seq}}(y, x_{0}), \quad (3.24)$$

which is similar to Eq. (3.23) but now the sequential source $S_{\text{seq}}(y, x_0)$ is given by a linear combination of products of point-to-all propagators (of the quark-lines of the connected three-point function without a current insertion) and γ-matrices (of the baryon interpolator and the projection operator).

For the three-point functions either the sequential source method (on some ensembles in combination with the coherent sink technique [70]) or a stochastic approach (described in the next section) is employed. The stochastic approach provides a computationally cost efficient way of evaluating the three-point functions for the whole of the baryon octet, however, additional noise is introduced, see section 3.3 for details. The relevant measurements for the nucleon (which has the worst signal-to-noise ratio of the octet) have already been performed with the sequential source method as part of other projects by our group, see, e.g., Ref. [71]. We use these data in our analysis and the stochastic approach for the correlation functions of the Σ and the Ξ baryons. Note that along the symmetric line ($m_\ell = m_s$) the hyperon three-point functions can be obtained as linear combinations of the contractions carried out for the currents $\bar{u}\Gamma_J u$ and $\bar{d}\Gamma_J d$ within the proton, see section 4.2.2 for more details. Therefore, no stochastic three-point functions are generated in these cases.

We typically realize four source-sink separations with $t/\text{fm} \approx \{0.7, 0.8, 1.0, 1.2\}$ in order to investigate excited state contamination and reliably extract the ground state baryon octet charges. Details of the fitting analysis are presented in section 3.4. Multiple measurements are performed per configuration, in particular for the larger source-sink separations to improve the signal, see Table D.2. The source positions are chosen randomly on each configuration in order to reduce autocorrelations. On ensembles with open boundary conditions in time only the spatial positions are varied and the source and sink time slices are restricted to the bulk of the lattice (sufficiently away from the boundaries), where translational symmetry is effectively restored.

3.3 Stochastic three-point correlation functions

In the following, the construction of the connected three-point correlation functions using a computationally efficient stochastic approach is described. This method was introduced for computing meson three-point functions in Ref. [72] and utilized for baryons in Refs. [73, 74] and also for mesons in Refs. [75, 76]. Similar stochastic approaches have been implemented by other groups, see, e.g., Refs. [77, 78]. For further details on the implementation within our group see Ref. [60] for the baryon and Ref. [79] for the meson three-point functions.

The sequential source method as discussed in the previous section has the disadvantage that one needs to compute a new quark propagator for each source-sink separation, sink momentum and baryon sink interpolator. Alternatively, one can estimate the all-to-all propagator stochastically. This introduces additional noise on top of the gauge noise, however, the quark-line diagram can be computed in a very efficient way. The stochastic approach allows one to factorize the three-point correlation function into a "spectator" and an "insertion" part which can be computed and stored independently with all spin indices and one colour index open. This is illustrated in Fig. 3.3 and explained in more detail below. The spectator and insertion parts can be contracted at a later (post-processing) stage with the appropriate spin and polarization matrices, such that arbitrary baryonic interpolators can be realized, making this method ideal for SU(3) flavour symmetry studies. Furthermore, no additional inversions are needed for different sink momenta.

As depicted in Fig. 3.4, we simultaneously compute the three-point functions for a baryon propagating (forwards) from source timeslice x_4 to sink timeslice $x_4^{\prime,\text{fwd}}$ and propagating (backwards) from x_4 to $x_4^{\prime,\text{bwd}}$. We start with the definition of the stochastic source
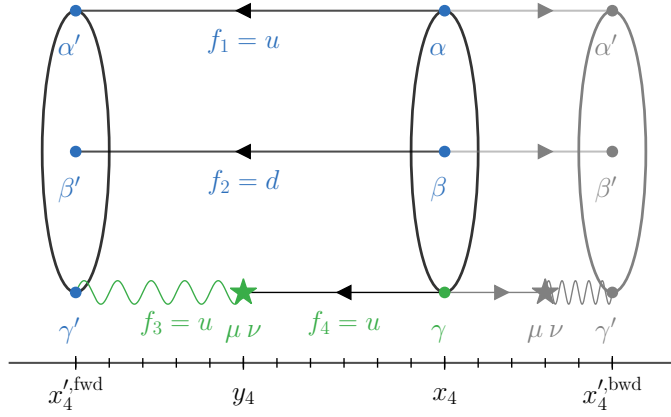
Figure 3.3: Schematic representation of the forward (left) and backward (right, shown in grey) propagating three-point correlation functions with open spin indices that are computed simultaneously with the stochastic approach. The indices corresponding to the spectator and insertion part from the factorization in Eq. (3.30) are colour-coded in blue and green, respectively. The (black) solid lines correspond to the standard point-to-all propagators, whereas the (green) wiggly lines represent stochastic timeslice-to-all propagators. The temporal positions of the forward/backward sink, insertion and source are labelled as $x_4^{\prime,\text{fwd}|\text{bwd}}$, y_4 and x_4, respectively. The flavour indices are chosen corresponding to a nucleon three-point function with a $\bar{u}\Gamma_J u$-current insertion.

and solution vectors which can be used to construct the timeslice-to-all propagator (shown as a green wiggly line in Fig. 3.3). In the following $i \in \{1, \ldots, N_{\text{sto}}\}$ is the "stochastic index", we denote spin indices with Greek letters, colour indices with Latin letters (other than f or i) and we use flavour indices $f_n \in \{u, d, s\}$. We introduce (time partitioned) complex $\mathbb{Z}_2$ noise vectors [80, 81]

$$\eta_i(x)_a^\alpha = \begin{cases} (\mathbb{Z}_2 \otimes i\mathbb{Z}_2)/\sqrt{2} & \text{if} \quad x_4 = x_4^{\prime,\text{fwd}|\text{bwd}} \\ \\ 0 & \text{otherwise}, \end{cases}, \tag{3.25}$$

where the noise vector has support on timeslices $x_4^{\prime,\text{fwd}}$ and $x_4^{\prime,\text{bwd}}$. The noise vectors have the properties

$$\frac{1}{N_{\text{sto}}} \sum_{i=1}^{N_{\text{sto}}} \eta_i(x)_a^\alpha = O\left(\frac{1}{\sqrt{N_{\text{sto}}}}\right), \tag{3.26}$$

$$\frac{1}{N_{\text{sto}}} \sum_{i=1}^{N_{\text{sto}}} \eta_i(x)_a^\alpha \eta_i^*(y)_b^\beta = \delta_{xy}\delta_{\alpha\beta}\delta_{ab} + O\left(\frac{1}{\sqrt{N_{\text{sto}}}}\right). \tag{3.27}$$

The solution vectors $s_{f,i}(y)$ are defined through the linear system

$$D_f(x,y)_{ab}^{\alpha\beta} s_{f,i}(y)_b^\beta = \eta_i(x)_a^\alpha, \tag{3.28}$$

where we sum over repeated indices (other than f) and $D_f(x,y)_{ab}^{\alpha\beta}$ is the Wilson-Dirac operator for the quark flavour f. Note that $s_{u,i} = s_{d,i}$ since our light quarks are mass-degenerate.

Using γ_5-Hermiticity ($\gamma_5 D_f \gamma_5 = D_f^\dagger$) and the properties given in Eqs. (3.26) and (3.27), the timeslice-to-all propagator connecting all points of the (forward and backward) sink
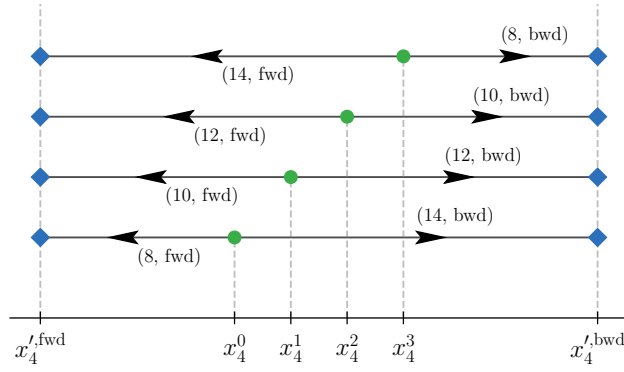
Figure 3.4: Sketch of the source and sink positions of the three-point functions realized using the stochastic approach. Blue diamonds depict the position of the forward ($x_x'^{,\mathrm{fwd}}$) and backward ($x_x'^{,\mathrm{bwd}}$) sink timeslices. Green points correspond to the source timeslices x_4^k for $k = 0, 1, 2, 3$. Each three-point function measurement is labelled by the source-sink separation, where the values given correspond to the set-up for the ensembles at $\beta = 3.40$.

timeslices x_4' to all points of any insertion timeslice y_4 can be estimated as

$$G_{f_3}(x', y)_{c'd}^{\gamma'\mu} \approx \frac{1}{N_{\mathrm{sto}}} \sum_{i=1}^{N_{\mathrm{sto}}} \left[\gamma_5 \eta_i(x')\right]_{c'}^{\gamma'} \left[\gamma_5 s_{f_3}^*(y)\right]_d^\mu. \tag{3.29}$$

Combining this timeslice-to-all propagator with point-to-all propagators for the source position x_4, baryonic three-point correlation functions can be factorized as visualized in Fig. 3.3 into a spectator part (S) and an insertion part (I), leaving all flavour and spin indices open:

$$C_{\mathrm{3pt}}(\mathbf{p}', \mathbf{q} | x_4', y_4, x_4)_{f_1 f_2 f_3 f_4}^{\alpha'\alpha\beta'\beta\gamma'\mu\nu\gamma}$$

$$\approx \frac{1}{N_{\mathrm{sto}}} \sum_{i=1}^{N_{\mathrm{sto}}} \sum_{c=1}^{3} \left(S_{f_1 f_2}(\mathbf{p}', x_4', x_4)_{ic}^{\alpha'\alpha\beta'\beta\gamma'} I_{f_3 f_4}(\mathbf{q}, y_4, x_4)_{ic}^{\mu\nu\gamma} \right). \tag{3.30}$$

The spectator and insertion parts are defined as

$$S_{f_1 f_2}(\mathbf{p}', x_4', x_4)_{ic}^{\alpha'\alpha\beta'\beta\gamma'}$$

$$:= \sum_{\mathbf{x}'} \left(\epsilon_{a'b'c'} \epsilon_{abc} G_{f_1}(x', x)_{a'a}^{\alpha'\alpha} G_{f_2}(x', x)_{b'b}^{\beta'\beta} \left[\gamma_5 \eta_i(x')\right]_{c'}^{\gamma'} e^{-i\mathbf{p}'\cdot(\mathbf{x}'-\mathbf{x})} \right), \tag{3.31}$$

$$I_{f_3 f_4}(\mathbf{q}, y_4, x_4)_{ic}^{\mu\nu\gamma} := \sum_{\mathbf{y}} \left[\gamma_5 s_{f_3,i}^*(y)\right]_d^\mu G_{f_4}(y, x)_{dc}^{\nu\gamma} e^{+i\mathbf{q}\cdot(\mathbf{y}-\mathbf{x})}. \tag{3.32}$$

Using these building blocks, three-point functions for given baryon interpolators and currents for any momentum combination can be constructed. Note that within this thesis only the case $\mathbf{q} = \mathbf{p}' = \mathbf{0}$ is considered. The point-to-all propagators within the spectator part are smeared at the source and at the sink, whereas G_{f_4} is only smeared at the source. The stochastic source is smeared too, however, this is carried out after solving Eq. (3.28). In principle, the spectator part also depends on f_3 because for $f_3 = s$ and $f_3 \in \{u, d\}$ different smearing parameters are used. We ignore the dependence of the spectator part on f_3 since the analysis of this work is restricted to $f_3, f_4 \in \{u, d\}$. For details on the smearing see the previous section. Using the same set of timeslice-to-all propagators, we compute point-to-all propagators for a number of different source positions at timeslices
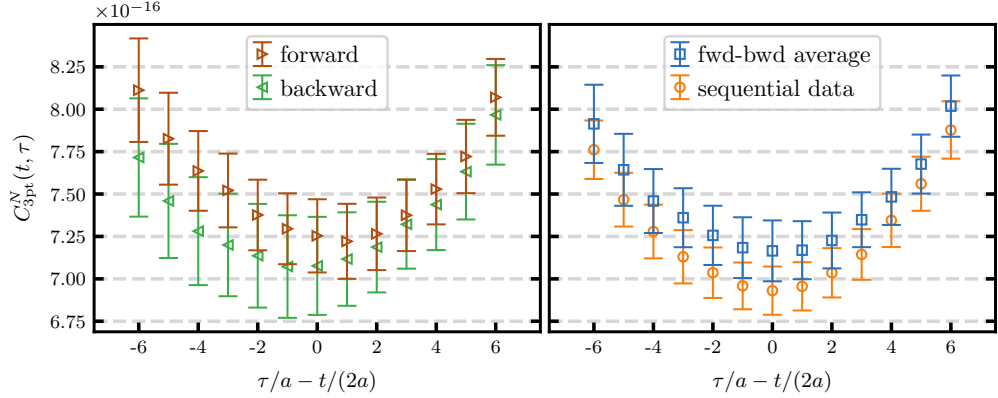
24

Figure 3.5: Left: polarized nucleon three-point correlation function propagating in the forward and backward directions for a $\bar{u}\gamma_y\gamma_z u$ current insertion obtained from one stochastic measurement on ensemble N200 ($a = 0.064\,\mathrm{fm}$). Note that two different source positions were needed to obtain the same source-sink separation $t = 14a$ in the two directions, see Fig. 3.4. Right: forward-backward average of the stochastic three-point function shown on the left compared to that obtained using the sequential source method (with one source position, propagating in the forward direction).

x_4 in-between $x_4'^{,\mathrm{bwd}}$ and $x_4'^{,\mathrm{fwd}}$ which allows to vary the source-sink distances, see Figs. 3.3 and 3.4.

The number of stochastic estimates N_{sto} is chosen by balancing the computational cost against the size of the stochastic noise introduced. We find that for $N_{\mathrm{sto}} \gtrsim 100$ the stochastic noise becomes relatively small compared to the gauge noise and we employ 100 estimates across all the ensembles. In some channels the signal obtained for the three-point function, after averaging over the forward and backward directions, is comparable to that obtained from the traditional sequential source method (for a single source, computed in the forward direction), as shown in Fig. 3.5. Nonetheless, when taking the ratio of the three-point function over the two-point function for the fitting analysis, discussed in the next section, a significant part of the gauge noise cancels, while the stochastic noise remains. This results in larger statistical errors in the ratio for the stochastic approach, which is a particular problem in the vector channel. A more detailed comparison of the two methods is given in Appendix C.

As mentioned above, only flavour conserving currents and zero momentum transfer are considered here. However, in the course of this thesis, the data to construct three-point functions with flavour changing currents containing up to one derivative for various different momenta was also obtained, enabling an extensive investigation of (generalized) form factors in the future. Similarly, meson three-point functions can be constructed by computing the relatively inexpensive meson spectator part and (re-)using the insertion part, see Ref. [SW4] for first results.

3.4 Extraction of matrix elements and excited state analysis

The spectral decompositions of the two- and three-point correlation functions read

$$C_{2\mathrm{pt}}^B(t) = \sum_n |Z_n^B|^2 e^{-E_n^B t} , \tag{3.33}$$

$$C_{3\mathrm{pt}}^B(t,\tau;\mathcal{O}_J) = \sum_{n,m} Z_n^B Z_m^{B*} \langle n|\mathcal{O}_J|m\rangle e^{-E_n^B(t-\tau)} e^{E_m^B \tau}, \tag{3.34}$$

where E_n^B is the energy of state $|n\rangle$ ($n = 0, 1, \ldots$), created when applying the baryon interpolator $\bar{\mathcal{B}}$ to the vacuum state $|\Omega\rangle$ and Z_n^B is the associated overlap factor $Z_n^B \propto \langle n|\bar{\mathcal{B}}|\Omega\rangle$. The ground state matrix elements of interest $\langle 0|\mathcal{O}_J|0\rangle = g_J^{B,\text{latt}}$ can be obtained in the limit of large time separations from the ratio of the three-point and two-point functions

$$R_J^B(t, \tau) = \frac{C_{3\text{pt}}^B(t, \tau; \mathcal{O}_J)}{C_{2\text{pt}}^B(t)} \xrightarrow{t, \tau \to \infty} g_J^{B,\text{latt}}. \tag{3.35}$$

However, the signal-to-noise ratio of the correlation functions deteriorates exponentially with the time separation. For a nucleon two-point function the signal-to-noise ratio falls as $\sim \exp(-(m_N - \frac{3}{2}M_\pi)t)$ [82, 83] and the same can be expected to hold for three-point functions. With current techniques it is not possible to achieve a reasonable signal for separations that are large enough to ensure ground state dominance. At moderate t and τ, one observes significant excited state contributions to the ratio. All states with the same quantum numbers as the baryon interpolator contribute to the sums in Eqs. (3.33) and (3.34), including multi-particle excitations such as $B\pi$ P-wave and $B\pi\pi$ S-wave scattering states. The spectrum of states becomes increasingly dense as one decreases the pion mass while keeping the spatial extent of the lattice sufficiently large, where the lowest lying excitations are multi-particle states, see, e.g., discussion and in particular Fig. 2 in Ref. [84].

One possible strategy is to first determine the energies of the ground state and lowest lying excitations by fitting to the two-point function (which is statistically more precise than the three-point function) with a suitable functional form. The energies can then be used in a fit to the three-point function (or the ratio R_J^B) to extract the charge g_J^B.[3] However, the three-quark baryon interpolators we use by design have only a small overlap with the multi-particle states containing five or more quarks and antiquarks and it is difficult to extract the lower lying excited state spectrum from the two-point function. Nonetheless, multi-particle states can significantly contribute to the three-point function if the transition matrix elements $\langle n|\mathcal{O}_J|0\rangle$ are large. Furthermore, depending on the current, different matrix elements, and hence excited state contributions, will dominate. In particular, one would expect the axial and scalar currents to couple to the $B\pi$ P-wave and $B\pi\pi$ S-wave states, respectively, while the tensor and vector currents may enhance transitions between B and $B\pi\pi$ states when $\pi\pi$ is in a P-wave.

The summation method [69] is an alternative approach, which involves summing the ratio over the operator insertion time $S_J^B(t) = \sum_{\tau=\tau_0}^{t-\tau_0} R_J^B(t, \tau)$, where one can show that the leading excited state contributions to $S_J^B(t)$ only depend on t (rather than also on $t - \tau$ and τ as for $R_J^B(t, \tau)$). However, one needs a large number of source-sink separations (more than the four values of t that are realized in this study) in order to extract reliable results from this approach.

These considerations motivate to extract the charges by fitting to the ratio of correlation functions using a fit form which takes into account the contributions from up to two excited states,

$$R_J^B(t, \tau) = b_0^J + b_1^J \left(e^{-\Delta E_1(t-\tau)} + e^{-\Delta E_1 \tau} \right) + b_2^J e^{-\Delta E_1 t}$$
$$+ b_3^J \left(e^{-\Delta E_2(t-\tau)} + e^{-\Delta E_2 \tau} \right) + b_4^J e^{-\Delta E_2 t}. \tag{3.36}$$

where $\Delta E_n = E_n^B - E_0^B$ denotes the energy gap between the ground state and the nth excited state of the baryon B. The amplitude $b_0^J = g_J^{B,\text{latt}}$ gives the charge, while $b_{1,3}^J$ and $b_{2,4}^J$ are related to the ground state to excited state and excited state to excited state

---

[3]Given the precision of the two-point function relative to that of the three-point function, this strategy is very similar to fitting $C_{2\text{pt}}^B$ and $C_{3\text{pt}}^B$ simultaneously.

Table 3.1: Summary of the fits performed. We vary the combinations of channels J that are fitted simultaneously as well as the number of excited states (ES) included in the fit and the fit interval $\tau \in [\delta t, t - \delta t]$ with $\delta t \in \{\delta t_1, \delta t_2\}$, where $\delta t_1 \approx 0.15\,\mathrm{fm}$, $\delta t_2 \approx 0.25\,\mathrm{fm}$. The last two columns indicate which parameters in Eq. (3.36) are fixed by a prior or set to zero. All other parameters are determined in the fit.

Fit	J	δt	ES	prior	fixed parameter
1	A, S, T	δt_1	1	-	$b_2^J, b_3^J, b_4^J, \Delta E_2$
2	A, S, T	δt_2	1	-	$b_2^J, b_3^J, b_4^J, \Delta E_2$
3	A, S, T, V	δt_1	1	-	$b_2^J, b_3^J, b_4^J, \Delta E_2$
4	A, S, T, V	δt_2	1	-	$b_2^J, b_3^J, b_4^J, \Delta E_2$
5	A, S, T	δt_1	2	ΔE_1	b_1^T, b_2^J, b_4^J
6	A, S, T	δt_2	2	ΔE_1	b_1^T, b_2^J, b_4^J
7	A, S, T, V	δt_1	2	ΔE_1	$b_1^{T,V}, b_2^J, b_4^J$
8	A, S, T, V	δt_2	2	ΔE_1	$b_1^{T,V}, b_2^J, b_4^J$
9	A, S, T	δt_1	2	ΔE_1	b_2^J, b_4^J
10	A, S, T	δt_2	2	ΔE_1	b_2^J, b_4^J
11	A, S, T, V	δt_1	2	ΔE_1	b_2^J, b_4^J
12	A, S, T, V	δt_2	2	ΔE_1	b_2^J, b_4^J
13	A, S, T	δt_1	2	ΔE_2	b_1^T, b_2^J, b_4^J
14	A, S, T	δt_2	2	ΔE_2	b_1^T, b_2^J, b_4^J
15	A, S, T, V	δt_1	2	ΔE_2	$b_1^{T,V}, b_2^J, b_4^J$
16	A, S, T, V	δt_2	2	ΔE_2	$b_1^{T,V}, b_2^J, b_4^J$
17	A, S, T	δt_1	2	ΔE_2	b_2^J, b_4^J
18	A, S, T	δt_2	2	ΔE_2	b_2^J, b_4^J
19	A, S, T, V	δt_1	2	ΔE_2	b_2^J, b_4^J
20	A, S, T, V	δt_2	2	ΔE_2	b_2^J, b_4^J

transition matrix elements, respectively. In practice, even when simultaneously fitting to all available source-sink separations, it is difficult to determine the energy gaps (and amplitudes) for a particular channel J. Similar to the strategy pursued in Ref. [85], we simultaneously fit to all four channels $J \in \{V, A, S, T\}$ for a given baryon. As the same energy gaps are present, the overall number of fit parameters is reduced and the fits are further constrained.

To ensure that the excited state contributions are sufficiently under control, a variety of different fits, summarized in Table 3.1, are carried out, where we vary:

- the data sets included in the fit: simultaneous fits are performed to the data for $J \in \{A, S, T, V\}$ and $J \in \{A, S, T\}$. As the axial, scalar and tensor channels are the main focus of this study, we only consider excluding the vector channel data.

- the parametrization: either one ('ES=1') or two ('ES=2') excited states are included in the fits. In the latter case, in order to stabilize the fit, we use a prior for ΔE_1 corresponding to the energy gap for the lowest lying multi-particle state. As a cross-check we repeat these fits using the results obtained for ΔE_2 as a prior and leaving ΔE_1 as a free parameter (see the fits labelled 13–20). In general, the contributions from excited state to excited state transitions could not be resolved and the parameters $b_{2,4}$ are set to zero. We also found that the tensor and vector currents couple more strongly to the second excited state, consistent with the expectations mentioned above, and the first excited state contributions are omitted for these channels in the 'ES=2' fits. Furthermore, due to the large statistical error of the stochastic three-point functions for the Σ and Ξ baryons in the vector channel (see Fig. 3.6 and the discussion in Appendix C), we are not able to resolve b_1^V (and analogously b_3^V). For these baryons we also set $b_{1,3}^V = 0$ in all the fits.

- the fit range: two fit intervals $\tau \in [\delta t_j, t - \delta t_j]$ are used with $\delta t_1 = n_1 a \approx 0.15\,\mathrm{fm}$ and $\delta t_2 = n_2 a \approx 0.25\,\mathrm{fm}$.[4]

A typical fit to the ratios for the cascade baryon is shown in Fig. 3.6 for ensemble N302 ($M_\pi = 348\,\mathrm{MeV}$ and $a = 0.049\,\mathrm{fm}$). The variation in the ground state matrix elements extracted from the 20 different fits is shown in Fig. 3.7, also for the nucleon on the same ensemble. See Fig. E.1 in Appendix E for the analogous plot for the Σ baryon. Overall, the results are consistent within errors, however, some trends in the results can be seen across the different ensembles. In the axial channel, in particular the results for the fits involving a single excited state (fits 1–4), tend to be lower than those involving two excited states (fits 5–20). The former are, in general, statistically more precise than the latter due to the smaller number of parameters in the fit.

In order to study the systematics arising from any residual excited state contamination in the final results at the physical point (in the continuum limit at infinite volume), the extrapolations, detailed in section 3.7, are performed for the results obtained from fits 1–4 ('ES=1') and fits 5–8 ('ES=2'), separately. For each set of fits, 500 samples are drawn from the combined bootstrap distributions of the four fit variations. The final result and error, shown as the green and blue bands in Fig. 3.7, correspond to the median and the 68% confidence interval, respectively. Note that we take the same 500 bootstrap samples for all the baryons to preserve correlations. The final results for all the ensembles are listed in Tables D.5, D.6 and D.7 for the nucleon, sigma and cascade baryons, respectively.

In terms of the energy gaps extracted, Fig. 3.7 shows that we find consistency across variations in the fit range and whether the vector channel data is included or not. However, the first excited energy gap ΔE_1 obtained from the single excited state fits tends to be

---

[4]Due to $n_j \geq 2$ and its quantization, δt_1 and δt_2 depend slightly on the lattice spacing: $\delta t_j \approx 0.20\,\mathrm{fm}, 0.29\,\mathrm{fm}$ ($\beta = 3.34$), $\delta t_j \approx 0.17\,\mathrm{fm}, 0.26\,\mathrm{fm}$ ($\beta = 3.40$), $\delta t_j \approx 0.15\,\mathrm{fm}, 0.23\,\mathrm{fm}$ ($\beta = 3.46$), $\delta t_j \approx 0.13\,\mathrm{fm}, 0.26\,\mathrm{fm}$ ($\beta = 3.55$), $\delta t_j \approx 0.15\,\mathrm{fm}, 0.25\,\mathrm{fm}$ ($\beta = 3.70$), $\delta t_j \approx 0.16\,\mathrm{fm}, 0.27\,\mathrm{fm}$ ($\beta = 3.85$).
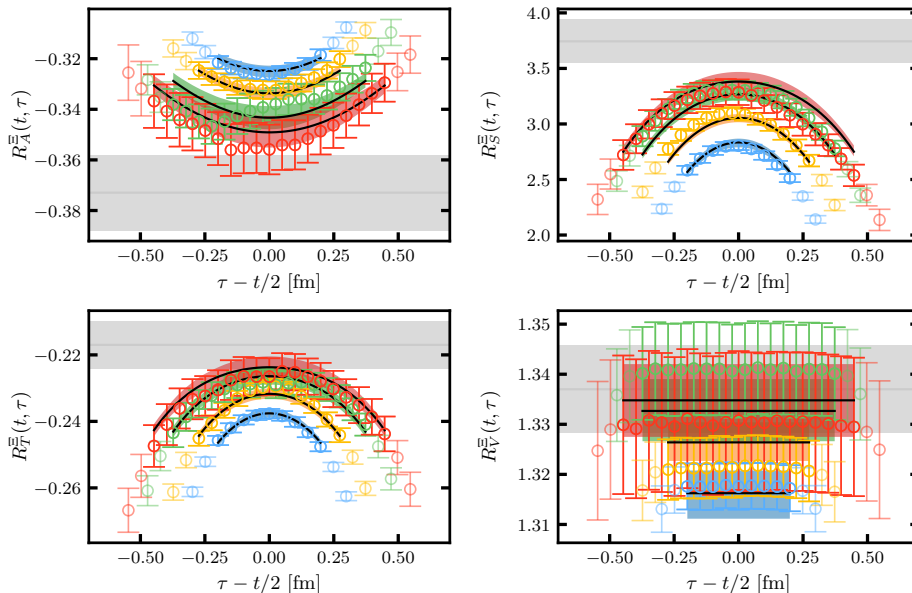
Figure 3.6: Unrenormalized ratios $R_J^\Xi(t,\tau)$, $J \in \{A, S, T, V\}$ (defined in Eq. (3.35)) for the cascade baryon on ensemble N302 ($M_\pi = 348\,\mathrm{MeV}$ and $a = 0.049\,\mathrm{fm}$), where $t \approx \{0.7, 0.8, 1.0, 1.2\}$ fm. The grey horizontal lines and bands show the results for the ground state matrix elements $\langle 0|\bar{u}\Gamma_J u - \bar{d}\Gamma_J d|0\rangle = g_J^{\Xi,\mathrm{latt}}$, obtained from a simultaneous fit to the ratios for all channels and source-sink separations using parametrization 7 (see Eq. (3.36) and Table 3.1). The data points with $\tau \in [\delta t, t - \delta t]$, where $\delta t = 2a$, are included in the fit (the faded data points are omitted), which is the maximum fit range possible for our action. The coloured curves show the expectation from the fit for each source-sink separation.

Figure 3.7: Results for the four unrenormalized charges of the nucleon (top) and cascade baryon (bottom) obtained from the fits listed in Table 3.1 for ensemble N302 ($M_\pi = 348\,\text{MeV}$ and $a = 0.049\,\text{fm}$). The green (blue) horizontal lines and bands indicate the final results and errors obtained from the median and 68% confidence level interval of the combined bootstrap distributions determined from the fits indicated by the green (blue) data points which include one (two) exc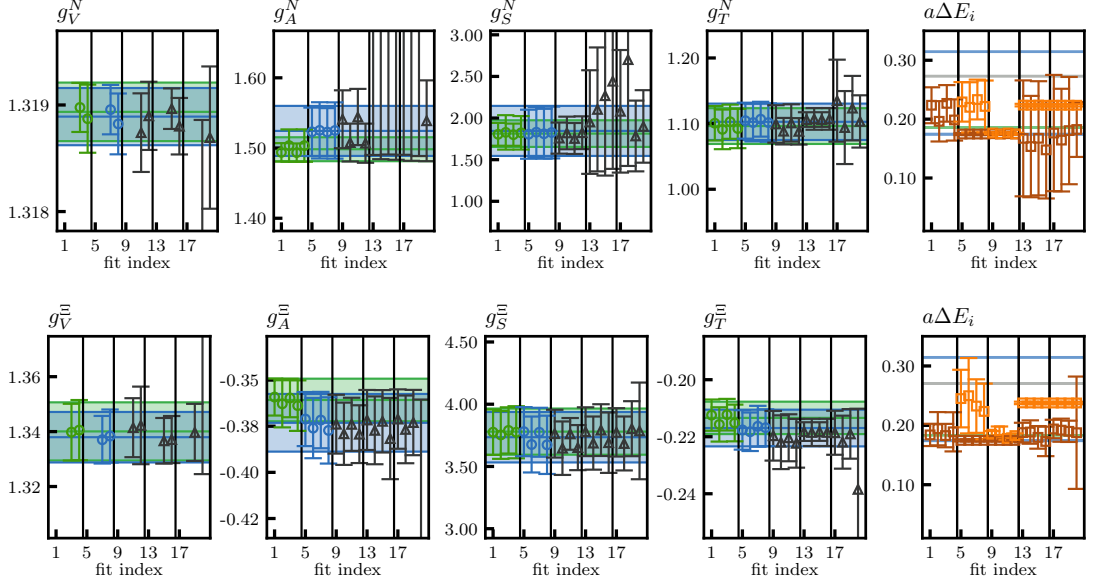ited state(s). On the right the energy gaps determined in the fits and those corresponding to the lowest lying multi-particle states are displayed using the same colour coding as in Fig. 3.8.
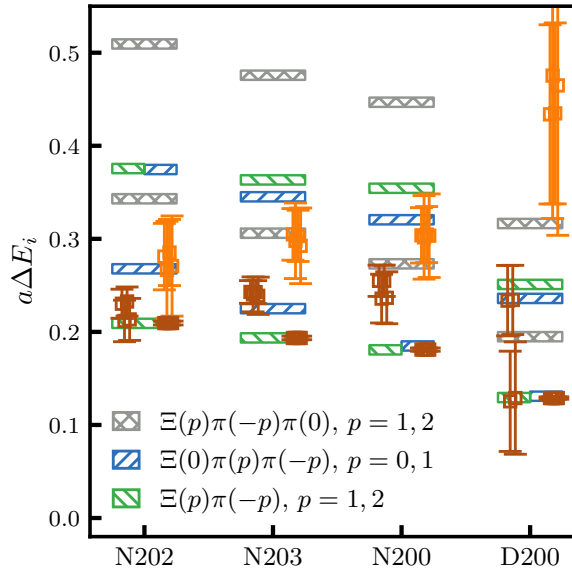
Figure 3.8: Results for the first and second excited state energy gaps of the cascade baryon, ΔE_1 (brown data points) and ΔE_2 (orange data points), respectively, determined on ensembles lying on the Tr $M =$ const. trajectory with $a = 0.064\,\text{fm}$. The pion mass decreases from left to right with $M_\pi = 414$ MeV for ensemble N202 and $M_\pi = 202$ MeV for ensemble D200, see Table D.1. For each ensemble, the ΔE_1 obtained using fits 1–4 of Table 3.1 are shown on the left and the ΔE_1 (fixed with a prior to the lowest multi-particle energy gap) and ΔE_2 resulting from fits 5–8 are displayed on the right. For comparison, the energy gaps of the lower lying non-interacting multi-particle states with the quantum numbers of the cascade baryon are shown as horizontal lines, where the momenta utilized for each hadron are indicated in lattice units.

higher than the lowest multi-particle level, in particular, as the pion mass is decreased, suggesting that contributions from higher excited states are significant. This can be seen in Fig. 3.8, where we compare the results for the energy gaps for the cascade baryon with the lower lying non-interacting $\Xi\pi$ and $\Xi\pi\pi$ states for four ensembles with $a = 0.064\,\mathrm{fm}$ and pion masses ranging from $414\,\mathrm{MeV}$ down to $202\,\mathrm{MeV}$. Note that the multi-particle levels are modified in a finite volume, although the corresponding energy shifts may be small for the large volumes realized here. There are a number of levels within roughly $500\,\mathrm{MeV}$ of the first excited state. Some levels lie close to each other and one would not expect that the difference can be resolved by fits with one or two excited states. The ΔE_2 energy gaps from the two excited state fits (with the first excited state fixed with a prior to the lowest multi-particle level) are consistent with the next level that is significantly above the first excited state, although for ensemble D200 the errors are too large to draw a conclusion. Given that more than one excited state is contributing significantly, we expect that the latter fits isolate the ground state contribution more reliably.

3.5 Non-perturbative renormalization and improvement

The isovector lattice charges, $g_J^{B,\mathrm{latt}}$, extracted in the previous section need to be matched to the continuum $\overline{\mathrm{MS}}$ scheme. The renormalized matrix elements suffer from discretization effects, however, the leading order effects are reduced to $O(a^2)$ when implementing full $O(a)$ improvement. In the forward limit, in addition to using a non-perturbatively $O(a)$ improved fermion action, this involves taking mass dependent terms into account. The following multiplicative factors are applied,

$$g_J^B = Z_J^k \left(1 + am_\ell b_J + 3a\bar{m}\tilde{b}_J\right) g_J^{B,\mathrm{latt}} + O(a^2), \tag{3.37}$$

for $J \in \{V, A, S, T\}$, where Z_J are the renormalization factors and b_J and $\tilde{b}_J$ are the $O(a)$ improvement coefficients. Note that the renormalization factors for the scalar and tensor currents depend on the scale, $Z_{S,T} = Z_{S,T}(\mu)$, where we take $\mu = 2\,\mathrm{GeV}$. The vector Ward identity lattice quark mass am_q is obtained from the hopping parameter κ_q ($q = \ell, s$) and the critical hopping parameter κ_{crit} via $am_q = (1/\kappa_q - 1/\kappa_{\mathrm{crit}})/2$. $\bar{m} = (2m_\ell + m_s)/3$ denotes the flavour averaged quark mass. The hopping parameters for all ensembles used within this work are tabulated in Table D.3. For κ_{crit} we utilize the interpolation formula [52]

$$\frac{1}{\kappa_{\mathrm{crit}}} = 8 - 0.402454g^2 \frac{1 + 0.28955g^2 - 0.1660g^6}{1 + 0.22770g^2 - 0.2540g^4}. \tag{3.38}$$

The improvement coefficients b_J and $\tilde{b}_J$ are determined non-perturbatively in Ref. [86]. We make use of updated preliminary values, which will appear in a future publication [87]. These are listed in Tables 3.2 and 3.3, respectively. Note that no estimates of $\tilde{b}_J$ are available for $\beta = 3.85$. Considering the size of the statistical errors, the general reduction of the $|\tilde{b}_J|$ values with increasing β (and the decreasing a), at this lattice spacing we set $\tilde{b}_J = 0$ for all J.

For the renormalization factors, we employ the values obtained in Ref. [88]. The factors are determined non-perturbatively in the RI$'$-SMOM (regularization independent symmetric momentum-subtraction) scheme [89, 90] and then (for Z_S and Z_T) converted to the $\overline{\mathrm{MS}}$ scheme using three-loop matching [91–93]. We remark that the techniques for implementing the Rome-Southampton method were extended in Ref. [88] to ensembles with open boundary conditions in time. This development enables us to utilize ensembles with $a < 0.06\,\mathrm{fm}$, where only open boundary conditions in time are available due to the need to maintain ergodicity.

Table 3.2: Improvement coefficients b_J for $J \in \{A, S, T, V\}$ from Refs. [86, 87].

β	b_A	b_S	b_T	b_V
3.34	1.249(16)	1.622(47)	1.471(11)	1.456(11)
3.4	1.244(16)	1.583(62)	1.4155(48)	1.428(11)
3.46	1.239(15)	1.567(74)	1.367(12)	1.410(13)
3.55	1.232(15)	1.606(98)	1.283(14)	1.388(17)
3.7	1.221(13)	1.49(11)	1.125(15)	1.309(22)
3.85	1.211(12)	1.33(16)	0.977(38)	1.247(26)

Table 3.3: Improvement coefficients $\tilde{b}_J$ for $J \in \{A, S, T, V\}$ from Refs. [86, 87]. Note that no results are available for $\beta = 3.85$.

β	$\tilde{b}_A$	$\tilde{b}_S$	$\tilde{b}_T$	$\tilde{b}_V$
3.34	-0.06(28)	-0.24(55)	1.02(16)	1.05(13)
3.4	-0.11(13)	-0.36(23)	0.49(17)	0.41(11)
3.46	0.08(11)	-0.421(83)	0.115(19)	0.158(28)
3.55	-0.03(13)	-0.25(12)	0.000(37)	0.069(42)
3.7	-0.047(75)	-0.274(65)	-0.0382(60)	-0.031(18)

Table 3.4: Set of renormalization factors taken from Ref. [88], denoted as Z_J^1 in the text. The factors are determined using the RI′-SMOM scheme and the 'fixed-scale method' with the perturbative subtraction of lattice artefacts. For Z_A and Z_V, the values correspond to those listed under Z_A' and Z_V', respectively, which are obtained using renormalization conditions consistent with the respective Ward identities. The statistical and systematic errors have been added in quadrature.

β	Z_A	$Z_S^{\overline{\mathrm{MS}}}(2\,\mathrm{GeV})$	$Z_T^{\overline{\mathrm{MS}}}(2\,\mathrm{GeV})$	Z_V
3.34	0.77610(58)	0.6072(26)	0.8443(35)	0.72690(71)
3.4	0.77940(36)	0.6027(25)	0.8560(35)	0.73290(67)
3.46	0.78240(32)	0.5985(25)	0.8665(36)	0.73870(71)
3.55	0.78740(22)	0.5930(25)	0.8820(37)	0.74740(82)
3.7	0.79560(98)	0.5846(24)	0.9055(42)	0.76150(94)
3.85	0.8040(13)	0.5764(25)	0.9276(42)	0.77430(76)

Table 3.5: Set of renormalization factors denoted as Z_J^2 in the text. These are determined as in Table 3.4 but this time using the 'fit method'.

β	Z_A	$Z_S^{\overline{\mathrm{MS}}}(2\,\mathrm{GeV})$	$Z_T^{\overline{\mathrm{MS}}}(2\,\mathrm{GeV})$	Z_V
3.34	0.7579(42)	0.6115(93)	0.8321(95)	0.7072(60)
3.4	0.7641(35)	0.6068(86)	0.8462(88)	0.7168(49)
3.46	0.7695(36)	0.6025(79)	0.8585(84)	0.7250(43)
3.55	0.7774(36)	0.5968(66)	0.8756(76)	0.7367(37)
3.7	0.7895(32)	0.5880(45)	0.9010(63)	0.7544(30)
3.85	0.8006(25)	0.5793(35)	0.9243(55)	0.7699(38)

A number of different methods are employed in Ref. [88] to determine the renormalization factors. In order to assess the systematic uncertainty arising from the matching in the final results for the charges at the physical point in the continuum limit, we make use of two sets of results, collected in Tables 3.4 and 3.5 and referred to as Z_J^1 and Z_J^2, respectively, in the following. The first set of results are extracted using the 'fixed-scale method', where the RI′-SMOM factors are determined at a fixed scale (ignoring discretization effects), while the second set are obtained by fitting the factors as a function of the scale and the lattice spacing, the 'fit method'. See Ref. [88] for further

Table 3.6: Renormalization factors Z_A and Z_V obtained from the interpolation formulas in Eqs. (C.7) and (C.8) in Ref. [94], denoted as Z_J^3 in the text.

β	Z_A	Z_V
3.34	0.7510(11)	0.7154(11)
3.4	0.75629(65)	0.72221(65)
3.46	0.76172(39)	0.72898(39)
3.55	0.76994(34)	0.73905(35)
3.7	0.78356(32)	0.75538(33)
3.85	0.79675(45)	0.77089(47)

details. In both cases, lattice artefacts are reduced by subtracting the perturbative one-loop expectation. For the axial and vector currents, we also consider a third set of renormalization factors, Z_J^3, listed in Table 3.6, that are obtained with the chirally rotated Schrödinger functional approach [95], see Ref. [94]. We emphasize that employing the different sets of renormalization factors should lead to consistent results for the charges in the continuum limit.

Within the analysis of the LECs presented in chapter 4, in addition to the axial charges $g_A^{B,latt}$ (see Eq. (3.37)), also the quark mass and the pion decay constant need to be renormalized. We also $O(a)$-improve these observables. Regarding the renormalization of the axial currents, we use the factors Z_A (denoted as Z_A^3) listed in Table 3.6. The renormalization factor $Z_M(g^2) = Z_A(g^2)/Z_P(g^2)$, required to translate the axial Ward identity (AWI) quark mass m^{AWI} into the renormalization group invariant (RGI) [96, 97] mass m, is given in Eq. (5.6) of Ref. [98]. We emphasize that both these factors have been computed entirely non-perturbatively. Using the improvement coefficients $b_A(g^2)$, $\tilde{b}_A(g^2)$, $b_P(g^2)$ and $\tilde{b}_P(g^2)$ [86], the observables can be renormalized and fully $O(a)$-improved at each value of the lattice coupling $g^2 = 6/\beta$ as follows:

$$m = Z_M \left[1 + am(b_A - b_P + 3\tilde{b}_A - 3\tilde{b}_P) \right] m^{\text{AWI}}, \tag{3.39}$$

$$F_\pi = Z_A^3 \left[1 + am(b_A + 3\tilde{b}_A) \right] F_\pi^{\text{latt}}, \tag{3.40}$$

where we assumed $m = m_\ell = m_s$, since in this analysis all ensembles incorporate exact SU(3) flavour symmetry.

3.6 Systematic effects in lattice QCD calculations

The results of the octet baryon charges determined from first principle lattice QCD calculations come with systematic uncertainties associated with

- not all quark flavours being simulated dynamically,
- unphysical quark masses,
- non-vanishing lattice spacing,
- finite volume,
- extraction of matrix elements from correlation functions at finite t, τ (fitting procedure),
- matching to the continuum $\overline{\text{MS}}$ scheme (renormalization).

In this study we employ gauge ensembles with $N_f = 2 + 1$ dynamical fermions. While in Nature six quark flavours exist, including the heavier charm (or even bottom or top)

quarks in the sea is not expected to lead to a discernible effect in the determination of the octet baryon charges. Further, we simulate the electrically neutral isosymmetric theory ($m_u = m_d$), which is broken in Nature. We take this into account and take the isospin corrected pion and kaon masses quoted in the FLAG 16 review [99] to define the physical point in the quark mass plane,

$$M_\pi^{\text{phys}} = 134.8(3)\,\text{MeV}, \qquad\qquad M_K^{\text{phys}} = 494.2(3)\,\text{MeV}. \qquad (3.41)$$

In chapter 5 isospin breaking effects on the up and down quark mass difference, the baryon masses and the pion baryon σ terms are discussed in more detail.

The 47 gauge ensembles analysed cover a range of pion masses between 430 MeV and 130 MeV (below the physical pion mass) and lie along three trajectories in the quark mass plan, see Fig. 2.3. Such excellent coverage of the quark mass plane enables the extrapolation/interpolation of the results for the charges to the physical point to be tightly constrained. In addition, considering the wide range of lattice spacings and spatial volumes and the high statistics available for most ensembles, all sources of systematic uncertainty associated with simulating at unphysical quark masses, finite lattice spacing and finite volume can be investigated. The strategy for performing a simultaneous quark mass, continuum and infinite volume extrapolation is given in the next section.

The problem of excited state contaminations in baryon matrix elements is well known and a careful analysis must be carried out to reliable determine the ground state matrix elements of interest, see section 3.4 for details. In order to study the systematics arising from any residual excited state contamination in the final results at the physical point (in the continuum limit at infinite volume), the extrapolations are performed for the results obtained from fits including one or two excited states in the fitting analysis, separately.

For details on the determination of the renormalization factors see discussion in section 3.5. Again, the extrapolations are carried out for different sets of renormalization factors to also assess the associated systematics.

3.7 Extrapolation strategy

In the final step of the analysis the renormalized charges g_J^B determined at unphysical quark masses, finite lattice spacing and finite spatial volume are extrapolated to the physical point in the continuum and infinite volume limits. We employ a similar strategy to the one outlined in Ref. [100] and choose continuum fit functions of the form

$$g_J^B(M_\pi, M_K, L, a = 0) = c_0 + c_\pi M_\pi^2 + c_K M_K^2 + c_V M_\pi^2 \frac{e^{-LM_\pi}}{\sqrt{LM_\pi}}, \qquad (3.42)$$

to parameterize the quark mass and finite volume dependence, where L is the spatial lattice extent and the coefficients c_X, $X \in \{0, \pi, K, V\}$ are understood to depend on the baryon B and the current J. The leading order coefficients c_0 give the charges in the SU(3) chiral limit, which can be expressed in terms of two LECs, e.g., F and D, for the axial charges, see Eq. (3.7).

Equation (3.42) is a phenomenological fit form based on the SU(3) ChPT expressions for the axial charge. It contains the expected $O(p^2)$ terms for the quark mass dependence and the dominant finite volume corrections. The $O(p^3)$ expressions for g_A^B [101–103] contain log terms with coefficients completely determined by the LECs F and D. In the study of the axial charges on the subset of ensembles with $m_s = m_\ell$ presented in chapter 4, it was found that including these terms did not provide a satisfactory description of the data. When terms arising from loop corrections that contain decuplet baryons are taken into account, additional LECs enter that are difficult to resolve. If the coefficient of the

Table 3.7: Values for $t_0^\star/a^2$ at each β-value as determined in Ref. [52].

β	3.34	3.4	3.46	3.55	3.7	3.85
$\frac{t_0^\star}{a^2}$	2.204(6)	2.888(8)	3.686(11)	5.157(15)	8.617(22)	13.988(34)

log term is left as a free parameter, one finds that the coefficient has the opposite sign to the ChPT expectation without decuplet loops. Similar observations have been made in the analysis of the octet baryon isovector charges presented in chapter 5 and this is also consistent with the findings of previous works, see, e.g., Refs. [104–106]. Finite volume effects appear at $O(p^3)$ with no additional LECs appearing in the coefficients. Again the signs of the corrections are the opposite to the trend seen in the data and, when included, it is difficult to resolve the effects of the decuplet baryons. As is shown in section 5.1, the data for all the charges are well described when the fit form is restricted to the dominant terms, with free coefficients c_0, c_π, c_K and c_V.

We remark that the same set of LECs appear in the $O(p^2)$ SU(3) ChPT expressions for the three different octet baryons (for a particular charge). Ideally, one would carry out a simultaneous fit to the whole baryon octet (taking the correlations between the g_J^B determined on the same ensemble into account). However, we obtain very similar results when fitting the g_J^B individually compared to fitting the results for all the octet baryons simultaneously. For simplicity, we choose to do the former, such that the coefficients c_X for the different baryons are independent of one another.

Lattice spacing effects also need to be taken into account and we add both mass independent and mass dependent terms to the continuum fit ansatz (Eq. (3.42)) to give

$$
\begin{aligned}
g_J^B(M_\pi, M_K, L, a) = \ &g_J^B(\mathcal{M}_\pi, \mathcal{M}_K, L, 0) \\
&+ c_a\, \mathrm{a}^2 + \bar{c}_a\overline{\mathcal{M}}^2\, \mathrm{a}^2 + \delta c_a \delta\mathcal{M}^2\, \mathrm{a}^2 + c_{a,3}\, \mathrm{a}^3,
\end{aligned}
\tag{3.43}
$$

where $\overline{\mathcal{M}}^2 = (2\mathcal{M}_K^2 + \mathcal{M}_\pi^2)/3$ and $\delta\mathcal{M}^2 = \mathcal{M}_K^2 - \mathcal{M}_\pi^2$. The meson masses are rescaled with the Wilson flow scale t_0 [107], $\mathcal{M}_{\pi,K} = \sqrt{8t_0}M_{\pi,K}$ to form dimensionless combinations. This rescaling is required to implement full $O(a)$ improvement (along with employing a fermion action and isovector currents that are non-perturbatively $O(a)$ improved) when simulating at fixed bare lattice coupling instead of at fixed lattice spacing, see section 4.1 of Ref. [52] for a detailed discussion of this issue. The values of t_0/a^2 and the pion and kaon masses in lattice units for the set of ensembles analysed here are given in Table D.3. We translate between different lattice spacings using $t_0^\star$, the value of t_0 along the symmetric line where $12t_0^\star M_\pi^2 = 1.110$ [108], i.e., $\mathrm{a} = a/\sqrt{8t_0^\star}$. The values, determined in Ref. [52], are listed in Table 3.7. Note that we include a term that is cubic in the lattice spacing in the fit form, however, this term is only utilized in the analysis of the vector charge, for which we have the most precise data.

To obtain results at the physical quark mass point, defined through Eq. (3.41), we make use of the scale setting parameter

$$
\sqrt{8t_{0,\text{phys}}} = 0.4098^{(20)}_{(25)}\ \text{fm},
\tag{3.44}
$$

determined in Ref. [52].

In practice, we choose to fit to the bare lattice charges $g_J^{B,\text{latt}}$ rather than the renormalized ones as this enables one to include the uncertainties of the renormalization and improvement factors (which are the same for all ensembles at fixed β) consistently.

Therefore, the final fit form reads

$$g_J^{B,\text{latt}} = \frac{g_J^B(M_\pi, M_K, L, a)}{Z_J^k(\beta)\left(1 + am_\ell b_J(\beta) + 3a\bar{m}\tilde{b}_J(\beta)\right)}, \tag{3.45}$$

where the dependence of the factors on the β-value is made explicit and the superscript k of Z_J^k refers to the different determinations of the renormalization factors that we consider, $k = 1, 2, 3$ for $J \in \{A, V\}$ and $k = 1, 2$ for $J \in \{S, T\}$ (see Tables 3.4, 3.5 and 3.6 in the previous section). A separate parameter for Z_J^k, b_J and $\tilde{b}_J$ is introduced for each β-value and corresponding "prior" terms are added to the χ^2-function. The statistical uncertainties of these quantities are incorporated by generating pseudo-bootstrap distributions, see end of Appendix B.1.

The systematic uncertainty in the determination of the charges at the physical point is investigated by varying the fit model and by employing different cuts on the ensembles that enter the fits. For the latter we consider

1) no cut: including all the available data points, denoted as data set 0, DS(0),

2) pion mass cut: excluding all ensembles with $M_\pi > 400\,\text{MeV}$, DS($M_\pi^{<400\,\text{MeV}}$),

3) pion mass cut: excluding all ensembles with $M_\pi > 300\,\text{MeV}$, DS($M_\pi^{<300\,\text{MeV}}$),

4) a lattice spacing cut: excluding the coarsest lattice spacing, i.e., the ensembles with $a \approx 0.098\,\text{fm}$, DS($a^{<0.1\,\text{fm}}$),

5) a volume cut: excluding all ensembles with $LM_\pi < 4$, DS($LM_\pi^{>4}$).

In some cases, more than one cut is applied, e.g., cut 2 and 4, with the data set denoted DS($M_\pi^{<400\,\text{MeV}}$, $a^{<0.1\,\text{fm}}$), etc.. The final results are obtained by carrying out the averaging procedure described in appendix B.4 which gives an average and error that incorporates both the statistical and systematic uncertainties.

4 | LEADING ORDER SU(3) LOW ENERGY CONSTANTS

Chiral perturbation theory (ChPT) is a central tool for the description and understanding of a multitude of hadronic processes. In this context, the interplay between ChPT and lattice simulations of QCD is of particular interest. While in Nature the quark masses are fixed, in lattice simulations these (and other simulation parameters) can be varied and the precision and the range of validity of truncated ChPT expansions can be explored systematically. Moreover, some of the low energy constants (LECs) of this effective field theory can be constrained or determined from lattice data, which complements phenomenological fits to experimental data that are obviously restricted to physical quark masses. Vice versa, ChPT augments lattice QCD simulations, providing parametrizations of the dependence of the results on the light quark masses and the simulation volume that are consistent with the dynamical breaking of chiral symmetry as well as with the global symmetries of QCD in the massless limit.

While the light pseudoscalar masses, decay constants, the chiral condensate and related mesonic quantities have been well explored in lattice QCD simulations and confronted with SU(2) ChPT predictions—see, e.g., section 5 in the recent FLAG review [14]—this is less so regarding baryonic observables. On the one hand, the lattice data are less precise for baryons, in particular towards small values of the quark masses. On the other hand, the number of independent LECs is larger and also the convergence properties of ChPT may be inferior in the baryonic sector. For instance, the mass gaps between octet and decuplet baryons are smaller than those between pseudoscalar mesons and vector meson resonances, which may necessitate the inclusion of decuplet baryons as explicit degrees of freedom, at least for some observables. Including hyperons into the ChPT analysis, in addition to the nucleon N (or the N and the Δ resonance), provides a wealth of additional information, whereas the number of baryonic LECs of flavour SU(3) ChPT increases only moderately relative to SU(2) ChPT. This makes SU(3) ChPT a particularly popular choice in the description of processes that involve baryons. One concern regarding phenomenological applications, however, is the convergence of SU(3) ChPT at the physical point itself, where neither the mass $M_{\eta_8} \approx (\frac{4}{3}M_K^2 - \frac{1}{3}M_\pi^2)^{1/2} \approx 565$ MeV of the would-be η_8 pseudoscalar meson, the kaon mass $M_K \approx 494$ MeV nor the average light meson mass $\overline{M} = (\frac{2}{3}M_K^2 + \frac{1}{3}M_\pi^2)^{1/2} \approx 411$ MeV are particularly small in comparison to the chiral symmetry breaking scale $\Lambda_\chi := 4\pi F_0 < 4\pi F_\pi \approx 1160$ MeV. While this may limit the practical applicability of SU(3) ChPT regarding some observables, the corresponding LECs are well-defined and can in principle be obtained from lattice QCD simulations.

Within most lattice simulations of $N_f = 2 + 1$ (or $N_f = 2 + 1 + 1$) QCD the mass of the light quark $m_\ell = m_u = m_d$ is varied while that of the strange quark m_s is kept approximately fixed near its physical value. In a few cases, instead $\text{Tr}M = m_u + m_d + m_s$ is kept constant [50, 63, 108, 109]. The former setting is ideal regarding SU(2) ChPT while neither choice is sufficient to determine SU(3) LECs, unless other quark mass combinations are added; in particular, one may want to reduce the trace of the mass

matrix TrM below its physical value. This can be achieved via a partially quenched strategy, see, e.g., Refs. [110–112], or, ideally, by realizing additional sea quark mass combinations [56, 74].

So far no comprehensive lattice QCD investigation of SU(3) ChPT exists, that includes pion masses smaller than 300 MeV or addresses the continuum limit—neither for mesons nor for baryons. The analysis presented in this chapter, which has already been published in similar or verbatim form in Ref. [SW1], starts to close this gap with a consistent, simultaneous analysis of several observables within the framework of SU(3) ChPT.

The results for the leading order (LO) mesonic LECs F_0 and B_0 and baryonic LECs m_0, F and D are obtained on $N_f = 3$ mass-degenerate gauge ensembles. The LECs F and D which are associated with the axial charges also enter the dependence of the octet baryon masses on the pseudoscalar meson masses at order p^3 (next-to-leading order (NLO) of heavy baryon ChPT (HBChPT) or next-to-next-to-leading order (NNLO) of covariant baryon ChPT (BChPT)). Note that for $m_\ell = m_s$ all the octet baryons masses are degenerate, however, this is not the case for the non-flavour singlet axial charges, where two independent combinations exist. The main quantity that determines the convergence properties of ChPT is the squared average pseudoscalar mass $\overline{M}^2$. The value realized in Nature corresponds to the largest quark mass values of the analysed gauge ensembles which cover a range in $\overline{M}^2$ that extends down to less than one third of that. If SU(3) ChPT is applicable at the physical quark mass point then it should also apply to this lattice data, in the continuum limit.

The reliable determination of LO LECs from an extrapolation to the chiral limit requires at least NLO ChPT. Naturally, it is *a priori* unknown whether higher order ChPT may be required within the window of available pseudoscalar masses or if ChPT is applicable at all. Including higher orders is of limited practicability in view of the finite number of data points and their statistical errors, due to the exploding number of new LECs. However, simultaneously analysing a number of different quantities that should be sensitive to the same set of LECs like baryon masses and their axial charges can serve as a consistency check and reduces the parametric uncertainty. Here the attempt is made to achieve exactly this, albeit only for the LO LECs. Previous analyses of lattice QCD data that aimed at determining LECs focused on one type of observable at a time. Ideally, however, one would wish to confirm that the same set of LECs can be employed consistently across a range of quantities.

The reminder of this chapter is organized as follows. Section 4.1 collects all SU(3) ChPT expressions for the quark mass and volume dependence that are relevant for the analysis in the special case $m_\ell = m_s$. Then, in section 4.2, details of the gauge ensembles employed, the analysis methods used, the renormalization and improvement of the pseudoscalar decay constant and the axial charges as well as the continuum and chiral limit extrapolation strategy, which have been discussed earlier in this thesis, are reviewed very briefly. Finally, in section 4.3 the LECs are determined and discussed, before the main results are again summarized in section 4.4. For completeness, additional ChPT expressions for the baryon mass and the axial charges are collected in Appendix F.

4.1 Meson and baryon SU(3) ChPT expressions

4.1.1 Infinite volume

Throughout this chapter isospin symmetry $m_\ell = m_u = m_d$ is assumed and only the SU(3) symmetric case $m := m_\ell = m_s$ is considered. The aim is to determine the LO mesonic (B_0 and F_0) and baryonic (m_0, F and D) SU(3) ChPT LECs. The ChPT expressions in which these LECs appear are conveniently expressed in terms of the quark

mass-dependent variables

$$x = \frac{2mB_0}{(4\pi F_0)^2}, \qquad\qquad \xi = \frac{M_\pi^2}{(4\pi F_0)^2}, \qquad\qquad \mathcal{L} = \log\left(\frac{M_\pi^2}{\mu^2}\right), \qquad (4.1)$$

where M_π denotes the pseudoscalar meson mass and $B_0 := \Sigma_0/F_0^2$ the Gell-Mann–Oakes–Renner (GMOR) parameter, whereas $\Sigma_0 := -\langle\bar{u}u\rangle|_{m=0} > 0$ and $F_0 := F_\pi|_{m=0}$ are the quark chiral condensate and the pseudoscalar decay constant, respectively, in the SU(3) chiral limit. The LO LECs do not depend on the scale μ. For the analysis of the mesonic case, it is convenient to set $\mu^{-2} = 8t_{0,\mathrm{ch}}$, using the Wilson scale parameter t_0 [107] in the chiral limit. From $t_{0,\mathrm{ch}}/t_0^* = 1.037(5)$ [52] and $(8t_0^*)^{-1/2} = 478(7)$ MeV [113], where $t_0^\star$ [108] is defined as the value of t_0 at the point where $12t_0^\star M_\pi^2 = 1.11$ (and $m_\ell = m_s$), we obtain $\mu = 469(7)$ MeV.

At NNLO in SU(N_f) ChPT the corrections to the GMOR relation and the pion mass-dependence of the pseudoscalar decay constant [114–116] read

$$M_\pi^2 = 2B_0m\left[1 + x(a_{10} + a_{11}\mathcal{L}) + x^2(a_{20} + a_{21}\mathcal{L} + a_{22}\mathcal{L}^2)\right], \qquad (4.2)$$

$$F_\pi = F_0\left[1 + x(b_{10} + b_{11}\mathcal{L}) + x^2(b_{20} + b_{21}\mathcal{L} + b_{22}\mathcal{L}^2)\right], \qquad (4.3)$$

where

$$a_{11} = \frac{1}{N_f}, \qquad\qquad a_{22} = \frac{9}{2N_f^2} - \frac{1}{2} + \frac{3N_f^2}{8}, \qquad (4.4)$$

$$b_{11} = -\frac{N_f}{2}, \qquad\qquad b_{22} = -\frac{1}{2} - \frac{3N_f^2}{16}. \qquad (4.5)$$

While a_{10}, b_{10}, a_{21} and b_{21} are combinations of NLO LECs, a_{20} and b_{20} are combinations of NNLO LECs. Whereas NLO and possibly NNLO corrections may turn out necessary to describe our lattice data for which 430 MeV $\gtrsim M_\pi \gtrsim$ 240 MeV, it needs to be seen whether all of these LECs can be resolved, in addition to lattice spacing effects.

The LO octet baryonic LECs are the nucleon mass in the chiral limit m_0 and the couplings F and D which parameterize the octet axial charges in the SU(3) chiral limit and also enter within the chiral expansions of other octet baryon observables, in particular the masses. In the $N_f = 3$ flavour symmetric case at $O(p^3)$ in BChPT the octet baryon mass m_B is given as [117, 118]

$$m_B = m_0 + \bar{b}M_\pi^2 + 2\xi M_\pi\left(\frac{5D^2}{3} + 3F^2\right)f_B(r) \qquad (4.6)$$

with $\bar{b} = -6b_0 - 4b_D$ being a combination of NLO LECs and $r = M_\pi/m_0$. In the extended on-mass-shell (EOMS) scheme [118–120] the loop function is given as

$$f_B(r) = -2\left[\sqrt{1 - \frac{r^2}{4}}\arccos\left(\frac{r}{2}\right) + \frac{r}{2}\log(r)\right], \qquad (4.7)$$

where we follow the standard convention to identify the renormalization scale with m_0. Expanding this function for small r, i.e., for $m_0 \to \infty$, one obtains the heavy baryon ChPT (HBChPT) limit [121, 122] $f_B(r) = -\pi + O(r)$. The EOMS BChPT expressions are also known at NNNLO [123], however, our present lattice data cannot constrain the additional free parameters.

Regarding the axial charges g_A^B, the pion mass dependence in the SU(3) case for the nucleon and the sigma baryon ($B \in \{N, \Sigma\}$) at $O(p^3)$ is given as [101–103]

$$g_A^N = D + F + c_N \xi + \bar{c}_N \xi \log\left(\frac{M_\pi}{m_0}\right) + d_N \xi^{3/2}, \tag{4.8}$$

$$g_A^\Sigma = 2F + c_\Sigma \xi + \bar{c}_\Sigma \xi \log\left(\frac{M_\pi}{m_0}\right) + d_\Sigma \xi^{3/2}, \tag{4.9}$$

where the coefficients,

$$\bar{c}_N = -\left[3(D+F) + \frac{1}{3}\left(27D^3 + 25D^2F + 45DF^2 + 63F^3\right)\right], \tag{4.10}$$

$$\bar{c}_\Sigma = -\left[6F + \frac{2}{3}F\left(25D^2 + 63F^2\right)\right], \tag{4.11}$$

are entirely determined by the LO LECs. Above, $d_N = d_\Sigma = 0$, however, such terms arise naturally when loop corrections that contain decuplet baryons are included [124]. For completeness, the corresponding expectations (as well as those for m_B) are referenced in Appendix F. Unfortunately, these expressions, involving the additional LECs Δ, $\mathcal{C}$ and $\mathcal{H}$, do not satisfactorily describe our data on g_A^B while fits to m_B suggest $\mathcal{C} \approx 0$. Including the logarithmic terms, a reasonable fit quality seems only possible when also adding the above phenomenological d_B-terms. However, such fits give very small values for F and D, that are at variance with the pion mass-dependence of m_B. Leaving $\bar{c}_B$ as free parameters, i.e., ignoring the ChPT expectation, the data even suggest $\bar{c}_B > 0$, opposite to the expectation of Eqs. (4.10) and (4.11). Similar tensions are evident also in recent data on g_A^N within SU(2) ChPT, see, e.g., Refs. [104–106]. This can be interpreted as a sign of large cancellations between pion and decuplet loop effects, a full understanding of which requires to further reduce the quark mass and/or to increase the ChPT order. For the purpose of determining the LO LECs and also in view of the precision of the lattice data, we will truncate Eqs. (4.8) and (4.9) at $O(p^2)$.

4.1.2 Finite volume corrections

Since ChPT also predicts the finite volume dependence, the associated corrections will be included. For the pseudoscalar meson mass and decay constant in the continuum limit the dependence on the linear spatial lattice extent L is given by [125, 126]

$$M_\pi^2(L) = M_\pi^2\left[1 + x\frac{1}{N_f}h(\lambda_\pi) + \cdots\right], \tag{4.12}$$

$$F_\pi(L) = F_\pi\left[1 - x\frac{N_f}{2}h(\lambda_\pi) + \cdots\right] \tag{4.13}$$

with $M_\pi = M_\pi(L = \infty)$, $F_\pi = F_\pi(L = \infty)$ and to this order one can substitute x by ξ. Above, $\lambda_\pi = LM_\pi$ and

$$h(\lambda) = 4\sum_{\mathbf{n}\neq\mathbf{0}}\frac{K_1(\lambda|\mathbf{n}|)}{\lambda|\mathbf{n}|}, \tag{4.14}$$

where $\mathbf{n} \in \mathbb{Z}^3$ and $K_n(x)$ denotes the modified Bessel function of the second kind of order n. Two-loop finite volume effects [127, 128] will not be considered since these contain the NLO LECs.

For the octet baryon mass the SU(2) BChPT result [129, 130] easily generalizes to SU(3):

$$m_B(L) = m_B + 4m_0\xi\left(\frac{5D^2}{3} + 3F^2\right)\int_0^\infty \mathrm{d}y \sum_{\mathbf{n}\neq\mathbf{0}} K_0\left(\lambda_\pi|\mathbf{n}|\sqrt{1 - y + \frac{y^2}{r^2}}\right), \tag{4.15}$$

where the expression is truncated at $O(p^3)$ and $r = M_\pi/m_0$ as above. Note that corrections to the baryon mass m_B due to transitions to decuplet baryons with the mass m_{D0} were first considered in Ref. [124]. For completeness, the corresponding $m_\ell = m_s$ expectations are collected in Appendix F.

In the case of the axial charges g_A^B, the finite volume corrections given in Appendix F have a sign opposite to the trend of the lattice data. It appears that—just like in the infinite volume case—the effect of decuplet baryons needs to be included, introducing three additional LECs which could not be resolved. Therefore, the infinite volume $O(p^2)$ ChPT expectation will be combined with the dominant ChPT finite volume term

$$g_A^B(L) = g_A^B + c_V^B \xi \frac{\exp\left(-LM_\pi\right)}{\sqrt{LM_\pi}}, \tag{4.16}$$

where c_V^B is a free phenomenological coefficient.

4.2 Lattice setup

This section will briefly review the lattice setup for the determination of the LECs. Details of most of the subjects outlined are already given in chapter 3. First, the gauge ensembles used in this part of the analysis are discussed. Subsequently, the determination of the relevant observables, including—where applicable—their renormalization and $O(a)$ improvement is summarized. Then, the results for the analysed ensembles are presented and the continuum, infinite volume and chiral extrapolation strategy is outlined.

4.2.1 Gauge ensembles

Details on the gauge ensembles are presented in section 2.3.2 (see also Table D.1) where an in-depth overview of all analysed ensembles is given. In this part of the analysis we only employ the subset of ensembles generated with $N_f = 3$ quark flavours. Thus, we only focus on the ensembles that are on the trajectory denoted as symmetric line, i.e., where the light and strange quark masses are degenerate ($m_u = m_d = m_s$) and SU(3) flavour symmetry is exact.

In total we analysed the fifteen ensembles compiled in Fig. 4.1 where the simulated parameter space is illustrated. The ensembles cover a range of six different lattice spacings $0.039\,\text{fm} \lesssim a \lesssim 0.098\,\text{fm}$, the pion masses range from around 430 MeV down to 240 MeV and volumes are realized between $3.3 \leq LM_\pi \leq 6.4$ where $LM_\pi \geq 4$ for the majority of the ensembles. Note that the two ensembles N306 and D250 are not included in the analysis because they were generated after the analysis had been finalized. However, a first preliminary update presented in the summary section 4.4 suggests that ensembles with lower pion masses are favourable to improve future analyses.

4.2.2 Analysis methods

The computation of the two- and three-point correlation functions which enables the analysis of the LECs is already described in section 3.2. Further, we employ the results of the scale parameters t_0/a^2 and $t_0^\star/a^2$ as well as the quark mass from the axial Ward identity (AWI), the pseudoscalar meson mass and the octet baryon mass which have been obtained within an extensive RQCD analysis [52] of the light hadron spectrum on most of the available CLS gauge ensembles. More details on the computation of the two-point functions, the extraction of the ground state masses and the statistical methods applied to account for autocorrelation effects and to compute covariance matrices between these quantities are described in Ref. [52].

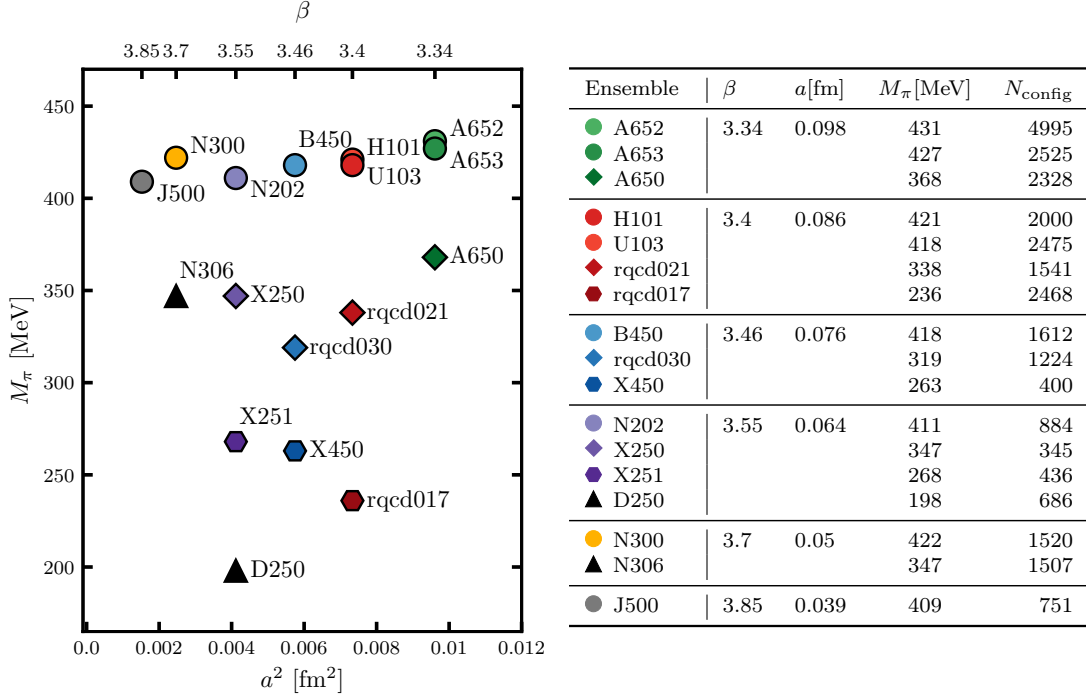| Ensemble	β	a[fm]	M_π[MeV]	N_{config}
🟢 A652	3.34	0.098	431	4995
🟢 A653			427	2525
🟢 A650			368	2328
🔴 H101	3.4	0.086	421	2000
🔴 U103			418	2475
🔴 rqcd021			338	1541
🔴 rqcd017			236	2468
🔵 B450	3.46	0.076	418	1612
🔵 rqcd030			319	1224
🔵 X450			263	400
🟣 N202	3.55	0.064	411	884
🟣 X250			347	345
🟣 X251			268	436
▲ D250			198	686
🟡 N300	3.7	0.05	422	1520
▲ N306			347	1507
⚫ J500	3.85	0.039	409	751

Figure 4.1: The parameter landscape and list of the ensembles analysed within this chapter. The same colour coding will be used throughout the analysis of the SU(3) LECs to identify the individual ensembles. Only the ensembles with colored symbols are included in the final analysis whereas N306 and D250 (labeled with black triangles) were only generated at a later time.

The pion decay constant and the AWI quark mass are also obtained from two-point functions, using similar methods as for the pseudoscalar mass. However, in this case the two-point functions are only smeared at the source. We follow the strategy detailed in Refs. [131] and [132] to compute these observables.

The calculation of the octet axial charges g_A^B, $B \in \{N, \Sigma\}$, for the nucleon and the sigma baryon, was part of the determination of the octet baryon charges presented in chapter 5, following Refs. [SW2, SW6]. Again, details on the computation of the three-point correlation functions $C_{3\text{pt}}^B(t, \tau; \mathcal{O}_A)$ are described in section 3.2. Note that the local isovector current combination $\mathcal{O}_A = \mathcal{O}_u - \mathcal{O}_d$, where $\mathcal{O}_q = \bar{q}\gamma_\mu\gamma_5 q$, is inserted at the time τ and no quark line-disconnected contributions appear. The fitting procedure slightly differs from the one outlined in section 3.4 and we briefly sketch the approach used in this analysis.

As already detailed in section 3.1, in the case of exact SU(3) flavour symmetry ($m_\ell = m_s$), all the axial charges g_A^B can be written as combinations of just two fundamental charges F_A and D_A:

$$g_A^N = F_A(m) + D_A(m), \quad g_A^\Lambda = 0, \quad g_A^\Sigma = 2F_A(m), \quad g_A^\Xi = F_A(m) - D_A(m), \quad (4.17)$$

where $F = F_A(0)$ and $D = D_A(0)$ are the LECs in the chiral limit which appear in the first order meson-baryon Lagrangian for three light quark flavours. Here we choose g_A^N and g_A^Σ as our basis where one obtains the combinations

$$F(m) = \frac{1}{2}g_A^\Sigma \xrightarrow{m \to 0} F, \quad D(m) = g_A^N - \frac{1}{2}g_A^\Sigma \xrightarrow{m \to 0} D. \quad (4.18)$$

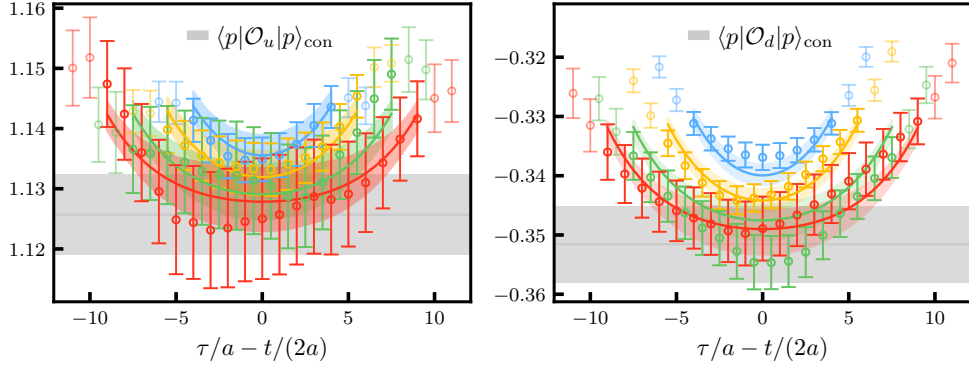The matrix element of interest for a baryon B can be obtained from a fit to the ratio

Figure 4.2: Simultaneous fit to all four source-sink separations of the ratios for $\langle p|\mathcal{O}_u|p\rangle_{\mathrm{con}} = 2F(m)$ and $\langle p|\mathcal{O}_d|p\rangle_{\mathrm{con}} = F(m) - D(m)$ on the ensemble N300. Only the dark data points are included in the fit. The grey band shows the ground state contribution and its error.

of three-point over two-point functions

$$R^B(t, \tau; \mathcal{O}_A) = \frac{C^B_{3\mathrm{pt}}(t, \tau; \mathcal{O}_A)}{C^B_{2\mathrm{pt}}(t)} \xrightarrow{t, \tau \to \infty} g^B_A, \tag{4.19}$$

see, e.g., section 3.4, for details. As an example, we show in Fig. 4.2 for the ensemble N300 a simultaneous fit for $\mathcal{O} \in \{\mathcal{O}_u, \mathcal{O}_d\}$,[1] to the ratios

$$R^p_{\mathrm{con}}(t, \tau; \mathcal{O}) = b_{0,\mathcal{O}} + b_{1,\mathcal{O}} e^{-\Delta m\, t/2} \cosh\left(\Delta m(\tau - t/2)\right) + b_{2,\mathcal{O}} e^{-\Delta m\, t} \tag{4.20}$$

for the proton (p), employing one and the same excited state mass gap Δm in both channels, where the subscript "con" indicates that we only consider the quark line-connected Wick contractions. Exploiting the fact that all the quarks are mass-degenerate, this gives the matrix elements $b_{0,\mathcal{O}_u} = g^\Sigma_A = 2F_A(m)$ and $b_{0,\mathcal{O}_d} = g^\Sigma_A - g^N_A = F_A(m) - D_A(m)$. The bootstrap error analysis is carried out using binned data with a bin size that is large compared to the integrated autocorrelation time, with the bootstraps matched to those of the other observables so that in the subsequent analysis all correlations can be taken into account.

4.2.3 Non-perturbative renormalization and improvement

The quark mass, the pion decay constant and the axial charges as extracted above need to be matched to the continuum $\overline{\mathrm{MS}}$ scheme. Details about the renormalization and $O(a)$ improvement coefficients are given section 3.5. Regarding the renormalization of the axial currents, here we only use one set of renormalization factors, namely Z_A from table 3.6 denoted as Z^3_A in the text. It is emphasized that both these factors have been computed entirely non-perturbatively.

Summarizing section 3.5, see Eqs. (3.39), (3.40) and (3.37), the observables can be renormalized and fully $O(a)$-improved at each value of the lattice coupling $g^2 = 6/\beta$ as follows:

$$m = Z_M \left[1 + am(b_A - b_P + 3\tilde{b}_A - 3\tilde{b}_P)\right] m^{\mathrm{AWI}}, \tag{4.21}$$

$$F_\pi = Z^3_A \left[1 + am(b_A + 3\tilde{b}_A)\right] F^{\mathrm{latt}}_\pi, \tag{4.22}$$

$$g^B_A = Z^3_A \left[1 + am(b_A + 3\tilde{b}_A)\right] g^{B,\mathrm{latt}}_A, \tag{4.23}$$

---

[1]We take the differences of a proton with spin-up and spin-down along the direction k.

where we have assumed $m = m_\ell = m_s$, since in this analysis all ensembles incorporate exact SU(3) flavour symmetry. The uncertainties of the renormalization factors and improvement coefficients are incorporated in the statistical analysis by means of pseudo-bootstrap distributions.

4.2.4 Lattice results

We will fit the squared pion mass M_π^2 and the pion decay constant F_π simultaneously as functions of the RGI quark mass m, whereas we parameterize the dependence of the baryon mass m_B and of the axial charges g_A^N and g_A^Σ in terms of the pion mass. Regarding the continuum limit extrapolation, the quantities t_0 and $t_0^\star$ are required, as described in the next section in more detail. In Table D.4 the corresponding results in lattice units for all the ensembles are summarized, with the exception of $t_0^\star/a^2$, listed in Table 4.1, whose values are common to all ensembles that share the same gauge coupling. Note that no axial charges have been determined on the ensembles A652 and rqcd017. However, ensemble A653 is very similar to A652 in terms of the simulation parameters while the rqcd017 volume is rather small and finite volume effects can be substantial, in particular for the axial charges.

Table 4.1: Values for $t_0^\star/a^2$ for each β-value taken from a preliminary analysis of Ref. [52] which slightly differ from the update values listed in Table 3.7.

β	3.34	3.4	3.46	3.55	3.7	3.85
$\frac{t_0^\star}{a^2}$	2.219(7)	2.908(3)	3.709(3)	5.180(4)	8.634(10)	13.984(31)

4.2.5 Extrapolation strategy

A reliable extraction of the LO SU(3) LECs in the chiral limit requires a chiral, infinite volume and continuum limit extrapolation. Ideally, one would carry out simultaneous fits to all the observables. In particular, the mesonic LEC F_0 also appears within the ChPT expansions of the baryonic observables. In principle, this is possible and even the full covariance matrices between aM_π, am, aF_π, am_B, g_A^N and g_A^Σ is available. However, the former three observables are much more precise in terms of their statistical accuracy than the baryonic ones. Therefore, any impact of the baryonic results onto the mesonic LECs should be negligible and we opt for a two stage procedure, first determining the mesonic LECs and then using the resulting value for $F_0/\sqrt{8t_{0,\text{ch}}}$ within the extraction of the baryonic LECs.

For the action, the axial current (needed for F_π, g_A^B and m) and the pseudoscalar current (needed for m), $O(a)$ improvement is implemented non-perturbatively. Therefore, if we would simulate at a fixed lattice spacing a, we would have full $O(a)$ improvement. However, instead we keep the unimproved, bare lattice coupling g^2 fixed which results in a correction term $\propto a\text{Tr}M$ for quantities aQ, that are measured in lattice units.[2] This term cancels when constructing dimensionless combinations $(\sqrt{8t_0}a^{-1})(aQ)$, using the scale parameter t_0/a^2 on the same ensemble. Therefore, to achieve full $O(a)$-improvement while varying the quark mass, we rescale all quantities $aQ \mapsto \sqrt{8t_0}Q$. This means that at the end of the analysis the dimensionful LECs m_0, F_0 and B_0 will be obtained in units of $\sqrt{8t_{0,\text{ch}}}$, which can then be converted into physical units.

---

[2] In fact this mass-dependent shift of the improved lattice coupling also affects the renormalization factors of the axial and pseudoscalar currents but this effect has been accounted for within the definition of the improvement coefficients $\tilde{b}_A$ and $\tilde{b}_P$ [86] of Eqs. (3.39)–(3.40).

The continuum fit functions $X(\mathcal{M}, L, a = 0)$, where $\mathcal{M} = \sqrt{8t_0}m$ and $\mathcal{M} = 8t_0 M_\pi^2$, respectively, for mesonic observables $X \in \{8t_0 M_\pi^2, \sqrt{8t_0}F_\pi\}$ and baryonic observables $X \in \{\sqrt{8t_0}m_B, g_A^N, g_A^\Sigma\}$, are summarized in Eqs. (4.1)–(4.9) and (4.12)–(4.16). Note that the dependence $t_0 = t_{0,\mathrm{ch}}[1 + k_1 x + (k_{20} + k_{21}\mathcal{L})x^2 + \ldots]$ [133] does not interfere with the universal ChPT logs and therefore neither the functional forms of the continuum formulae nor the LECs are affected by the rescaling of all dimensionful quantities in units of t_0. Nevertheless, it should be remarked that some of the higher order LECs, which we do not determine here, would require some knowledge about the LECs k_1 etc., that are associated with t_0. Regarding the lattice spacing-dependence, we assume the factorization

$$X(\mathcal{M}, L, a) = X(\mathcal{M}, L, 0) \cdot \left[1 + \frac{a^2}{8t_0^\star}\left(c_a^X + \bar{c}_a^X 8t_0 M_\pi^2\right)\right] \qquad (4.24)$$

into the continuum parametrization times mass-independent and mass-dependent lattice spacing effects, where c_a^X and $\bar{c}_a^X$ are independent fit parameters for each observable X.

The systematic errors of the LECs will be estimated by varying the fit model and by employing different cuts on the ensembles that enter the fit:

1. no cut: including all the available data points,

2. pion mass cut: excluding all ensembles with $M_\pi > 400$ MeV,

3. lattice spacing cut: excluding the coarsest lattice spacing, i.e., the ensembles with $a \approx 0.098$ fm,

4. volume cut: excluding all ensembles with $LM_\pi < 4$.

We then carry out the model averaging procedure described in Appendix B.4.

4.3 Results and discussion

In the following we determine the LO SU(3) mesonic LECs B_0 and F_0 as well as the LO SU(3) baryonic LECs m_0, F and D. Subsequently, we compare the results with recent determinations taken from the literature.

4.3.1 Mesonic LECs

The LO mesonic LECs B_0 and F_0 are determined by simultaneous fits to the pion mass and decay constant as functions of the quark mass, the volume and the lattice spacing as described above. The fits are carried out including the errors of and the correlations between the pion decay constant, the pion mass and the quark mass within each ensemble. The resulting χ^2-values are fully correlated.

Including only the mass-independent discretization terms of Eq. (4.24) and carrying out fits employing the NLO ChPT expressions, i.e., truncating the quark mass and the volume dependence at $O(x)$, we are able to resolve all parameters reasonably well. Figure 4.3 illustrates the resulting quark mass-dependence of the pion decay constant and the squared pion mass, respectively, from a combined fit to all the available data points. This fit to 30 points requires six parameters ($\sqrt{8t_0}B_0$, $\sqrt{8t_0}F_0$, a_{10}, b_{10}, $c_a^{M_\pi}$ and $c_a^{F_\pi}$) while the coefficients of the logs, $a_{11} = 1/3$ and $b_{11} = -3/2$, are fixed, see Eqs. (4.4) and (4.5). For a better visualization of the deviations from the linear GMOR relation, in the right plot in Fig. 4.3 we have divided the squared pion mass by the quark mass (all in units of $8t_0$). This ratio approaches the GMOR expectation $2B_0\sqrt{8t_{0,\mathrm{ch}}}$ in the chiral limit. The deviation from a linear dependence is caused by b_{11}. This, as well as
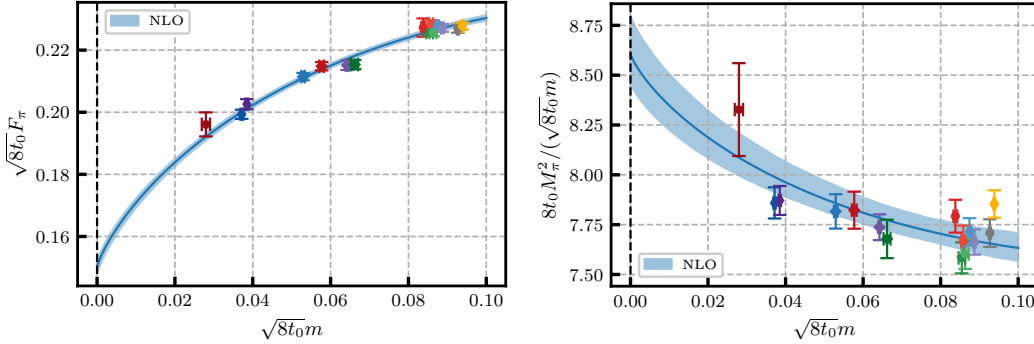
Figure 4.3: Left: Extrapolation of the pion decay constant F_π to the chiral limit. The data points are corrected for discretization and finite volume effects according to the parameters obtained from a combined fit to the pseudoscalar decay constant and mass on all the available data points employing the NLO ChPT ansatz. The blue band shows the NLO expression for the quark mass dependence. Right: The same as in the left panel for the ratio of the squared pion mass over the quark mass M_π^2/m.

Table 4.2: Results for the LO mesonic LECs F_0 and B_0 in units of $1/\sqrt{8t_{0,\mathrm{ch}}} = 469(7)$ MeV obtained from fits to the NLO ChPT expression and different subsets of the parameter space spanned. The subsets are defined at the end of section 4.2.5.

Fit	χ^2/N_{dof}	$\sqrt{8t_{0,\mathrm{ch}}}F_0$	$\sqrt{8t_{0,\mathrm{ch}}}B_0$
1	0.9322	0.1504(19)	4.302(81)
2	0.7146	0.1565(30)	4.10(14)
3	0.3444	0.1485(22)	4.118(86)
4	1.0500	0.1489(22)	4.364(89)

the curvature observed in the left plot of Fig. 4.3 that is due to a_{11}, is in agreement with the data.

Since this simple fit describes the data very well, adding further parameters does not improve the situation: allowing for the mass-dependent discretization terms $\bar{c}_a^X \neq 0$ in Eq. (4.24), does not significantly change the values of χ^2/N_{dof}, F_0 or B_0. However, the errors for the fit parameters c_A^X, a_{10} and b_{10} increase considerably and on the reduced data sets, when incorporating the cuts described at the end of section 4.2.5, stable fits become impossible. Similarly, when allowing for the $O(x^2)$ (NNLO) terms in the continuum fit functions (Eqs. (4.2) and (4.3)), the statistical errors of all parameters increase while the higher order parameters are either comparable with zero or cannot be resolved reliably due to cancellations. After exploring these alternative parametrizations, in view of the range and quality of the present data, only the four parameter NLO continuum fit in conjunction with the two parameters that account for mass-independent $O(a^2)$ effects are included into the analysis. Further, the parametrization uncertainty is explored by imposing the cuts on the data that are defined at the end of section 4.2.5. Carrying out the fits on these four sets of ensembles and performing the model averaging procedure as described in Appendix B.4, we obtain

$$\sqrt{8t_{0,\mathrm{ch}}}F_0 = 0.1502^{(56)}_{(29)}, \qquad \sqrt{8t_{0,\mathrm{ch}}}B_0 = 4.22^{(15)}_{(16)}, \qquad (4.25)$$

where the errors include the systematics. The individual results for each fit are listed in Table 4.2 and compiled in Fig. 4.4, where also the final result is indicated.
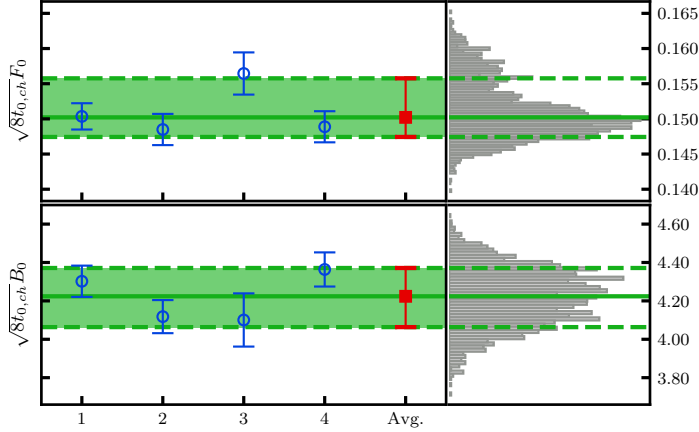
Figure 4.4: Final result for the LO mesonic LECs F_0 and B_0 (red point and green error band) obtained from individual fits (blue points) by performing the model averaging procedure described in Appendix B.4. The model averaged distribution is shown as a histogram on the right where also the median and the 68% confidence level interval are indicated (green lines).

4.3.2 Baryonic LECs

In analogy to the analysis of the mesonic observables, we carry out a simultaneous extrapolation of the octet baryon mass and the axial charges for the nucleon and the sigma baryon. The continuum expressions for the dependence of these three observables on the pion mass M_π and the lattice extent L are given in Eqs. (4.6)–(4.9), (4.15) and (4.16). Again, lattice spacing effects are parameterized as in Eq. (4.24). For F_0, the pion decay constant in the chiral limit, that enters in the definition of ξ (see Eq. (4.1)), we use the result obtained in the previous section 4.3.1. HBChPT should give the same set of LO LECs m_0, F and D as BChPT in the EOMS prescription. To investigate the impact of different truncations of the chiral expansion, in addition to the BChPT fits, we also carry out a HBChPT analysis, replacing the loop function in Eq. (4.7) as $f_B(r) \mapsto -\pi$.

The pion mass dependence of the axial charges appears to be mild. As already pointed out at the end of section 4.1.1, the logarithmic corrections suggested by ChPT without decuplet loops differ in sign from what the data suggest. This—within the available window of pion masses—can only be compensated for by corrections of $O(\xi^{3/2})$ and higher
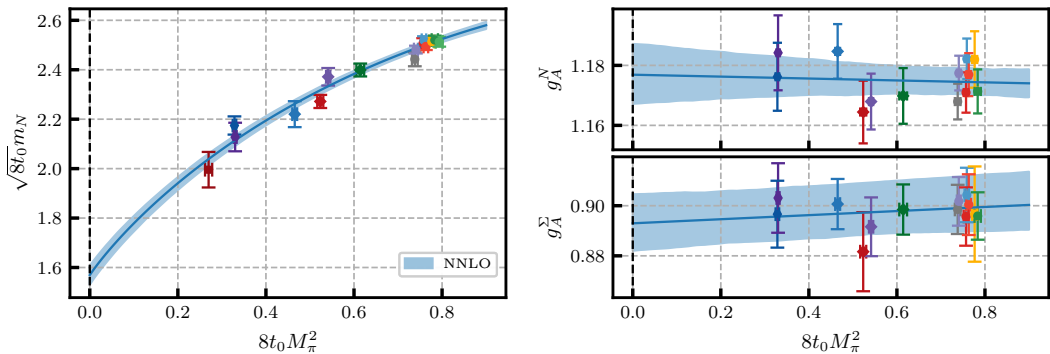

Figure 4.5: Left: Extrapolation of the nucleon mass m_N to the chiral limit. The data points are corrected for discretization and finite volume effects according to the parameters obtained from a combined fit to the nucleon mass and the two axial charges on all the available data points. The blue band shows the NNLO BChPT expression for the pion mass dependence. Right: The same as in the left panel for the axial charges of the nucleon and the sigma baryon. The blue band shows the NLO ($O(p^2)$) chiral extrapolation.

47

Table 4.3: Results for the LO baryonic LECs m_0 (octet baryon mass in the chiral limit), F and D obtained from fits to the BChPT (B) and HBChPT (H) expressions on different subsets of ensembles. The subsets are defined at the end of section 4.2.5.

Fit	χ^2/N_{dof}	$\sqrt{8t_{0,\text{ch}}}m_0$	F	D
1 (H)	1.1710	1.325(49)	0.4455(59)	0.729(10)
1 (B)	0.9451	1.570(39)	0.4465(59)	0.730(10)
2 (H)	1.4793	1.447(70)	0.4489(82)	0.741(12)
2 (B)	1.2450	1.608(64)	0.4492(82)	0.742(12)
3 (H)	1.3788	1.341(51)	0.4442(61)	0.726(11)
3 (B)	1.1174	1.570(42)	0.4449(61)	0.728(11)
4 (H)	1.2265	1.339(50)	0.4447(61)	0.725(10)
4 (B)	0.9689	1.587(41)	0.4456(61)	0.727(10)

and/or by including effects of the decuplet baryons, adding the additional LECs Δ, $\mathcal{C}$ and $\mathcal{H}$. The same observation is made regarding finite volume effects, whose sign can only be reconciled with the data if decuplet loops are included. The relevant formulae are listed in Appendix F but, given the statistical error of the data, these additional contributions cannot be explored. Therefore, regarding the axial charges, Eqs. (4.8) and (4.9) are truncated at $O(\xi)$, i.e., a NLO ($O(p^2)$) analysis is carried out. Regarding the finite volume effects, only the leading term (see Eq. (4.16)) is taken into account, with phenomenological coefficients c_V^N and c_V^Σ. Turning to the baryon mass, one is able to employ the full NNLO ($O(p^3)$) expressions, both for the pion mass-dependence and the finite volume behaviour. It is also found that the baryon mass data is well described when including decuplet loops. However, in this case, the LEC $\mathcal{C}$ is found to be compatible with zero within large errors, suggesting that the impact of the decuplet on the octet baryon mass is small.

In Fig. 4.5 the pion mass dependencies of the nucleon mass and of the axial charges are shown, respectively, for a combined fit to all the available data points. The fit is to 41 data points (15 ensembles for the baryon mass and 13 ensembles for each of the axial charges). It requires 11 parameters: m_0, F, D, $\bar{b}$, c_N, c_Σ, c_V^N, c_V^Σ, c_a^N, $c_a^{g_A^N}$ and $c_a^{g_A^\Sigma}$, i.e., six (combinations of) LECs, two finite volume parameters for the axial charges and three parameters to describe discretization effects. The same variations of the data set as in the meson case are carried out. In addition, both BChPT and HBChPT for the pion mass-dependence of the baryon mass are explored, giving eight distinct results that are collected in Table 4.3 and shown in Fig. 4.6.

BChPT is found to give better fit qualities than HBChPT which is why the former fits dominate the averaging procedure. The BChPT results for m_0 are systematically larger than those of HBChPT which suggests a larger curvature of the data. Since F and D are mostly determined by the axial charges, where to the order employed here no difference between BChPT and HBChPT exists, these values are largely unaffected by the parametrization. The final, averaged results read:

$$\sqrt{8t_{0,\text{ch}}}m_0 = 1.57^{(5)}_{(6)}, \qquad F = 0.447^{(6)}_{(7)}, \qquad D = 0.730^{(11)}_{(11)}. \qquad (4.26)$$

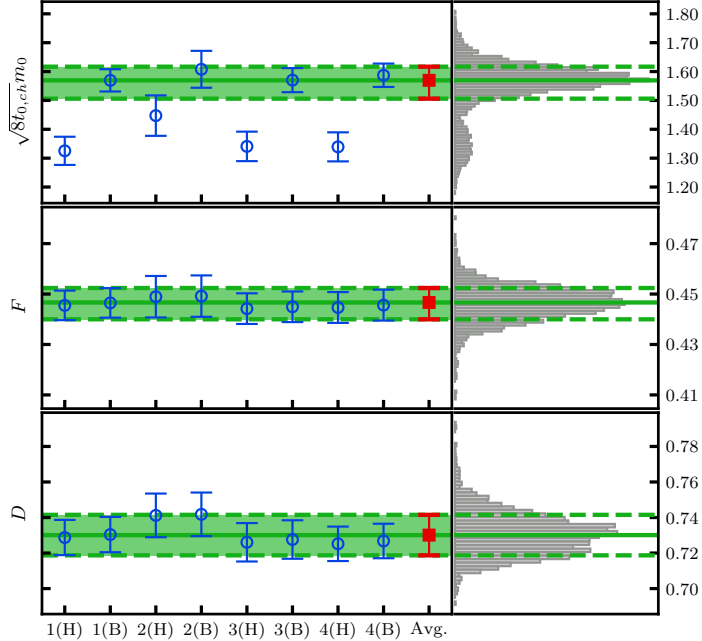Again, the errors include the systematics of the extrapolation.

Figure 4.6: The same as Fig. 4.4 but for the LO baryonic LECs m_0, F and D. For each cut there are two data points: BChPT (B) and HBChPT (H).

4.3.3 Comparison with other recent determinations

We employ the value $(8t_{0,\mathrm{ch}})^{-1/2} = \mu = 469(7)$ MeV to convert the results into physical units. As already explained in section 4.1.1, this value is obtained by combining $t_{0,\mathrm{ch}}/t_0^* = 1.037(5)$ [52] with $(8t_0^*)^{-1/2} = 478(7)$ MeV [113]. The mesonic LECs (with systematic uncertainties included in the errors) then read

$$F_0 = 70^{(3)}_{(2)} \text{ MeV} \quad \text{and} \quad \Sigma_0^{1/3}(\mathrm{RGI}) = 214^{(7)}_{(5)} \text{ MeV} , \tag{4.27}$$

where $\Sigma_0 = B_0 F_0^2$. Note that $\Sigma_0(\mathrm{RGI})$ refers to the value of the chiral condensate in the RGI scheme with $N_f = 3$ active sea quark flavours. Using version 3 of the MATHEMATICA implementation of the RUNDEC package [134, 135] at five loop accuracy in the quark mass anomalous dimension- and the β-functions, we obtain the conversion factor $m(\mathrm{RGI}) = 1.330(14)(7)m(\overline{\mathrm{MS}}, 2\,\mathrm{GeV})$ for the quark mass between the RGI and the $\overline{\mathrm{MS}}$ schemes.[3] The first error corresponds to the uncertainty of the three-flavour Λ-parameter [113], whereas the second error is the difference between five- and four-loop running. Using the scale-independence of $m\Sigma_0$ and taking the third root, one obtains

$$\Sigma_0^{1/3}(\overline{\mathrm{MS}}, 2\,\mathrm{GeV}) = 236^{(7)}_{(6)} \text{ MeV} . \tag{4.28}$$

Figure 4.7 shows a comparison of the results for F_0 and Σ_0 with the most recent determinations from SU(3) ChPT analyses of other groups, also see the present FLAG review [14] for a detailed discussion. One issue with $N_f = 2 + 1(+1)$ simulations is that the strange quark mass is usually kept close to its physical value, which limits the sensitivity of observables to the deviation of F_0 and B_0 from their SU(2) ChPT counter parts and necessitates partially quenched analyses. The only other simulation with $N_f = 3$ mass-degenerate quarks was carried out over a decade ago by JLQCD/TWQCD [136].

---

[3]The normalization of the RGI mass used in RUNDEC3 differs from the one employed here. References [14, 96, 97] share the convention employed here.
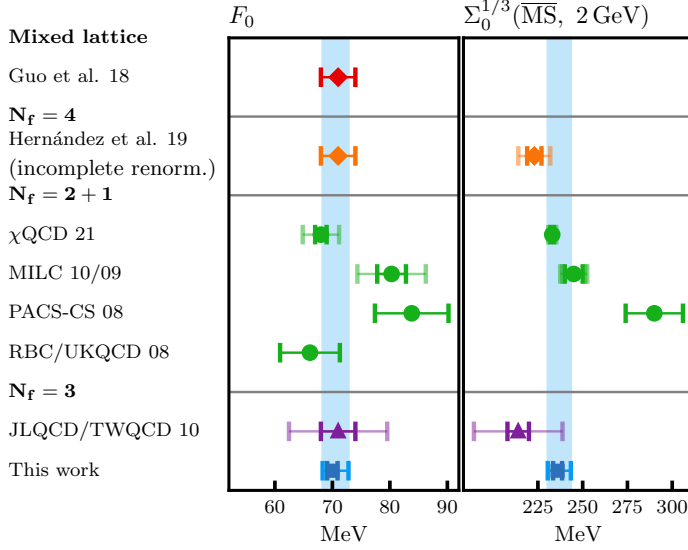
Figure 4.7: Comparison with the most recent SU(3) ChPT determinations of F_0 and $\Sigma_0 = B_0 F_0^2$ from other groups. The latter is in the $\overline{\mathrm{MS}}$ scheme at the scale 2 GeV with three active flavours. Note that the result labelled "$N_f = 4$" is for the $N_f = 3$ LECs, however, extrapolated from $N_f = 4$ simulations at different numbers of colours. Dark error bars correspond to the statistical error only, whereas the lighter error bars include a systematic error estimate, added in quadrature.

From an analysis of several lattice data sets Guo et al. [137] estimated $F_0 = 71(3)$ MeV. Hernández et al. [138] find from a large N_c scaling analysis of $N_f = 4$ and $N_c = 3$–6 lattice data $F_0 = 71(3)$ MeV and $\Sigma_0^{1/3} = 223(4)(8)$ MeV for $N_f = N_c = 3$. Simulating $N_f = 3$ flavours, JLQCD/TWCQD [136] determine $F_0 = 71(3)(8)$ MeV and $\Sigma_0 = 214(6)(24)$ MeV. Employing $N_f = 2 + 1$ flavour simulations, the most recent determinations of F_0 are $68(1)(3)$ MeV by χQCD [112], $80.3(2.5)(5.4)$ MeV by MILC [139], $66.1(5.2)$ MeV by RBC/UKCQD [140] and $83.8(6.4)$ MeV by PACS-CS [141]. For $\Sigma_0^{1/3}$ in the $\overline{\mathrm{MS}}$ scheme at 2 GeV, χQCD [112] find $233(1)(2)$ MeV, MILC [142] quote $245(5)(4)(4)$ MeV, while PACS-CS [141] report $290(16)$ MeV. In summary, all the results for the mesonic LECs agree within their errors, with the exception of PACS-CS [141], in particular regarding the chiral condensate.

A compilation of the most recent results for the octet baryon mass in the SU(3) chiral limit, m_0, is shown in Fig. 4.8. Including the systematic uncertainties and converted into physical units, the result for m_0 from Eq. (4.26) reads

$$m_0 = 736^{(25)}_{(32)} \text{ MeV}. \tag{4.29}$$

Carrying out SU(3) HBChPT or BChPT analyses of data from $N_f = 2 + 1$ flavour simulations for m_0, Walker-Loud [110] predicts $899(40)$ MeV, BMW [143] find $750(150)$ MeV and Martin Camalich et al. [144] obtain $756(32)$ MeV. Investigating multiple lattice data sets, Guo et al. [145, 146] obtain $870(3)$ MeV (mean and error estimated from the two fit results quoted in Ref. [146]) and Ren et al. [147] $884(11)$ MeV. A number of earlier results exists [123, 148–151], which are not displayed in the figure. While it is difficult to estimate realistic errors for the two very global fits to lattice data [145, 147], there is disagreement between the result for m_0 found here and Walker-Loud [110] who obtains a much larger value.

In Fig. 4.9 the results from Eq. (4.26) for the two baryonic LECs F and D are compared with results obtained from lattice as well as phenomenological determinations.

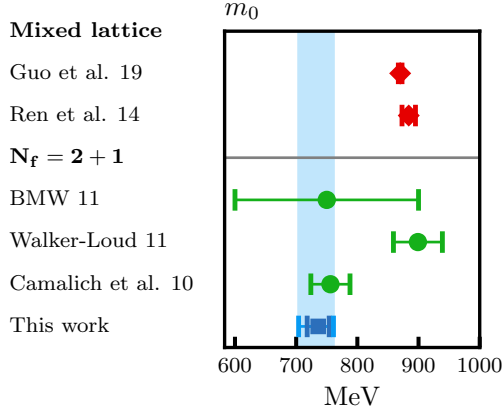From a lattice QCD calculation of the axial charges, Lin and Orginos [15] determine

Figure 4.8: Comparison with the most recent determinations of the octet baryon mass in the $N_f = 3$ chiral limit m_0, obtained from fits to Lattice QCD results.

$F = 0.453(5)(19)$ and $D = 0.715(6)(29)$ with $N_f = 2 + 1$ flavours. Later Savanur and Lin [18] find $F = 0.438(7)(6)$ and $D = 0.708(1)(6)$, this time with $N_f = 2 + 1 + 1$ flavours. Both values, however, refer to the physical quark mass point, where the definition of F and D is ambiguous, rather than to the chiral limit. From the baryon masses, Walker-Loud [110] finds $F = 0.47(3)$ and $D = 0.70(5)$. Most phenomenological predictions are inferred from semileptonic hyperon decays. A selection of such analyses contains Jenkins et al. [124], Savage et al. [152], Flores et al. [153], Cabibbo et al. [154], Ratcliffe [155] and Ledwig et al. [103]. Regarding F, there is no clear contradiction when comparing any pair of results within the stated errors. With respect to D, however, Flores et al. [153] and Cabibbo et al. [154]—while obtaining central values very similar to those of Savage et al. [152] and Ratcliffe [155]—are at variance with the lattice determinations, within their errors. Note that the lattice results agree with each other, however, this should change if the precision was increased since two of the studies give numbers that correspond to the physical strange quark mass, rather than to the $N_f = 3$ chiral limit.
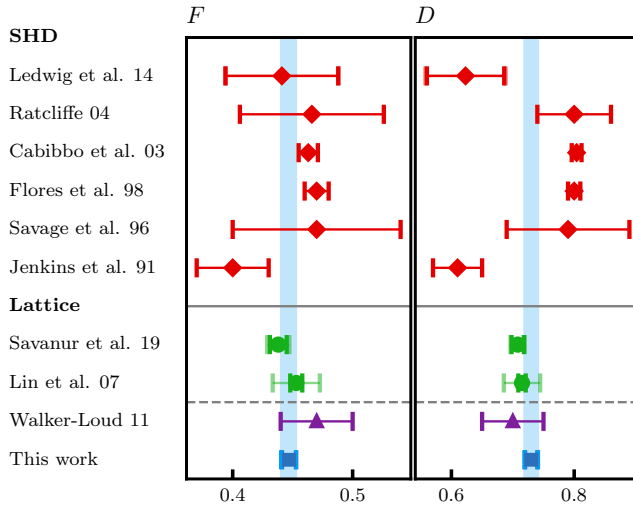

Figure 4.9: Comparison of our results for the LECs F and D with results obtained from lattice QCD calculations of the hyperon axial charges (green points)—albeit for physical quark masses, rather than in the chiral limit—and the baryon mass (purple point). In addition, we show selected results obtained from measurements of semileptonic hyperon decays.

4.4 Summary and outlook

In this part of the thesis, we performed a simultaneous determination of all LO mesonic (B_0, F_0) and octet baryonic (m_0, F, D) SU(3) ChPT LECs, using $N_f = 3$ lattice QCD simulations. The analysis is based on fifteen gauge ensembles, spanning a range of pion

masses from 430 MeV down to 240 MeV across six different lattice spacings between $a \approx 0.039$ fm and $a \approx 0.098$ fm and spatial lattice sizes between $3.3 \leq LM_\pi \leq 6.4$. It was found that a consistent description of the pion mass and volume dependence of the octet baryon mass and the axial charges was possible with the same set of LECs. Systematic errors were assessed and included by imposing cuts on the pion mass, the lattice spacing and the volume. For the baryon mass both covariant BChPT and HBChPT were employed. The resulting LECs are as follows ($\Sigma_0 = F_0^2 B_0$):

$$F_0 = 70^{(3)}_{(2)} \text{ MeV} , \qquad\qquad m_0 = 736^{(25)}_{(32)} \text{ MeV} ,$$

$$\Sigma_0^{1/3} = 214^{(7)}_{(5)} \text{ MeV (RGI)} , \qquad\qquad F = 0.447^{(6)}_{(7)} ,$$

$$= 236^{(7)}_{(6)} \text{ MeV } (\overline{\text{MS}}, 2 \text{ GeV}) , \qquad\qquad D = 0.730^{(11)}_{(11)} ,$$

$$B_0 = 1.98^{(7)}_{(8)} \text{ GeV (RGI)} , \qquad\qquad \frac{F}{D} = 0.612^{(14)}_{(12)} ,$$

$$= 2.63^{(10)}_{(10)} \text{ GeV } (\overline{\text{MS}}, 2 \text{ GeV}) ,$$

where the uncertainties of the chiral, continuum and infinite volume extrapolation as well as of the conversion into physical units are included in the error. The RGI and $\overline{\text{MS}}$ results above refer to the three-flavour scheme. Comparing the mesonic SU(3) LECs $X_0 \in \{F_0, \Sigma_0, B_0\}$ with their SU(2) ChPT counterparts X, where the strange quark mass is fixed at its physical value, in the $\overline{\text{MS}}$ scheme with three active flavours at 2 GeV one finds: the decay constant $F_0 < F \approx 86$ MeV [5, 14] and the chiral condensate $\Sigma_0 < \Sigma \approx (270 \text{ MeV})^3$ [14] decrease significantly as the strange quark mass is sent to zero, whereas the GMOR parameter $B_0 \approx B \approx 2.66$ GeV remains unaffected within its present uncertainty. Regarding baryonic LECs, we obtain $F/D = 0.612^{(14)}_{(12)}$ which is close to the SU(6) quark model expectation $F/D = 2/3$, see, e.g., Ref. [124], which is consistent with the large-N_c limit [156].

Figure 4.10 shows a fit to the pion decay constant and pion mass including updated statistics and additional ensembles (N306 and in particular D250 with $M_\pi \approx 200$ MeV). As can be seen, further constraining the mass-dependence by including ensembles with lighter pion masses would be very interesting. In particular regarding the axial couplings this would be very favourable to improve future analyses.
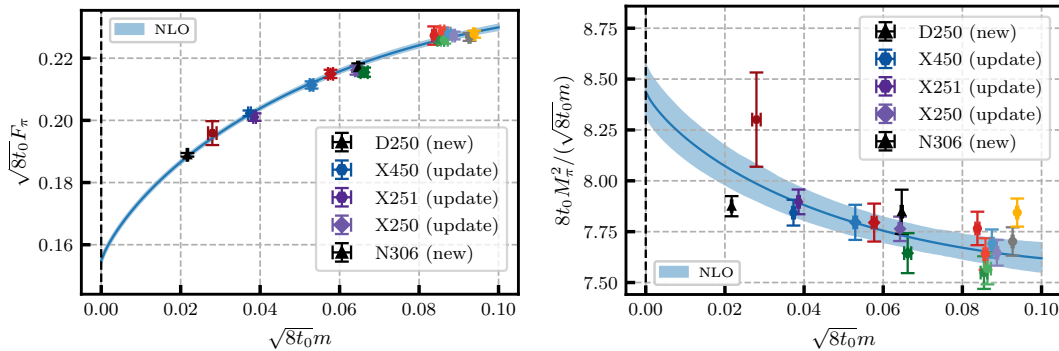

Figure 4.10: Same as Fig. 4.3 but for a preliminary fit including new statistics on the ensembles X250, X251 and X450 as well as two new data points corresponding the ensembles N306 and D250.

5 | OCTET BARYON ISOVECTOR CHARGES

A charge of a hadron parameterizes the strength of its interaction at small momentum transfer with a particle that couples to this particular charge. For instance, the isovector axial charge determines the β-decay rate of the neutron. At the same time, this charge corresponds to the difference between the contribution of the spin of the up quarks minus the spin of the down quarks to the total longitudinal spin of a nucleon in the light front frame that is used in the collinear description of deep inelastic scattering. This intimate connection to spin physics at large virtualities and, more specifically, to the decomposition of the longitudinal proton spin into contributions of the gluon total angular momentum and the spins and angular momenta for the different quark flavours [6, 7] opens up a whole area of intense experimental and theoretical research: the first Mellin moment of the helicity structure functions $g_1(x)$ is related to the sum of the individual spins of the quarks within the proton. For lattice determinations of the individual quark contributions to its first and third moments, see, e.g., Refs. [8–12] and Ref. [157], respectively. Due to the lack of experimental data on $g_1(x)$, in particular at small Bjorken-scale x, and difficulties in the flavour separation, usually additional information is used in determinations of the helicity parton distribution functions (PDFs) from global fits to experimental data [158–162]. In addition to the axial charge g_A of the proton, this includes information from hyperon decays, in combination with SU(3) flavour symmetry relations whose validity need to be checked.

In this chapter we establish the size of the corrections to SU(3) flavour symmetry in the axial sector and also for the scalar and the tensor isovector charges of the octet baryons: in analogy to the connection between axial charges and the first moments of helicity PDFs, the tensor charges are related to first moments of transversity PDFs. This was exploited recently in a global fit by the JAM Collaboration [163, 164]. Since no tensor or scalar couplings contribute to tree-level Standard Model processes, such interactions may hint at new physics and it is important to constrain new interactions (once discovered) using lattice QCD input, see, e.g., Ref. [13] for a detailed discussion. SU(3) flavour symmetry among the scalar charges is also instrumental regarding recent tensions between different determinations of the pion nucleon σ term, see Ref. [52] for a summary of latest phenomenological and lattice QCD results and, e.g., the discussion in section 10 of Ref. [165] about the connection between OZI violation, (approximate) SU(3) flavour symmetry and the value of the pion nucleon σ term. Finally, the scalar isovector charges relate the QCD part of the mass splitting between isospin partners to the difference of the up and down quark masses.

Assuming SU(3) flavour symmetry, the charges for the whole baryon octet in a given channel only depend on two independent parameters. For the proton and the axial charge, this relation reads $g_A = F_A + D_A$, where in the massless limit F_A and D_A correspond to the leading order LECs F and D, respectively, as determined in chapter 4. Already in the first lattice calculations of the axial charge of the proton [64, 166], that were carried out in the quenched approximation[1], F_A and D_A have been determined separately. However,

---

[1]i.e., without including sea quarks in the simulations

in spite of the long history of nucleon structure calculations, SU(3) flavour symmetry breaking is relatively little explored using lattice QCD: only very few investigations of axial charges of the baryon octet exist to date [15–19] and only one of these includes the scalar and tensor charges [19]. Here we compute these charges for the light baryon octet.

In section 5.1, the results for the isovector charges in the continuum, infinite volume limit at physical quark masses are presented. Subsequently, in section 5.2, SU(3) symmetry breaking effects are discussed and the up and down quark mass difference is determined from the scalar charge of the Σ baryon. Furthermore, isospin breaking effects on the baryon masses are split into QCD and QED contributions and isospin breaking corrections to the pion baryon σ terms are determined. Throughout this section we also compare the results to literature values, before summarizing the main results in section 5.3.

Note that the octet baryon isovector charges and some related quantities are defined in chapter 3.1 while an overview of the analysed gauge ensembles was given in section 2.3.2. Further details about the lattice set-up were given throughout chapter 3. Therein, in particular, details about the methods used to obtain two- and three-point correlation functions, the excited state analysis performed to extract the ground state matrix elements, the non-perturbative renormalization and order a improvement and the infinite volume, continuum limit and quark mass extrapolation strategy are given.

This chapter has already been published in similar or verbatim form in Ref. [SW2].

5.1 Continuum, infinite volume and physical quark mass limit

In the following, the extrapolations to the physical point in the continuum and infinite volume limits of the isovector vector (V), axial (A), scalar (S) and tensor (T) charges for the nucleon (N), sigma (Σ) and cascade (Ξ) octet baryons are presented.

5.1.1 Vector charges

The isovector vector charges for the nucleon, cascade and sigma baryons are $g_V^N = g_V^\Xi = 1$ and $g_V^\Sigma = 2$, up to second order isospin breaking corrections [167]. These values also apply to our isospin symmetric lattice results in the continuum limit for any quark mass combination and volume. A determination of the vector charges provides an important cross-check of our analysis methods and allows us to demonstrate that all systematics are under control.

To start with, we display the ratios of the hyperon charges over the nucleon charge in Fig. 5.1. The renormalization factors drop out in the ratio and lattice spacing effects are expected to cancel to some extent. As one can see, the results align very well with the expected values.

For the individual charges, we perform a continuum extrapolation of the data using the fit form

$$g_V = c_0 + c_a \, \mathrm{a}^2 + \bar{c}_a \overline{\mathcal{M}}^2 \, \mathrm{a}^2 + \delta c_a \delta \mathcal{M}^2 \, \mathrm{a}^2 + c_{a,3} \, \mathrm{a}^3. \tag{5.1}$$

Note that there is no dependence on the pion or kaon mass nor on the spatial volume in the continuum limit. $\mathcal{M}^2$ and $\delta \mathcal{M}^2$ represent the flavour average and difference of the kaon and pion masses squared, rescaled with the scale parameter t_0, while the lattice spacing $\mathrm{a} = a/\sqrt{8t_0^*}$. See section 3.7 for further details of the extrapolation procedure. We implement full $O(a)$ improvement and leading discretization effects are quadratic in the lattice spacing. However, the data for the nucleon vector charge are statistically very precise and higher order effects can be resolved. This motivates the addition of the cubic term in Eq. (5.1). The data for g_V^Σ and g_V^Ξ are less precise as they are determined
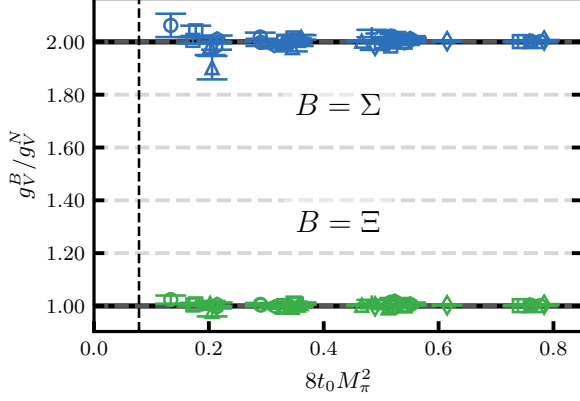
Figure 5.1: Ratio of the hyperon ($B = \Sigma, \Xi$) vector charges over the nucleon charge, g_V^B/g_V^N, as a function of the rescaled pion mass squared ($8t_0 M_\pi^2 = \mathcal{M}_\pi^2$). The data were extracted using two excited states in the fitting analysis, see section 3.4.

employing the stochastic approach outlined in section 3.3 which introduces additional noise, see Appendix C for further discussion.

The data are well described by Eq. (5.1), as demonstrated by the fit, shown in Fig. 5.2, for g_V^N which has a goodness of fit of $\chi^2/N_{\mathrm{dof}} = 0.92$. The data are extracted using two excited states in the fitting analysis (see section 3.4) and we employ the most precise determination of the renormalization factors (Z_V^3, see Table 3.6). A cut of $M_\pi < 400$ MeV is imposed on the ensembles entering the fit, however, fits including all data points are
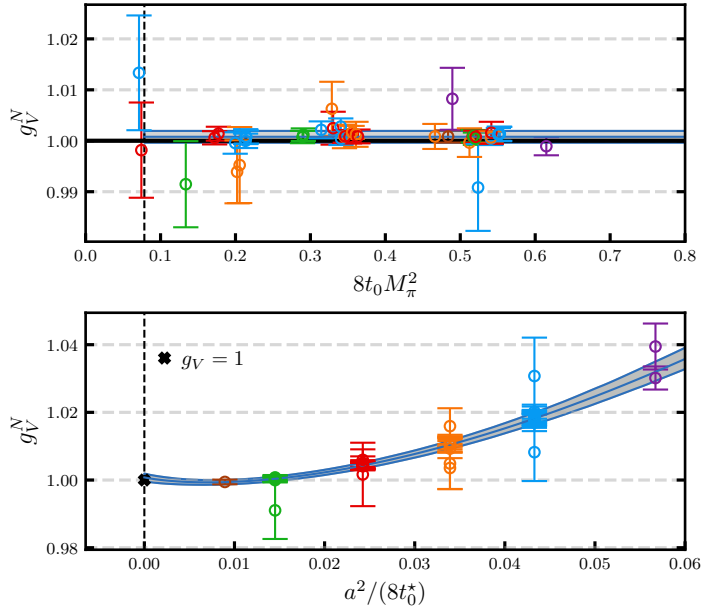

Figure 5.2: Continuum limit extrapolation of the nucleon isovector vector charge g_V^N for a five parameter fit (Eq. (5.1)) using the renormalization factors Z_V^3 (see Table 3.6) and imposing the cut $M_\pi < 400$ MeV. The data were extracted including two excited states in the fitting analysis, see section 3.4. The upper panel shows the data points corrected for discretization effects according to the fit. They are consistent with $g_V^N = 1$. The bottom panel shows the lattice spacing dependence at the physical point. The blue lines and grey bands indicate the expectations from the fit. For better visibility, the data point for ensemble D452, which has a relatively large error (see Table D.5), is not displayed.
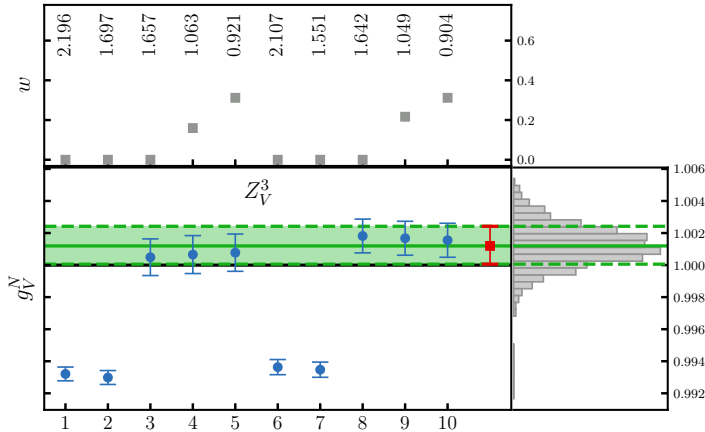
Figure 5.3: Results for the nucleon vector charge g_V^N in the continuum limit at the physical point obtained using Z_V^3 (see Table 3.6) and five different parametrizations applied to data set $\mathrm{DS}(M_\pi^{<400\,\mathrm{MeV}})$ (fits to Eq. (3.43) with different coefficients set to zero labelled 1,...,5, see the text) and $\mathrm{DS}(M_\pi^{<400\,\mathrm{MeV}}, a^{<0.1\,\mathrm{fm}})$ (6,...,10). See section 3.7 for the definitions of the data sets. The data were extracted including two excited states in the fitting analysis, see section 3.4. The model average (performed as described in Appendix B.4) is shown as the red data point and the green horizontal line and band. On the right the model averaged distribution is displayed as a histogram where also the median and the 68% confidence level interval, which form the final result, are indicated (green lines). The top panel shows the weights (grey points) assigned to the individual fits, with the corresponding χ^2/N_{dof} values given above.

also performed, as detailed below. When the data are corrected for the discretization effects according to the fit, we see consistency with $g_V^N = 1$, for all pion and kaon masses. Using the fit to shift the data points to the physical point, we observe that the lattice spacing dependence is moderate but statistically significant, with a 3–4% deviation from the continuum value at the coarsest lattice spacing (lower panel of Fig. 5.2).

In order to investigate the uncertainty arising from the choice of parametrization and the importance of the different terms, we repeat the extrapolations employing five different parametrizations (listed in terms of the coefficients of the terms entering the fit): $(1, \{c_0, c_a\})$, $(2, \{c_0, c_a, \delta c_a\})$, $(3, \{c_0, c_a, c_{a,3}\})$, $(4, \{c_0, c_a, c_{a,3}, \delta c_a\})$ and $(5, \{c_0, c_a, c_{a,3}, \bar{c}_a, \delta c_a\})$. Regarding the lattice spacing dependence, the mass independent term c_a is always included as the other terms are formally at a higher order. These five fits are performed on two data sets. The first set contains ensembles with $M_\pi < 400\,\mathrm{MeV}$ (data set $\mathrm{DS}(M_\pi^{<400\,\mathrm{MeV}})$), while in the second set the ensembles with the coarsest lattice spacing are also excluded ($\mathrm{DS}(M_\pi^{<400\,\mathrm{MeV}}, a^{<0.1\,\mathrm{fm}})$, +5 is added to the fit number). See the end of section 3.7 for the definitions of the data sets.

The results for g_V^N, displayed in Fig. 5.3, show that the cubic term and at least one mass dependent term are needed to obtain a reasonable description of the data in terms of the χ^2/N_{dof}. Two of the fit forms with large χ^2/N_{dof} values (corresponding to fits 1, 2 and 6, 7, with negligible weight in the model averaging procedure, see Appendix B.4) give values that are inconsistent with the continuum expectation. The results are stable under the removal of the coarsest ensembles. Performing the model averaging procedure, the final result for the nucleon, given in the last row of the first column of Table 5.1, agrees with the expectation $g_V^N = 1$ within a combined statistical and systematic uncertainty of about 1‰.

The above analysis is also performed utilizing the sets of renormalization factors Z_V^1 and Z_V^2, determined via the RI′-SMOM scheme [88]. The results for the nucleon vector charge are compared in Fig. 5.4. The uncertainties on these factors are larger, in particular for Z_V^2, than those of set Z_V^3, which is derived using the chirally rotated Schrödinger
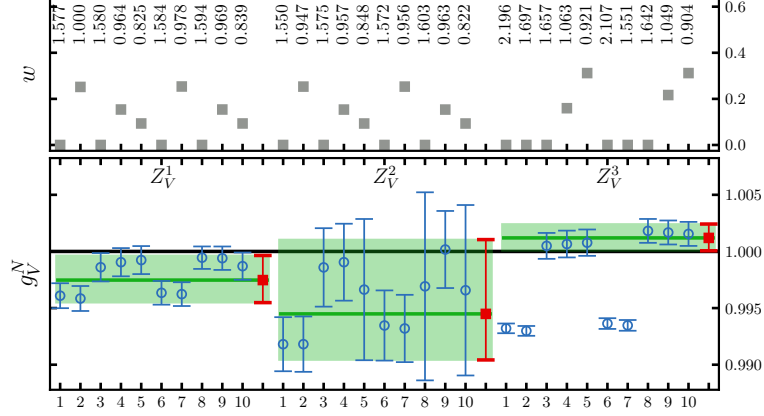
Figure 5.4: Results for the nucleon vector charge g_V^N as in Fig. 5.3 but now also including those obtained employing Z_V^1 and Z_V^2.
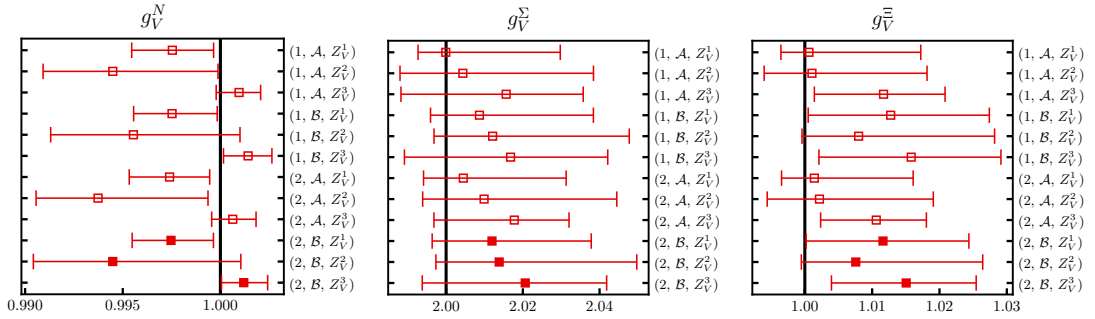

Figure 5.5: Overview of the results for the vector charges g_V^B, $B \in \{N, \Sigma, \Xi\}$, obtained from different data sets. These are labelled by the number of excited states used in the fitting analysis (ES=1, 2), the pion mass cut imposed (denoted $\mathcal{A}$ or $\mathcal{B}$) and the set of renormalization factors employed (Z_V^k, $k = 1, 2, 3$). Each data point represents a model averaged result. The label $\mathcal{A}$ indicates that 15 fits (5 fit variations applied to three data sets, DS(0), DS($M_\pi^{<400\,\mathrm{MeV}}$) and DS($a^{<0.1\,\mathrm{fm}}$)) are averaged, while the results labelled with $\mathcal{B}$ are based on the set of 10 fits utilized in Fig. 5.3 (5 fit variations applied to two data sets, DS($M_\pi^{<400\,\mathrm{MeV}}$) and DS($M_\pi^{<400\,\mathrm{MeV}}$, $a^{<0.1\,\mathrm{fm}}$)). See section 3.7 for the definitions of the data sets. The final results for each Z_V^k (filled squares) are listed in Table 5.1.

functional approach [94]. This translates into larger errors for g_V^N for those fits. The lattice spacing dependence is somewhat different: the first quadratic mass dependent term in Eq. (5.1) and the cubic term can no longer be fully resolved and also parametrization $(2, \{c_0, c_a, \delta c_a\})$ gives a $\chi^2/N_{\mathrm{dof}} = 1.00\ (0.95)$ when employing Z_V^1 (Z_V^2).

The systematic uncertainty of the results due to residual excited state contamination and the range of pion masses employed in the extrapolations is also considered. Figure 5.5 shows the model averaged results discussed so far, displayed as filled squares, and also those obtained using several other sets of fits. These are labelled in terms of the number of excited states (one or two) included in the fitting analysis, the cuts imposed on the pion mass ($\mathcal{A}$ or $\mathcal{B}$) and the renormalization factors utilized. For the results from pion mass cut $\mathcal{A}$, 15 fits enter the model average, the five different parametrizations are applied to three data sets DS(0), DS($M_\pi^{<400\,\mathrm{MeV}}$) and DS($a^{<0.1\,\mathrm{fm}}$). Note that the first and third data set include ensembles with pion masses up to 430 MeV. For mass cut $\mathcal{B}$, data sets DS($M_\pi^{<400\,\mathrm{MeV}}$) and DS($M_\pi^{<400\,\mathrm{MeV}}$, $a^{<0.1\,\mathrm{fm}}$) are used, giving 10 fits in total. The results only depend on the choice of renormalization factors, suggesting that the systematic uncertainties due to excited state contamination and the cut made on the pion mass are

Table 5.1: Results for g_V^B, $B \in \{N, \Sigma, \Xi\}$, obtained with three different sets of renormalization factors. The errors include the statistical and all the systematic uncertainties.

Renormalization	g_V^N	g_V^Σ	g_V^Ξ
Z_V^1 (Table 3.4)	$0.9975^{(22)}_{(20)}$	$2.012^{(26)}_{(16)}$	$1.012^{(13)}_{(11)}$
Z_V^2 (Table 3.5)	$0.9945^{(66)}_{(41)}$	$2.014^{(36)}_{(16)}$	$1.008^{(19)}_{(8)}$
Z_V^3 (Table 3.6)	$1.0012^{(12)}_{(11)}$	$2.021^{(21)}_{(27)}$	$1.015^{(10)}_{(11)}$

very small.

Repeating the whole procedure for the sigma and the cascade baryons gives vector charges which are also consistent with the expected values to within $1.5\,\sigma$, as shown in Fig. 5.5 (see Figs. E.2 and E.3 in Appendix E for the individual fits for mass cut $\mathcal{B}$). The statistical noise introduced by the stochastic approach dominates, leading to much less precise values and very little variation between the results for the different hyperon data sets. We take the values obtained from the data sets $(2, \mathcal{B}, Z_V^k)$, listed in Table 5.1, as our estimates of the vector charges as these data sets give the most reliable determinations of the charges across the different channels (as discussed in the following subsections).

Overall, the results demonstrate that the systematics arising from excited state contamination, renormalization and finite lattice spacing are under control in our analysis in this channel (to within an error of 1‰ for the nucleon).

5.1.2 Axial charges

In the following we present the results for the nucleon, sigma and cascade isovector axial charges g_A^B, $B \in \{N, \Sigma, \Xi\}$. The nucleon axial charge is very precisely measured in experiment, $\lambda = g_A^N/g_V^N = 1.2754(13)$ [5], and serves as another benchmark quantity when assessing the size of the systematics of the final results. Note, however, that possible differences of up to 2%, due to radiative corrections, between λ computed in QCD and an effective λ measured in experiment have been discussed recently [168, 169]. Lattice determinations of g_A^N are known to be sensitive to excited state contributions, finite volume effects and other systematics. Whereas there is a long history of lattice QCD calculations of g_A^N, see, e.g., the FLAG 21 review [14], there are very few lattice computations of hyperon axial charges [15–19] and only few phenomenological estimates exist from measurements of semileptonic hyperon decay rates.

We carry out simultaneous continuum, quark mass and finite volume extrapolations to the individual baryon charges employing the parametrization in Eq. (3.43) (with the continuum form in Eq. (3.42)). The discretization effects are found to be fairly mild and we are not able to resolve the quadratic mass dependent terms or a cubic term. These terms are omitted throughout. As already mentioned in section 3.7 we are also not able to resolve any higher order ChPT terms in the continuum parametrization.

A five parameter fit, with free coefficients $\{c_0, c_\pi, c_K, c_V, c_a\}$, describes the data well, as demonstrated in Fig. 5.6 for the nucleon (with $\chi^2/N_{\text{dof}} = 0.86$) and Fig. 5.7 for the sigma and cascade baryons (with $\chi^2/N_{\text{dof}} = 0.85$ and 1.25, respectively). The data are extracted using two excited states ('ES=2') in the fitting analysis (see section 3.4) and renormalized with factors Z_A^3 (that are the most precise of the three determinations considered, see Table 3.6). For the cascade baryon, with two strange quarks, the data on the three quark mass trajectories (Tr $M = $ const., $m_s = $ const. and $m_\ell = m_s$) are clearly delineated, however, note the different scale on the right of Fig. 5.7. The availability of
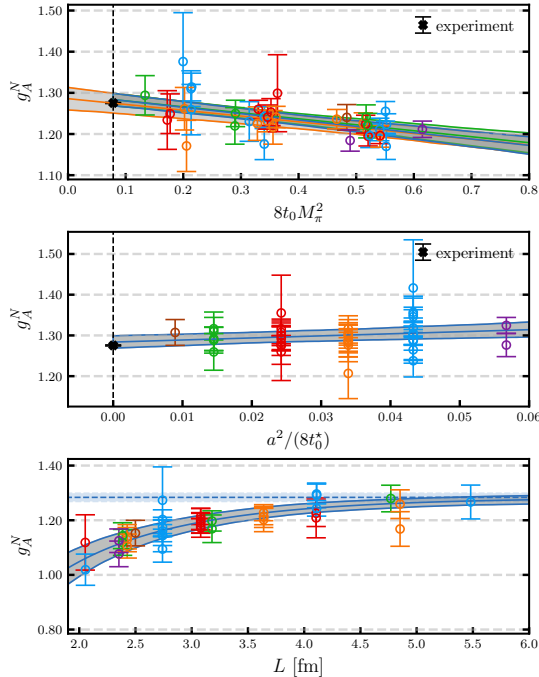
Figure 5.6: Simultaneous quark mass, continuum and finite volume extrapolation of the nucleon isovector axial charge g_A^N extracted on ensembles with $M_\pi < 400\,\text{MeV}$ using two excited states in the fitting analysis (see section 3.4) and renormalization factors Z_A^3 (see Table 3.6). A five parameter fit form is employed, see the text. (Top) Pion mass dependence of g_A^N, where the data points are corrected, using the fit, for finite volume and discretization effects and shifted (depending on the ensemble) to kaon masses corresponding to the $\text{Tr}\,M = \text{const.}$ and $m_s = \text{const.}$ trajectories. The fit is shown as a grey band with the three trajectories, including the symmetric line, distinguished by blue, green and orange lines, respectively. The vertical dashed line indicates the physical point. (Middle) Lattice spacing dependence at the physical point in the infinite volume limit. (Bottom) Finite volume dependence at the physical point in the continuum limit. The dashed blue line (band) indicates the infinite volume result. For better visibility, the data points for ensembles D150, E250 and D452, which have relatively large errors (see Table D.5), are not displayed. The black cross at the physical point indicates the experimental value [5].

ensembles on two trajectories which intersect at the physical point helps to constrain the physical value of the axial charge. In terms of the finite volume effects, only the nucleon shows a significant dependence on the spatial extent. The quark mass dependence is also pronounced in this case.

As in the vector case, we quantify the systematics associated with the extraction of the charges at the physical point (in the continuum and infinite volume limits) by varying the parametrization and the set of ensembles that are included in the fit. We consider two fit forms $(1, \{c_0, c_\pi, c_K, c_V, c_a\})$ and $(2, \{c_0, c_\pi, c_K, c_V, c_a, \delta c_a\})$ and four data sets, $\text{DS}(M_\pi^{<400\,\text{MeV}})$, $\text{DS}(M_\pi^{<300\,\text{MeV}})$, $\text{DS}(M_\pi^{<400\,\text{MeV}}, a^{<0.1\,\text{fm}})$ and $\text{DS}(M_\pi^{<400\,\text{MeV}}, LM_\pi^{>4})$, see section 3.7 for their definitions.

The results of the eight fits and their model averages for the three different determinations of the renormalization factors are shown in Fig. 5.8 for the nucleon and in Fig. E.4 of Appendix E for the hyperon axial charges. In all cases, we find consistent results across the different fits and choice of renormalization factor suggesting that the statistical errors dominate. The additional lattice spacing term is not properly resolved with the goodness of fit only changing slightly, while the errors on the coefficients increase. For the nucleon and sigma baryon, all fits have a $\chi^2/N_{\text{dof}} < 1$ and are given a similar weight in the model
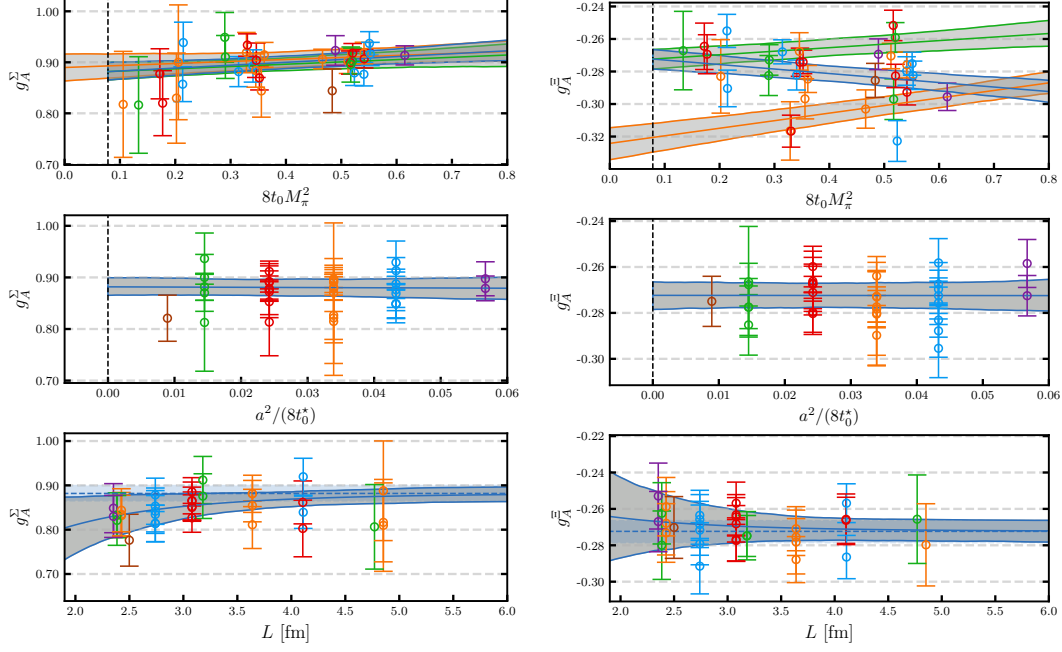
Figure 5.7: The same as Fig. 5.6 for the isovector axial charges g_A^B of the sigma baryon (left) and the cascade baryon (right). For better visibility, the data points for ensembles D452 and D451, which have relatively large errors (see Table D.7), are not displayed for the cascade baryon. Compared to the nucleon, for the analysis of the hyperon charges a reduced set of ensembles is employed, see Tables D.6 and D.7 for a complete list of ensembles.
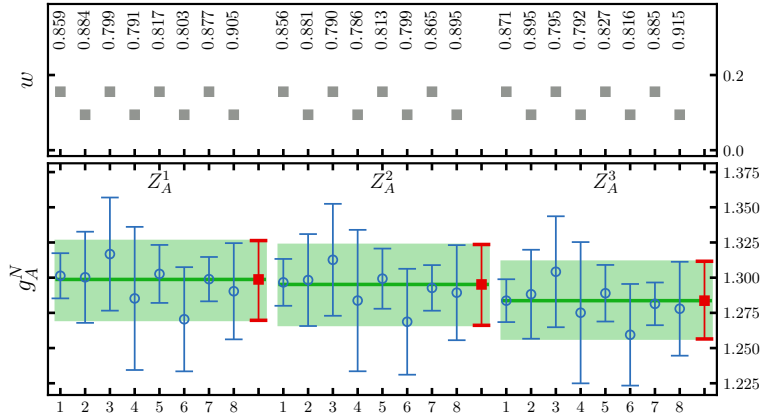

Figure 5.8: The same as Fig. 5.4 for the nucleon axial charge g_A^N. The eight fits correspond to two fit variations, see the text, applied to four data sets, $DS(M_\pi^{<400\,\text{MeV}})$, $DS(M_\pi^{<300\,\text{MeV}})$, $DS(M_\pi^{<400\,\text{MeV}}, a^{<0.1\,\text{fm}})$ and $DS(M_\pi^{<400\,\text{MeV}}, LM_\pi^{>4})$. The data are extracted using two excited states in the fitting analysis, see section 3.4.

average, while for the cascade baryon, the cut $M_\pi^{<300\,\text{MeV}}$ is needed to achieve a goodness of fit around 1 and these fits have the highest weight factors.

In order to further explore the systematics, additional data sets are considered. We assess the sensitivity of the results to excited state contributions by performing extrapolations of the data extracted using only one excited state ('ES=1') in the fitting analysis. In addition, as only the $O(p^2)$ ChPT terms are included in the continuum parametrization, we test the description of the quark mass dependence by performing 10 fits, involving the two parametrization variations above, applied to five data sets, $DS(0)$, $DS(M_\pi^{<400\,\text{MeV}})$,
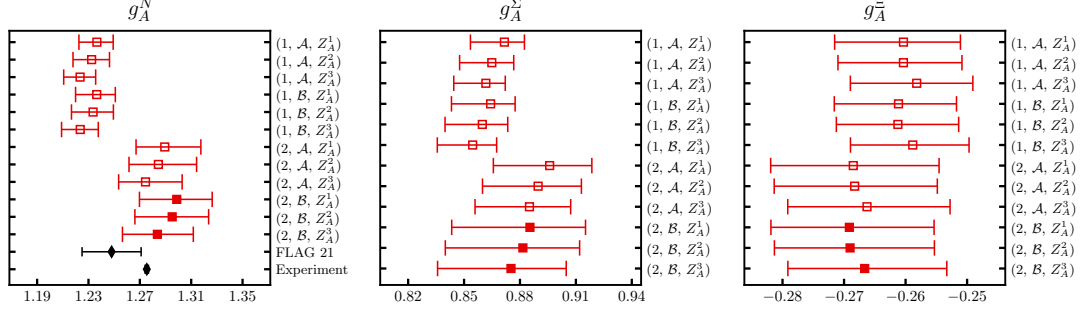
Figure 5.9: The same as Fig. 5.5 for the nucleon, sigma and cascade axial charges. The label $\mathcal{A}$ indicates that 10 fits enter the model average corresponding to two fit variations, see the text, applied to 5 data sets, DS(0), DS($M_\pi^{<400\,\mathrm{MeV}}$), DS($M_\pi^{<300\,\mathrm{MeV}}$), DS($a^{<0.1\,\mathrm{fm}}$) and DS($LM_\pi^{>4}$). For the data points labelled with $\mathcal{B}$, the results of the 8 fits employed in Fig. 5.8 are averaged. For the nucleon, the FLAG 21 average for $N_f = 2+1$ [85, 170] and the experimental value [5] are indicated (black diamonds)

DS($M_\pi^{<300\,\mathrm{MeV}}$), DS($a^{<0.1\,\mathrm{fm}}$) and DS($LM_\pi^{>4}$). The first, fourth and fifth data sets include ensembles with pion masses up to 430 MeV.

The results for the axial charges from model averaging the 10 fits (denoted $\mathcal{A}$) employing the 5 data sets and also from the 8 fits (denoted $\mathcal{B}$) using the 4 data sets given above, for the 'ES=1' and 'ES=2' data and the different renormalization factors are displayed in Fig. 5.9. Very little variation is seen in the results in terms of the range of pion masses included and, as before, the renormalization factors employed, suggesting the associated systematics are accounted for within the combined statistical and systematic error (which includes the uncertainty due to lattice spacing and finite volume effects). However, the results are sensitive to the number of excited states included in the fitting analysis. This is only a significant effect for the nucleon, for which the 'ES=1' results lie around $2.5\,\sigma$ below experiment. Similar underestimates of g_A^N have been observed in many earlier lattice studies [14].

As detailed in section 3.4, more than one excited state is contributing significantly to the ratio of three-point over two-point correlation functions and including two excited states in the fitting analysis enables the ground state matrix element to be isolated more reliably. Considering the pion mass cuts, to be conservative we take the results of the model averages of the $\mathcal{B}$ data sets (where all the ensembles have $M_\pi < 400\,\mathrm{MeV}$) as only the dominant mass dependent terms are included in the continuum parametrization. The estimates, corresponding to the ('ES=2', $\mathcal{B}$, Z_A^k) results in Fig. 5.9, are listed in Table 5.2.

Table 5.2: Results for g_A^B, $B \in \{N, \Sigma, \Xi\}$, obtained with three different sets of renormalization factors. The errors include the statistical and all the systematic uncertainties.

Renormalization	g_A^N	g_A^Σ	g_A^Ξ
Z_A^1 (Table 3.4)	$1.299^{(28)}_{(29)}$	$0.885^{(30)}_{(42)}$	$-0.269^{(14)}_{(13)}$
Z_A^2 (Table 3.5)	$1.295^{(28)}_{(29)}$	$0.882^{(30)}_{(42)}$	$-0.269^{(14)}_{(12)}$
Z_A^3 (Table 3.6)	$1.284^{(28)}_{(27)}$	$0.875^{(30)}_{(39)}$	$-0.267^{(13)}_{(12)}$

5.1.3 Scalar charges

As there is no isovector scalar current interaction at tree-level in the Standard Model, the scalar charges cannot be measured directly in experiment. However, the conserved vector current (CVC) relation can be used to estimate the charges from determinations of the up and down quark mass difference, $\delta_m = m_u - m_d$, and the QCD contribution to baryon mass isospin splittings, e.g., between the mass of the proton and the neutron, $\Delta m_N^{\rm QCD}$, (for g_S^N see Eq. (5.20) below). Reference [171] finds $g_S^N = 1.02(11)$ employing lattice estimates for δ_m and an average of lattice and phenomenological values for $\Delta m_N^{\rm QCD}$, which is consistent with the FLAG 21 [14] $N_f = 2 + 1$ result of $g_S^N = 1.13(14)$ [85]. Estimates can also be made of the isovector scalar charges of the other octet baryons, see the discussion in section 5.2.1. Conversely, direct determinations of the scalar charges can be used to predict δ_m, as presented in section 5.2.3. So far, there has been only one previous study of the hyperon scalar charges [19].

For the extrapolation of the scalar charges and the extraction of the value at the physical point, we follow the same procedures as for the axial channel, presented in the previous subsection. The five parameter fit (with coefficients $\{c_0, c_\pi, c_K, c_V, c_a\}$) can again account for the observed quark mass, lattice spacing and volume dependence as illustrated in Fig. 5.10 for the nucleon (with $\chi^2/N_{\rm dof} = 0.56$) and Fig. E.7 of Appendix E for the sigma and cascade baryons (with $\chi^2/N_{\rm dof} = 0.97$ and 1.14, respectively). The data are extracted using two excited states in the fitting analysis. For both hyperons, the quark mass and lattice spacing effects can be resolved, in contrast to the nucleon, while for all baryons the dependence on the spatial volume is marginal. When investigating the systematics in the estimates of the charges at the physical point, we perform model averages of the results of ($\mathcal{A}$): 8 fits from the two fit variations (as for the axial case) and the four data sets, DS(0), DS($M_\pi^{<400\,{\rm MeV}}$), DS($a^{<0.1\,{\rm fm}}$) and DS($LM_\pi^{>4}$), ($\mathcal{B}$): 6 fits from the two fit variations to the three data sets DS($M_\pi^{<400\,{\rm MeV}}$), DS($M_\pi^{<400\,{\rm MeV}}, a^{<0.1\,{\rm fm}}$)
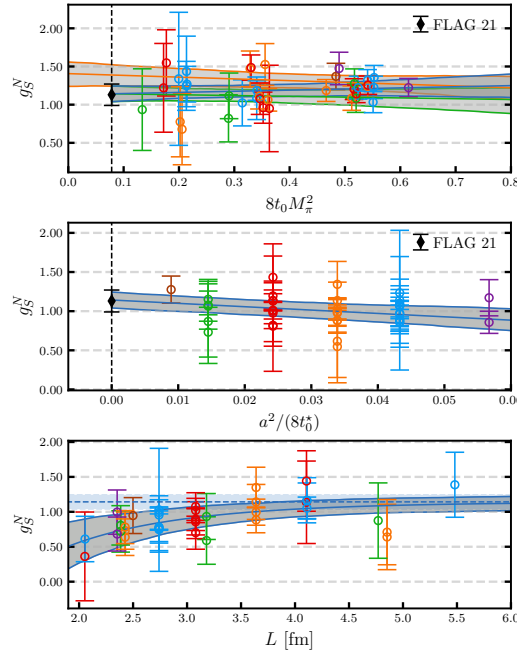

Figure 5.10: The same as Fig. 5.6 for the nucleon scalar charge g_S^N. The factors Z_S^1 are used for the matching (see Table 3.4). For orientation, the FLAG 21 result for $N_f = 2 + 1$ [85] is indicated (black diamond) at the physical point. For better visibility, the data points for ensembles D150, E250 and D452, which have relatively large errors (see Table D.5), are not displayed.
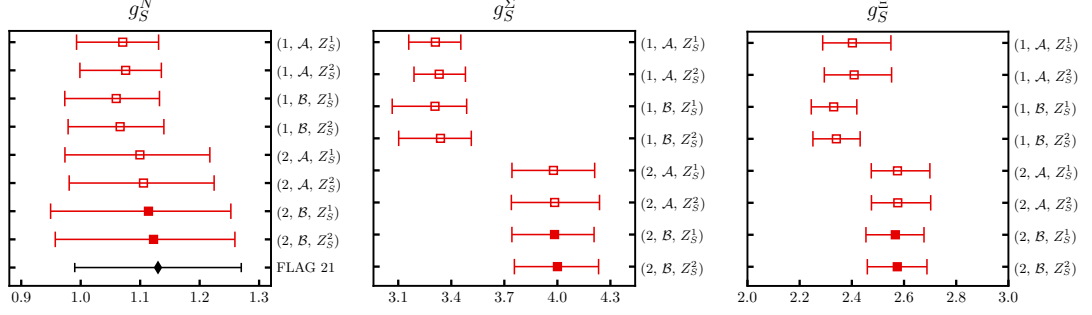
Figure 5.11: The same as Fig. 5.5 for the nucleon, sigma and cascade scalar charges. The label $\mathcal{A}$ indicates that 8 fits enter the model average corresponding to two fit variations, see the text, applied to 4 data sets, DS(0), DS($M_\pi^{<400\,\mathrm{MeV}}$), DS($a^{<0.1\,\mathrm{fm}}$) and DS($LM_\pi^{>4}$). For the data points labelled with $\mathcal{B}$, the two fit variations are performed on 3 data sets, DS($M_\pi^{<400\,\mathrm{MeV}}$), DS($M_\pi^{<400\,\mathrm{MeV}}$, $a^{<0.1\,\mathrm{fm}}$) and DS($M_\pi^{<400\,\mathrm{MeV}}$, $LM_\pi^{>4}$), giving a total of 6 fits for the average. For the nucleon, the FLAG 21 result for $N_f = 2 + 1$ [85] is also shown (black diamond).

and DS($M_\pi^{<400\,\mathrm{MeV}}$, $LM_\pi^{>4}$). Note that a cut on the pion mass $M_\pi < 300\,\mathrm{MeV}$ is not considered. The scalar matrix elements are generally less precise than the axial ones and utilizing such a reduced data set leads to instabilities in the extrapolation and spurious values of the coefficients.

For illustration, the values from the individual fits and the model averages over the $\mathcal{B}$ data sets for the two different determinations of the renormalization factors are given in Fig. E.5 in Appendix E. The results are consistent across the different fits, although the weights vary. The values of the scalar charges for all the model averages performed are compiled in Fig. 5.11. There are no significant variations in the results obtained using the different renormalization factors and data sets ($\mathcal{A}$ or $\mathcal{B}$). For the nucleon, there is also agreement between the values for the data extracted including one ('ES=1') or two ('ES=2') excited states in the fitting analysis and consistency with the current FLAG 21 result. For the sigma baryon, and to a lesser extent for the cascade baryon, there is a tension between the 'ES=1' and 'ES=2' determinations. As discussed previously, the ('ES=2', $\mathcal{B}$, Z_S^k) values are considered the most reliable. These are listed in Table 5.3.

Table 5.3: Results for g_S^B, $B \in \{N, \Sigma, \Xi\}$, obtained with two different sets of renormalization factors. The errors include the statistical and all the systematic uncertainties.

Renormalization	g_S^N	g_S^Σ	g_S^Ξ
Z_S^1 (Table 3.4)	$1.11^{(14)}_{(16)}$	$3.98^{(22)}_{(24)}$	$2.57^{(11)}_{(11)}$
Z_S^2 (Table 3.5)	$1.12^{(14)}_{(17)}$	$4.00^{(23)}_{(24)}$	$2.57^{(11)}_{(11)}$

5.1.4 Tensor charges

In the isosymmetric limit, the nucleon tensor charge is equal to the first moment of the nucleon isovector transversity parton distribution function. Due to the lack of experimental data, estimates of g_T^N from phenomenological fits have very large uncertainties, unless some assumptions are made. In fact, in some analyses, the fit is constrained to reproduce the lattice results for the isovector charge, see Refs. [163, 164]. The FLAG 21 review [14] gives as the $N_f = 2 + 1$ value for the nucleon tensor charge the result of Ref. [85],
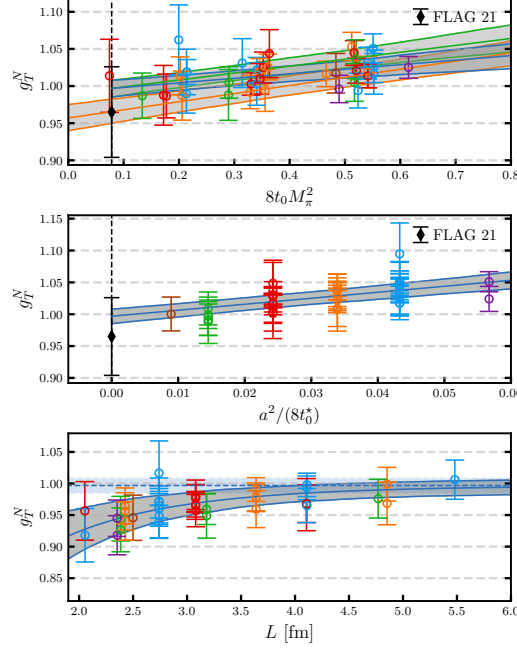
Figure 5.12: The same as Fig. 5.6 for the nucleon tensor charge g_T^N. The factors Z_T^1 are used for the matching (see Table 3.4). For orientation, the FLAG 21 result for $N_f = 2 + 1$ [85] is indicated (black diamond) at the physical point. For better visibility, the data points for ensembles D150 and D452, which have relatively large errors (see Table D.5), are not displayed.

$g_T^N = 0.965(61)$, whereas, as far as we know, there is only one previous study of the hyperon tensor charges [19].

The extraction of the octet baryon tensor charges at the physical point follows the analysis of the axial charges in section 5.1.2. In particular, the parametrizations employed and the data sets considered are the same. Figure 5.12 displays a typical example of an extrapolation for the nucleon tensor charge for a five parameter fit with a $\chi^2/N_{\rm dof} = 0.63$. See Fig. E.8 in Appendix E for the analogous figures for the sigma and cascade baryons. The variation of the fits with the parametrization and the data sets utilized and the corresponding model averages, for the data sets with pion mass cut $\mathcal{B}$ (see section 5.1.2), are shown in Fig. E.6.

An overview of the model averaged results for all variations of the input data is given in Fig. 5.13. The agreement between the different determinations suggests the systematics
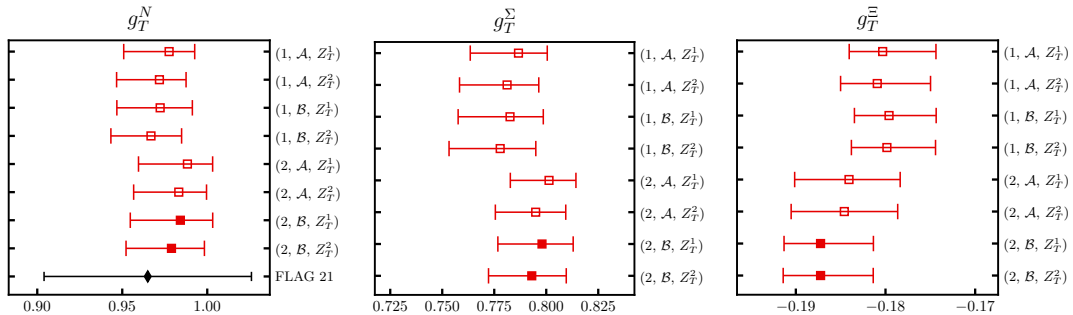

Figure 5.13: The same as Fig. 5.5 for the nucleon, sigma and cascade tensor charges. For the nucleon, the FLAG 21 result for $N_f = 2 + 1$ [85] is also shown (black diamond).

associated with the extrapolation are under control. Although the results utilizing data extracted with two excited states ('ES=2') in the fitting analysis are consistently above or below those extracted from the 'ES=1' data, considering the size of the errors of the model averages (which combine the statistical and systematic uncertainties), the differences are not significant. The estimates for the tensor charges, corresponding to the ('ES=2', $\mathcal{B}$, Z_T^k) values, are listed in Table 5.4.

Table 5.4: Results for g_T^B, $B \in \{N, \Sigma, \Xi\}$, obtained with two different sets of renormalization factors. The errors include the statistical and all the systematic uncertainties.

Renormalization	g_T^N	g_T^Σ	g_T^Ξ
Z_T^1 (Table 3.4)	$0.984^{(19)}_{(29)}$	$0.798^{(15)}_{(21)}$	$-0.1872^{(59)}_{(41)}$
Z_T^2 (Table 3.5)	$0.979^{(19)}_{(27)}$	$0.793^{(17)}_{(21)}$	$-0.1872^{(59)}_{(42)}$

5.2 Discussion of the results

The values for the vector, axial, scalar and tensor charges of the nucleon, sigma and cascade baryons are given in Tables 5.1, 5.2, 5.3 and 5.4, respectively. In each case, we take the most precise value as the final result, i.e., the one obtained using Z_V^3 and Z_A^3 for the vector and axial channels, respectively, and Z_S^1 and Z_T^1 for the scalar and the tensor. In the following we compare with previous determinations of the charges taken from the literature and discuss the SU(3) flavour symmetry breaking effects in the different channels. We use the conserved vector current relation and the result for the scalar charge of the sigma baryon to determine the up and down quark mass difference. Further, we compute the QCD contributions to baryon isospin mass splittings and evaluate the isospin breaking effects on the pion baryon σ terms.

5.2.1 Individual charges

We first consider the axial charges where the final values read

$$g_A^N = 1.284^{(28)}_{(27)}, \qquad g_A^\Sigma = 0.875^{(30)}_{(39)}, \qquad g_A^\Xi = -0.267^{(13)}_{(12)}. \qquad (5.2)$$

The result for the nucleon compares favourably with the experimental value $\lambda = g_A^N/g_V^N = 1.2754(13)$ [5] and the FLAG 21 [14] average for $N_f = 2 + 1$, $g_A^N = 1.248(23)$. The latter is based on the determinations in Refs. [85, 170]. All sources of systematic uncertainty must be reasonably under control to be included in the FLAG average and a number of more recent studies incorporate continuum, quark mass and finite volume extrapolations. A compilation of results for g_A^N is displayed in Fig. 5.14. Although the determinations are separated in terms of the number of dynamical fermions employed, including charm quarks in the sea is not expected to lead to a discernible effect.

Regarding the hyperon axial charges, far fewer works exist. Lin *et al.* [15, 183] performed the first study, utilizing $N_f = 2 + 1$ ensembles with pion masses ranging between 350 MeV and 750 MeV and a single lattice spacing of 0.12 fm. After an extrapolation to the physical pion mass they obtain $g_A^\Sigma = 0.900(42)_{\text{stat}}(54)_{\text{sys}}$ and $g_A^\Xi = -0.277(15)_{\text{stat}}(19)_{\text{sys}}$, where estimates of finite volume and discretization effects are included in the systematic uncertainty. Note that their result for g_A^Σ is multiplied by a factor of two to match our normalization convention. In Refs. [17, 184] ETMC determined all octet
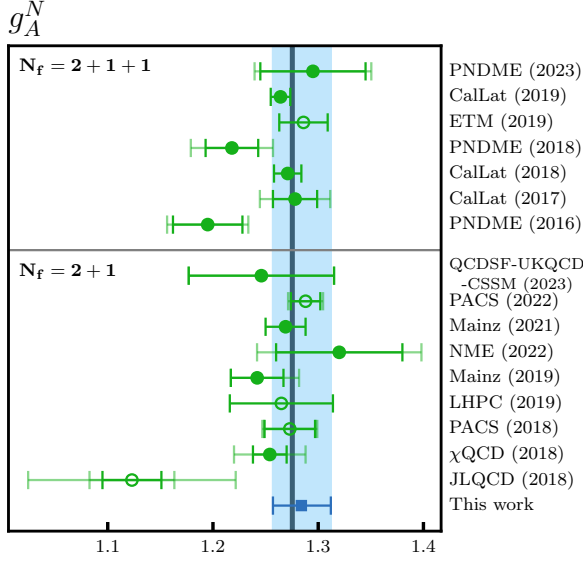
Figure 5.14: Compilation of recent lattice determinations of the nucleon axial charge g_A^N with $N_f = 2 + 1$ [19, 85, 170, 172–177] and $N_f = 2 + 1 + 1$ [104, 105, 178–182] dynamical fermions. Values with filled symbols were obtained via a chiral, continuum and finite volume extrapolation. The vertical black line gives the experimental result [5].

and decuplet (i.e., nucleon, hyperon and Δ) axial couplings employing $N_f = 2 + 1 + 1$ ensembles with pion masses between $210\,\mathrm{MeV}$ and $430\,\mathrm{MeV}$ and two lattice spacings $a \in \{0.065\,\mathrm{fm}, 0.082\,\mathrm{fm}\}$. Using a simple linear ansatz for the quark mass extrapolation, they quote $g_A^\Sigma = 0.7629(218)_\mathrm{stat}$ and $g_A^\Xi = -0.2479(87)_\mathrm{stat}$, where the errors are purely statistical.

More recently, Savanur et $al.$ [18] extracted the axial charges on $N_f = 2 + 1 + 1$ ensembles with three different lattice spacings $a \in \{0.06\,\mathrm{fm}, 0.09\,\mathrm{fm}, 0.12\,\mathrm{fm}\}$, pion masses between $135\,\mathrm{MeV}$ and $310\,\mathrm{MeV}$ and volumes in the range $3.3 \leq LM_\pi \leq 5.5$. The ratios g_A^Σ/g_A^N and g_A^Ξ/g_A^N are extrapolated taking the quark mass dependence and lattice spacing and finite volume effects into account. The experimental value of g_A^N is then used to obtain $g_A^\Sigma = 0.891(11)_\mathrm{stat}(13)_\mathrm{sys}$ (again multiplied by a factor of two to meet our conventions) and $g_A^\Xi = -0.2703(47)_\mathrm{stat}(13)_\mathrm{sys}$. Finally, QCDSF-UKQCD-CSSM presented results for the isovector axial, scalar and tensor charges in Ref. [19]. They employ $N_f = 2 + 1$ ensembles lying on a $\mathrm{Tr}M = \mathrm{const.}$ trajectory with pion masses ranging between $220\,\mathrm{MeV}$ and $470\,\mathrm{MeV}$ and five different values of the lattice spacing in the range $(0.052-0.082)\,\mathrm{fm}$. The Feynman-Hellmann theorem is used to calculate the baryon matrix elements. Performing an extrapolation to the physical mass point including lattice spacing and finite volume effects, they find $g_A^\Sigma = 0.876(26)_\mathrm{stat}(09)_\mathrm{sys}$ and $g_A^\Xi = -0.206(22)_\mathrm{stat}(19)_\mathrm{sys}$.

We also mention the earlier studies of Erkol et $al.$ [16] ($N_f = 2$), utilizing pion masses above $500\,\mathrm{MeV}$, and QCDSF-UKQCD ($N_f = 2 + 1$) carried out at a single lattice spacing [185].

In Fig. 5.15 we compare the ratios of the hyperon axial charges over the nucleon axial charge, g_A^B/g_A^N, from Refs. [15, 17, 18], obtained on individual ensembles to our results. A comparison of the charges themselves cannot be made since, as mentioned above, Savanur et $al.$ only present results for the ratio. As the strange quark mass is held approximately constant in these works, only our results from the $m_s = \mathrm{const.}$ trajectory are displayed. Similarly, the QCDSF-UKQCD-CSSM values are omitted as the ensembles utilized lie on a $\mathrm{Tr}M = \mathrm{const.}$ trajectory. We observe reasonable agreement between the data. Note that our continuum, infinite volume limit result (the grey band in the figure) for g_A^Σ/g_A^N lies slightly below the central values of most of our $m_s = \mathrm{const.}$ data points.

The individual hyperon axial charges at the physical point are shown in Fig. 5.16, along with a number of phenomenological determinations employing a variety of quark models [186, 188, 189], the chiral soliton model [187] and SU(3) covariant baryon ChPT [103].
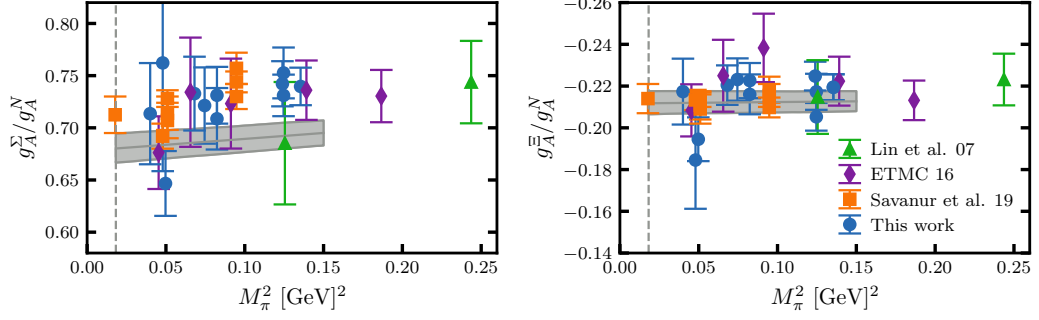
Figure 5.15: Comparison of lattice determinations [15, 17, 18] of the hyperon axial charges for the sigma and cascade baryons normalized to the nucleon axial charge. Some of the results from Lin *et al.* at heavier pion masses are not shown. The grey vertical dashed line indicates the physical pion mass point. Only our results from the $m_s = \text{const.}$ trajectory are shown. The grey bands indicate the (continuum limit, infinite volume) quark mass behaviour according to the fits displayed in Figs. 5.6 and 5.7. Note that the data points are not corrected for finite volume or discretization effects. All data are converted to our phase and normalization conventions, Eqs. (3.1)–(3.6). The Lin *et al.* and ETMC results are obtained by taking the ratio of the individual charges and employing error propagation.
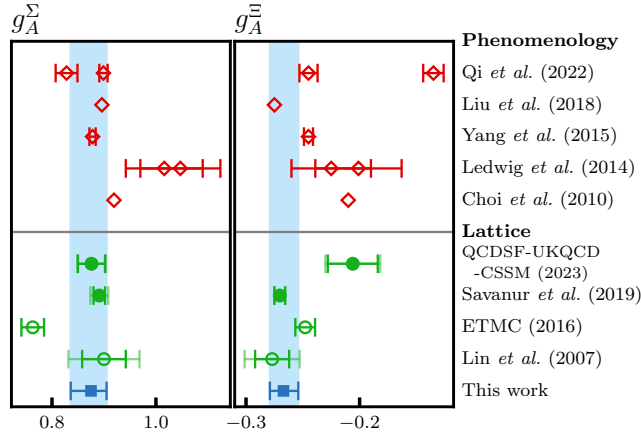
Figure 5.16: Comparison of our results for the axial charges g_A^Σ and g_A^Ξ (blue symbols and error bands) with other lattice determinations [15, 17–19] and phenomenological estimates [103, 186–189]. Values with filled symbols were obtained via a chiral, continuum and finite volume extrapolation. All results are converted to our phase and normalization conventions, Eqs. (3.1)–(3.6).

Within errors, the lattice results are consistent apart from the rather low value for g_A^Σ from ETMC [17] and the rather high value for g_A^Ξ from QCDSF-UKQCD-CSSM [19]. The phenomenological estimates for g_A^Σ are in reasonable agreement with our value, while there is a large spread in the expectations for g_A^Ξ.

We remark that, in analogy to the CVC relation (discussed in section 5.2.3 below), the axial Ward identity, $\partial_\mu(\bar{u}\gamma_\mu\gamma_5 d) = i(m_d + m_u)\bar{u}\gamma_5 d$, connects the axial and pseudoscalar charges,

$$g_P^B = \frac{m_B}{m_\ell} g_A^B, \tag{5.3}$$

where m_B and m_ℓ correspond to the baryon and the light quark mass, respectively. This relation was employed in Ref. [171] to determine the pseudoscalar charge of the nucleon, which is defined as the pseudoscalar form factor in the forward limit. Taking the baryon masses of isosymmetric QCD from Table 14 of Ref. [52] and the isospin averaged light quark mass $m_\ell = 3.381(40)$ MeV in the $N_f = 4$ flavour $\overline{\text{MS}}$ scheme at $\mu = 2\,\text{GeV}$ from

Figure 5.17: As in Fig. 5.14 for the nucleon scalar charge g_S^N with $N_f = 2 + 1$ [19, 85, 172, 174–177, 190, 191] and $N_f = 2 + 1 + 1$ [105, 178, 180, 182] dynamical fermions. González-Alonso *et al.* estimate the scalar charge via the conserved vector current (CVC) relation [171].
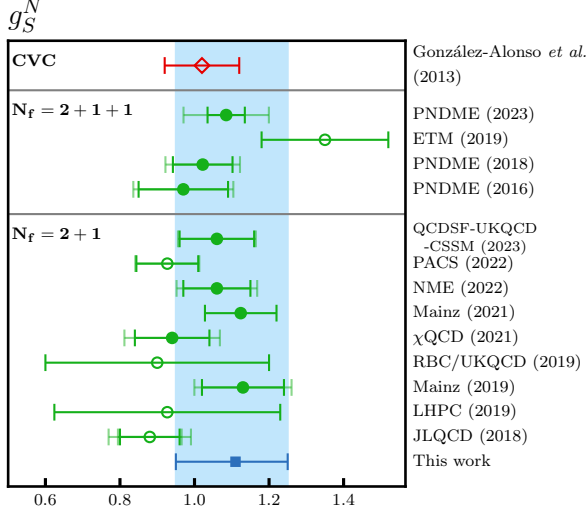
the FLAG 21 review [14], we find

$$g_{P,N_f=4}^N = 356^{(9)}_{(9)}, \qquad g_{P,N_f=4}^\Sigma = 308^{(11)}_{(14)}, \qquad g_{P,N_f=4}^\Xi = -104^{(5)}_{(5)}. \qquad (5.4)$$

Turning to the scalar charges, the final results in the three flavour $\overline{\text{MS}}$ scheme at $\mu = 2\,\text{GeV}$ read[2]

$$g_S^N = 1.11^{(14)}_{(16)}, \qquad g_S^\Sigma = 3.98^{(22)}_{(24)}, \qquad g_S^\Xi = 2.57^{(11)}_{(11)}. \qquad (5.5)$$

For the nucleon, our result for g_S^N agrees with the FLAG 21 value $g_S^N = 1.13(14)$ for $N_f = 2+1$ [14] (taken from Ref. [85]) and more recent lattice determinations, see Fig. 5.17. There is only one previous lattice determination of the hyperon scalar couplings by QCDSF-UKQCD-CSSM [19], who obtain $g_S^\Sigma = 2.80(24)_{\text{stat}}(05)_{\text{sys}}$ and $g_S^\Xi = 1.59(11)_{\text{stat}}(04)_{\text{sys}}$. These values are much smaller than ours.

One can also employ the CVC relation and estimates of the QCD contribution to the isospin mass splittings and the light quark mass difference to determine the scalar charges. For a detailed discussion see section 5.2.3 below. Reference [171] obtains $g_S^N = 1.02(11)$ assuming $\Delta m_N^{\text{QCD}} = m_p^{\text{QCD}} - m_n^{\text{QCD}} = -2.58(18)\,\text{MeV}$ and the quark mass difference $\delta_m = m_u - m_d = -2.52(19)\,\text{MeV}$. Similarly, using the results by BMWc on the light quark mass splitting [197] and their QCD contributions to the baryon mass splittings [53], we obtain

$$g_S^N = 1.05(13), \qquad g_S^\Sigma = 3.35(19), \qquad g_S^\Xi = 2.29(15), \qquad (5.6)$$

which agree with our results to within two standard deviations. Note that a smaller value for $|\delta_m|$ (see section 5.2.3) would uniformly increase these charges.

Regarding the tensor charges we find in the three flavour $\overline{\text{MS}}$ scheme at $\mu = 2\,\text{GeV}$

$$g_T^N = 0.984^{(19)}_{(29)}, \qquad g_T^\Sigma = 0.798^{(15)}_{(21)}, \qquad g_T^\Xi = -0.1872^{(59)}_{(41)}. \qquad (5.7)$$

Since the anomalous dimension of the tensor bilinear is smaller than for the scalar case, we would expect no statistically relevant difference between the $N_f = 3$ and $N_f = 4$

---

[2]Using Version 3 of RunDec [134], we compute the conversion factor from $N_f = 3$ to $N_f = 4$: $1.00082(2)_\Lambda(1)_{\text{pert}}(56)_{m_c} = 1.0008(6)$. The errors reflect the uncertainty of the Λ-parameter [113], the difference between 5-loop running [192, 193]/4-loop decoupling [194–196] and 4-loop running/3-loop decoupling and a 200 MeV uncertainty in the charm quark on-shell mass, respectively: at $\mu = 2\,\text{GeV}$ there is no noteworthy difference between $N_f = 3$ and $N_f = 4$ $\overline{\text{MS}}$ pseudo(scalar) charges.
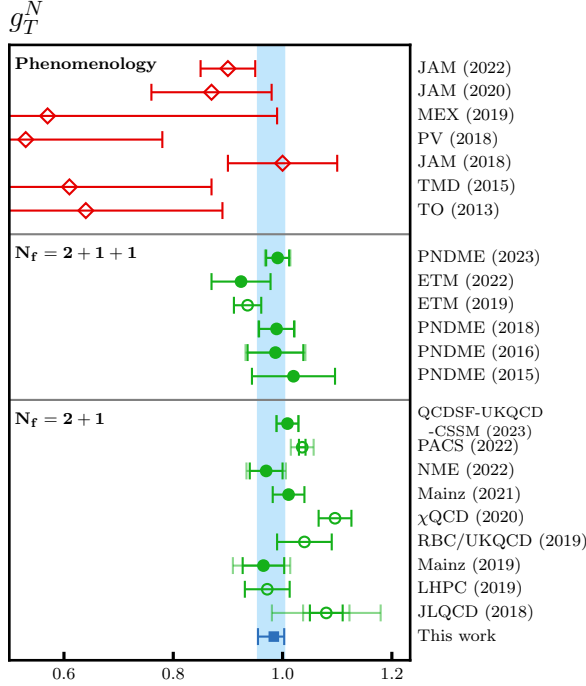
g_T^N

Phenomenology		JAM (2022)
		JAM (2020)
		MEX (2019)
		PV (2018)
		JAM (2018)
		TMD (2015)
		TO (2013)
$N_f = 2 + 1 + 1$		PNDME (2023)
		ETM (2022)
		ETM (2019)
		PNDME (2018)
		PNDME (2016)
		PNDME (2015)
$N_f = 2 + 1$		QCDSF-UKQCD -CSSM (2023)
		PACS (2022)
		NME (2022)
		Mainz (2021)
		χQCD (2020)
		RBC/UKQCD (2019)
		Mainz (2019)
		LHPC (2019)
		JLQCD (2018)
		This work

Figure 5.18: As in Fig. 5.14 for the nucleon tensor charge g_T^N with $N_f = 2 + 1$ [19, 85, 172, 174–177, 190, 198] and $N_f = 2 + 1 + 1$ [105, 178, 180, 182, 199, 200] dynamical fermions. Recent phenomenological estimates are also displayed for comparison [163, 164, 201–205]. Values with filled symbols were obtained via a quark mass, continuum and finite volume extrapolation. In addition, the filled ETM (2022) [200] point is obtained from a continuum limit extrapolation of results determined on three physical point ensembles with large spatial volumes.

schemes at $\mu = 2\,\text{GeV}$. The nucleon charge agrees with the FLAG 21 [14] value of $g_T^N = 0.965(61)$ [85] for $N_f = 2 + 1$ and other recent lattice studies. These are shown in Fig. 5.18 along with determinations from phenomenology. The large uncertainties of the latter reflect the lack of experimental data. In particular, in Refs. [163, 164] the JAM collaboration constrain the first Mellin moment of the isovector combination of the transverse parton distribution functions to reproduce a lattice result for g_T^N. QCDSF-UKQCD-CSSM also determined the hyperon tensor charges [19]. Their results $g_T^\Sigma = 0.805(15)_{\text{stat}}(02)_{\text{sys}}$ and $g_T^\Xi = -0.1952(74)_{\text{stat}}(10)_{\text{sys}}$ are in good agreement with ours.

5.2.2 SU(3) flavour symmetry breaking

In this work we determined the octet baryon isovector charges at many different positions in the quark mass plane. On the SU(3) flavour symmetric line, i.e., for $m = m_\ell = m_s$, the baryon charges $g_J^B(m)$ can be decomposed into two functions, $F_J(m)$ and $D_J(m)$, see section 3.1. In this section we investigate SU(3) flavour symmetry breaking, i.e., the extent of violation of Eqs. (3.8)–(3.10). The vector Ward identity (conserved vector current, CVC relation) implies that $g_V^N = g_V^\Xi = F_V = 1$ and $g_V^\Sigma = 2F_V$, i.e., in this case the above relations also hold for $m_s \neq m_\ell$, with $F_V(m) = 1$ and $D_V(m) = 0$. For the other channels $J \neq V$, the functions $D_J(m)$ and $F_J(m)$ are not uniquely determined at the physical point, where $m_s \gg m_\ell$. At this quark mass point we will find the approximate ratios $D_A/F_A \approx (1.6 - 1.95)$, $D_T/F_T \approx 1.5$ and $D_S/F_S \approx -0.5$. The first ratio can be compared to the SU(6) quark model expectation $D_A(m)/F_A(m) = 3/2$ (see, e.g., ref. [124]), which is consistent with the large-N_c limit [156]. For the axial charges g_A^B, the values of these functions in the SU(3) chiral limit correspond to the LECs $F = F_A(0)$ and $D = D_A(0)$, see chapter 4 for further details.

Estimates of baryon structure observables often rely on SU(3) flavour symmetry arguments, however, it is not known *a priori* to what extent this symmetry is broken for $m_s \neq m_\ell$ and, in particular, at the physical point. Since within this analysis, we only determined three isovector charges ($B \in \{N, \Sigma, \Xi\}$) for each channel ($J \in \{A, S, T\}$), we
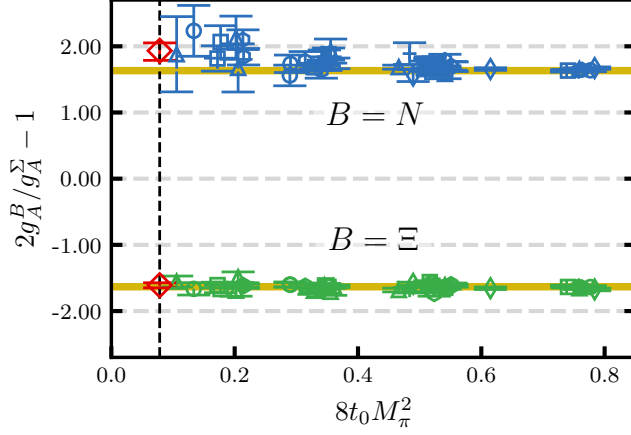
Figure 5.19: The ratios $2g_A^B/g_A^\Sigma - 1$ for $B \in \{N, \Xi\}$ as a function of the pion mass squared. The latter are rescaled with the Wilson flow scale t_0. The red diamonds are the continuum and infinite volume limit results at the physical point (indicated by the dashed line) obtained from our extrapolations of the individual charges. The yellow bands depict the $m_s = m_\ell = 0$ predictions obtained from the SU(3) LECs F and D determined in section 4.3.2.

cannot follow the systematic approach to investigate SU(3) flavour symmetry breaking of matrix elements proposed in Ref. [63]. Nevertheless, constructing appropriate ratios from the individual charges will provide us with estimates of the flavour symmetry breaking effects for each channel.

Using Eqs. (3.8)–(3.10), we obtain for $m = m_s = m_\ell$

$$\frac{2g_J^B(m)}{g_J^\Sigma(m)} - 1 = \pm\frac{D_J(m)}{F_J(m)}, \tag{5.8}$$

where '+' and '−' corresponds to $B = N$ and $B = \Xi$, respectively. Figure 5.19 shows these combinations for the axial charges, as functions of the squared pion mass, compared to the chiral, continuum limit expectations $\pm F/D$ (yellow bands) determined from the LECs F and D obtained in section 4.3.2. The chiral limit value of F/D obtained here from the extrapolation of the individual charges is in agreement within less then two σ with this previous study. The data shown in the figure are not corrected for volume or lattice spacing effects. Note that the renormalization factors and improvement coefficients and, possibly, other systematics cancel from Eq. (5.8). In the ratio including the Ξ over the Σ axial charge we see little difference from the chiral limit expectation, which is consistent
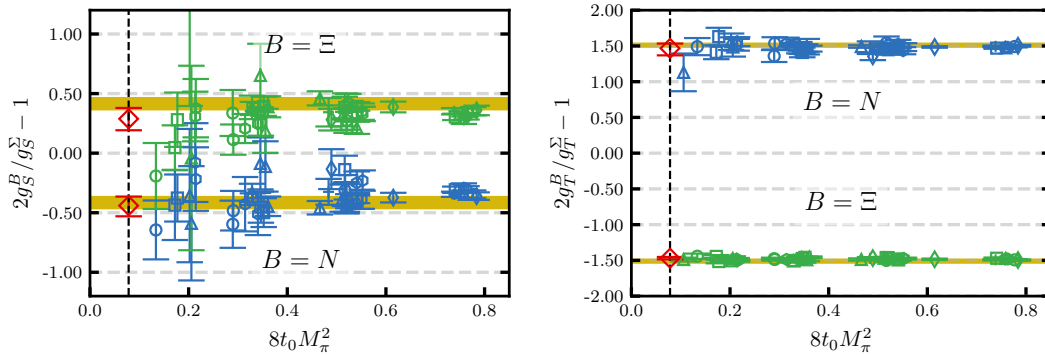

Figure 5.20: The same as Fig. 5.19 for the scalar (right) and tensor (left) channel. The yellow bands depict the $m_s = m_\ell = 0$ predictions $\pm F_J(0)/D_J(0)$ for $J \in \{S, T\}$ obtained from the extrapolations of the individual charges.

70

Table 5.5: The combinations $2g_J^B/g_J^\Sigma - 1$ of Eq. (5.8) with $B \in \{N, \Xi\}$ at the physical point, in the continuum and infinite volume limit. These are computed from the individual charges in Tables 5.2 (for Z_A^3), 5.3 and 5.4 (for Z_J^1). The last row gives the combination $D_J(0)/F_J(0)$ in the chiral, continuum and infinite volume limit (yellow bands in Figs. 5.19 and 5.20). The value for D/F is taken from section 4.3.2 (model averaging recomputed for D/F instead of F/D), while the other combinations are computed from the individual charges in the chiral, continuum and infinite volume limit as $D_J/F_J = (g_J^N - g_J^\Xi)/g_J^\Sigma$.

B	$2g_A^B/g_A^\Sigma - 1$	$2g_S^B/g_S^\Sigma - 1$	$2g_T^B/g_T^\Sigma - 1$
N	$1.93^{(12)}_{(15)}$	$-0.441^{(76)}_{(89)}$	$1.467^{(67)}_{(99)}$
Ξ	$-1.609^{(37)}_{(40)}$	$0.288^{(91)}_{(96)}$	$-1.469^{(17)}_{(16)}$
$D_J(0)/F_J(0)$	$1.641^{(27)}_{(44)}$	$-0.416^{(46)}_{(49)}$	$1.530^{(54)}_{(56)}$

with Fig. 5.7, whereas the symmetry breaking effect of the combination involving g_A^N/g_A^Σ can be attributed to the pion mass dependence of g_A^N, see Fig. 5.6. The red symbols at the physical point (dashed vertical line) correspond to the continuum, infinite volume limit extrapolated results, listed in Table 5.5 for the combinations Eq. (5.8).

In Fig. 5.20 the combinations Eq. (5.8) are shown for the isovector scalar charges. These are compared to our SU(3) chiral limit extrapolated results (yellow bands) and the continuum, infinite volume limit results at the physical point (red diamonds). We find no statistically significant symmetry breaking in this case. However, the statistical errors are larger than for the axial case and also $F_S > F_A$. Therefore, we cannot exclude symmetry breaking of a similar size as for the axial charges, in particular, in the ratio of the Ξ over the Σ baryon charge. Finally, we carry out the same comparison for the tensor charges (see again Fig. 5.20). In this case, within errors of a few per cent, no flavour symmetry violation is seen. Moreover, $D_T(m)/F_T(m) = D_T(0)/F_T(0)$ within errors.

In order to quantify the symmetry breaking effect between matrix elements involving the current J as a function of the quark mass splitting $m_s - m_\ell$, we define

$$\delta_{SU(3)}^J = \frac{g_J^\Xi + g_J^N - g_J^\Sigma}{g_J^\Xi + g_J^N + g_J^\Sigma}, \tag{5.9}$$

where for $m_s = m_\ell$, $\delta_{SU(3)}^J = (2F_J - 2F_J)/(2F_J + 2F_J) = 0$, see Eqs. (3.8)–(3.10). Also from these ratios some of the systematics as well as the renormalization factors and improvement terms will cancel. We define a dimensionless SU(3) breaking parameter $x = (M_K^2 - M_\pi^2)/(2M_K^2 + M_\pi^2) \sim m_s - m_\ell$ and assume a polynomial dependence

$$\delta_{SU(3)}^J(x) = \sum_{n>0} a_n^J x^n. \tag{5.10}$$

The data for $\delta_{SU(3)}^A(x)$ depicted in Fig. 5.21 become more and more positive as the physical point (vertical dashed line) is approached. This observation agrees with findings from earlier studies [15–19]. We fit to data for which the average quark mass is kept constant (blue circles). However, there is no significant difference between these and the $m_s \approx$ const. points (black squares). Both linear and quadratic fits in x ($a_n^A = 0$ for $n \neq 1$ and $a_n^A = 0$ for $n \neq 2$, respectively) give adequate descriptions of the data and agree with our continuum, infinite volume limit extrapolated physical point result (red diamond)

$$\delta_{SU(3)}^A = 0.075^{(23)}_{(27)}, \tag{5.11}$$

derived from the values for the individual charges. Effects of this sign and magnitude were also reported previously. ETMC [17] find $g_A^N + g_A^\Xi - g_A^\Sigma = 0.147(24)$, whereas Savanur and Lin [18] quote $(g_A^N + g_A^\Xi - g_A^\Sigma)/g_A^N = 0.087(15)$.
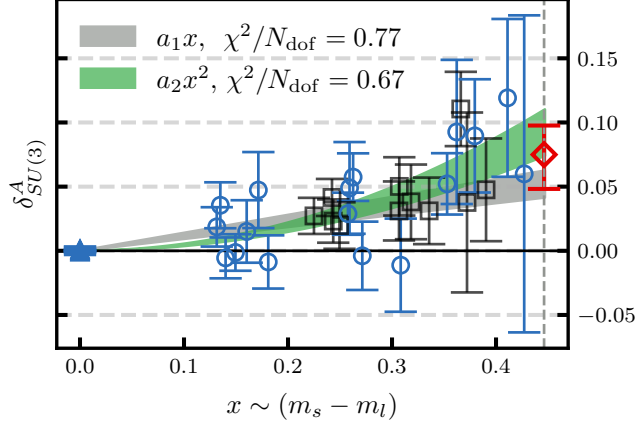
Figure 5.21: The SU(3) symmetry breaking ratio $\delta^A_{SU(3)}(x)$ (Eq. (5.10)) for the axial charges as a function of $x = (M_K^2 - M_\pi^2)/(2M_K^2 + M_\pi^2)$. The grey (green) band shows the result from a linear (quadratic) one parameter fit including only the blue data points that correspond to the ensembles on the Tr M = const. line. Black data points correspond to ensembles on the m_s = const. trajectory. The vertical grey dashed line indicates the physical point. The red diamond corresponds to the result derived from the values for the individual charges, see section 5.2.1.
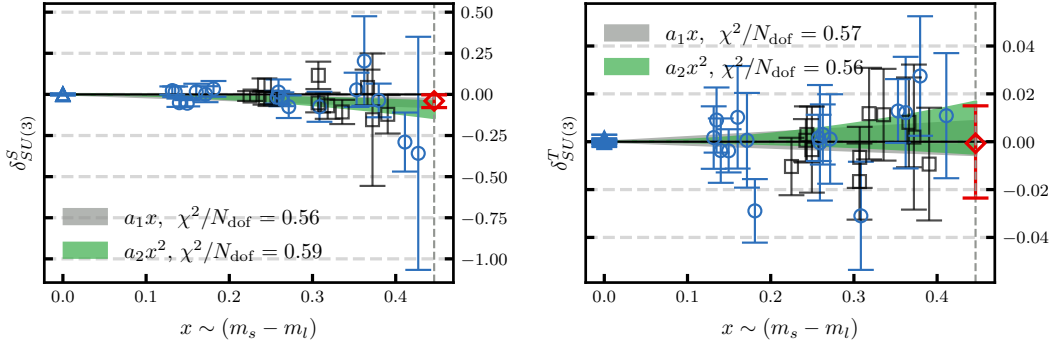
Figure 5.22: The same as Fig. 5.21 for the scalar (left) and tensor (right) charges.

For $J \neq A$ no statistically significant effects were observed. Nevertheless, for completeness we carry out the same analysis for $J \in \{S, T\}$, see Fig. 5.22. Our continuum, infinite volume limit extrapolated physical point results

$$\delta^S_{SU(3)} = -0.040^{(37)}_{(41)}, \qquad \delta^T_{SU(3)} = -0.001^{(16)}_{(23)} \tag{5.12}$$

provide upper limits on the relative size of SU(3) flavour violation at the physical point.

5.2.3 The up and down quark mass difference

The results on the scalar charges, in particular, g^Σ_S, enable us to determine the quark mass splitting $\delta_m = m_u - m_d$. While we simulate the isosymmetric theory, in Nature this symmetry is broken. The extent of isospin symmetry breaking is determined by two small parameters, δ_m/Λ_{QCD} and the fine structure constant α_{QED}, which are similar in size. The vector Ward identity relates δ_m to the QCD contributions to mass splittings within an isomultiplet. In particular, to leading order in δ_m/Λ_{QCD} and α_{QED}, the difference between the Σ^+ and Σ^- baryon masses is a pure QCD effect from which, with our knowledge of g^Σ_S, we can extract δ_m without additional assumptions.

We consider isospin multiplets of baryons $B^Q \in \{N^Q, \Sigma^Q, \Xi^Q\}$ with electric charges $Q = I_3 + \frac{1}{2}(1 + S) \in \{0, \pm 1\}$ ($N^+ = p$, $N^0 = n$) and define the mass differences

$\Delta m_{BQ+1} = m_{BQ+1} - m_{BQ}$. Note that for the Σ there are two differences [5],

$$\Delta m_{\Sigma+} = m_{\Sigma+} - m_{\Sigma^0} = -3.27(7)\,\text{MeV}, \tag{5.13}$$

$$\Delta m_{\Sigma^0} = m_{\Sigma^0} - m_{\Sigma-} = -4.81(4)\,\text{MeV}. \tag{5.14}$$

The other splittings read [5]

$$\Delta m_\Xi = -6.85(21)\,\text{MeV}, \quad \Delta m_N \approx -1.293\,\text{MeV}. \tag{5.15}$$

The mass differences can be split into QCD ($\sim \delta_m$) and QED ($\sim \alpha_{\text{QED}} \Lambda_{\text{QCD}}$) contributions:

$$\Delta m_B = \Delta m_B^{\text{QCD}} + \Delta m_B^{\text{QED}}. \tag{5.16}$$

The splitting depends on the scale, the renormalization scheme and the matching conventions between QCD and QCD+QED. The Cottingham formula [206] relates the leading QED contribution to hadron masses to the total electric charge squared times a function of the unpolarized Compton forward-amplitude, i.e., to leading order in α_{QED} the electric contribution to charge-neutral hadron masses should vanish (as was suggested in the massless limit by Dashen [207]). Moreover, for $\delta_m = 0$ this implies that the leading QED contributions to the masses of the Σ^+ and Σ^- baryons are the same. Therefore, up to $\mathcal{O}(\alpha_{\text{QED}}, \delta_m/\Lambda_{\text{QCD}}) \cdot \delta_m$ terms,

$$\Delta m_\Sigma^{\text{QCD}} = \frac{1}{2}(m_{\Sigma+} - m_{\Sigma-}) = -4.04(4)\,\text{MeV}, \tag{5.17}$$

$$\Delta m_{\Sigma+}^{\text{QED}} = \frac{1}{2}(m_{\Sigma+} + m_{\Sigma-}) - m_{\Sigma^0} = 0.77(5)\,\text{MeV} = -\Delta m_{\Sigma^0}^{\text{QED}}. \tag{5.18}$$

From the Ademollo-Gatto theorem [167] we know that the leading isospin breaking effects on the vector charges $g_V^N = g_V^\Xi = 1$ and $g_V^\Sigma = 2$ are quadratic functions of $\delta_m/\Lambda_{\text{QCD}}$ and α_{QED}, whereas the scalar charges g_S^B are subject to linear corrections in α_{QED} and $\delta_m/\Lambda_{\text{QCD}}$.

The Lorentz decomposition of the on-shell QCD matrix element for the isovector vector current between baryons $B' = B^{Q+1}$ and $B = B^Q$ (that differ by $\Delta I_3 = 1$ in their isospin) gives (see Eq. (3.1))

$$i\partial^\mu \langle B'(p')|\bar{d}\gamma_\mu u|B(p)\rangle = g_V^{B'B} i\partial^\mu \bar{u}_{B'}(p')\gamma_\mu u_B(p)$$
$$= g_V^{B'B} \Delta m_B^{\text{QCD}}[1 + \mathcal{O}(\delta_m/\Lambda_{\text{QCD}})], \tag{5.19}$$

where the leading correction is due to $q_0 = p_0' - p_0 = \Delta m_B^{\text{QCD}} = |\mathbf{q}|$. In the last step we used the equations of motion. Combining this with the vector Ward identity $i\partial^\mu \bar{d}\gamma_\mu u = (m_u - m_d)\bar{d}u$ gives

$$g_V^{B'B} \Delta m_B^{\text{QCD}} = g_S^{B'B}(m_u - m_d) \tag{5.20}$$

as the QCD contribution to the mass difference, with corrections that are suppressed by powers of the symmetry breaking parameters. Note that the normalization convention of the charges g_J^B defined in Eq. (3.3),

$$g_J^{pn} = g_J^N, \quad g_J^{\Sigma^+\Sigma^0} = -g_J^\Sigma/\sqrt{2}, \quad g_J^{\Xi^0\Xi^-} = -g_J^\Xi,$$

cancels in the above equation so that we can replace $g_J^{B'B} \mapsto g_J^B$ to obtain

$$\delta_m = m_u - m_d = \frac{g_V^B}{g_S^B} \Delta m_B^{\text{QCD}}, \tag{5.21}$$

Table 5.6: Comparison of the light quark mass difference. FNAL-MILC [209] and MILC [210] only quote the ratios $m_u/m_d = 0.4556^{(131)}_{(93)}$ and $m_u/m_d = 0.4529^{(157)}_{(82)}$, respectively (all errors added in quadrature). Using the FLAG 21 [14] average $m_\ell = 3.410(43)$, we combine these results to form $\delta_m = 2m_\ell(m_u/m_d - 1)/(m_u/m_d + 1)$ and compute the error by error propagation. The values listed under CVC are obtained applying Eq. (5.21) for the nucleon using the $N_f = 2+1+1$ and $N_f = 2+1$ value for g_S^N (in the $\overline{\text{MS}}$ scheme at $\mu = 2\,\text{GeV}$) from FLAG 21 [14] and $\Delta m_N^{\text{QCD}} = -1.87(16)\,\text{MeV}$ from [211].

	N_f	δ_m/MeV
RM123 [212]	$2+1+1$	$-2.38(18)$
FNAL-MILC [209]	$2+1+1$	$-2.55^{(9)}_{(7)}$
MILC [210]	$2+1+1$	$-2.57^{(11)}_{(6)}$
CVC [14, 211]	$2+1+1$	$-1.83(24)$
BMWc [197]	$2+1$	$-2.41(12)$
CVC [14, 211]	$2+1$	$-1.65(25)$
This work	$2+1$	$-2.03(12)$

which we refer to as the CVC relation.[3]

Applying Eq. (5.21) for the Σ baryon and using our physical point, continuum and infinite volume limit result $g_S^\Sigma = 3.98^{(22)}_{(24)}$, as well as assuming $g_V^\Sigma = 2$, we obtain in the $N_f = 3$ $\overline{\text{MS}}$ scheme at $\mu = 2\,\text{GeV}$

$$m_u - m_d = -2.03^{(12)}_{(12)}\,\text{MeV}. \tag{5.22}$$

We expect $|\mathcal{O}(\delta_m/\Lambda_{\text{QCD}}, \alpha_{\text{QED}})| \lesssim 1\%$ corrections from higher order effects to this result, which we can neglect at the present level of accuracy.

We compare our value of δ_m with results from the literature in Table 5.6. This includes the $N_f = 2+1$ result of BMWc [197] and the $N_f = 2+1+1$ continuum limit results of RM123 [212], FNAL-MILC [209] and MILC [210]. In the latter two cases we convert results for m_u/m_d into δ_m as described in the table caption. We see a tension between the previous determinations and our result on the two to three σ level.

We remark that all the previous results utilize the dependence of the pion and kaon masses on the quark masses and the electromagnetic coupling. We consider our method of determining the quark mass splitting from the scalar coupling g_S^Σ and the mass difference between the Σ^+ and the Σ^- baryons as more direct. In Ref. [211] $\Delta m_N^{\text{QCD}} = -1.87(16)\,\text{MeV}$ (which agrees within errors with lattice determinations, including ours, see below) is determined from experimental input. A larger (negative) QCD difference would require a larger QED contribution to the proton mass. As discussed above, the QED contribution to the mass of the Σ^+ baryon is $0.77(5)\,\text{MeV}$ (similar in size to $\Delta m_N^{\text{QED}} = 0.58(16)\,\text{MeV}$ [211]) and it would be surprising if this increased when replacing a strange quark by a down quark. Assuming $\Delta m_N^{\text{QCD}} = -1.87(16)\,\text{MeV}$ and a value $\delta_m \approx -2.50(10)\,\text{MeV}$ as suggested by Refs. [197, 209, 210, 212] would require a coupling $g_S^N = 0.75(7)$ to satisfy the CVC relation Eq. (5.21). This in turn is hard to reconcile with the majority of lattice results compiled in Fig. 5.17. With a lower value for $|\delta_m|$ (and/or a larger $|\Delta m_N^{\text{QCD}}|$) this inconsistency disappears.

---

[3]Note that also the relations between $g_S^{B'B}$ and g_S^B receive $\mathcal{O}(\alpha_{\text{QED}})$ corrections. Therefore terms $\propto m_\ell \alpha_{\text{QED}}$, $\propto \delta_m \alpha_{\text{QED}}$ and $\propto \delta_m^2/\Lambda_{\text{QCD}}$ can be added to Eq. (5.21). Since m_ℓ is similar in size to δ_m, we can neglect the first of these terms too, whose appearance is related to the mixing in QCD+QED of m_ℓ and δ_m under renormalization. Using the $\overline{\text{MS}}$ scheme at $\mu = 2\,\text{GeV}$ corresponds to the suggestion of Ref. [208], however, for quark masses $m_\ell \sim \delta_m$ this additional scale-dependence can be neglected with good accuracy, as pointed out above. In addition, there are small $\mathcal{O}(\alpha_{\text{QED}}^2 \Lambda_{\text{QCD}})$ terms due to the QED contributions to the β- and γ-functions, which are also of higher order.

5.2.4 QCD and QED isospin breaking effects on the baryon masses

We proceed to compute the QED contributions to the proton and Ξ^- masses, $\Delta m_N^{\mathrm{QED}}$ and $-\Delta m_\Xi^{\mathrm{QED}}$:

$$\Delta m_N^{\mathrm{QED}} = \Delta m_N - g_S^N (m_u - m_d)$$
$$= \Delta m_N - \frac{2g_S^N}{g_S^\Sigma} \Delta m_\Sigma^{\mathrm{QCD}}, \tag{5.23}$$

$$\Delta m_\Xi^{\mathrm{QED}} = \Delta m_\Xi - \frac{2g_S^\Xi}{g_S^\Sigma} \Delta m_\Sigma^{\mathrm{QCD}}. \tag{5.24}$$

This gives

$$\Delta m_N^{\mathrm{QED}} = 0.97_{(36)}^{(31)} \, \mathrm{MeV}, \qquad \Delta m_N^{\mathrm{QCD}} = -2.26_{(36)}^{(31)} \, \mathrm{MeV}, \tag{5.25}$$

$$\Delta m_\Sigma^{\mathrm{QED}} = 0.77(05) \, \mathrm{MeV}, \qquad \Delta m_\Sigma^{\mathrm{QCD}} = -4.04(04) \, \mathrm{MeV}, \tag{5.26}$$

$$\Delta m_\Xi^{\mathrm{QED}} = -1.65_{(39)}^{(37)} \, \mathrm{MeV}, \qquad \Delta m_\Xi^{\mathrm{QCD}} = -5.20_{(44)}^{(42)} \, \mathrm{MeV}. \tag{5.27}$$

For completeness we included the values for the Σ baryons that we determined from the experimental masses alone, without lattice input. The above mass splittings agree with the BMWc [53] continuum limit results from simulations of QCD plus QED, see Fig. 5.23 (errors added in quadrature). Nevertheless, as mentioned above, the value of δ_m, reported by BMWc [197] from simulations of QCD with quenched QED, differs by 2.2 standard deviations from our result in Eq. (5.22). Also other lattice results on the QCD contribution to the mass-splittings (summarized in Fig. 5.23), obtained at a single lattice spacing from Endres *et al.* [213] using $\mathrm{QED}_{\mathrm{TL}}$ and $\mathrm{QED}_{\mathrm{M}}$, Brantley *et al.* [214] and CSSM-QCDSF-UKQCD [215] agree within errors.

We mention the possibility of an enhancement of the (higher order) $\delta_m^2/\Lambda_{\mathrm{QCD}}$ correction to the Σ^0 mass due to the possibility of mixing with the Λ^0, which, however, appears
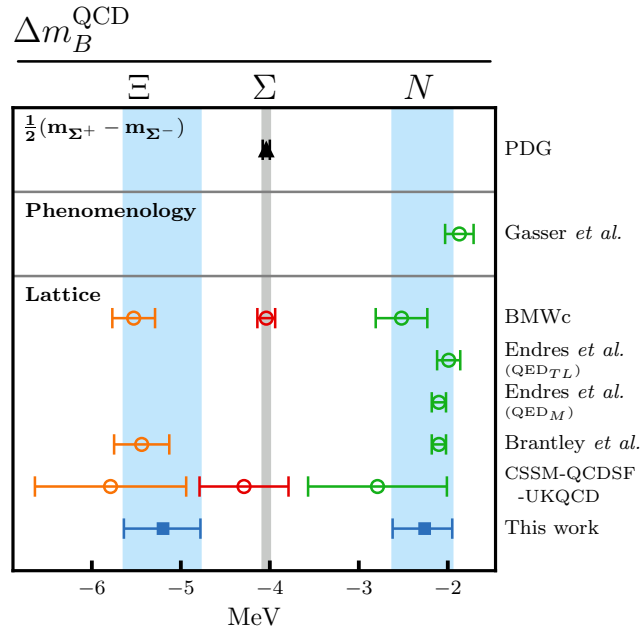

Figure 5.23: Comparison of the QCD contributions to isospin mass splittings [5, 53, 211, 213–215]. Note that in our normalization $m_{\Sigma^+} - m_{\Sigma^-} \approx 2\Delta m_\Sigma^{\mathrm{QCD}}$. Endres *et al.* [213] only quote values for $\Delta m_N^{\mathrm{QED}}$ from which we compute $\Delta m_N^{\mathrm{QCD}}$ employing the experimental proton-neutron mass splitting.

to be a very small effect [216]. A positive contribution to the Σ^0 mass would increase $\Delta m_\Sigma^{\text{QED}}$ but leave $\Delta m_\Sigma^{\text{QCD}}$ (and therefore the quark mass difference Eq. (5.22)) invariant.

The electromagnetic contributions to the p, $\Sigma^\pm$ and Ξ^- masses are all similar to 1 MeV, with an enhancement for the heavier, more compact cascade baryon. Recently, combining the Cottingham formula [206] with experimental input from elastic scattering and parton distribution functions, the value $\Delta m_N^{\text{QED}} = 0.58(16)$ MeV was determined in Ref. [211]. While within errors our result Eq. (5.25) agrees with this value, the number obtained in Ref. [211] is more inline with the suggested ordering $\Delta m_N^{\text{QED}} < \Delta m_\Sigma^{\text{QED}} < -\Delta m_\Xi^{\text{QED}}$. Combining their value with our determination of g_S^N gives $\delta_m = -1.69^{(28)}_{(26)}$ MeV, somewhat smaller in modulus than our result Eq. (5.22) and certainly in tension with, e.g., $\delta_m = -2.41(12)$ MeV [197].

We find that the effect of $m_d > m_u$ on the Ξ and Σ mass splittings is much bigger than for the nucleon since this is proportional to g_S^B/g_V^B and $g_S^N < g_S^\Sigma/2 < g_S^\Xi$. This hierarchy is due to $g_S^N \approx F_S + D_S$, $g_S^\Sigma/2 \approx F_S$ and $g_S^\Xi \approx F_S - D_S$ with $F_S > 0$ and $D_S < 0$. Interestingly, the pion baryon σ terms $\sigma_{\pi B} = \sigma_{uB} + \sigma_{dB}$ that encode the up plus down quark mass contribution to the baryon masses exhibit the opposite ordering [52], $\sigma_{\pi N} > \sigma_{\pi \Sigma} > \sigma_{\pi \Xi}$.

5.2.5 Isospin breaking effects on the pion baryon σ terms

Having determined the quark mass differences, we can also compute the leading isospin violating corrections to the pion baryon σ terms $\sigma_{\pi B} = \sigma_{uB} + \sigma_{dB}$. One can either work with matrix elements [217], using the identity

$$m_u \bar{u}u + m_d \bar{d}d = m_\ell \left(\bar{u}u + \bar{d}d \right) + \frac{\delta_m}{2} \left(\bar{u}u - \bar{d}d \right), \tag{5.28}$$

or one can start from the Feynman-Hellmann theorem

$$\sigma_{qB} = m_q \frac{\langle B|\bar{q}q|B\rangle}{\langle B|B\rangle} = m_q \frac{\partial m_B}{\partial m_q}. \tag{5.29}$$

Writing $m_p = m_N + \Delta m_N^{\text{QCD}}/2 + \Delta m_N^{\text{QED}}$ and $m_n = m_N - \Delta m_N^{\text{QCD}}/2$, where $\Delta m_N^{\text{QCD}} = \delta_m g_S^N/g_V^N$, and realizing that the dependence of the QED contributions on the quark masses is of higher order in the isospin breaking, we obtain at linear order

$$\sigma_{\pi p} = m_u \frac{\partial m_p}{\partial m_u} + m_d \frac{\partial m_p}{\partial m_d} = \sigma_{\pi N} + \frac{1}{2}\Delta m_N^{\text{QCD}}, \tag{5.30}$$

$$\sigma_{\pi n} = m_u \frac{\partial m_n}{\partial m_u} + m_d \frac{\partial m_n}{\partial m_d} = \sigma_{\pi N} - \frac{1}{2}\Delta m_N^{\text{QCD}}. \tag{5.31}$$

The same can be carried out for the $\Sigma^\pm$, Ξ^0 and Ξ^- baryons. Using the results for the σ terms of the isosymmetric theory of Ref. [52], we obtain

$$\sigma_{\pi p} = 42.8^{(4.7)}_{(4.7)} \text{ MeV}, \qquad \sigma_{\pi n} = 45.0^{(4.7)}_{(4.7)} \text{ MeV}, \tag{5.32}$$

$$\sigma_{\pi \Sigma^+} = 21.9^{(3.8)}_{(6.1)} \text{ MeV}, \qquad \sigma_{\pi \Sigma^-} = 29.9^{(3.8)}_{(6.1)} \text{ MeV}, \tag{5.33}$$

$$\sigma_{\pi \Xi^0} = 8.6^{(4.5)}_{(6.4)} \text{ MeV}, \qquad \sigma_{\pi \Xi^-} = 13.8^{(4.5)}_{(6.4)} \text{ MeV}, \tag{5.34}$$

whereas the pion σ term for the Σ^0 is not affected at linear order: $\sigma_{\pi \Sigma^0} \approx \sigma_{\pi \Sigma} = 25.9^{(3.8)}_{(6.1)}$ MeV. We refrain from further decomposing the pion baryon σ terms into the individual up and down quark contributions. However, this can easily be accomplished [217]. It is worth noting that $(\sigma_{\pi \Xi^-} - \sigma_{\pi \Xi^0})/\sigma_{\pi \Xi} \gg (\sigma_{\pi n} - \sigma_{\pi p})/\sigma_{\pi N}$, in spite of the same isospin difference.

5.3 Summary

We determined the axial, scalar and tensor isovector charges of the nucleon, sigma and cascade baryons using $N_f = 2+1$ lattice QCD simulations. The analysis is based on 47 gauge ensembles, spanning a range of pion masses from $430\,\text{MeV}$ down to a near physical value of $130\,\text{MeV}$ across six different lattice spacings between $a \approx 0.039\,\text{fm}$ and $a \approx 0.098\,\text{fm}$ and linear spatial lattice extents $3.0\,M_\pi^{-1} \le L \le 6.5\,M_\pi^{-1}$. The availability of ensembles lying on three trajectories in the quark mass plane enables SU(3) flavour symmetry breaking to be explored systematically and the quark mass dependence of the charges to be tightly constrained. Simultaneous extrapolations to the physical point in the continuum and infinite volume limit are performed. Systematic errors are assessed by imposing cuts on the pion mass, the lattice spacing and the volume as well as using different sets of renormalization factors. The results (in the $\overline{\text{MS}}$ scheme at $\mu = 2\,\text{GeV}$) for the nucleon charges are

$$g_A^N = 1.284_{(27)}^{(28)}, \qquad g_S^N = 1.11_{(16)}^{(14)}, \qquad g_T^N = 0.984_{(29)}^{(19)}.$$

For the hyperon charges we find

$$g_A^\Sigma = 0.875_{(39)}^{(30)}, \qquad g_S^\Sigma = 3.98_{(24)}^{(22)}, \qquad g_T^\Sigma = 0.798_{(21)}^{(15)},$$
$$g_A^\Xi = -0.267_{(12)}^{(13)}, \qquad g_S^\Xi = 2.57_{(11)}^{(11)}, \qquad g_T^\Xi = -0.1872_{(41)}^{(59)}.$$

A comparison with previous works is presented in section 5.2.1. We quantify SU(3) symmetry breaking effects for the axial charge at the physical point in terms of the combination

$$\delta_{\text{SU}(3)}^A = \frac{g_A^\Xi + g_A^N - g_A^\Sigma}{g_A^\Xi + g_A^N + g_A^\Sigma} = 0.075_{(27)}^{(23)},$$

see Fig. 5.21. In particular the axial charge of the nucleon deviates from its value in the SU(3) chiral limit, as can be seen in Fig. 5.19. No significant symmetry breaking is observed for the other charges within current precision, see Figs. 5.20 and 5.22.

To cross-check the analysis methods, the vector charges are determined and the expected values, $g_V^N = g_V^\Xi = 1$ and $g_V^\Sigma = 2$, are reproduced reasonably well:

$$g_V^N = 1.0012_{(11)}^{(12)}, \qquad g_V^\Sigma = 2.021_{(27)}^{(21)}, \qquad g_V^\Xi = 1.015_{(11)}^{(10)}.$$

Furthermore, we exploit the conserved vector current relation to predict the quark mass difference

$$\delta_m = m_u - m_d = -2.03(12)\,\text{MeV}$$

from the scalar charge of the Σ baryon. We utilize this to decompose isospin mass splittings between the baryons into QCD and QED contributions (see Eqs. (5.25)–(5.27)) and to predict the leading isospin corrections to the pion baryon σ terms (see Eqs. (5.32)–(5.34)).

6 | CONCLUSION

In this thesis the non-perturbative method of lattice QCD was used to investigate octet baryon structure observables from first principles. In particular, the goal of this work was to gain further insights into the structure of hyperons, study SU(3) flavour symmetry breaking effects and to determine leading order SU(3) ChPT LECs such as F and D which enter the expansion of every baryonic quantity.

In the first part of the thesis a consistent and simultaneous analysis of several observables within the framework of SU(3) ChPT was carried out and we determined the leading order mesonic (B_0 and F_0) and baryonic (m_0, F and D) SU(3) ChPT LECs. See section 4.4 for a summary of the results. To this end we employed only the subset of the gauge ensembles lying on the quark mass trajectory where exact SU(3) flavour symmetry, i.e., $m_u = m_d = m_s$, holds. We found that a consistent description of the pion mass and volume dependence of the axial charges and the octet baryon mass was possible with the same set of LECs.

In the second part, a computationally efficient stochastic approach was employed, which allows for the simultaneous evaluation of the three-point correlation functions of all octet (and decuplet) baryons with a variety of current insertions and momentum combinations. Here we determined the axial, scalar and tensor isovector charges of the nucleon, sigma and cascade baryons employing a large set of $N_f = 2 + 1$ gauge ensembles lying on three different trajectories in the quark mass plane. The available set of ensembles allows us to take all systematic effects associated with unphysical quark masses, finite lattice spacing and finite volumes in the extrapolations to the physical point in the continuum and infinite volume limits into account. Further, this set-up allows us to test the validity of SU(3) flavour symmetry assumptions, where we find moderate symmetry breaking effects for the axial charges at the physical quark mass point, while no significant effects are found for the other charges within current uncertainties. For a summary of the results see section 5.3. Notably, this direct determination of the charges enables us to determine the up and down quark mass difference, to compute the QCD contributions to baryon isospin mass splittings and to evaluate the isospin breaking effects on the pion baryon σ terms.

As demonstrated here, in the cases of the vector and the nucleon axial charges, once all systematic effects are sufficiently under control, lattice QCD calculations are able to reproduce physical results and hence are able to make predictions with high precision. This work is a first step towards determining hyperon decay form factors which are relevant for the study of CP violation [218] and which can be directly compared to experimental results obtained from, e.g., the future PANDA experiment. The next steps are to perform a similar analysis, as presented here (c.f. Ref. [SW2]), of the (generalized) isovector charges of the unpolarized, polarized and transversity parton distribution function momentum fractions $\langle x \rangle_{u^+ - d^+}$, $\langle x \rangle_{\Delta u^- - \Delta d^-}$ and $\langle x \rangle_{\delta u^+ - \delta d^+}$. First results were already presented in Ref. [SW6], while a complementary study of the baryon octet σ terms on the same data set is already ongoing [SW7, SW8]. At the same time we are also in the process of increasing the available statistics in terms of three-point function measurements, in particular at ensembles with pion masses below 200 MeV. This will help us to improve our

determinations of the ground state matrix elements and reduce the overall uncertainties in the results for the charges. Regarding the determinations of the LECs, future plans are to extend the $N_f = 3$ study presented in this work (c.f. Ref. [SW1]) to the $N_f = 2 + 1$ case in order to further improve the accuracy, to test the applicability range of SU(3) ChPT and also to determine higher order LECs.

A │ DEFINITIONS AND CONVENTIONS

Throughout this thesis the definitions and conventions outlined in the following are used.

A.1 General conventions

Unless stated otherwise bracketed Latin letters (e.g., $(x) = (\mathbf{x}, t), (x, y), \dots$) denote four dimensional spacetime positions, where bold letters indicate the three dimensional spatial components. Lowercase Greek letters ($\alpha, \beta, \gamma, \dots$) denote the Dirac spin indices and lowercase Latin letters ($a, b, c, \dots$) the (fundamental) colour indices. For the latter two sets of indices we employ the Einstein convention summing over repeated indices.

As is common in the field of particle physics we make use of natural units where the speed of light c and the reduced Planck constant $\hbar$ are set to one, i.e.,

$$c \equiv \hbar \equiv 1, \tag{A.1}$$

which allows one to convert between energy/momentum and distance scales using

$$197.3269804 \, \text{MeV} = 1 \, \text{fm}^{-1}. \tag{A.2}$$

A.2 Dirac matrices

The defining property of the Dirac γ-matrices ($\gamma_\mu^M, \mu = 0, 1, 2, 3$) to satisfy the Clifford algebra in the Minkowski metric is the anti-commutation relation

$$\left\{ \gamma_\mu^M, \gamma_\nu^M \right\} = 2 g_{\mu\nu} \mathbb{1}, \tag{A.3}$$

with $g_{\mu\nu} = \text{diag}(+1, -1, -1, -1)$, while in the Euclidean space the γ-matrices ($\gamma_\mu, \mu = 1, 2, 3, 4$) are defined through

$$\{ \gamma_\mu, \gamma_\nu \} = 2 \delta_{\mu\nu} \mathbb{1}. \tag{A.4}$$

Further the "fifth" γ-matrix γ_5 is defined as the product

$$\gamma_5 \equiv \gamma_1 \gamma_2 \gamma_3 \gamma_4, \tag{A.5}$$

where $\gamma_5^2 = \mathbb{1}$. The charge conjugation matrix C, defined by the relation $C \gamma_\mu C^{-1} = -\gamma_\mu^T$, is given by

$$C = i \gamma_2 \gamma_4 \tag{A.6}$$

and in addition we define (the commutator)

$$\sigma_{\mu\nu} = \frac{1}{2} \left[\gamma_\mu, \gamma_\nu \right]. \tag{A.7}$$

In the following the explicit representation of the γ-matrices in the chiral representation in the Euclidean space as used in the CHROMA [219] software package is given. This representation is employed to construct the interpolators and currents, as discussed in section 3.2 and the matrices are given by

$$
\gamma_1 \equiv \gamma_x = \begin{pmatrix} 0 & 0 & 0 & i \\ 0 & 0 & i & 0 \\ 0 & -i & 0 & 0 \\ -i & 0 & 0 & 0 \end{pmatrix}, \quad \gamma_2 \equiv \gamma_y = \begin{pmatrix} 0 & 0 & 0 & -1 \\ 0 & 0 & 1 & 0 \\ 0 & 1 & 0 & 0 \\ -1 & 0 & 0 & 0 \end{pmatrix},
$$

$$
\gamma_3 \equiv \gamma_z = \begin{pmatrix} 0 & 0 & i & 0 \\ 0 & 0 & 0 & -i \\ -i & 0 & 0 & 0 \\ 0 & i & 0 & 0 \end{pmatrix}, \quad \gamma_4 \equiv \gamma_t = \begin{pmatrix} 0 & 0 & 1 & 0 \\ 0 & 0 & 0 & 1 \\ 1 & 0 & 0 & 0 \\ 0 & 1 & 0 & 0 \end{pmatrix},
$$

(A.8)

$$
\gamma_5 \equiv \gamma_1 \gamma_2 \gamma_3 \gamma_4 = \mathrm{diag}(+1, +1, -1, -1). \tag{A.9}
$$

Note that $\gamma_\mu^\dagger = \gamma_\mu$ (for $\mu = 1, 2, 3, 4, 5$).

B | STATISTICAL ANALYSIS

Applying first principle lattice QCD calculations enables us to compute, e.g., baryon structure observables which can be compared to experimental measurements or to phenomenological obtained results. In order to perform a throughout reliable comparison between experimental or lattice QCD predictions a careful analysis including statistical and systematic uncertainties is essential. In the following we will outline some of the basic concepts and methods applied within the data analysis part of this thesis.

A typical gauge ensemble consists of a number of N consecutive gauge field configurations i separated by Monte Carlo time. On each configuration one can perform measurements of an observable y_i as, e.g., the measurements of two- and three-point correlation functions discussed in section 3.2. Taking into account reweighting factors w_i associated with each configuration, see Refs. [50–52] for details, an estimate for the expectation value $\langle y \rangle$ of the observable y can be obtained by the weighted ensemble mean

$$\overline{y} = \frac{\sum_{i=1}^{N} w_i y_i}{\sum_{i=1}^{N} w_i}. \tag{B.1}$$

While there are different methods to estimate the statistical error of the ensemble mean $\overline{y}$ in this work we rely on the binned bootstrap resampling method as described below. Other widely used methods are jackknife resampling as well as the so-called Γ-method [220]. The latter is based on the estimation of autocorrelation functions and was applied in the analysis of Refs. [221, 222] which was carried out on some of the data sets created and analysed within this work. Consistency was found between the errors of the ratios of three- over two-point functions as well as the errors of fit parameters from fits to these ratios estimated via the bootstrap method and the Γ-method.

In this Appendix, first the binned bootstrap resampling method, used to estimate statistical errors, is described in section B.1 and details about the construction of covariance matrices used within the extrapolations are given in section B.2. The fitting method is then described in section B.3. Further, the model averaging procedure used to obtain final results that incorporate both the statistical and systematic uncertainties is detailed in section B.4.

B.1 Binned bootstrap resampling

The bootstrap [223] resampling technique allows one to estimate the statistical error of, e.g., the ensemble mean as defined in Eq. (B.1), but also of any arbitrary secondary quantity in a straightforward way. Further, bootstrap resampling can be combined with binning of measurements on consecutive configurations which reduces the correlations between measurements and leads to a more reliable error estimate.

Since in a Monte Carlo simulation configurations are not independent from prior ones, the naive computed error might be underestimated if autocorrelations are not taken into account. We therefore create binned data sets of $N' = \lfloor N/N_{\text{bin}} \rfloor$ configurations (i.e.,

dropping potential residual configurations at the end of a stream) by computing averages
as

$$[w_i y_i]^{\text{bin}} = \frac{1}{N_{\text{bin}}} \sum_{j \in \mathcal{N}^i_{\text{bin}}} w_j y_j, \qquad\qquad [w_i]^{\text{bin}} = \frac{1}{N_{\text{bin}}} \sum_{j \in \mathcal{N}^i_{\text{bin}}} w_j, \qquad\text{(B.2)}$$

where now $i \in \{1, \ldots, N'\}$ and $\mathcal{N}^i_{\text{bin}} = \{(i-1) \cdot N_{\text{bin}} + 1, \ldots, i \cdot N_{\text{bin}}\}$. Note that if
$N \bmod N_{\text{bin}} = 0$ the mean as defined in Eq. (B.1) is invariant under binning. For
increasing bin-size N_{bin} one finds an increasing error reaching an asymptotic value when
the binned configurations can be considered uncorrelated. Within the analysis in this work
we chose $N_{\text{bin}} = \min[8, \lfloor N/160 \rfloor]$ to still have a sufficiently large number of configurations
on ensembles with smaller statistics. In the following we assume all data to be binned
and drop the superscripts ($'$, $^{\text{bin}}$) again.

To estimate the statistical error of an arbitrary (derived) observable O we create
N_B bootstrap samples $\mathcal{B}_k$ by uniformly drawing N (out of N) configurations allowing
for repetitions. We then compute the observable $O(\mathcal{B}_k)$ on each bootstrap sample and
estimate the error σ_O by

$$\sigma_O^2 = \frac{1}{N_B - 1} \sum_{k=1}^{N_B} \left(O(\mathcal{B}_k) - \bar{O}^B\right)^2, \qquad \bar{O}^B = \frac{1}{N_B} \sum_{k=1}^{N_B} O(\mathcal{B}_k). \qquad\text{(B.3)}$$

Throughout the analysis we use a fixed bootstrap sample size of $N_B = 500$ on all ensembles
which allows to easily combine different results within an ensemble (e.g., constructing
ratios of three- over two-point correlation functions) as well as between ensembles (e.g.,
estimating parameters from a joint extrapolation to the physical point). Further, we take
the observable O computed on the original data set as our central value and quote results
as

$$O \pm \sigma_O, \qquad\text{(B.4)}$$

where the error is computed solely from the bootstrap samples. The distribution of the
samples $O(\mathcal{B}_k)$ imitates independent measurements and allows one to extract for example
the 68% confidence interval spanned by O_{low} and O_{up}. From this another possible and
more robust estimate for the central value and the error can be obtained as

$$\widehat{O} \pm \Delta O, \qquad\text{(B.5)}$$

where

$$\widehat{O} = \frac{O_{\text{up}} + O_{\text{low}}}{2}, \qquad \Delta O = \frac{O_{\text{up}} - O_{\text{low}}}{2}. \qquad\text{(B.6)}$$

In principle one is also able to give asymmetric errors which we will not consider here but
implement in the estimation of the final results employing the model averaging approach
described in section B.4 below.

For some quantities like, e.g., renormalization and improvement factors, where only
central values (y) and errors (Δy) but no bootstrap samples are available we incorporate
the uncertainties by means of pseudo-bootstrap distributions in the statistical analysis.
To this end we draw $N_B = 500$ random samples $\tilde{\mathcal{B}}_k$ from a Gaussian distribution with
mean $\mu = y$ and standard deviation $\sigma = \Delta y$. Due to the finite number of samples the
mean $\tilde{\mu}$ and standard error $\tilde{\sigma}$ computed from the set of pseudo-bootstrap samples $\{\tilde{\mathcal{B}}\}$
do not exactly match the ones from the original distribution. In order to correct for this
small effect we rescale and shift the pseudo-bootstrap samples as

$$\tilde{\mathcal{B}}_k \to \left(\tilde{\mathcal{B}}_k - \tilde{\mu}\right) \frac{\Delta y}{\tilde{\sigma}} + y. \qquad\text{(B.7)}$$

B.2 Covariance matrix

Applying the bootstrap method described in the previous section one also is able to estimate the covariance between different observables y_i and y_j as

$$\text{Cov}_{y_i,y_j} = \frac{1}{N_B - 1} \sum_{k=1}^{N_B} \left(y_i(\mathcal{B}_k) - \bar{y}_i^B\right) \left(y_j(\mathcal{B}_k) - \bar{y}_j^B\right), \tag{B.8}$$

where for $i = j$ one obtains the variance $\sigma_{y_i}^2$. For n observables this allows one to construct the $n \times n$ covariance matrix

$$C = \begin{pmatrix} \sigma_{y_1}^2 & \text{Cov}_{y_1,y_2} & \cdots & \text{Cov}_{y_1,y_n} \\ \text{Cov}_{y_2,y_1} & \sigma_{y_2}^2 & \cdots & \text{Cov}_{y_2,y_n} \\ \vdots & \vdots & \ddots & \vdots \\ \text{Cov}_{y_n,y_1} & \text{Cov}_{y_n,y_2} & \cdots & \sigma_{y_n}^2 \end{pmatrix}, \tag{B.9}$$

which is needed to construct the χ^2-functional used in the fitting method as described in the next section in more detail.

In some cases, the observables included in the fits correspond to functions of correlated variables y_i. To correctly take all correlations into account we therefore have to construct covariance matrices including error propagation. Defining a function $\mathbf{f}$ of the n correlated variables y_i having m components, i.e.,

$$\mathbf{f}(y_1, \cdots, y_n) = \begin{pmatrix} f_1(y_1, \cdots, y_n) \\ \vdots \\ f_m(y_1, \cdots, y_n) \end{pmatrix}, \tag{B.10}$$

the $m \times m$ covariance matrix including error propagation can be computed as

$$C_{kk'} = \sum_{i=1}^{n} \frac{\partial f_k}{\partial y_i} \frac{\partial f_{k'}}{\partial y_i} \sigma_{y_i}^2 + \sum_{i=1}^{n} \sum_{j \neq i} \frac{\partial f_k}{\partial y_i} \frac{\partial f_{k'}}{\partial y_j} \text{Cov}_{y_i,y_j}. \tag{B.11}$$

In a more compact way using matrix notation this can be written as

$$C = J\Sigma J^T, \tag{B.12}$$

where J is the $m \times n$ Jacobian matrix of the vector function $\mathbf{f}$ and Σ the covariance matrix as defined in Eq. (B.9). As an instructive example we consider the case

$$\mathbf{f} = \begin{pmatrix} Z_A f_\pi \\ m_\pi^2 \\ Z_M m_\ell \end{pmatrix}, \quad \Sigma = \begin{pmatrix} \sigma_{Z_A}^2 & 0 & 0 & 0 & 0 \\ 0 & \sigma_{f_\pi}^2 & \text{Cov}_{f_\pi,m_\pi} & 0 & \text{Cov}_{f_\pi,m_l} \\ 0 & \text{Cov}_{f_\pi,m_\pi} & \sigma_{m_\pi}^2 & 0 & \text{Cov}_{m_\pi,m_l} \\ 0 & 0 & 0 & \sigma_{Z_M}^2 & 0 \\ 0 & \text{Cov}_{f_\pi,m_l} & \text{Cov}_{m_\pi,m_l} & 0 & \sigma_{m_l}^2 \end{pmatrix} \tag{B.13}$$

which yields the covariance matrix

$$C = \begin{pmatrix} Z_A^2 \sigma_{f_\pi}^2 + \sigma_{Z_A}^2 f_\pi^2 & 2Z_A \text{Cov}_{f_\pi,m_\pi} m_\pi & Z_A Z_M \text{Cov}_{f_\pi,m_l} \\ 2Z_A \text{Cov}_{f_\pi,m_\pi} m_\pi & 4\sigma_{m_\pi}^2 m_\pi^2 & 2Z_M \text{Cov}_{m_\pi,m_l} m_\pi \\ Z_A Z_M \text{Cov}_{f_\pi,m_l} & 2Z_M \text{Cov}_{m_\pi,m_l} m_\pi & Z_M^2 \sigma_{m_l}^2 + \sigma_{Z_M}^2 m_l^2 \end{pmatrix}, \tag{B.14}$$

as applied in the fits discussed in section 4.3.1.

B.3 Fitting

In the analysis of baryon structure observables fits to correlation functions or to observables determined on different ensembles play a central role. We will carry out fits by minimizing the χ^2-functional defined as

$$\chi^2\left[\{p\}\right] = \sum_X \delta y_X^T C_X^{-1} \delta y_X \tag{B.15}$$

with respect to a set of parameters $\{p\}$ that parametrizes a fit model $f(\{x\}; \{p\})$, $\{x\}$ being a set of arbitrary variables. Here C_X^{-1} is the inverse of the $n \times n$ covariance matrix as discussed in the previous section and δy_X is the n-dimensional vector

$$\delta y_X = \begin{pmatrix} y_1^X - f_1^X(\{x\}; \{p\}) \\ \vdots \\ y_n^X - f_n^X(\{x\}; \{p\}) \end{pmatrix}, \tag{B.16}$$

where the data points are denoted by y. The summation index X can label any arbitrary set of data/fit model $(y_i^X / f_i^X(\dots))$ which allows one to very easily construct uncorrelated, block correlated or fully correlated fits as well as adding additional 'prior' terms. For a particular fit the number of degrees of freedom is given by $N_{\text{dof}} = n - k$, where n and k are the number of all data points and all fit parameters added to the χ^2-functional, respectively.

As a simple example we take a two-point correlation function $C_{2\text{pt}}^B(t) = y(t)$ and fit the data $y(t_i) = y_i$ to the function $f_i(t_i; \{a, m\}) = ae^{-mt_i}$. The parameters $\{a, m\}$ describe amplitude and mass for the baryon ground state B and $i = 1, \dots, n$ labels the number of data points. This can easily be extended to three-point correlation functions $C_{3\text{pt}}^B(\tau, t)$ where one usually performs simultaneous fits to multiple values of the source-sink separation t and which allows to extract specific matrix elements.

The other type of fits is given by the extrapolations as discussed in section 3.7. Again, we consider as an example the fits carried out in section 4.3.1. Here the expectation values for the pion decay constant and the pion mass are simultaneously fitted as a functions of the quark mass where all three observables are determined on the same ensemble. In this case we have

$$\delta y_X = \begin{pmatrix} y_1^X(f_\pi) - f_1(\{m_\ell^X, \dots\}; \{p\}) \\ y_2^X(m_\pi^2) - f_2(\{m_\ell^X, \dots\}; \{p\}) \\ y_3^X(m_\ell) - f_3(m_\ell^X) \end{pmatrix}, \tag{B.17}$$

where the corresponding parametrization for f_1 and f_2 are given in Eqs. (4.3) and (4.2), $f_3(m_\ell^X) = m_\ell^X$ and X labels a particular ensemble. For simplicity we suppress the additional function arguments denoting them by $(, \dots)$. Including the covariance matrix as defined in Eq. (B.14) we minimize the χ^2-functional with respect to all variables $\{m_\ell, \dots\}$ and parameters $\{p\}$. In this way we are able to perform fully correlated fits and incorporate all errors and correlations in the analysis.

To take also the statistical errors of parameters which are completely uncorrelated to all other parameters into account we can simply add an additional 'prior' term to the χ^2-functional which reduces to the (1-dimensional) form $(y^m - p^m)^2/\sigma_{p^m}^2$. Note that such terms do not alter the number of degrees of freedom since one basically adds one new data point y^m for each parameter p^m and also do not affect the stability of the fit. In the extrapolations we make use of these prior terms to include, e.g., the uncertainties of the renormalization and improvement factors by adding a term for each β-value where the data points are incorporated by means of pseudo-bootstrap distributions.

For the minimization we use the Minuit algorithms [224] which are widely used in the field of high energy physics and estimate the statistical errors of the fit parameters via the bootstrap method. Carrying out the fits on each bootstrap sample can become computer time intensive. Hence it is noteworthy that Minuit can also provide an estimate for the errors of the fit parameters by investigating the shape of the χ^2-function around its minimum, where in general we find consistency between the Minuit and the bootstrap error estimates.

B.4 Model averaging

In lattice QCD calculations one often has to perform simultaneous extrapolations to the chiral or physical quark mass, continuum and infinite volume limits to obtain results of the physical observables one is interested in. Within this work we will rely on the model averaging procedure outlined in the following in order to incorporate the systematic uncertainties associated with unphysical quark masses, finite lattice spacing and finite volumes within these extrapolations in the final results. This section has already been published in similar or verbatim form in Ref. [SW1].

To address systematic effects we carry out fits varying the fit function (e.g., BChPT vs. HBChPT as described in section 4.3.2) as well as the number of data points included. This gives us a set of N_M different results, one for each model j, from which we compute an average and its uncertainty that includes the statistical error and the systematic uncertainty due to the model variation.

One widely used approach is to assign a weight w_j given by the Akaike information criterion (AIC) [225] to each model j in the model averaging procedure. Here we employ the weights

$$w_j = A \exp \left\{ -\frac{1}{2} \left[\max \left(\chi_j^2, N_{\mathrm{dof},j} \right) - N_{\mathrm{dof},j} + k_j \right] \right\}, \tag{B.18}$$

see, e.g., Eq. (161) of the e-print version of Ref. [226] and references therein.[1] The normalization A is such that $\sum_i^{N_M} w_i = 1$. χ_j^2 denotes the χ^2-value of the fit to model j, k_j the number of fit parameters and $N_{\mathrm{dof},j} = n_j - k_j$ the number of degrees of freedom. By replacing $\chi^2 \mapsto \max(\chi^2, N_{\mathrm{dof}})$, we deviate somewhat from Ref. [226] in so far as reducing the χ^2-value below N_{dof} will not further increase the weight. The rationale for this choice is that if the fit function perfectly described the data then a value $\chi^2 < N_{\mathrm{dof}}$ should not be more likely than the expected value $\chi^2 = N_{\mathrm{dof}}$. The above equation extends the AIC to also varying the number of data points n_j and not only the fit function. It is valid as long as there are no correlations between the removed and the remaining data points, the fit function is smooth and the parametrization does not depend on the data space. This applies to our case where we reduce the number of data points by removing entire ensembles and carry out the same set of fits for every data set.

For each parameter a that we are interested in, we generate for each model j a bootstrap distribution $a_j(\mathcal{B})$ with $N_B = 500$ bootstrap samples $\mathcal{B}$. The (normalized) bootstrap histograms are usually normal distributed,

$$f_j(a) = \frac{1}{\sqrt{2\pi}\sigma_j} \exp \left\{ -\frac{1}{2} \left(\frac{a - a_j}{\sigma_j} \right)^2 \right\}, \tag{B.19}$$

---

[1]Recently, instead of subtracting $N_{\mathrm{dof}} - k$ from χ^2 in the exponent, in Ref. [227] it has been suggested to subtract $-2n_{\mathrm{cut}} - 2k = \mathrm{const} + 2N_{\mathrm{dof}}$, where n_{cut} is the number of removed data points. This seems counter-intuitive: since for a good fit $\chi^2 \sim N_{\mathrm{dof}}$, this change would result in a very strong preference for fits that include as many data points as possible, even if the corresponding χ^2/N_{dof}-values were significantly larger.

with a mean a_j and a standard deviation σ_j. From the (discrete) histograms, we obtain the model averaged distribution

$$f(a) = \sum_j w_j f_j(a), \tag{B.20}$$

from which we take the median and the 1σ confidence interval determined by the 15.9% and 84.1% percentiles as the model average $\bar{a}$ and its upper and lower confidence limits $\bar{a} + \Delta a_+$ and $\bar{a} - \Delta a_-$. We then quote the average and its total error as $\bar{a}_{\Delta a_-}^{\Delta a_+}$. This procedure is for example illustrated in Figs. 4.4 and 4.6, where the histograms are coarsely binned for a better visualization.

C | DETAILS OF THE THREE-POINT FUNCTION MEASUREMENTS

The following comparison of the stochastic and sequential source methods has already been published in similar or verbatim form in Ref. [SW2].

The connected three-point functions for all the octet baryons have been computed utilizing the computationally efficient stochastic approach outlined in section 3.3. This approach introduces additional stochastic noise on top of the gauge noise. In the analysis presented, for the nucleon, we make use of statistically more precise three-point correlation function measurements determined via the sequential source method as part of other projects. In the following, we compare the computational costs of the stochastic and the sequential source methods and the results for the ratios of the three-point over two-point functions for the nucleon.

As a typical example, we consider the measurements performed on ensemble N200 ($M_\pi = 286$ MeV and $a = 0.064$ fm). For our set-up, illustrated in Figs. 3.3 and 3.4, a total of 4×12 solves are needed for the 4 source positions of the point-to-all propagators. To form the three-point functions for the nucleon an additional $N_{\mathrm{sto}} = 100$ light stochastic solves (for the timeslice-to-all propagators connecting the sink and current timeslices, the wiggly lines in Fig. 3.3) are performed. This set-up provides 8 measurements of the nucleon three-point function (as shown in Fig. 3.4, with the source-sink separations $t/a = 11$, 14, 16, 19) and includes all polarizations (and the unpolarized case) as well as a range of sink momenta (almost) for free. In principle, decuplet baryon three-point functions can also be constructed at the analysis stage. This set-up is evaluated twice on each configuration leading to a total of 296 inversions. Similarly, an additional $(4 \times 12 + 100) \times 2$ strange solves are performed in order to form the three-point functions for all the (octet and decuplet) hyperons, including strangeness changing currents that are not considered here.

In the sequential source set-up, we compute the three-point function for the nucleon at rest, again for source-sink separations $t/a = 11$, 14, 16 and 19. Ten measurements are carried out per configuration (corresponding to 1, 2, 3 and 4 measurements for each t, respectively), where in each case the two light quark flavours (u and d) of the current and the four possible polarizations of the nucleon require 2×4 sequential sources to be constructed. This amounts to performing $(4 + 10 \times 2 \times 4) \times 12 = 1008$ light solves. The additional 4×12 inversions refer to the point-to-all propagators for 4 different source positions that connect the source to the sink (and the current). This is three-times the cost of the stochastic approach (for the nucleon three-point functions), which realizes a range of sink momenta.

The ratios of the three-point over two-point functions for the nucleon obtained from the two different approaches are compared in Fig. C.1. A significant part of the gauge noise cancels in the ratio, while the (additional) stochastic noise remains. For our set-up, this leads to larger statistical errors for the stochastic data compared to the sequential source results. This difference can clearly be seen for the ratio in the vector channel, for which the gauge noise is minimal, however, the difference is less pronounced for the other charges. For the sigma and cascade baryons we generally find a good statistical signal in
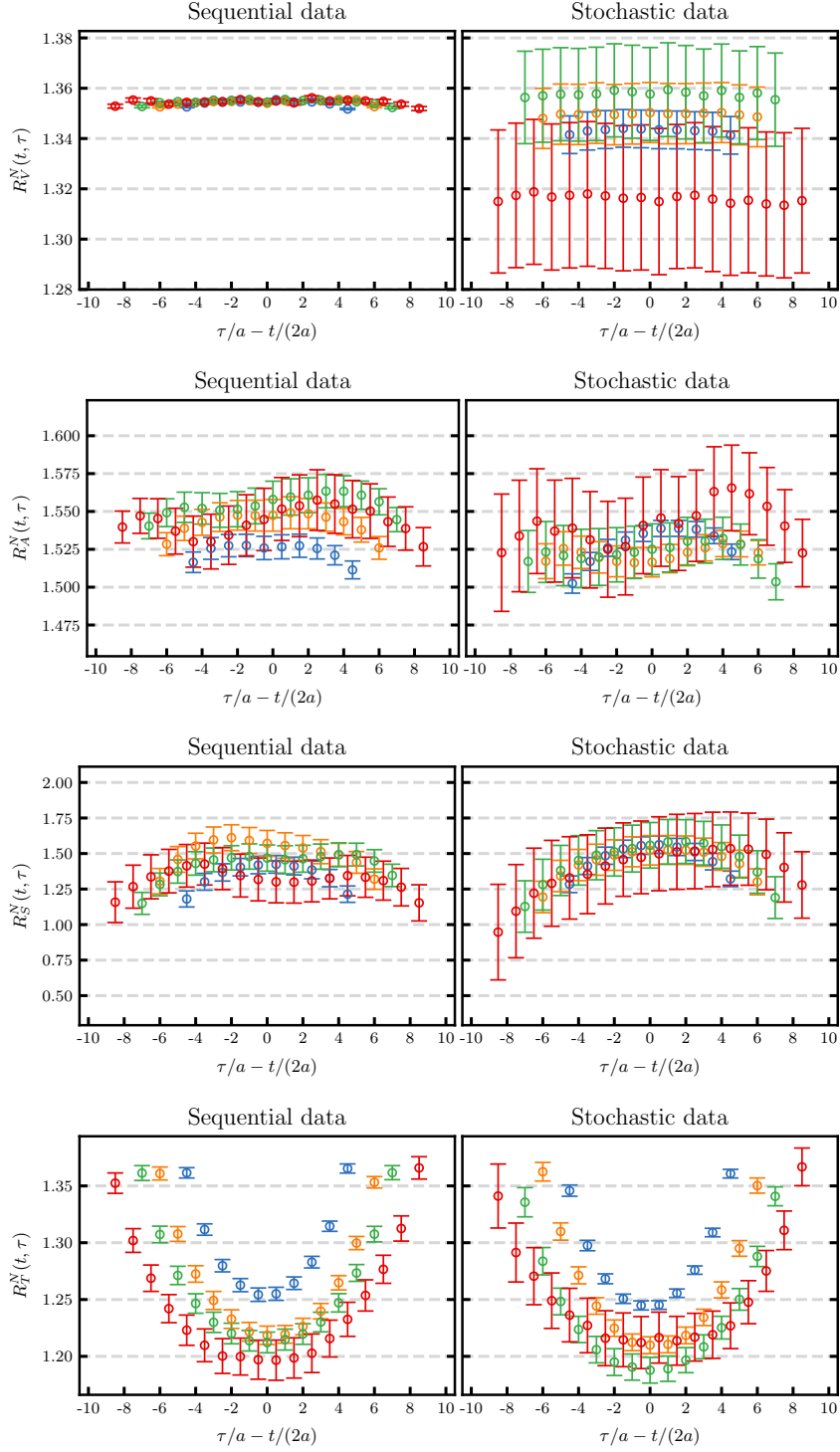
Figure C.1: Unrenormalized ratio of three-point over two-point functions for the nucleon vector, axial, scalar and tensor charge (from top to bottom) on ensemble N200. The left hand side shows the data from the sequential source method from 1,2,3 and 4 measurements (for increasing values of t) compared to the same measurements obtained from the stochastic approach with four measurements for each value of t on the right hand side.
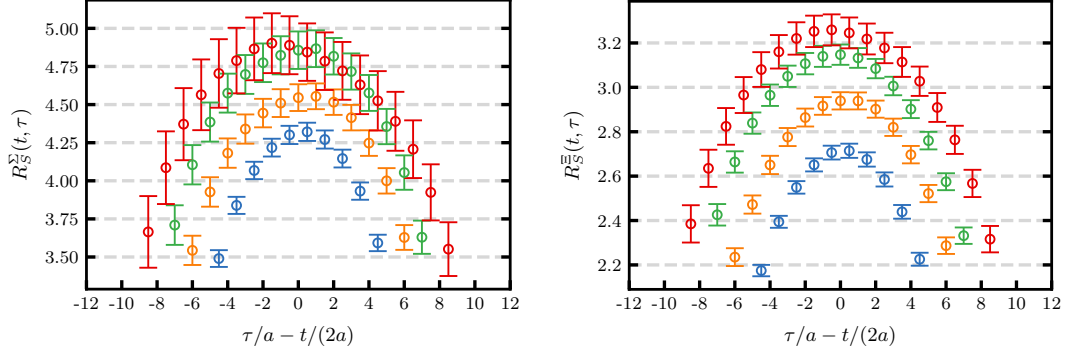
Figure C.2: Unrenormalized ratio of three-point over two-point functions for the scalar charge of the sigma (left) and cascade (right) baryon on ensemble N200.

the ratios employing the stochastic approach, see Fig. C.2, although, also in this case the ratios for the hyperon vector charges suffer from large errors.

In the case of a large-scale analysis effort including high statistics, as carried out in the course of this thesis, the disk space required to store the stochastic three-point function data is significant. The individual spectator (S) and insertion (I) parts as defined in Eqs. (3.31) and (3.32), respectively, are stored with all indices open. In general this amounts to $N = N[S] + N[I]$ complex double precision floating point numbers for each gauge field configuration where

$$N[S] = N_F^S \cdot N_{\mathbf{p}'} \cdot N_{\mathrm{snk}} \cdot N_{\mathrm{src}} \cdot N_{\mathrm{sto}} \cdot N_c \cdot N_s^5 \,, \tag{C.1}$$

$$N[I] = N_F^I \cdot N_{\mathbf{q}} \cdot N_{\partial_\mu} \cdot N_\tau \cdot N_{\mathrm{src}} \cdot N_{\mathrm{sto}} \cdot N_c \cdot N_s^2 \,. \tag{C.2}$$

Here $N_F^{S/I}$ denotes the number of flavour combinations for the spectator and insertion parts (typically 4 and 2, respectively), $N_{\mathbf{p}}$ gives the number of momentum combinations for a maximum momentum $|\mathbf{p}|$ (with $\mathbf{p}$ either being the sink momentum $\mathbf{p}'$ or the momentum transfer $\mathbf{q}$), $N_{\mathrm{src/snk}}$ corresponds to the number of source (4) and sink (2) positions, $N_c = 3$ and $N_s = 4$ are the dimensions of colour and spin space and N_τ is the number of current insertion timeslices, usually the distance between the two sink timeslices times the number of sources, see Figs. 3.3 and 3.4.[1] N_{∂_μ} refers to the number of derivatives included in the current insertion. All currents including up to one derivative $(N_{\partial_\mu} = 1+4)$ were computed, although only the currents without derivatives are presented in this work. This adds up to a file size of the order of GBs for a single gauge field configuration and disk space usage of the order of TBs for a typical CLS gauge ensemble. Within the project of this thesis, in total nearly 2 PBs of stochastic three-point function data has been generated. Storing the data with all indices open allows for a very flexible analysis. Octet or decuplet baryon three-point functions can be constructed from the spectator and insertion parts for different polarizations, current insertions as well as for a large number of momentum combinations.

---

[1] In practice, in contrast to the sequential source data, data points with current insertion at the source and sink are not stored for the stochastic method.

D | LATTICE DATA

Several tables are provided: Table D.1 lists all ensembles (and related parameters) analysed within this work where additional details are given in Tables D.2 and D.3. Table D.4 gives the results used in the analysis of the LECs in chapter 4, while the results for the unrenormalized charges of the three octet baryons, analysed in chapter 5, are collected in Tables D.5–D.7.

Table D.1: List of the gauge ensembles analysed in this work. The rqcdxyz ensembles were generated by the RQCD group using the BQCD code [228], whereas all other ensembles were created within the CLS effort. Note that for H102 there are two replicas. These have the same parameters but were generated with slightly different algorithmic set-ups and, therefore, have to be analysed separately. N401 and N451 differ in terms of the boundary conditions (bc) imposed in the time direction (open (o) and anti-periodic (p), respectively). The lattice spacings a are determined in Ref. [52]. The last column gives N_{cnfg}, the number of configurations analysed.

Ensemble	β	a[fm]	trajectory	bc	$N_t \cdot N_s^3$	M_π[MeV]	M_K[MeV]	LM_π	N_{cnfg}
A650	3.34	0.098	sym	p	$48 \cdot 24^3$	371	371	4.43	5062
A653			tr M/sym	p	$48 \cdot 24^3$	429	429	5.12	2525
A654			tr M	p	$48 \cdot 24^3$	338	459	4.04	2533
rqcd021	3.4	0.086	sym	p	$32 \cdot 32^3$	340	340	4.73	1541
H101			tr M/sym	o	$96 \cdot 32^3$	423	423	5.88	2000
U103			tr M/sym	o	$128 \cdot 24^3$	420	420	4.38	2470
H102r001			tr M	o	$96 \cdot 32^3$	354	442	4.92	997
H102r002			tr M	o	$96 \cdot 32^3$	359	444	4.99	1000
U102			tr M	o	$128 \cdot 24^3$	357	445	3.72	2210
N101			tr M	o	$128 \cdot 48^3$	281	467	5.86	1457
H105			tr M	o	$96 \cdot 32^3$	281	468	3.91	2038
D101			tr M	o	$128 \cdot 64^3$	222	476	6.18	608
C101			tr M	o	$96 \cdot 48^3$	222	476	4.63	2000
S100			tr M	o	$128 \cdot 32^3$	214	476	2.98	983
D150			tr M/ms	p	$128 \cdot 64^3$	127	482	3.53	603
H107			ms	o	$96 \cdot 32^3$	368	550	5.12	1564
H106			ms	o	$96 \cdot 32^3$	273	520	3.80	1553
C102			ms	o	$96 \cdot 48^3$	223	504	4.65	1500
rqcd030	3.46	0.076	sym	p	$64 \cdot 32^3$	319	319	3.93	1224
X450			sym	p	$64 \cdot 48^3$	265	265	4.90	400
B450			tr M/sym	p	$64 \cdot 32^3$	421	421	5.19	1612
S400			tr M	o	$128 \cdot 32^3$	354	445	4.36	2872
N451			tr M	p	$128 \cdot 48^3$	289	466	5.34	1011
N401			tr M	o	$128 \cdot 48^3$	287	464	5.30	1086
D450			tr M	p	$128 \cdot 64^3$	216	480	5.32	621
D452			tr M	p	$128 \cdot 64^3$	156	488	3.84	1000
B452			ms	p	$64 \cdot 32^3$	352	548	4.34	1944
N450			ms	p	$128 \cdot 48^3$	287	528	5.30	1132
D451			ms	p	$128 \cdot 64^3$	219	507	5.39	458
X250	3.55	0.064	sym	p	$64 \cdot 48^3$	350	350	5.47	1493
X251			sym	p	$64 \cdot 48^3$	268	268	4.19	1474
N202			tr M/sym	o	$128 \cdot 48^3$	414	414	6.47	883
N203			tr M	o	$128 \cdot 48^3$	348	445	5.44	1543
N200			tr M	o	$128 \cdot 48^3$	286	466	4.47	1712
S201			tr M	o	$128 \cdot 32^3$	290	471	3.02	2092
D200			tr M	o	$128 \cdot 64^3$	202	484	4.21	2001
E250			tr M/ms	p	$192 \cdot 96^3$	131	493	4.10	490
N204			ms	o	$128 \cdot 48^3$	353	549	5.52	1500
N201			ms	o	$128 \cdot 48^3$	287	527	4.49	1522
D201			ms	o	$128 \cdot 64^3$	200	504	4.17	1078
N300	3.7	0.049	tr M/sym	o	$128 \cdot 48^3$	425	425	5.15	1539
N302			tr M	o	$128 \cdot 48^3$	348	455	4.21	1383
J303			tr M	o	$192 \cdot 64^3$	259	479	4.18	998
E300			tr M	o	$192 \cdot 96^3$	176	496	4.26	1038
N304			ms	o	$128 \cdot 48^3$	353	558	4.27	1652
J304			ms	o	$192 \cdot 64^3$	261	527	4.21	1630
J500	3.85	0.039	tr M/sym	o	$192 \cdot 64^3$	413	413	5.24	1837
J501			tr M	o	$192 \cdot 64^3$	336	448	4.26	1018

Table D.2: Gauge ensembles as listed in table D.1. In the last column t denotes the source-sink separation of the connected three-point functions. The subscript (superscript) given for each separation indicates the number of measurements performed using the sequential source (stochastic) method on each configuration (see Secs. 3.2 and 3.3).

Ensemble	β	a[fm]	t/a
A650	3.34	0.098	$7_3, 9_3, 11_3, 13_4$
A653			$7_3, 9_3, 11_3, 13_4$
A654			$7_3^2, 9_3^2, 11_3^2, 13_4^2$
rqcd021	3.4	0.086	$8_2, 10_2, 12_4, 14_4$
H101			$8_2, 10_2, 12_2, 14_2$
U103			$8_1, 10_2, 12_3, 14_4$
H102r001			$8_1^4, 10_2^4, 12_3^4, 14_4^4$
H102r002			$8_1^4, 10_2^4, 12_3^4, 14_4^4$
U102			$8_1, 10_2, 12_3, 14_4$
N101			$8_1, 10_2, 12_3, 14_4$
H105			$8_1^2, 10_2^2, 12_3^2, 14_4^2$
D101			$8_1, 10_2, 12_3, 14_4$
C101			$8_1^2, 10_2^2, 12_3^2, 14_4^2$
S100			$8_1, 10_2, 12_3, 14_4$
D150			$8_1, 10_2, 12_3, 14_4$
H107			$8_2^2, 10_2^2, 12_3^2, 14_4^2$
H106			$8_2^4, 10_2^4, 12_3^4, 14_4^4$
C102			$8_2^4, 10_2^4, 12_3^4, 14_4^4$
rqcd030	3.46	0.076	$9_4, 11_4, 13_8, 16_8$
X450			$9_2, 11_2, 13_4, 16_4$
B450			$9_3, 11_3, 14_3, 16_4$
S400			$9_1^2, 11_2^2, 13_3, 14^2, 16_4^2$
N451			$9_4^4, 11_4^4, 13_4, 14^4, 16_4^4$
N401			$9_1^2, 11_2^2, 13_3, 14^2, 16_4^2$
D450			$9_4^2, 11_4^2, 13_4, 14^2, 16_4^2$
D452			$9^4, 11^4, 14^4, 16^4$
B452			$9_3^2, 11_3^2, 13_3, 14^2, 16_4^2$
N450			$9_4^2, 11_4^2, 13_4, 14^2, 16_4^2$
D451			$9_4^2, 11_4^2, 13_4, 14^2, 16_4^2$
X250	3.55	0.064	$11_2, 14_2, 16_4, 19_4$
X251			$11_4, 14_4, 16_8, 19_8$
N202			$11_1, 14_2, 16_2, 19_4$
N203			$11_1^4, 14_2^4, 16_3^4, 19_4^4$
N200			$11_1^4, 14_2^4, 16_3^4, 19_4^4$
S201			$11_1, 14_2, 16_3, 19_4$
D200			$11_1^2, 14_2^2, 16_3^2, 19_4^2$
E250			$11_4, 14_4, 16_4, 19_4$
N204			$11_2^2, 14_2^2, 16_3^2, 19_4^2$
N201			$11_2^2, 14_2^2, 16_3^2, 19_4^2$
D201			$11_1^4, 14_2^4, 16_3^4, 19_4^4$
N300	3.7	0.049	$14_1, 17_2, 21_2, 24_4$
N302			$14_1^2, 17_2^2, 21_3^2, 24_4^2$
J303			$14_2^2, 17_4^2, 21_6^2, 24_8^2$
E300			$14_3^2, 17_3^2, 21_6^2, 24_6^2$
N304			$14_3^2, 17_3^2, 21_3^2, 24_4^2$
J304			$14_3^2, 17_3^2, 21_3^2, 24_4^2$
J500	3.85	0.039	$17_1, 22_2, 27_3, 32_4$
J501			$17_1^2, 22_2^2, 27_3^2, 32_4^2$

Table D.3: List of the hopping parameters κ_ℓ and κ_s as set in the generation of the $N_f = 2+1$ CLS and RQCD gauge ensembles used within this work. Further we tabulate the Wilson flow scale parameter t_0/a^2 and the pion and kaon masses M_π and M_K we make use of in our analysis and which were determined in Ref. [52] and an update thereof.

Ensemble	κ_ℓ	κ_s	t_0/a^2	aM_π	aM_K
A653	0.1365716	0.1365716	2.1729(50)	0.21235(94)	0.21235(94)
A650	0.136600	0.136600	2.2878(72)	0.1833(13)	0.1833(13)
A654	0.136750	0.136216193	2.1950(77)	0.1669(11)	0.22714(91)
H101	0.13675962	0.13675962	2.8545(81)	0.18283(57)	0.18283(57)
U103	0.13675962	0.13675962	2.8815(57)	0.18133(61)	0.18133(61)
H107	0.13694566590798	0.136203165143476	2.7193(76)	0.15913(73)	0.23745(53)
H102r002	0.136865	0.136549339	2.8792(90)	0.15490(92)	0.19193(77)
U102	0.136865	0.136549339	2.8932(63)	0.15444(84)	0.19235(61)
H102r001	0.136865	0.136549339	2.8840(89)	0.15311(98)	0.19089(78)
rqcd021	0.136813	0.136813	3.032(15)	0.14694(88)	0.14694(88)
H105	0.136970	0.13634079	2.8917(65)	0.1213(14)	0.20233(64)
N101	0.136970	0.13634079	2.8948(39)	0.12132(58)	0.20156(30)
H106	0.137015570024	0.136148704478	2.8227(68)	0.1180(21)	0.22471(67)
C102	0.13705084580022	0.13612906255557	2.8682(47)	0.09644(77)	0.21783(36)
C101	0.137030	0.136222041	2.9176(38)	0.09586(64)	0.20561(33)
D101	0.137030	0.136222041	2.910(10)	0.0958(11)	0.20572(45)
S100	0.137030	0.136222041	2.9212(91)	0.0924(31)	0.20551(57)
D150	0.137088	0.13610755	2.9476(30)	0.05497(79)	0.20834(17)
B450	0.136890	0.136890	3.663(11)	0.16095(49)	0.16095(49)
S400	0.136984	0.136702387	3.6919(74)	0.13535(42)	0.17031(38)
B452	0.1370455	0.136378044	3.5286(66)	0.13471(47)	0.20972(34)
rqcd030	0.1369587	0.1369587	3.914(15)	0.12202(68)	0.12202(68)
N451	0.1370616	0.1365480771	3.6822(46)	0.11067(32)	0.17828(20)
N401	0.1370616	0.1365480771	3.6844(52)	0.10984(57)	0.17759(37)
N450	0.1370986	0.136352601	3.5920(42)	0.10965(31)	0.20176(18)
X450	0.136994	0.136994	3.9935(92)	0.10142(62)	0.10142(62)
D451	0.137140	0.136337761	3.6684(36)	0.08370(31)	0.19385(15)
D450	0.137126	0.136420428639937	3.7076(75)	0.08255(41)	0.18354(12)
D452	0.137163675	0.136345904546	3.7251(37)	0.05961(50)	0.18647(13)
N202	0.137000	0.137000	5.165(14)	0.13388(35)	0.13388(35)
N204	0.137112	0.136575049	4.9473(79)	0.11423(33)	0.17734(29)
X250	0.137050	0.137050	5.283(28)	0.11319(39)	0.11319(39)
N203	0.137080	0.136840284	5.1465(63)	0.11245(30)	0.14399(24)
S201	0.137140	0.13672086	5.1638(91)	0.09379(47)	0.15220(37)
N201	0.13715968	0.136561319	5.0427(75)	0.09268(31)	0.17040(22)
N200	0.137140	0.13672086	5.1600(71)	0.09236(29)	0.15061(24)
X251	0.137100	0.137100	5.483(26)	0.08678(40)	0.08678(40)
D200	0.137200	0.136601748	5.1793(39)	0.06540(33)	0.15652(15)
D201	0.1372067	0.136546844	5.1378(66)	0.06472(42)	0.16302(18)
E250	0.137232867	0.136536633	5.2027(41)	0.04227(23)	0.159370(61)
N300	0.137000	0.137000	8.576(21)	0.10642(38)	0.10642(38)
N304	0.137079325093654	0.136665430105663	8.322(20)	0.08840(33)	0.13960(31)
N302	0.137064	0.1368721791358	8.539(19)	0.08701(41)	0.11370(36)
J304	0.137130	0.1366569203	8.497(12)	0.06538(18)	0.13181(14)
J303	0.137123	0.1367546608	8.615(14)	0.06481(19)	0.11975(16)
E300	0.137163	0.1366751636177327	8.6241(74)	0.04402(20)	0.12397(15)
J500	0.136852	0.136852	14.013(34)	0.08116(34)	0.08116(34)
J501	0.1369032	0.136749715	13.928(39)	0.06589(26)	0.08798(23)

Table D.4: Results for the ensembles used in the analysis of the low energy constants presented in chapter 4. The scale parameter t_0/a^2, the renormalized pion decay constant F_π (where $F_\pi = f_\pi/\sqrt{2}$), the pion mass M_π, the baryon mass m_B, the RGI quark mass m as well as the renormalized axial charges for the nucleon g_A^N and the Σ baryon g_A^Σ, respectively.

Ensemble	t_0/a^2	aF_π	aM_π	am_B	am	g_A^N	g_A^Σ
A652	2.1697(56)	0.04985(29)	0.2140(10)	0.5842(41)	0.02072(21)		
A653	2.1729(50)	0.04980(25)	0.21245(93)	0.5855(37)	0.02050(20)	1.1670(85)	0.8903(61)
A650	2.2878(72)	0.04598(36)	0.1835(13)	0.5469(54)	0.01547(21)	1.1489(94)	0.8822(74)
H101	2.8545(81)	0.04499(23)	0.18286(57)	0.5074(18)	0.01796(10)	1.1818(87)	0.9014(78)
U103	2.8815(57)	0.04386(57)	0.18158(60)	0.5193(30)	0.01745(10)	1.1334(74)	0.8692(72)
rqcd021	3.032(15)	0.04084(23)	0.14702(88)	0.4508(47)	0.01172(12)	1.1548(90)	0.873(12)
rqcd017	3.251(13)	0.03505(68)	0.1022(15)	0.388(13)	0.00548(21)		
B450	3.663(11)	0.03999(13)	0.16103(49)	0.4582(24)	0.016154(82)	1.1723(58)	0.8962(71)
rqcd030	3.914(15)	0.03535(18)	0.12221(68)	0.3957(90)	0.009460(80)	1.1437(89)	0.8723(70)
X450	3.9935(92)	0.03358(21)	0.10144(62)	0.3764(61)	0.006574(57)	1.175(10)	0.894(11)
N202	5.165(14)	0.03419(18)	0.13389(35)	0.3799(18)	0.013802(46)	1.1806(58)	0.9026(70)
X250	5.283(28)	0.03195(19)	0.11321(39)	0.3597(51)	0.009880(47)	1.1650(89)	0.8884(93)
X251	5.483(26)	0.02932(21)	0.08684(40)	0.3185(85)	0.005812(47)	1.165(13)	0.889(14)
N300	8.576(21)	0.02680(12)	0.10647(38)	0.3035(13)	0.011332(30)	1.1639(86)	0.884(17)
J500	14.013(40)	0.02106(11)	0.08119(34)	0.2313(26)	0.008755(21)	1.1514(50)	0.8873(84)

Table D.5: Results for the unrenormalized nucleon charges $g_J^{N,\text{latt}}$ for $J \in \{A, S, T, V\}$. #ES labels the number of excited states used to determine the ground state matrix element, see the discussion in section 3.4.

#ES	1				2			
Ensemble	$g_A^{N,\text{latt}}$	$g_S^{N,\text{latt}}$	$g_T^{N,\text{latt}}$	$g_V^{N,\text{latt}}$	$g_A^{N,\text{latt}}$	$g_S^{N,\text{latt}}$	$g_T^{N,\text{latt}}$	$g_V^{N,\text{latt}}$
A653	1.563(17)	1.449(60)	1.273(13)	1.4140(24)	1.589(18)	1.43(10)	1.279(13)	1.4136(21)
A650	1.554(13)	1.468(68)	1.236(10)	1.4173(35)	1.581(18)	1.41(13)	1.243(12)	1.4171(32)
A654	1.545(22)	1.62(21)	1.216(30)	1.4353(85)	1.538(33)	1.76(34)	1.211(19)	1.4365(87)
H101	1.5662(88)	1.760(55)	1.221(13)	1.39160(46)	1.584(16)	1.795(88)	1.224(13)	1.39152(46)
U103	1.495(17)	1.61(11)	1.219(23)	1.39001(77)	1.511(26)	1.68(13)	1.227(18)	1.38990(66)
H107	1.630(37)	1.46(13)	1.248(19)	1.40067(98)	1.667(29)	1.34(17)	1.260(20)	1.40051(77)
H102r002	1.596(21)	1.70(15)	1.221(22)	1.3986(11)	1.616(29)	1.84(21)	1.231(21)	1.39817(87)
U102[a]	1.449(41)	1.42(17)	1.180(56)	1.3988(22)	1.448(41)	1.32(24)	1.194(31)	1.3982(11)
H102r001	1.582(15)	1.67(10)	1.230(21)	1.39706(67)	1.598(32)	1.78(19)	1.235(21)	1.39698(62)
rqcd021	1.546(16)	1.67(12)	1.188(22)	1.383(13)	1.567(30)	1.60(23)	1.190(22)	1.383(12)
H105	1.533(29)	1.44(20)	1.194(37)	1.4077(18)	1.524(51)	1.29(44)	1.199(32)	1.4074(15)
N101[a]	1.623(19)	1.662(87)	1.229(16)	1.40416(63)	1.670(32)	1.64(21)	1.236(18)	1.40411(53)
H106	1.589(34)	1.30(27)	1.223(35)	1.4084(20)	1.597(64)	1.20(50)	1.231(37)	1.4081(17)
C102	1.699(36)	1.70(32)	1.184(25)	1.4083(13)	1.755(58)	1.74(54)	1.198(29)	1.4083(12)
C101	1.675(37)	1.67(17)	1.214(17)	1.40908(85)	1.758(44)	1.76(40)	1.232(18)	1.40872(69)
D101[a]	1.647(51)	1.74(34)	1.222(40)	1.4091(18)	1.700(80)	2.09(77)	1.236(36)	1.4088(11)
S100[a]	1.86(98)	1.6(1.2)	1.27(21)	1.4091(49)	1.75(16)	1.6(1.5)	1.257(57)	1.4072(25)
D150[a]	1.49(21)	2.8(2.9)	0.88(23)	1.430(13)	1.39(31)	5.0(4.0)	0.92(14)	1.430(15)
B450	1.549(12)	1.642(72)	1.228(13)	1.3729(31)	1.587(18)	1.61(13)	1.233(14)	1.3724(27)
S400	1.525(13)	1.645(90)	1.191(22)	1.37682(65)	1.523(28)	1.63(17)	1.193(20)	1.37683(59)
B452	1.555(15)	1.49(10)	1.232(17)	1.3781(38)	1.568(30)	1.39(24)	1.235(19)	1.3781(36)
rqcd030	1.510(14)	1.531(92)	1.178(15)	1.3769(33)	1.553(27)	1.47(20)	1.182(16)	1.3769(30)
N451	1.595(14)	1.603(89)	1.212(15)	1.3828(35)	1.636(31)	1.49(21)	1.217(18)	1.3828(30)
N401	1.584(26)	2.00(27)	1.166(37)	1.3836(11)	1.603(51)	2.27(46)	1.180(31)	1.38328(91)
N450	1.598(13)	1.67(11)	1.208(17)	1.3840(29)	1.625(31)	1.58(26)	1.210(19)	1.3838(29)
X450	1.558(23)	1.99(18)	1.166(23)	1.3884(78)	1.606(51)	2.15(37)	1.174(24)	1.3873(69)
D451	1.583(25)	1.42(25)	1.175(36)	1.3807(78)	1.554(80)	0.88(77)	1.176(38)	1.379(10)
D450	1.623(25)	1.46(30)	1.201(22)	1.3761(90)	1.672(66)	1.04(77)	1.207(27)	1.3769(84)
D452[b]	1.54(21)	0.1(4.5)	0.95(19)	1.07(42)	1.53(32)	-1.0(5.1)	1.00(13)	1.13(22)
N202	1.537(12)	1.926(84)	1.170(17)	1.34793(29)	1.556(20)	2.03(11)	1.179(16)	1.34780(28)
N204	1.570(13)	1.694(91)	1.200(14)	1.35344(39)	1.587(25)	1.80(19)	1.205(15)	1.35335(37)
X250	1.5232(98)	1.814(80)	1.163(14)	1.3513(25)	1.546(19)	1.88(15)	1.167(14)	1.3512(23)
N203	1.532(10)	1.748(68)	1.176(16)	1.35169(27)	1.545(26)	1.69(15)	1.176(16)	1.35169(27)
S201[a]	1.436(25)	1.49(21)	1.155(41)	1.35576(78)	1.52(12)	0.82(98)	1.160(41)	1.3555(10)
N201	1.568(18)	1.67(16)	1.158(21)	1.35653(50)	1.594(36)	1.54(35)	1.162(23)	1.35649(49)
N200	1.565(21)	1.47(15)	1.174(19)	1.35533(37)	1.607(40)	1.33(32)	1.179(22)	1.35530(34)
X251	1.532(25)	1.94(16)	1.135(14)	1.3568(56)	1.604(25)	2.18(26)	1.149(14)	1.3558(41)
D200	1.582(24)	1.94(30)	1.136(32)	1.35952(43)	1.617(61)	2.37(72)	1.140(32)	1.35997(77)
D201	1.562(35)	1.60(41)	1.135(48)	1.35922(82)	1.597(91)	1.82(98)	1.141(45)	1.35922(67)
E250[a]	1.66(14)	1.8(1.2)	1.134(77)	1.353(28)	2.00(20)	3.2(3.8)	1.175(55)	1.358(13)
N300	1.479(12)	1.813(95)	1.149(20)	1.31543(19)	1.485(22)	1.83(14)	1.152(19)	1.31540(16)
N304	1.495(23)	1.64(18)	1.137(28)	1.31926(32)	1.501(36)	1.52(31)	1.140(27)	1.31924(31)
N302	1.498(19)	1.82(18)	1.097(29)	1.31893(29)	1.523(35)	1.83(30)	1.103(27)	1.31889(27)
J304	1.529(19)	1.77(22)	1.107(22)	1.32310(36)	1.567(39)	1.67(51)	1.113(23)	1.32305(37)
J303	1.518(17)	1.51(14)	1.096(29)	1.32206(21)	1.526(56)	1.16(53)	1.094(36)	1.32198(25)
E300	1.557(37)	1.67(36)	1.086(25)	1.3135(88)	1.646(61)	1.44(92)	1.100(33)	1.312(11)
J500	1.451(11)	1.858(92)	1.108(18)	1.29090(12)	1.453(18)	1.91(11)	1.114(13)	1.290855(87)
J501	1.484(37)	2.13(30)	1.072(59)	1.29352(16)	1.499(38)	2.10(28)	1.088(29)	1.29349(19)

[a]Ensemble only enters the analysis of the nucleon charges since no data for the hyperon charges are available.

[b]The nucleon three-point functions are computed with the "stochastic" approach. (For all the other ensembles the sequential source method was used.)

Table D.6: Results for the unrenormalized hyperon charges $g_J^{\Sigma,\text{latt}}$ for $J \in \{A, S, T, V\}$. #ES labels the number of excited states used to determine the ground state matrix element, see the discussion in section 3.4. The three-point functions are computed employing the "stochastic" approach.

#ES		1				2		
Ensemble	$g_A^{\Sigma,\text{latt}}$	$g_S^{\Sigma,\text{latt}}$	$g_T^{\Sigma,\text{latt}}$	$g_V^{\Sigma,\text{latt}}$	$g_A^{\Sigma,\text{latt}}$	$g_S^{\Sigma,\text{latt}}$	$g_T^{\Sigma,\text{latt}}$	$g_V^{\Sigma,\text{latt}}$
A653	1.180(10)	4.40(14)	1.018(14)	2.8354(32)	1.189(16)	4.45(14)	1.023(12)	2.8347(27)
A650	1.1764(90)	4.46(12)	0.9968(95)	2.8381(39)	1.190(16)	4.49(15)	1.000(10)	2.8380(37)
A654	1.173(12)	4.01(16)	1.028(13)	2.852(12)	1.204(37)	4.11(30)	1.028(16)	2.850(14)
H101	1.1877(81)	5.03(12)	0.982(10)	2.78711(66)	1.198(13)	5.12(14)	0.987(10)	2.78686(65)
U103	1.137(13)	4.69(18)	0.983(16)	2.78535(89)	1.147(21)	4.75(18)	0.989(16)	2.78507(80)
H107	1.207(18)	4.25(19)	1.030(12)	2.823(15)	1.232(28)	4.35(27)	1.036(13)	2.820(11)
H102r002	1.177(13)	4.67(17)	0.988(13)	2.807(14)	1.199(25)	4.77(22)	0.992(14)	2.805(12)
H102r001	1.157(14)	4.73(19)	0.973(16)	2.788(11)	1.146(27)	4.79(28)	0.978(17)	2.788(11)
rqcd021	1.149(15)	5.27(24)	0.958(19)	2.790(14)	1.145(27)	5.35(33)	0.962(19)	2.790(13)
H105	1.147(22)	4.83(44)	0.958(23)	2.812(20)	1.162(40)	5.25(55)	0.969(21)	2.809(16)
H106	1.139(15)	4.24(20)	0.968(16)	2.796(15)	1.149(38)	4.27(48)	0.970(19)	2.796(15)
C102	1.140(19)	4.32(29)	0.950(27)	2.791(23)	1.133(45)	3.94(76)	0.952(22)	2.792(18)
C101	1.174(21)	4.58(43)	0.957(22)	2.837(21)	1.240(51)	4.80(94)	0.963(21)	2.834(17)
B450	1.1743(76)	4.80(14)	0.992(11)	2.7464(30)	1.195(15)	4.90(18)	0.997(11)	2.7460(28)
S400	1.159(16)	5.25(29)	0.945(17)	2.751(13)	1.180(23)	5.43(27)	0.962(16)	2.752(11)
B452	1.147(13)	4.33(18)	0.990(16)	2.764(13)	1.163(28)	4.45(33)	0.994(16)	2.763(12)
rqcd030	1.140(12)	5.20(22)	0.944(16)	2.7576(35)	1.157(22)	5.41(33)	0.950(15)	2.7573(33)
N451	1.168(15)	4.90(34)	0.976(14)	2.795(18)	1.193(30)	5.43(38)	0.988(11)	2.789(12)
N401	1.130(52)	5.22(68)	0.933(50)	2.781(42)	1.100(67)	5.23(82)	0.949(33)	2.776(31)
N450	1.148(18)	4.11(17)	0.994(20)	2.738(24)	1.154(43)	3.54(65)	0.992(17)	2.737(21)
X450	1.168(23)	6.05(38)	0.924(25)	2.7700(84)	1.195(49)	6.38(58)	0.933(25)	2.7690(79)
D451	1.143(53)	4.79(95)	0.955(38)	2.67(10)	1.18(15)	3.8(3.0)	0.948(45)	2.624(56)
D450	1.129(63)	4.9(1.1)	0.938(52)	2.721(77)	1.09(11)	3.9(2.1)	0.944(42)	2.730(48)
D452	1.115(52)	4.8(1.1)	0.923(52)	2.789(28)	1.07(14)	5.3(2.6)	0.935(44)	2.787(29)
N202	1.166(10)	5.68(20)	0.939(12)	2.69777(45)	1.182(16)	5.85(15)	0.955(13)	2.69721(41)
N204	1.1465(91)	4.30(12)	0.980(11)	2.686(11)	1.160(26)	4.22(30)	0.979(12)	2.686(12)
X250	1.1549(88)	5.85(20)	0.928(12)	2.7051(32)	1.167(16)	6.12(21)	0.940(12)	2.7046(27)
N203	1.156(12)	5.60(26)	0.941(10)	2.7246(96)	1.182(19)	6.05(22)	0.9623(87)	2.7184(69)
N201	1.150(17)	5.22(43)	0.953(18)	2.737(17)	1.163(42)	5.70(53)	0.965(17)	2.733(14)
N200	1.119(13)	5.03(24)	0.947(13)	2.721(11)	1.116(26)	5.37(36)	0.954(12)	2.720(10)
X251	1.145(16)	6.59(33)	0.903(13)	2.7165(69)	1.195(24)	7.06(37)	0.916(14)	2.7145(55)
D200	1.082(48)	6.4(1.4)	0.841(59)	2.774(26)	1.058(82)	7.7(1.8)	0.867(38)	2.777(29)
D201	1.125(34)	5.7(1.3)	0.924(37)	2.730(31)	1.133(62)	6.8(1.2)	0.944(24)	2.726(19)
N300	1.121(12)	5.52(19)	0.918(17)	2.63208(25)	1.126(19)	5.59(18)	0.925(16)	2.63197(23)
N304	1.106(18)	4.84(31)	0.925(21)	2.642(17)	1.130(30)	4.87(45)	0.928(20)	2.641(15)
N302	1.086(26)	5.41(35)	0.864(34)	2.668(25)	1.118(42)	5.38(49)	0.868(26)	2.666(21)
J304	1.091(29)	5.95(65)	0.864(30)	2.646(25)	1.149(54)	6.61(74)	0.879(23)	2.645(18)
J303	1.100(19)	5.23(59)	0.914(22)	2.671(31)	1.198(61)	5.88(96)	0.927(17)	2.669(26)
E300	1.047(93)	7.9(3.8)	0.853(57)	2.728(87)	1.04(12)	9.1(3.1)	0.884(41)	2.705(55)
J500	1.100(10)	5.78(20)	0.887(13)	2.58250(15)	1.106(15)	5.82(16)	0.894(11)	2.58241(12)
J501	1.053(35)	6.01(86)	0.857(46)	2.629(22)	1.038(54)	6.26(66)	0.878(22)	2.628(19)

Table D.7: Results for the unrenormalized hyperon charges $g_J^{\Xi,\text{latt}}$ for $J \in \{A, S, T, V\}$. #ES labels the number of excited states used to determine the ground state matrix element, see the discussion in section 3.4. The three-point functions are computed employing the "stochastic" approach.

#ES			1				2	
Ensemble	$g_A^{\Xi,\text{latt}}$	$g_S^{\Xi,\text{latt}}$	$g_T^{\Xi,\text{latt}}$	$g_V^{\Xi,\text{latt}}$	$g_A^{\Xi,\text{latt}}$	$g_S^{\Xi,\text{latt}}$	$g_T^{\Xi,\text{latt}}$	$g_V^{\Xi,\text{latt}}$
A653	-0.399(16)	3.13(18)	-0.2495(54)	1.4229(30)	-0.401(11)	3.019(89)	-0.2534(38)	1.4206(21)
A650	-0.3849(96)	3.13(11)	-0.2375(43)	1.4213(28)	-0.3905(95)	3.109(92)	-0.2423(43)	1.4211(20)
A654	-0.3528(58)	2.65(12)	-0.2407(47)	1.4344(67)	-0.354(12)	2.63(17)	-0.2408(59)	1.4349(67)
H101	-0.3810(53)	3.331(91)	-0.2342(41)	1.39556(41)	-0.3854(82)	3.349(93)	-0.2371(48)	1.39528(40)
U103	-0.3580(67)	3.09(11)	-0.2389(48)	1.39547(47)	-0.362(12)	3.05(14)	-0.2380(43)	1.39563(47)
H107	-0.3602(71)	2.89(16)	-0.2413(41)	1.4165(82)	-0.3653(77)	2.93(12)	-0.2453(38)	1.4126(64)
H102r002	-0.3707(54)	3.122(91)	-0.2336(34)	1.4045(52)	-0.3708(92)	3.16(12)	-0.2357(42)	1.4038(48)
H102r001	-0.3671(52)	3.12(10)	-0.2362(35)	1.3987(55)	-0.3683(99)	3.16(14)	-0.2383(45)	1.3987(52)
rqcd021	-0.418(17)	3.93(22)	-0.2211(82)	1.415(15)	-0.425(16)	3.81(21)	-0.2275(71)	1.409(10)
H105	-0.370(11)	3.25(26)	-0.2214(68)	1.4050(86)	-0.372(11)	3.24(22)	-0.2261(72)	1.4047(73)
H106	-0.3448(45)	2.605(83)	-0.2347(27)	1.4052(42)	-0.3553(84)	2.56(22)	-0.2359(39)	1.4049(46)
C102	-0.3431(42)	2.672(96)	-0.2296(41)	1.4007(52)	-0.341(13)	2.52(28)	-0.2286(50)	1.4000(57)
C101	-0.373(23)	3.15(38)	-0.2398(58)	1.423(13)	-0.387(14)	3.19(35)	-0.2436(33)	1.4177(99)
B450	-0.3822(73)	3.321(81)	-0.2322(46)	1.3737(22)	-0.3914(98)	3.289(96)	-0.2352(56)	1.3737(19)
S400	-0.3560(57)	3.20(12)	-0.2332(41)	1.3774(56)	-0.3577(91)	3.28(13)	-0.2373(50)	1.3778(51)
B452	-0.3484(52)	2.873(96)	-0.2309(35)	1.3669(53)	-0.3523(85)	2.90(13)	-0.2333(45)	1.3680(57)
rqcd030	-0.384(11)	3.93(22)	-0.2249(65)	1.3819(34)	-0.394(14)	3.96(25)	-0.2313(67)	1.3807(28)
N451	-0.3693(57)	3.55(15)	-0.2183(42)	1.3969(68)	-0.3720(94)	3.74(17)	-0.2248(46)	1.3948(55)
N401	-0.372(13)	3.17(18)	-0.2296(58)	1.389(13)	-0.389(16)	3.07(32)	-0.2325(68)	1.388(12)
N450	-0.3489(63)	2.92(14)	-0.2294(42)	1.3764(77)	-0.351(14)	2.87(27)	-0.2297(59)	1.3759(78)
X450	-0.403(18)	4.29(31)	-0.2314(88)	1.3809(53)	-0.414(23)	4.39(34)	-0.2369(74)	1.3810(45)
D451	-0.308(19)	2.70(25)	-0.226(19)	1.361(35)	-0.286(36)	1.87(98)	-0.225(13)	1.351(24)
D450	-0.365(21)	3.79(88)	-0.2334(98)	1.391(18)	-0.372(29)	4.27(62)	-0.2377(53)	1.391(11)
D452	-0.320(13)	3.75(66)	-0.2213(80)	1.399(13)	-0.292(33)	4.41(95)	-0.2268(84)	1.397(11)
N202	-0.3758(48)	3.78(10)	-0.2202(41)	1.34982(24)	-0.3759(89)	3.817(99)	-0.2244(50)	1.34959(23)
N204	-0.3365(44)	2.916(92)	-0.2262(35)	1.3484(47)	-0.326(11)	2.91(15)	-0.2252(46)	1.3479(51)
X250	-0.3753(54)	4.18(14)	-0.2195(43)	1.3541(24)	-0.3782(80)	4.26(14)	-0.2257(46)	1.3536(19)
N203	-0.3612(42)	3.652(95)	-0.2178(30)	1.3549(53)	-0.3649(75)	3.74(12)	-0.2220(36)	1.3542(47)
N201	-0.350(11)	3.44(32)	-0.2222(49)	1.377(12)	-0.355(10)	3.56(20)	-0.2285(47)	1.3714(79)
N200	-0.3515(42)	3.58(13)	-0.2147(38)	1.3665(49)	-0.3542(78)	3.73(16)	-0.2184(42)	1.3653(43)
X251	-0.3942(89)	4.68(18)	-0.2226(60)	1.3600(46)	-0.409(11)	4.84(21)	-0.2295(43)	1.3576(40)
D200	-0.347(16)	4.2(1.0)	-0.2127(76)	1.3738(89)	-0.350(15)	4.69(49)	-0.2237(51)	1.3707(70)
D201	-0.3393(78)	3.38(26)	-0.2082(60)	1.3647(83)	-0.344(17)	3.47(51)	-0.2100(74)	1.3645(84)
N300	-0.3596(58)	3.74(10)	-0.2246(45)	1.31662(16)	-0.359(10)	3.78(11)	-0.2279(49)	1.31649(12)
N304	-0.3307(51)	3.12(11)	-0.2196(43)	1.3182(66)	-0.325(10)	3.09(17)	-0.2169(42)	1.3175(70)
N302	-0.361(11)	3.77(19)	-0.2136(60)	1.341(11)	-0.373(15)	3.72(22)	-0.2170(66)	1.3383(89)
J304	-0.3366(73)	3.45(22)	-0.2090(50)	1.3286(83)	-0.346(11)	3.63(28)	-0.2143(58)	1.3277(67)
J303	-0.3416(75)	3.66(23)	-0.2133(48)	1.3306(94)	-0.358(15)	3.88(34)	-0.2208(59)	1.3298(81)
E300	-0.334(17)	3.75(49)	-0.194(13)	1.342(14)	-0.340(31)	3.5(1.0)	-0.195(14)	1.344(17)
J500	-0.3508(46)	3.89(11)	-0.2174(36)	1.291575(73)	-0.3454(91)	3.93(11)	-0.2198(38)	1.291515(71)
J501	-0.353(10)	4.14(25)	-0.2055(62)	1.314(11)	-0.356(13)	4.17(21)	-0.2071(55)	1.3135(98)

E | ADDITIONAL FIGURES

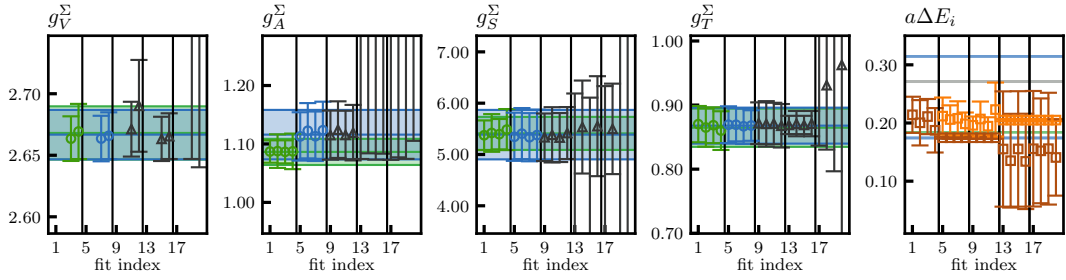Additional figures (Figs. E.1–E.8) related to the analysis in chapter 5 are provided.

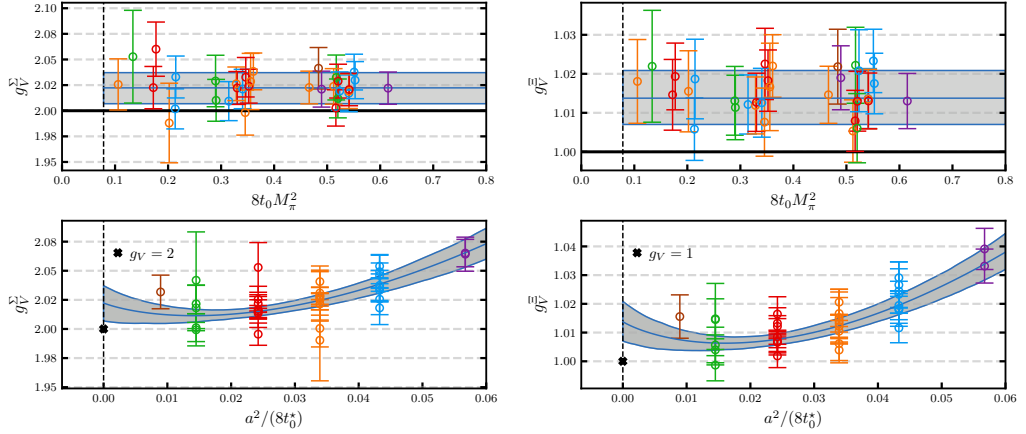Figure E.1: The same as Fig. 3.7 for the sigma baryon.

Figure E.2: The same as Fig. 5.2 for the isovector vector charges g_V^B of the sigma baryon (left) and the cascade baryon (right). For better visibility, the data points for ensemble D451, which have large errors (see Tables D.6 and D.7), are not displayed. See Tables D.6 and D.7 for the set of ensembles used.
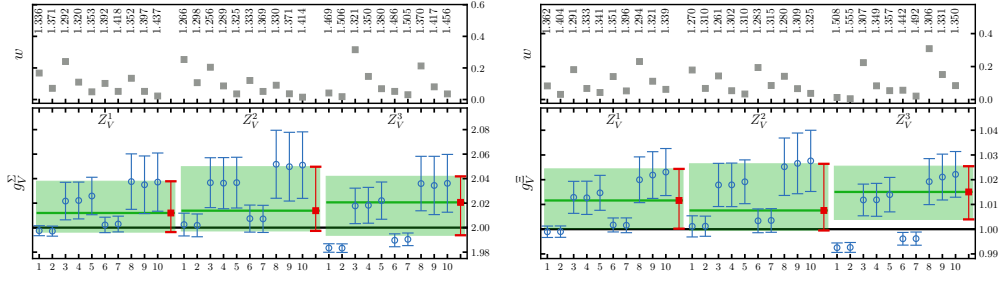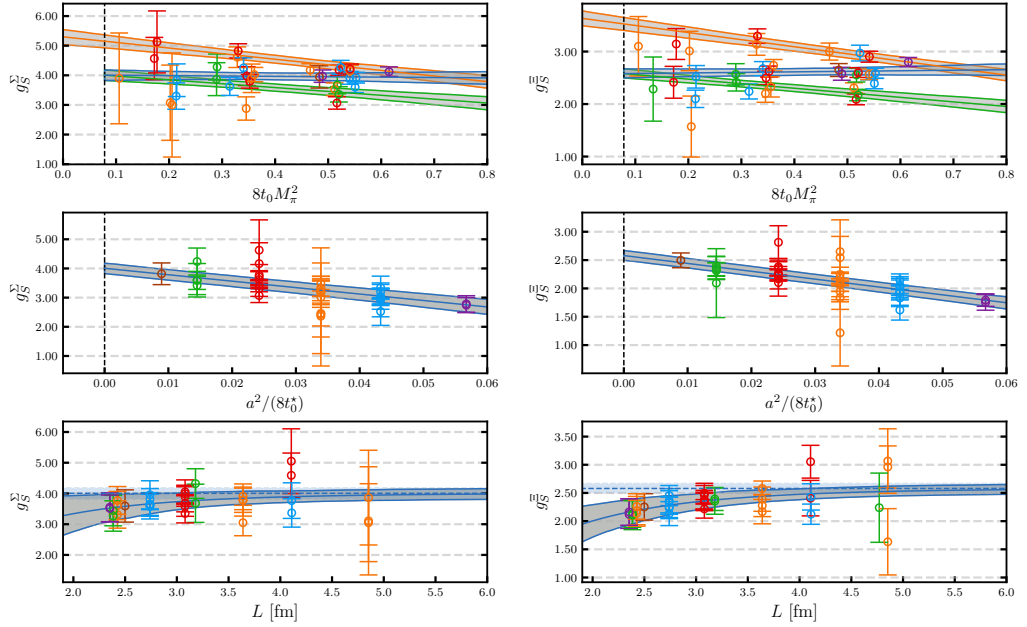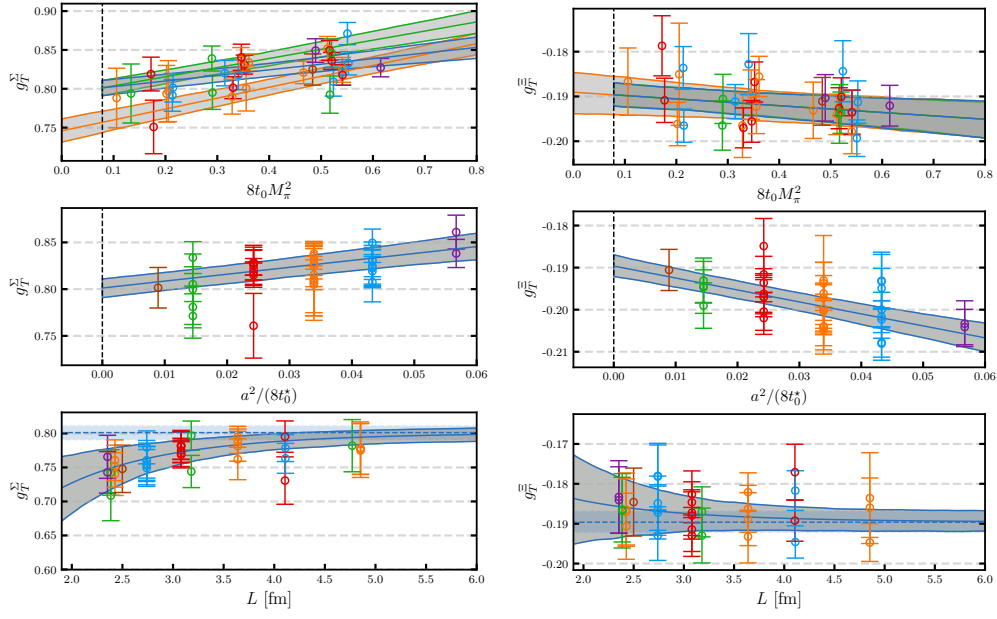
Figure E.3: The same as Fig. 5.4 for the vector charge g_V^B of the sigma (right) and cascade (left) baryon.
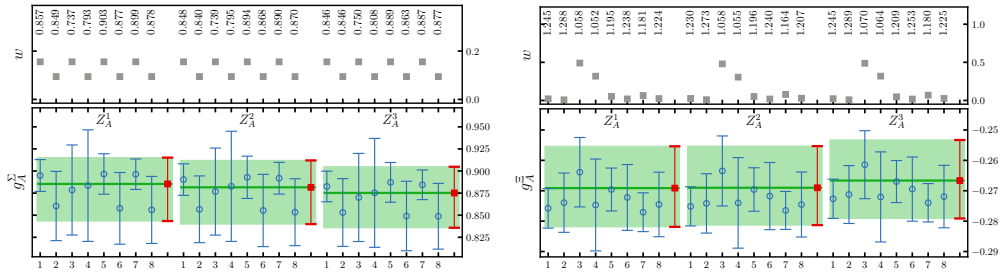
Figure E.4: The same as Fig. 5.8 for the axial charge g_B^B of the sigma (right) and cascade (left) baryon.
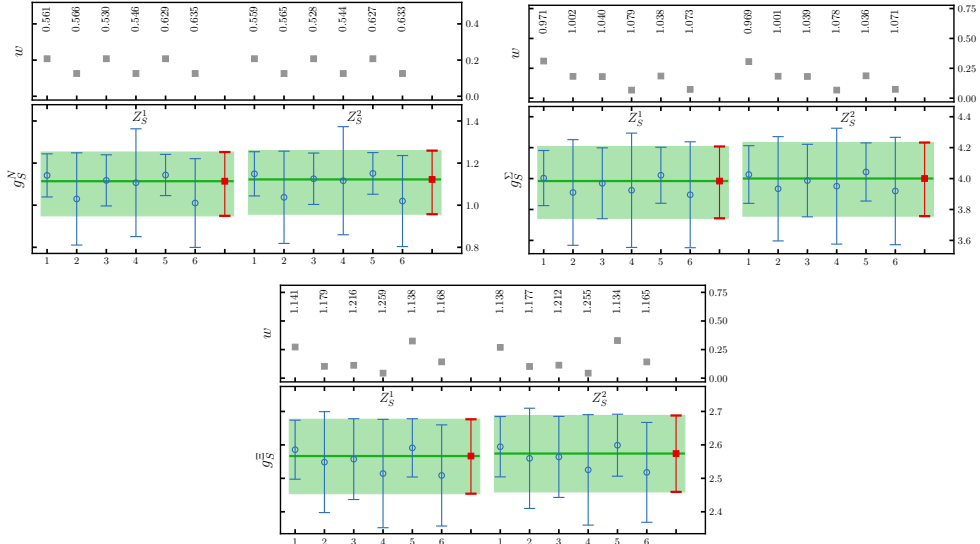
Figure E.5: The same as Fig. 5.8 for the scalar charge g_S^B of the nucleon (top, left), sigma (top, right) and cascade (bottom) baryons. The six fits correspond to two fit variations, see the text, applied to three data sets, $DS(M_\pi^{<400\,MeV})$, $DS(M_\pi^{<400\,MeV}, a^{<0.1\,fm})$ and $DS(M_\pi^{<400\,MeV}, LM_\pi^{>4})$. The data are extracted using two excited states in the fitting analysis, see section 3.4. Only two different sets of renormalization factors are used.
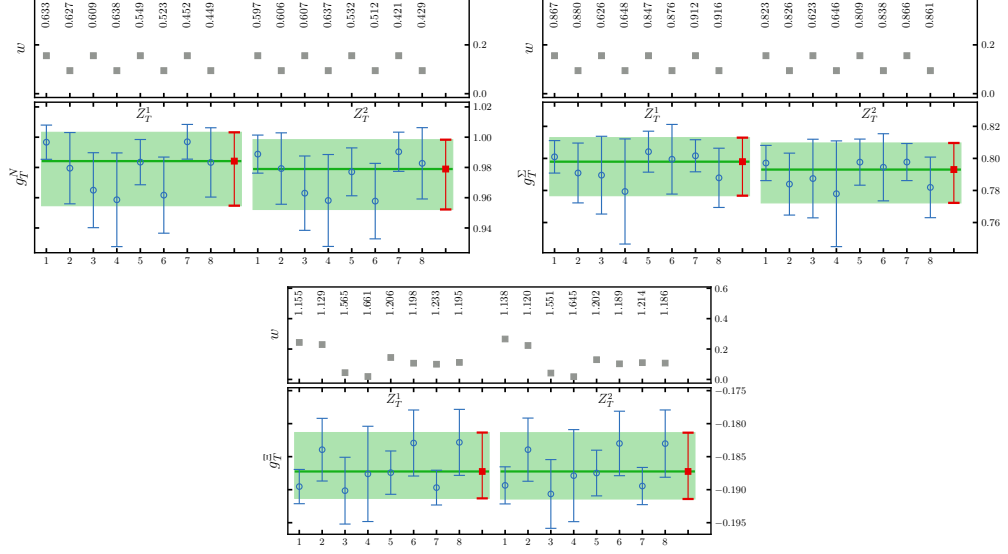
Figure E.6: The same as Fig. 5.8 for the tensor charge g_T^B for the nucleon (top, left), sigma (top, right) and cascade (bottom) baryons. The data are extracted using two excited states in the fitting analysis, see section 3.4. Only two different sets of renormalization factors are used.

Figure E.7: The same as Fig. 5.10 for the isovector scalar charges g_S^B of the sigma baryon (left) and the cascade baryon (right). For better visibility, the data point for ensemble E300, which has a relatively large error (see Table D.6), is not displayed for the sigma baryon. See Tables D.6 and D.7 for the set of ensembles used.

Figure E.8: The same as Fig. 5.12 for the isovector tensor charges g_T^B of the sigma baryon (left) and the cascade baryon (right). For better visibility, the data point for ensemble E300, which has a relatively large error (see Table D.7), is not displayed for the cascade baryon. See Tables D.6 and D.7 for the set of ensembles used.

F | FURTHER CHPT EXPRESSIONS

In this appendix, which has already been published in verbatim form in Appendix A of Ref. [SW1], we collect ChPT expressions that were not used in the final analysis. In particular, these are expressions that include decuplet loops (and therefore additional LECs that we were unable to resolve) and the finite volume effects for the axial charges. Regarding the latter, these have been computed using SU(2) HBChPT [229] and confirmed in SU(2) BChPT [230]. We define the function

$$h_1(\lambda_\pi) = \sum_{\mathbf{n} \neq \mathbf{0}} \left[K_0(\lambda_\pi |\mathbf{n}|) - \frac{K_1(\lambda_\pi |\mathbf{n}|)}{\lambda_\pi |\mathbf{n}|} \right], \tag{F.1}$$

that corresponds to $\mathbf{F_1}$ of Ref. [229] while for $h(\lambda)$, defined in Eq. (4.14): $h(\lambda_\pi) = -(8/3)\mathbf{F_3}(M_\pi, L)$. Again $\lambda_\pi = LM_\pi$. The SU(3) finite size effects in the flavour symmetric limit (utilizing the couplings that are tabulated in Ref. [103] and truncating at $\mathcal{O}(p^3)$) read:

$$g_A^N(L) = g_A^N - \frac{3}{2}(D+F)\xi h(\lambda_\pi) + \frac{2}{9}\left(27D^3 + 25D^2F + 45DF^2 + 63F^3\right)\xi h_1(\lambda_\pi), \tag{F.2}$$

$$g_A^\Sigma(L) = g_A^\Sigma - 3F\xi h(\lambda_\pi) + \frac{4}{9}F\left(25D^2 + 63F^2\right)\xi h_1(\lambda_\pi). \tag{F.3}$$

The gap between the decuplet and octet baryon mass in the chiral limit $\Delta = m_{D0} - m_0$ is within the range covered by our pion masses. Therefore, decuplet loop effects may in principle be relevant. Indeed, neglecting such terms, the finite volume effects of g_A^B have a sign opposite to what we see in the data. Already in Ref. [124] corrections due to transitions to decuplet baryons were considered. The full SU(3) result [144] for the octet baryon mass for the case $m_s = m_\ell$, to be added to Eq. (4.6), reads:[1]

$$m_B \mapsto m_B - \frac{\Delta^3}{(4\pi F_0)^2}\frac{5}{3}\mathcal{C}^2\left[\left(2 - 3\frac{M_\pi^2}{\Delta^2}\right)\log\left(\frac{M_\pi}{2\Delta}\right) + \frac{M_\pi^2}{2\Delta^2} + 2\left(1 - \frac{M_\pi^2}{\Delta^2}\right)w\left(\frac{M_\pi}{\Delta}\right)\right], \tag{F.4}$$

$$w(r) = \begin{cases} -\left(r^2 - 1\right)^{1/2}\arccos\left(r^{-1}\right) & , \quad r \geq 1 \\ \left(1 - r^2\right)^{1/2}\log\left(r^{-1} + \sqrt{r^{-2} - 1}\right) & , \quad r < 1 \end{cases} \tag{F.5}$$

with the additional LECs $\mathcal{C}$ and Δ. Regarding the above decuplet baryon effects, we restrict ourselves to the heavy baryon approximation. The full EOMS BChPT result can be found in Ref. [144]. Note that the decuplet decouples as $M_\pi \to 0$ as it should since in this case the extra term is proportional to $[3 - 4\log(M_\pi/(2\Delta))]M_\pi^4/(\Delta F_0^2)$, which is

---

[1]For the LEC $\mathcal{C}$ we use the normalization of Refs. [111, 124, 231], where $\mathcal{C}^2 = g_{\Delta N\pi}^2$ [232].

of a higher order in the chiral expansion. The associated finite volume corrections to Eq. (4.15) read [130, 233]

$$m_B(L) \mapsto m_B(L) + \frac{5}{3}\mathcal{C}^2 \xi \frac{m_0^3}{(m_0 + \Delta)^2}$$

$$\int_0^\infty dy \left\{ \left(2 - y + \frac{\Delta}{m_0} \right) f(y) \sum_{\mathbf{n} \neq \mathbf{0}} \left[f(y) K_0(\lambda_\pi |\mathbf{n}| f(y)) - \frac{K_1(\lambda_\pi |\mathbf{n}| f(y))}{\lambda_\pi |\mathbf{n}|} \right] \right\},$$

$$(F.6)$$

where

$$f(y) = \sqrt{1 + M_\pi^{-2} \left[(\Delta^2 + 2m_0\Delta - M_\pi^2) y + m_0^2 y^2 \right]}. \qquad (F.7)$$

We refer to Ref. [144] for the full SU(3) result and to Refs. [130, 233] for the corresponding finite volume corrections.

For the axial charges, we start from Ref. [229] and implement the decoupling constraints [234, 235] at $\mathcal{O}(p^3)$. We obtain for the special $N_f = 3$ case $m_s = m_\ell$:

$$g_A^B \mapsto g_A^B - j_B \frac{\Delta^2}{16\pi^2 F_0^2} J(M_\pi/\Delta) - n_B \frac{\Delta^2}{16\pi^2 F_0^2} N(M_\pi/\Delta), \qquad (F.8)$$

where

$$J(r) = -r^2 - \left(2 - r^2\right) \log\left(\frac{r}{2}\right) - 2w(r), \qquad (F.9)$$

$$N(r) = -\frac{r^2}{3} + \frac{\pi r^3}{3} - \left(\frac{2}{3} - r^2\right) \log\left(\frac{r}{2}\right) - \frac{2}{3} \left(1 - r^2\right) w(r) \qquad (F.10)$$

and the coefficients are given as

$$j_N = 5 \left(F + D + \frac{8}{27}\mathcal{H} \right) \mathcal{C}^2, \qquad n_N = -4 \left(\frac{11}{9}D + F \right) \mathcal{C}^2, \qquad (F.11)$$

$$j_\Sigma = 10 \left(F + \frac{5}{27}\mathcal{H} \right) \mathcal{C}^2, \qquad n_\Sigma = -\frac{40}{9}D\,\mathcal{C}^2. \qquad (F.12)$$

We remind the reader that the term $d_B \xi^{3/2}$ within Eqs. (4.8) and (4.9) does not appear at $\mathcal{O}(p^3)$ in the chiral expansion but is purely phenomenological. However, the function $\Delta^2 N(M_\pi/\Delta)$ contains a genuine term $\propto \xi^{3/2}(4\pi F_0)/\Delta$, justifying the inclusion of that parameter.

Regarding finite volume effects, we infer from Ref. [229] (see also Ref. [230]) that the following terms need to be added to Eqs. (F.2)–(F.3)[2]

$$g_A^B(L) \mapsto g_A^B(L) + \frac{4}{3}\xi \left[j_B \mathbf{F_2}(LM_\pi, M_\pi/\Delta) - \frac{9}{8}n_B \mathbf{F_4}(LM_\pi, M_\pi/\Delta) \right], \qquad (F.13)$$

where $\mathbf{F_2}$ and $\mathbf{F_4}$ are defined in Ref. [229].

---

[2]Note that a typo in Eq. (A15) of [SW1] (superscripts $_N$ instead of $_B$) was corrected here.

REFERENCES

[1] M. Gell-Mann, *A schematic model of baryons and mesons*, *Phys. Lett.* **8** (1964) 214–215.

[2] G. Zweig, *An SU(3) model for strong interaction symmetry and its breaking. Version 2*, pp. 22–101. 2, 1964.

[3] D. Page and S. Reddy, *Dense matter in compact stars: Theoretical developments and observational constraints*, *Ann. Rev. Nucl. Part. Sci.* **56** (2006) 327–374, [astro-ph/0608360].

[4] PANDA collaboration, G. Barucca et al., *PANDA Phase One*, *Eur. Phys. J. A* **57** (2021) 184, [2101.11877].

[5] PARTICLE DATA GROUP collaboration, R. L. Workman and Others, *Review of Particle Physics*, *PTEP* **2022** (2022) 083C01.

[6] X.-D. Ji, *Gauge-invariant decomposition of nucleon spin*, *Phys. Rev. Lett.* **78** (1997) 610, [hep-ph/9603249].

[7] R. L. Jaffe and A. Manohar, *The g_1 problem: Fact and fantasy on the spin of the proton*, *Nucl. Phys. B* **337** (1990) 509.

[8] QCDSF collaboration, G. S. Bali et al., *Strangeness contribution to the proton spin from lattice QCD*, *Phys. Rev. Lett.* **108** (2012) 222001, [1112.3354].

[9] M. Engelhardt, *Strange quark contributions to nucleon mass and spin from lattice QCD*, *Phys. Rev. D* **86** (2012) 114510, [1210.0025].

[10] χQCD collaboration, M. Gong, Y.-B. Yang, J. Liang, A. Alexandru, T. Draper and K.-F. Liu, *Strange and charm quark spins from the anomalous Ward identity*, *Phys. Rev. D* **95** (2017) 114509, [1511.03671].

[11] ETM collaboration, C. Alexandrou, M. Constantinou, K. Hadjiyiannakou, K. Jansen, C. Kallidonis, G. Koutsou et al., *Nucleon spin and momentum decomposition using lattice QCD simulations*, *Phys. Rev. Lett.* **119** (2017) 142002, [1706.02973].

[12] J. Green, N. Hasan, S. Meinel, M. Engelhardt, S. Krieg, J. Laeuchli et al., *Up, down, and strange nucleon axial form factors from lattice QCD*, *Phys. Rev. D* **95** (2017) 114502, [1703.06703].

[13] T. Bhattacharya, V. Cirigliano, S. D. Cohen, A. Filipuzzi, M. Gonzalez-Alonso, M. L. Graesser et al., *Probing novel scalar and tensor interactions from (ultra)cold neutrons to the LHC*, *Phys. Rev. D* **85** (2012) 054512, [1110.6448].

[14] FLAVOUR LATTICE AVERAGING GROUP (FLAG) collaboration, Y. Aoki et al., *FLAG Review 2021*, *Eur. Phys. J. C* **82** (2022) 869, [2111.09849].

[15] H.-W. Lin and K. Orginos, *First calculation of hyperon axial couplings from lattice QCD*, *Phys. Rev. D* **79** (2009) 034507, [`0712.1214`].

[16] G. Erkol, M. Oka and T. T. Takahashi, *Axial charges of octet baryons in two-flavor Lattice QCD*, *Phys. Lett. B* **686** (2010) 36, [`0911.2447`].

[17] C. Alexandrou, K. Hadjiyiannakou and C. Kallidonis, *Axial charges of hyperons and charmed baryons using $N_f = 2 + 1 + 1$ twisted mass fermions*, *Phys. Rev. D* **94** (2016) 034502, [`1606.01650`].

[18] A. Savanur and H.-W. Lin, *Lattice-QCD determination of the hyperon axial couplings in the continuum limit*, *Phys. Rev. D* **102** (2020) 014501, [`1901.00018`].

[19] QCDSF-UKQCD-CSSM collaboration, R. E. Smail et al., *Constraining beyond the Standard Model nucleon isovector charges*, `2304.02866`.

[20] H. Fritzsch, M. Gell-Mann and H. Leutwyler, *Advantages of the color octet gluon picture*, *Phys. Lett. B* **47** (1973) 365–368.

[21] D. J. Gross and F. Wilczek, *Ultraviolet behavior of nonabelian gauge theories*, *Phys. Rev. Lett.* **30** (1973) 1343–1346.

[22] H. D. Politzer, *Reliable perturbative results for strong interactions?*, *Phys. Rev. Lett.* **30** (1973) 1346–1349.

[23] M. E. Peskin and D. V. Schroeder, *An introduction to quantum field theory*. Westview Press, New York, 1995.

[24] C. Gattringer and C. Lang, *Quantum Chromodynamics on the Lattice - An Introductory Presentation*. Springer Science & Business Media, Berlin Heidelberg, 2010. aufl. ed., 2009.

[25] C. Hoelbling, *Lattice QCD: concepts, techniques and some results*, *Acta Phys. Polon.* **B45** (2014) 2143, [`1410.3403`].

[26] S. Weishäupl, *Lattice studies of the charmonium spectrum*, Master's thesis, Universität Regensburg, September, 2017.

[27] Y. Nambu and G. Jona-Lasinio, *Dynamical model of elementary particles based on an analogy with superconductivity. 1.*, *Phys. Rev.* **122** (1961) 345–358.

[28] K. G. Wilson, *Confinement of quarks*, *Phys. Rev. D* **10** (1974) 2445–2459.

[29] R. P. Feynman, *Space-time approach to nonrelativistic quantum mechanics*, *Rev. Mod. Phys.* **20** (1948) 367–387.

[30] B. Sheikholeslami and R. Wohlert, *Improved continuum limit lattice action for QCD with Wilson fermions*, *Nucl. Phys.* **B259** (1985) 572.

[31] M. Lüscher, S. Sint, R. Sommer and P. Weisz, *Chiral symmetry and O(a) improvement in lattice QCD*, *Nucl. Phys. B* **478** (1996) 365–400, [`hep-lat/9605038`].

[32] K. Symanzik, *Continuum limit and improved action in lattice theories. 1. Principles and phi**4 theory*, *Nucl. Phys. B* **226** (1983) 187–204.

[33] K. Symanzik, *Continuum limit and improved action in lattice theories. 2. O(N) nonlinear sigma model in perturbation theory*, *Nucl. Phys. B* **226** (1983) 205–227.

[34] M. Lüscher and P. Weisz, *On-Shell improved lattice gauge theories*, *Commun. Math. Phys.* **97** (1985) 59.

[35] J. Bulava and S. Schaefer, *Improvement of $N_f = 3$ lattice QCD with Wilson fermions and tree-level improved gauge action*, *Nucl. Phys. B* **874** (2013) 188–197, [1304.7093].

[36] H. B. Nielsen and M. Ninomiya, *Absence of neutrinos on a lattice. 1. Proof by homotopy theory*, *Nucl. Phys. B* **185** (1981) 20.

[37] H. B. Nielsen and M. Ninomiya, *No go theorem for regularizing chiral fermions*, *Phys. Lett. B* **105** (1981) 219–223.

[38] H. Nielsen and M. Ninomiya, *Absence of neutrinos on a lattice. 2. intuitive topological proof*, *Nuclear Physics B* **193** (1981) 173–194.

[39] M. Luscher and P. Weisz, *Computation of the action for on-shell improved lattice gauge theories at weak coupling*, *Phys. Lett.* **158B** (1985) 250–254.

[40] P. Weisz, *Continuum limit improved lattice action for pure Yang-Mills theory. 1.*, *Nucl. Phys. B* **212** (1983) 1–17.

[41] FLAVOUR LATTICE AVERAGING GROUP (FLAG) collaboration, S. Aoki, Y. Aoki, D. Bečirević, T. Blum, G. Colangelo, S. Collins et al., *FLAG Review 2019*, *The European Physical Journal C* **80** (Feb, 2020) .

[42] M. Creutz, *Quarks, Gluons and Lattices*. Oxford University Press, 1983, 10.1017/9781009290395.

[43] M. Lüscher, *Computational strategies in lattice QCD*, in *Les Houches Summer School: Session 93: Modern perspectives in lattice QCD: Quantum field theory and high performance computing*, pp. 331–399, 2, 2010, 1002.4232.

[44] S. Duane, A. D. Kennedy, B. J. Pendleton and D. Roweth, *Hybrid Monte Carlo*, *Phys. Lett. B* **195** (1987) 216–222.

[45] M. Lüscher, *Stochastic locality and master-field simulations of very large lattices*, *EPJ Web Conf.* **175** (2018) 01002, [1707.09758].

[46] N. Metropolis, A. W. Rosenbluth, M. N. Rosenbluth, A. H. Teller and E. Teller, *Equation of state calculations by fast computing machines*, *The Journal of Chemical Physics* **21** (1953) 1087–1092.

[47] M. Lüscher et al., "openQCD – Simulation programs for lattice QCD." http://luscher.web.cern.ch/luscher/openQCD/.

[48] M. Lüscher and S. Schaefer, *Lattice QCD with open boundary conditions and twisted-mass reweighting*, *Comput. Phys. Commun.* **184** (2013) 519–528, [1206.2809].

[49] M. A. Clark and A. D. Kennedy, *Accelerating dynamical fermion computations using the rational hybrid Monte Carlo (RHMC) algorithm with multiple pseudofermion fields*, *Phys. Rev. Lett.* **98** (2007) 051601, [hep-lat/0608015].

[50] CLS collaboration, M. Bruno et al., *Simulation of QCD with $N_f = 2 + 1$ flavors of non-perturbatively improved Wilson fermions*, *J. High Energy Phys.* **02** (2015) 043, [1411.3982].

[51] D. Mohler and S. Schaefer, *Remarks on strange-quark simulations with Wilson fermions*, *Phys. Rev. D* **102** (2020) 074506, [2003.13359].

[52] RQCD collaboration, G. S. Bali, S. Collins, P. Georg, D. Jenkins, P. Korcyl, A. Schäfer et al., *Scale setting and the light baryon spectrum in $N_f = 2 + 1$ QCD with Wilson fermions*, *J. High Energy Phys.* **05** (11, 2023) 035, [2211.03744].

[53] S. Borsanyi et al., *Ab initio calculation of the neutron-proton mass difference*, *Science* **347** (2015) 1452–1455, [1406.4088].

[54] M. Lüscher and S. Schaefer, *Lattice QCD without topology barriers*, *J. High Energy Phys.* **07** (2011) 036, [1105.4749].

[55] ALPHA collaboration, S. Schaefer, R. Sommer and F. Virotta, *Critical slowing down and error analysis in lattice QCD simulations*, *Nucl. Phys. B* **845** (2011) 93–119, [1009.5228].

[56] RQCD collaboration, G. S. Bali, E. E. Scholz, J. Simeth and W. Söldner, *Lattice simulations with $N_f = 2 + 1$ improved Wilson fermions at a fixed strange quark mass*, *Phys. Rev. D* **94** (2016) 074501, [1606.09039].

[57] G. Bali et al., *Lattice gauge ensembles and data management*, *Proc. Sci.* **LATTICE2022** (2022) 203, [2212.10138].

[58] Jülich Supercomputing Centre, *JUWELS: Modular Tier-0/1 Supercomputer at the Jülich Supercomputing Centre*, *J. of large-scale research facilities* **5** (2019) A135.

[59] Jülich Supercomputing Centre, *JURECA: Modular supercomputer at Jülich Supercomputing Centre*, *J. of large-scale research facilities* **4** (2018) A132.

[60] R. H. Rödl, *Nucleon generalized form factors from two-flavor lattice QCD and stochastic three-point functions with open indices*, Ph.D. thesis, Universität Regensburg, 2020.

[61] B. Borasoy and U.-G. Meissner, *Chiral expansion of baryon masses and σ-terms*, *Annals Phys.* **254** (1997) 192, [hep-ph/9607432].

[62] A. N. Cooke, R. Horsley, Y. Nakamura, D. Pleiter, P. E. L. Rakow, G. Schierholz et al., *The effects of flavour symmetry breaking on hadron matrix elements*, *Proc. Sci.* **LATTICE2012** (2012) 116, [1212.2564].

[63] QCDSF-UKQCD-CSSM collaboration, J. M. Bickerton, R. Horsley, Y. Nakamura, H. Perlt, D. Pleiter, P. E. L. Rakow et al., *Patterns of flavor symmetry breaking in hadron matrix elements involving u , d , and s quarks*, *Phys. Rev. D* **100** (2019) 114516, [1909.02521].

[64] S. Güsken, U. Löw, K.-H. Mütter, R. Sommer, A. Patel and K. Schilling, *Nonsinglet axial vector couplings of the baryon octet in lattice QCD*, *Phys. Lett. B* **227** (1989) 266–269.

[65] UKQCD collaboration, C. R. Allton et al., *Gauge invariant smearing and matrix correlators using Wilson fermions at beta = 6.2*, *Phys. Rev.* **D47** (1993) 5128–5137, [hep-lat/9303009].

[66] APE collaboration, M. Falcioni, M. L. Paciello, G. Parisi and B. Taglienti, *Again on SU(3) glueball mass*, *Nucl. Phys.* **B251** (1985) 624–632.

[67] A. Hasenfratz and F. Knechtli, *Flavor symmetry and the static potential with hypercubic blocking*, *Phys. Rev.* **D64** (2001) 034504, [hep-lat/0103029].

[68] C. Morningstar and M. J. Peardon, *Analytic smearing of SU(3) link variables in lattice QCD*, *Phys. Rev. D* **69** (2004) 054501, [hep-lat/0311018].

[69] L. Maiani, G. Martinelli, M. L. Paciello and B. Taglienti, *Scalar densities and baryon mass differences in lattice QCD with Wilson fermions*, *Nucl. Phys.* **B293** (1987) 420.

[70] LHPC collaboration, J. D. Bratt et al., *Nucleon structure from mixed action calculations using 2+1 flavors of asqtad sea and domain wall valence fermions*, *Phys. Rev. D* **82** (2010) 094502, [1001.3620].

[71] RQCD collaboration, G. S. Bali, L. Barca, S. Collins, M. Gruber, M. Löffler, A. Schäfer et al., *Nucleon axial structure from lattice QCD*, *J. High Energy Phys.* **05** (2020) 126, [1911.13150].

[72] R. Evans, G. Bali and S. Collins, *Improved semileptonic form factor calculations in Lattice QCD*, *Phys. Rev. D* **82** (2010) 094501, [1008.3293].

[73] G. S. Bali, S. Collins, B. Gläßle, M. Göckeler, J. Najjar, R. Rödl et al., *Nucleon structure from stochastic estimators*, *Proc. Sci.* **LATTICE2013** (2014) 271, [1311.1718].

[74] G. S. Bali, S. Collins, P. Korcyl, R. Rödl, S. Weishäupl and T. Wurm, *Hyperon couplings from $N_f = 2 + 1$ lattice QCD*, *Proc. Sci.* **LATTICE2019** (2019) 099, [1907.13454].

[75] G. S. Bali, S. Collins, B. Gläßle, S. Heybrock, P. Korcyl, M. Löffler et al., *Baryonic and mesonic 3-point functions with open spin indices*, *EPJ Web Conf.* **175** (2018) 06014, [1711.02384].

[76] RQCD collaboration, M. Löffler, P. Wein, T. Wurm, S. Weishäupl, D. Jenkins, R. Rödl et al., *Mellin moments of spin dependent and independent PDFs of the pion and rho meson*, *Phys. Rev. D* **105** (2022) 014505, [2108.07544].

[77] ETM collaboration, C. Alexandrou, S. Dinter, V. Drach, K. Jansen, K. Hadjiyiannakou and D. B. Renner, *A stochastic method for computing hadronic matrix elements*, *Eur. Phys. J. C* **74** (2014) 2692, [1302.2608].

[78] Y.-B. Yang, A. Alexandru, T. Draper, M. Gong and K.-F. Liu, *Stochastic method with low mode substitution for nucleon isovector matrix elements*, *Phys. Rev. D* **93** (2016) 034503, [1509.04616].

[79] M. Löffler, *Moments of parton distribution functions for the pion and rho meson from $N_f = 2 + 1$ lattice QCD*, Ph.D. thesis, Universität Regensburg, 2022.

[80] S.-J. Dong and K.-F. Liu, *Stochastic estimation with Z(2) noise*, *Phys. Lett. B* **328** (1994) 130–136, [hep-lat/9308015].

[81] S. Bernardson, P. McCarty and C. Thron, *Monte Carlo methods for estimating linear combinations of inverse matrix entries in lattice QCD*, *Comput. Phys. Commun.* **78** (1993) 256–264.

[82] H. W. Hamber, E. Marinari, G. Parisi and C. Rebbi, *Considerations on numerical analysis of QCD*, *Nucl. Phys. B* **225** (1983) 475.

[83] G. P. Lepage, *The Analysis of Algorithms for Lattice Field Theory*, in *Theoretical advanced study institute in elementary particle physics*, 6, 1989.

[84] J. Green, *Systematics in nucleon matrix element calculations*, *Proc. Sci.* **LATTICE2018** (2018) 016, [1812.10574].

[85] T. Harris, G. von Hippel, P. Junnarkar, H. B. Meyer, K. Ottnad, J. Wilhelm et al., *Nucleon isovector charges and twist-2 matrix elements with $N_f = 2 + 1$ dynamical Wilson quarks*, *Phys. Rev. D* **100** (2019) 034513, [1905.01291].

[86] P. Korcyl and G. S. Bali, *Non-perturbative determination of improvement coefficients using coordinate space correlators in $N_f = 2 + 1$ lattice QCD*, *Proc. Sci.* **LATTICE2016** (2016) 190, [1609.09477].

[87] G. S. Bali, K. G. Chetyrkin, P. Korcyl and J. Simeth, *Non-perturbative determination of quark-mass independent improvement coefficients in $N_f = 2 + 1$ lattice QCD*, in preparation (2023) .

[88] RQCD collaboration, G. S. Bali et al., *Nonperturbative renormalization in lattice QCD with three flavors of Clover fermions: Using periodic and open boundary conditions*, *Phys. Rev. D* **103** (2021) 094511, [2012.06284].

[89] G. Martinelli, C. Pittori, C. T. Sachrajda, M. Testa and A. Vladikas, *A general method for nonperturbative renormalization of lattice operators*, *Nucl. Phys. B* **445** (1995) 81–108, [hep-lat/9411010].

[90] C. Sturm, Y. Aoki, N. H. Christ, T. Izubuchi, C. T. C. Sachrajda and A. Soni, *Renormalization of quark bilinear operators in a momentum-subtraction scheme with a nonexceptional subtraction point*, *Phys. Rev. D* **80** (2009) 014501, [0901.2599].

[91] B. A. Kniehl and O. L. Veretin, *Bilinear quark operators in the RI/SMOM scheme at three loops*, *Phys. Lett. B* **804** (2020) 135398, [2002.10894].

[92] A. Bednyakov and A. Pikelner, *Quark masses: N3LO bridge from* RI/SMOM *to* $\overline{\text{MS}}$ *scheme*, *Phys. Rev. D* **101** (2020) 091501, [2002.12758].

[93] B. A. Kniehl and O. L. Veretin, *Moments $n = 2$ and $n = 3$ of the Wilson twist-two operators at three loops in the RI'/SMOM scheme*, *Nucl. Phys. B* **961** (2020) 115229, [2009.11325].

[94] M. Dalla Brida, T. Korzec, S. Sint and P. Vilaseca, *High precision renormalization of the flavour non-singlet Noether currents in lattice QCD with Wilson quarks*, *Eur. Phys. J. C* **79** (2019) 23, [1808.09236].

[95] S. Sint, *The chirally rotated Schrödinger functional with Wilson fermions and automatic O(a) improvement*, *Nucl. Phys. B* **847** (2011) 491–531, [1008.4857].

[96] E. G. Floratos, S. Narison and E. de Rafael, *Spectral function sum rules in quantum chromodynamics. 1. Charged currents sector*, *Nucl. Phys.* **B155** (1979) 115.

[97] J. Gasser and H. Leutwyler, *Quark masses*, *Phys. Rept.* **87** (1982) 77.

[98] ALPHA collaboration, I. Campos, P. Fritzsch, C. Pena, D. Preti, A. Ramos and A. Vladikas, *Non-perturbative quark mass renormalisation and running in $N_f = 3$ QCD*, *Eur. Phys. J. C* **78** (2018) 387, [1802.05243].

112

[99] FLAVOUR LATTICE AVERAGING GROUP (FLAG) collaboration, S. Aoki et al., *Review of lattice results concerning low-energy particle physics*, *Eur. Phys. J. C* **77** (2017) 112, [1607.00299].

[100] RQCD collaboration, G. S. Bali, S. Collins, W. Söldner and S. Weishäupl, *Leading order mesonic and baryonic SU(3) low energy constants from $N_f = 3$ lattice QCD*, *Phys. Rev. D* **105** (2022) 054516, [2201.05591].

[101] E. E. Jenkins and A. V. Manohar, *Baryon chiral perturbation theory using a heavy fermion Lagrangian*, *Phys. Lett. B* **255** (1991) 558–562.

[102] J. Bijnens, H. Sonoda and M. B. Wise, *On the validity of chiral perturbation theory for weak hyperon decays*, *Nucl. Phys.* **B261** (1985) 185–198.

[103] T. Ledwig, J. Martin Camalich, L. S. Geng and M. J. Vicente Vacas, *Octet-baryon axial-vector charges and SU(3)-breaking effects in the semileptonic hyperon decays*, *Phys. Rev. D* **90** (2014) 054502, [1405.5456].

[104] C. C. Chang et al., *A per-cent-level determination of the nucleon axial coupling from quantum chromodynamics*, *Nature* **558** (2018) 91–94, [1805.12130].

[105] R. Gupta, Y.-C. Jang, B. Yoon, H.-W. Lin, V. Cirigliano and T. Bhattacharya, *Isovector charges of the nucleon from $2 + 1 + 1$-flavor lattice QCD*, *Phys. Rev. D* **98** (2018) 034503, [1806.09006].

[106] M. F. M. Lutz, U. Sauerwein and R. G. E. Timmermans, *On the axial-vector form factor of the nucleon and chiral symmetry*, *Eur. Phys. J. C* **80** (2020) 844, [2003.10158].

[107] M. Lüscher, *Properties and uses of the Wilson flow in lattice QCD*, *J. High Energy Phys.* **08** (2010) 071, [1006.4518].

[108] M. Bruno, T. Korzec and S. Schaefer, *Setting the scale for the CLS $2 + 1$ flavor ensembles*, *Phys. Rev. D* **95** (2017) 074504, [1608.08900].

[109] QCDSF-UKQCD collaboration, W. Bietenholz et al., *Tuning the strange quark mass in lattice simulations*, *Phys. Lett. B* **690** (2010) 436–441, [1003.1114].

[110] A. Walker-Loud, *Evidence for non-analytic light quark mass dependence in the baryon spectrum*, *Phys. Rev. D* **86** (2012) 074509, [1112.2658].

[111] NPLQCD collaboration, S. R. Beane, E. Chang, W. Detmold, H. W. Lin, T. C. Luu, K. Orginos et al., *High statistics analysis using anisotropic clover lattices: (IV) volume dependence of light hadron masses*, *Phys. Rev. D* **84** (2011) 014507, [1104.4101].

[112] J. Liang, A. Alexandru, Y.-J. Bi, T. Draper, K.-F. Liu and Y.-B. Yang, *Detecting flavor content of the vacuum using the dirac operator spectrum*, 2021.

[113] ALPHA collaboration, M. Bruno, M. Dalla Brida, P. Fritzsch, T. Korzec, A. Ramos, S. Schaefer et al., *QCD Coupling from a nonperturbative determination of the three-flavor Λ parameter*, *Phys. Rev. Lett.* **119** (2017) 102001, [1706.03821].

[114] J. Gasser and H. Leutwyler, *Chiral perturbation theory: Expansions in the mass of the strange quark*, *Nucl. Phys.* **B250** (1985) 465–516.

[115] G. Amoros, J. Bijnens and P. Talavera, *Two point functions at two loops in three flavor chiral perturbation theory*, *Nucl. Phys.* **B568** (2000) 319–363, [hep-ph/9907264].

[116] J. Bijnens, K. Kampf and S. Lanz, *Leading logarithms in N-flavour mesonic Chiral Perturbation Theory*, *Nucl. Phys.* **B873** (2013) 137–164, [1303.3125].

[117] P. J. Ellis and K. Torikoshi, *Baryon masses in chiral perturbation theory with infrared regularization*, *Phys. Rev. C* **61** (2000) 015205, [nucl-th/9904017].

[118] B. C. Lehnhart, J. Gegelia and S. Scherer, *Baryon masses and nucleon sigma terms in manifestly Lorentz-invariant baryon chiral perturbation theory*, *J. Phys. G* **31** (2005) 89–104, [hep-ph/0412092].

[119] J. Gegelia and G. Japaridze, *Matching heavy particle approach to relativistic theory*, *Phys. Rev. D* **60** (1999) 114038, [hep-ph/9908377].

[120] T. Fuchs, J. Gegelia, G. Japaridze and S. Scherer, *Renormalization of relativistic baryon chiral perturbation theory and power counting*, *Phys. Rev. D* **68** (2003) 056005, [hep-ph/0302117].

[121] J. Gasser, M. E. Sainio and A. Švarc, *Nucleons with chiral loops*, *Nucl. Phys.* **B307** (1988) 779–853.

[122] V. Bernard, N. Kaiser, J. Kambor and U. G. Meissner, *Chiral structure of the nucleon*, *Nucl. Phys.* **B388** (1992) 315–345.

[123] X. L. Ren, L. S. Geng, J. Martin Camalich, J. Meng and H. Toki, *Octet baryon masses in next-to-next-to-next-to-leading order covariant baryon chiral perturbation theory*, *J. High Energy Phys.* **12** (2012) 073, [1209.3641].

[124] E. E. Jenkins and A. V. Manohar, *Chiral corrections to the baryon axial currents*, *Phys. Lett. B* **259** (1991) 353.

[125] J. Gasser and H. Leutwyler, *Light quarks at low temperatures*, *Phys. Lett. B* **184** (1987) 83–88.

[126] J. Gasser and H. Leutwyler, *Spontaneously broken symmetries: Effective Lagrangians at finite volume*, *Nucl. Phys.* **B307** (1988) 763–778.

[127] G. Colangelo, S. Dürr and C. Haefeli, *Finite volume effects for meson masses and decay constants*, *Nucl. Phys.* **B721** (2005) 136–174, [hep-lat/0503014].

[128] J. Bijnens and T. Rössler, *Finite volume at two loops in chiral perturbation theory*, *J. High Energy Phys.* **01** (2015) 034, [1411.6384].

[129] QCDSF-UKQCD collaboration, A. Ali Khan et al., *The nucleon mass in $N_f = 2$ lattice QCD: Finite size effects from chiral perturbation theory*, *Nucl. Phys.* **B689** (2004) 175–194, [hep-lat/0312030].

[130] M. Procura, B. Musch, T. Wollenweber, T. Hemmert and W. Weise, *Nucleon mass: From lattice QCD to the chiral limit*, *Phys. Rev. D* **73** (2006) 114510, [hep-lat/0603001].

[131] M. Bruno, P. Korcyl, T. Korzec, S. Lottini and S. Schaefer, *On the extraction of spectral quantities with open boundary conditions*, *Proc. Sci.* **LATTICE2014** (2014) 089, [1411.5207].

[132] S. Collins, K. Eckert, J. Heitger, S. Hofmann and W. Soeldner, *Leptonic decay constants for D-mesons from 3-flavour CLS ensembles*, *EPJ Web Conf.* **175** (2018) 13019, [1711.08657].

[133] O. Bär and M. Golterman, *Chiral perturbation theory for gradient flow observables*, *Phys. Rev. D* **89** (2014) 034505, [1312.4999].

[134] F. Herren and M. Steinhauser, *Version 3 of RunDec and CRunDec*, *Comput. Phys. Commun.* **224** (2018) 333, [1703.03751].

[135] K. G. Chetyrkin, J. H. Kühn and M. Steinhauser, *RunDec: A Mathematica package for running and decoupling of the strong coupling and quark masses*, *Comput. Phys. Commun.* **133** (2000) 43, [hep-ph/0004189].

[136] JLQCD AND TWQCD collaboration, H. Fukaya, S. Aoki, T. Chiu, S. Hashimoto, T. Kaneko, J. Noaki et al., *Determination of the chiral condensate from QCD Dirac spectrum on the lattice*, *Phys. Rev. D* **83** (2011) 074501, [1012.4052].

[137] X.-Y. Guo and M. F. M. Lutz, *On light vector mesons and chiral SU(3) extrapolations*, *Nucl. Phys. A* **988** (2019) 48–58, [1810.07078].

[138] P. Hernández, C. Pena and F. Romero-López, *Large N_c scaling of meson masses and decay constants*, *Eur. Phys. J. C* **79** (2019) 865, [1907.11511].

[139] MILC collaboration, A. Bazavov et al., *Results for light pseudoscalar mesons*, *Proc. Sci.* **LATTICE2010** (2010) 074, [1012.0868].

[140] RBC-UKQCD collaboration, C. Allton et al., *Physical results from 2 + 1 flavor fomain wall QCD and SU(2) chiral perturbation theory*, *Phys. Rev. D* **78** (2008) 114509, [0804.0473].

[141] PACS-CS collaboration, S. Aoki et al., *2 + 1 Flavor lattice QCD toward the physical point*, *Phys. Rev. D* **79** (2009) 034503, [0807.1661].

[142] MILC collaboration, A. Bazavov et al., *MILC results for light pseudoscalars*, *Proc. Sci.* **CD09** (2009) 007, [0910.2966].

[143] BMW collaboration, S. Dürr et al., *Sigma term and strangeness content of octet baryons*, *Phys. Rev. D* **85** (2012) 014509, [1109.4265].

[144] J. Martin Camalich, L. S. Geng and M. J. Vicente Vacas, *The lowest-lying baryon masses in covariant SU(3)-flavor chiral perturbation theory*, *Phys. Rev. D* **82** (2010) 074504, [1003.1929].

[145] M. F. M. Lutz, Y. Heo and X.-Y. Guo, *On the convergence of the chiral expansion for the baryon ground-state masses*, *Nucl. Phys. A* **977** (2018) 146–207, [1801.06417].

[146] X.-Y. Guo, Y. Heo and M. F. M. Lutz, *On a first order transition in QCD with up, down and strange quarks*, *Eur. Phys. J. C* **80** (2020) 260, [1907.00714].

[147] X.-L. Ren, L.-S. Geng and J. Meng, *Scalar strangeness content of the nucleon and baryon sigma terms*, *Phys. Rev. D* **91** (2015) 051502, [1404.4799].

[148] A. Walker-Loud et al., *Light hadron spectroscopy using domain wall valence quarks on an Asqtad sea*, *Phys. Rev. D* **79** (2009) 054502, [0806.4549].

[149] PACS-CS collaboration, K.-I. Ishikawa et al., *SU(2) and SU(3) chiral perturbation theory analyses on baryon masses in $2 + 1$ flavor lattice QCD*, *Phys. Rev. D* **80** (2009) 054502, [0905.0962].

[150] X.-L. Ren, L.-S. Geng and J. Meng, *Baryon chiral perturbation theory with Wilson fermions up to $\mathcal{O}(a^2)$ and discretization effects of latest $n_f = 2 + 1$ LQCD octet baryon masses*, *Eur. Phys. J. C* **74** (2014) 2754, [1311.7234].

[151] M. F. M. Lutz, R. Bavontaweepanya, C. Kobdaj and K. Schwarz, *Finite volume effects in the chiral extrapolation of baryon masses*, *Phys. Rev. D* **90** (2014) 054505, [1401.7805].

[152] M. J. Savage and J. Walden, *SU(3) breaking in neutral current axial matrix elements and the spin content of the nucleon*, *Phys. Rev. D* **55** (1997) 5376–5384, [hep-ph/9611210].

[153] R. Flores-Mendieta, E. E. Jenkins and A. V. Manohar, *SU(3) symmetry breaking in hyperon semileptonic decays*, *Phys. Rev. D* **58** (1998) 094028, [hep-ph/9805416].

[154] N. Cabibbo, E. C. Swallow and R. Winston, *Semileptonic hyperon decays*, *Ann. Rev. Nucl. Part. Sci.* **53** (2003) 39–75, [hep-ph/0307298].

[155] P. G. Ratcliffe, *Hyperon beta decay and the CKM matrix*, *Czech. J. Phys.* **54** (2004) B11–B20, [hep-ph/0402063].

[156] R. F. Dashen and A. V. Manohar, *$1/N_c$ corrections to the baryon axial currents in QCD*, *Phys. Lett. B* **315** (1993) 438, [hep-ph/9307242].

[157] RQCD collaboration, S. Bürger, T. Wurm, M. Löffler, M. Göckeler, G. Bali, S. Collins et al., *Lattice results for the longitudinal spin structure and color forces on quarks in a nucleon*, *Phys. Rev. D* **105** (2022) 054504, [2111.08306].

[158] D. de Florian, R. Sassot, M. Stratmann and W. Vogelsang, *Global analysis of helicity parton densities and their uncertainties*, *Phys. Rev. Lett.* **101** (2008) 072001, [0804.0422].

[159] J. Blümlein and H. Böttcher, *QCD analysis of polarized deep inelastic scattering data*, *Nucl. Phys. B* **841** (2010) 205–230, [1005.3113].

[160] NNPDF collaboration, E. R. Nocera, R. D. Ball, S. Forte, G. Ridolfi and J. Rojo, *A first unbiased global determination of polarized PDFs and their uncertainties*, *Nucl. Phys. B* **887** (2014) 276–308, [1406.5539].

[161] JAM collaboration, N. Sato, W. Melnitchouk, S. E. Kuhn, J. J. Ethier and A. Accardi, *Iterative Monte Carlo analysis of spin-dependent parton distributions*, *Phys. Rev. D* **93** (2016) 074005, [1601.07782].

[162] JAM collaboration, J. J. Ethier, N. Sato and W. Melnitchouk, *First simultaneous extraction of spin-dependent parton distributions and fragmentation functions from a global QCD analysis*, *Phys. Rev. Lett.* **119** (2017) 132001, [1705.05889].

[163] JAM collaboration, H.-W. Lin, W. Melnitchouk, A. Prokudin, N. Sato and H. Shows, *First Monte Carlo global analysis of nucleon transversity with lattice QCD constraints*, *Phys. Rev. Lett.* **120** (2018) 152502, [1710.09858].

[164] JAM collaboration, L. Gamberg, M. Malda, J. A. Miller, D. Pitonyak, A. Prokudin and N. Sato, *Updated QCD global analysis of single transverse-spin asymmetries: Extracting $\tilde{H}$, and the role of the Soffer bound and lattice QCD*, *Phys. Rev. D* **106** (2022) 034014, [2205.00999].

[165] H. Leutwyler, *Theoretical aspects of chiral dynamics*, *Proc. Sci.* **CD15** (2015) 022, [1510.07511].

[166] F. Fucito, G. Parisi and S. Petrarca, *First evaluation of g_A/g_V in lattice QCD in the quenched approximation*, *Phys. Lett. B* **115** (1982) 148.

[167] M. Ademollo and R. Gatto, *Nonrenormalization theorem for the strangeness violating vector currents*, *Phys. Rev. Lett.* **13** (1964) 264.

[168] L. Hayen, *Standard model $\mathcal{O}(\alpha)$ renormalization of g_A and its impact on new physics searches*, *Phys. Rev. D* **103** (2021) 113001, [2010.07262].

[169] V. Cirigliano, J. de Vries, L. Hayen, E. Mereghetti and A. Walker-Loud, *Pion-induced radiative corrections to neutron β decay*, *Phys. Rev. Lett.* **129** (2022) 121801, [2202.10439].

[170] J. Liang, Y.-B. Yang, T. Draper, M. Gong and K.-F. Liu, *Quark spins and anomalous Ward identity*, *Phys. Rev. D* **98** (2018) 074505, [1806.08366].

[171] M. González-Alonso and J. Martin Camalich, *Isospin breaking in the nucleon mass and the sensitivity of β decays to new physics*, *Phys. Rev. Lett.* **112** (2014) 042501, [1309.4434].

[172] JLQCD collaboration, N. Yamanaka, S. Hashimoto, T. Kaneko and H. Ohki, *Nucleon charges with dynamical overlap fermions*, *Phys. Rev. D* **98** (2018) 054516, [1805.10507].

[173] PACS collaboration, E. Shintani, K.-I. Ishikawa, Y. Kuramashi, S. Sasaki and T. Yamazaki, *Nucleon form factors and root-mean-square radii on a (10.8 fm)^4 lattice at the physical point*, *Phys. Rev. D* **99** (2019) 014510, [1811.07292].

[174] LHPC collaboration, N. Hasan, J. Green, S. Meinel, M. Engelhardt, S. Krieg, J. Negele et al., *Nucleon axial, scalar, and tensor charges using lattice QCD at the physical pion mass*, *Phys. Rev. D* **99** (2019) 114505, [1903.06487].

[175] NME collaboration, S. Park, R. Gupta, B. Yoon, S. Mondal, T. Bhattacharya, Y.-C. Jang et al., *Precision nucleon charges and form factors using (2 + 1)-flavor lattice QCD*, *Phys. Rev. D* **105** (2022) 054505, [2103.05599].

[176] K. Ottnad, D. Djukanovic, T. Harris, H. B. Meyer, G. von Hippel and H. Wittig, *Improved analysis of nucleon isovector charges and twist-2 matrix elements on CLS $N_f = 2 + 1$ ensembles*, *Proc. Sci.* **LATTICE2021** (2022) 343, [2110.10500].

[177] PACS collaboration, R. Tsuji, N. Tsukamoto, Y. Aoki, K.-I. Ishikawa, Y. Kuramashi, S. Sasaki et al., *Nucleon isovector couplings in $N_f = 2 + 1$ lattice QCD at the physical point*, *Phys. Rev. D* **106** (2022) 094505, [2207.11914].

[178] PNDME collaboration, T. Bhattacharya, V. Cirigliano, S. Cohen, R. Gupta, H.-W. Lin and B. Yoon, *Axial, scalar and tensor charges of the nucleon from 2 + 1 + 1-flavor lattice QCD*, *Phys. Rev. D* **94** (2016) 054508, [1606.07049].

[179] E. Berkowitz et al., *An accurate calculation of the nucleon axial charge with lattice QCD*, 1704.01114.

[180] ETM collaboration, C. Alexandrou, S. Bacchio, M. Constantinou, J. Finkenrath, K. Hadjiyiannakou, K. Jansen et al., *Nucleon axial, tensor, and scalar charges and σ-terms in lattice QCD*, *Phys. Rev. D* **102** (2020) 054517, [1909.00485].

[181] A. Walker-Loud et al., *Lattice QCD determination of g_A*, *Proc. Sci.* **CD2018** (2020) 020, [1912.08321].

[182] PNDME collaboration, Y.-C. Jang, R. Gupta, T. Bhattacharya, B. Yoon and H.-W. Lin, *Nucleon isovector axial form factors*, 2305.11330.

[183] H.-W. Lin, *Nucleon structure and hyperon form factor from lattice QCD*, 0707.3844.

[184] C. Alexandrou, K. Hadjiyiannakou, K. Jansen and C. Kallidonis, *Sigma-terms and axial charges for hyperons and charmed baryons*, *Proc. Sci.* **Lattice2013** (2014) 279, [1404.6355].

[185] QCDSF-UKQCD collaboration, M. Göckeler, P. Hägler, R. Horsley, Y. Nakamura, D. Pleiter, P. E. L. Rakow et al., *Baryon axial charges and momentum fractions with $N_f = 2 + 1$ dynamical fermions*, *Proc. Sci.* **LATTICE2010** (2010) 163, [1102.3407].

[186] K.-S. Choi, W. Plessas and R. F. Wagenbrunn, *Axial charges of octet and decuplet baryons*, *Phys. Rev. D* **82** (2010) 014007, [1005.0337].

[187] G.-S. Yang and H.-C. Kim, *Hyperon semileptonic decay constants with flavor SU(3) symmetry breaking*, *Phys. Rev. C* **92** (2015) 035206, [1504.04453].

[188] X. Y. Liu, D. Samart, K. Khosonthongkee, A. Limphirat, K. Xu and Y. Yan, *Axial charges of octet and decuplet baryons in a perturbative chiral quark model*, *Phys. Rev. C* **97** (2018) 055206.

[189] R. Qi, J.-B. Wang, G. Li, C.-S. An, C.-R. Deng and J.-J. Xie, *Investigations on the flavor-dependent axial charges of the octet baryons*, *Phys. Rev. C* **105** (2022) 065204, [2205.14419].

[190] RBC AND UKQCD collaboration, M. Abramczyk, T. Blum, T. Izubuchi, C. Jung, M. Lin, A. Lytle et al., *Nucleon mass and isovector couplings in $2 + 1$-flavor dynamical domain-wall lattice QCD near physical mass*, *Phys. Rev. D* **101** (2020) 034510, [1911.03524].

[191] χQCD collaboration, L. Liu, T. Chen, T. Draper, J. Liang, K.-F. Liu, G. Wang et al., *Nucleon isovector scalar charge from overlap fermions*, *Phys. Rev. D* **104** (2021) 094503, [2103.12933].

[192] P. A. Baikov, K. G. Chetyrkin and J. H. Kühn, *Five-loop running of the QCD coupling constant*, *Phys. Rev. Lett.* **118** (2017) 082002, [1606.08659].

[193] P. A. Baikov, K. G. Chetyrkin and J. H. Kühn, *Five-loop fermion anomalous dimension for a general gauge group from four-loop massless propagators*, *J. High Energy Phys.* **04** (2017) 119, [1702.01458].

[194] Y. Schröder and M. Steinhauser, *Four-loop decoupling relations for the strong coupling*, *J. High Energy Phys.* **01** (2006) 051, [hep-ph/0512058].

[195] T. Liu and M. Steinhauser, *Decoupling of heavy quarks at four loops and effective Higgs-fermion coupling*, *Phys. Lett. B* **746** (2015) 330, [1502.04719].

[196] P. Marquard, A. V. Smirnov, V. A. Smirnov, M. Steinhauser and D. Wellmann, $\overline{\text{MS}}$-*on-shell quark mass relation up to four loops in QCD and a general SU(N) gauge group*, *Phys. Rev. D* **94** (2016) 074025, [1606.06754].

[197] Z. Fodor, C. Hoelbling, S. Krieg, L. Lellouch, T. Lippert, A. Portelli et al., *Up and down quark masses and corrections to Dashen's theorem from lattice QCD and quenched QED*, *Phys. Rev. Lett.* **117** (2016) 082001, [1604.07112].

[198] χQCD collaboration, D. Horkel, Y. Bi, M. Constantinou, T. Draper, J. Liang, K.-F. Liu et al., *Nucleon isovector tensor charge from lattice QCD using chiral fermions*, *Phys. Rev. D* **101** (2020) 094501, [2002.06699].

[199] PNDME collaboration, T. Bhattacharya, V. Cirigliano, S. Cohen, R. Gupta, A. Joseph, H.-W. Lin et al., *Iso-vector and iso-scalar tensor charges of the nucleon from lattice QCD*, *Phys. Rev. D* **92** (2015) 094511, [1506.06411].

[200] ETM collaboration, C. Alexandrou et al., *Moments of the nucleon transverse quark spin densities using lattice QCD*, *Phys. Rev. D* **107** (2023) 054504, [2202.09871].

[201] M. Anselmino, M. Boglione, U. D'Alesio, S. Melis, F. Murgia and A. Prokudin, *Simultaneous extraction of transversity and Collins functions from new SIDIS and e^+e^- data*, *Phys. Rev. D* **87** (2013) 094019, [1303.3822].

[202] Z.-B. Kang, A. Prokudin, P. Sun and F. Yuan, *Extraction of quark transversity distribution and Collins fragmentation functions with QCD evolution*, *Phys. Rev. D* **93** (2016) 014009, [1505.05589].

[203] M. Radici and A. Bacchetta, *First extraction of transversity from a global analysis of electron-proton and proton-proton data*, *Phys. Rev. Lett.* **120** (2018) 192001, [1802.05212].

[204] J. Benel, A. Courtoy and R. Ferro-Hernandez, *A constrained fit of the valence transversity distributions from dihadron production*, *Eur. Phys. J. C* **80** (2020) 465, [1912.03289].

[205] JAM collaboration, J. Cammarota, L. Gamberg, Z.-B. Kang, J. A. Miller, D. Pitonyak, A. Prokudin et al., *Origin of single transverse-spin asymmetries in high-energy collisions*, *Phys. Rev. D* **102** (2020) 054002, [2002.08384].

[206] W. N. Cottingham, *The neutron proton mass difference and electron scattering experiments*, *Annals Phys.* **25** (1963) 424.

[207] R. F. Dashen, *Chiral SU(3) × SU(3) as a symmetry of the strong interactions*, *Phys. Rev.* **183** (1969) 1245.

[208] J. Gasser, A. Rusetsky and I. Scimemi, *Electromagnetic corrections in hadronic processes*, *Eur. Phys. J. C* **32** (2003) 97, [hep-ph/0305260].

[209] FERMILAB LATTICE AND MILC collaboration, A. Bazavov et al., *B- and D-meson leptonic decay constants from four-flavor lattice QCD*, *Phys. Rev. D* **98** (2018) 074512, [1712.09262].

[210] MILC collaboration, S. Basak et al., *Lattice computation of the electromagnetic contributions to kaon and pion masses*, *Phys. Rev. D* **99** (2019) 034503, [1807.05556].

[211] J. Gasser, H. Leutwyler and A. Rusetsky, *On the mass difference between proton and neutron*, *Phys. Lett. B* **814** (2021) 136087, [2003.13612].

[212] RM123 collaboration, D. Giusti, V. Lubicz, C. Tarantino, G. Martinelli, F. Sanfilippo, S. Simula et al., *Leading isospin-breaking corrections to pion, kaon and charmed-meson masses with twisted-mass fermions*, *Phys. Rev. D* **95** (2017) 114504, [1704.06561].

[213] M. G. Endres, A. Shindler, B. C. Tiburzi and A. Walker-Loud, *Massive photons: An infrared regularization scheme for lattice QCD+QED*, *Phys. Rev. Lett.* **117** (2016) 072002, [1507.08916].

[214] D. A. Brantley, B. Joó, E. V. Mastropas, E. Mereghetti, H. Monge-Camacho, B. C. Tiburzi et al., *Strong isospin violation and chiral logarithms in the baryon spectrum*, 1612.07733.

[215] CSSM-QCDSF-UKQCD collaboration, R. Horsley et al., *Isospin splittings in the decuplet baryon spectrum from dynamical QCD+QED*, *J. Phys. G* **46** (2019) 115004, [1904.02304].

[216] QCDSF-UKQCD collaboration, R. Horsley, J. Najjar, Y. Nakamura, H. Perlt, D. Pleiter, P. E. L. Rakow et al., *Lattice determination of Sigma-Lambda mixing*, *Phys. Rev. D* **91** (2015) 074512, [1411.7665].

[217] S. Dürr et al., *Lattice computation of the nucleon scalar quark contents at the physical point*, *Phys. Rev. Lett.* **116** (2016) 172001, [1510.08013].

[218] N. Salone, P. Adlarson, V. Batozskaya, A. Kupsc, S. Leupold and J. Tandean, *Study of CP violation in hyperon decays at super-charm-tau factories with a polarized electron beam*, *Phys. Rev. D* **105** (2022) 116022, [2203.03035].

[219] SciDAC, LHPC and UKQCD collaboration, R. G. Edwards and B. Joó, *The Chroma software system for lattice QCD*, *Nucl. Phys. B Proc. Suppl.* **140** (2005) 832, [hep-lat/0409003].

[220] ALPHA collaboration, U. Wolff, *Monte Carlo errors with less errors*, *Comput. Phys. Commun.* **156** (2004) 143–153, [hep-lat/0306017].

[221] P. L. J. Petrak, G. S. Bali, S. Collins, J. Heitger, D. Jenkins, S. Weishäupl et al., *Towards the determination of sigma terms for the baryon octet on $N_f = 2 + 1$ CLS ensembles*, *Proc. Sci.* **LATTICE2021** (2022) 072, [2112.00586].

[222] P. L. J. Petrak, G. S. Bali, S. Collins, J. Heitger, D. Jenkins and S. Weishäupl, *Sigma terms of the baryon octet in $N_f = 2 + 1$ QCD with Wilson quarks*, *Proc. Sci.* **LATTICE2022** (2023) 112, [2301.03871].

[223] B. Efron, *Computers and the theory of statistics: Thinking the unthinkable*, *SIAM Review* **21** (1979) 460–480, [https://doi.org/10.1137/1021092].

[224] F. James and M. Roos, *Minuit: A system for function minimization and analysis of the parameter errors and correlations*, *Comput. Phys. Commun.* **10** (1975) 343–367.

[225] H. Akaike, *Information theory and an extension of the maximum likelihood principle*, *Springer Series in Statistics* (1998) .

[226] BMW collaboration, S. Borsanyi et al., *Leading hadronic contribution to the muon magnetic moment from lattice QCD*, *Nature* **593** (2021) 51–55, [2002.12347].

[227] W. I. Jay and E. T. Neil, *Bayesian model averaging for analysis of lattice field theory results*, *Phys. Rev. D* **103** (2021) 114502, [2008.01069].

[228] Y. Nakamura and H. Stüben, *BQCD - Berlin quantum chromodynamics program*, *Proc. Sci.* **LATTICE2010** (2010) 040, [1011.0199].

[229] S. R. Beane and M. J. Savage, *Baryon axial charge in a finite volume*, *Phys. Rev. D* **70** (2004) 074029, [hep-ph/0404131].

[230] QCDSF collaboration, A. A. Khan et al., *Axial coupling constant of the nucleon for two flavours of dynamical quarks in finite and infinite volume*, *Phys. Rev. D* **74** (2006) 094508, [hep-lat/0603028].

[231] A. Walker-Loud, *Octet baryon masses in partially quenched chiral perturbation theory*, *Nucl. Phys. A* **747** (2005) 476–507, [hep-lat/0405007].

[232] S. R. Beane, *Nucleon masses and magnetic moments in a finite volume*, *Phys. Rev. D* **70** (2004) 034507, [hep-lat/0403015].

[233] L.-S. Geng, X.-L. Ren, J. Martin-Camalich and W. Weise, *Finite-volume effects on octet-baryon masses in covariant baryon chiral perturbation theory*, *Phys. Rev. D* **84** (2011) 074024, [1108.2231].

[234] V. Bernard, H. W. Fearing, T. R. Hemmert and U. G. Meissner, *The form-factors of the nucleon at small momentum transfer*, *Nucl. Phys. A* **635** (1998) 121–145, [hep-ph/9801297].

[235] T. R. Hemmert, M. Procura and W. Weise, *Quark mass dependence of the nucleon axial vector coupling constant*, *Phys. Rev. D* **68** (2003) 075009, [hep-lat/0303002].

[236] Jülich Supercomputing Centre, *HDF Cloud – Helmholtz Data Federation Cloud Resources at the Jülich Supercomputing Centre*, *J. of large-scale research facilities* **5** (2019) A137.

[237] S. Heybrock, M. Rottmann, P. Georg and T. Wettig, *Adaptive algebraic multigrid on SIMD architectures*, *Proc. Sci.* **LATTICE2015** (2016) 036, [1512.04506].

[238] P. Georg, D. Richtmann and T. Wettig, *DD-αAMG on QPACE 3*, *EPJ Web Conf.* **175** (2018) 02007, [1710.07041].

[239] A. Frommer, K. Kahl, S. Krieg, B. Leder and M. Rottmann, *Adaptive aggregation based domain decomposition multigrid for the lattice Wilson Dirac operator*, *SIAM J. Sci. Comput.* **36** (2014) A1581–A1608, [1303.1377].

[240] M. Lüscher, *Deflation acceleration of lattice QCD simulations*, *J. High Energy Phys.* **12** (2007) 011, [0710.5417].

[241] C. R. Harris, K. J. Millman, S. J. van der Walt, R. Gommers, P. Virtanen, D. Cournapeau et al., *Array programming with NumPy*, *Nature* **585** (Sept., 2020) 357–362.

[242] S. Behnel, R. Bradshaw, C. Citro, L. Dalcin, D. S. Seljebotn and K. Smith, *Cython: The best of both worlds*, *Computing in Science & Engineering* **13** (2011) 31–39.

[243] J. D. Hunter, *Matplotlib: A 2D graphics environment*, *Computing in Science and Engineering* **9** (2007) 90–95.

[244] T. Tantau, *The TikZ and PGF packages*, 2015.

[245] J. Ellson, E. Gansner, L. Koutsofios, S. C. North and G. Woodhull, *Graphviz–open source graph drawing tools*, in *Graph Drawing*, pp. 483–484, Springer Berlin Heidelberg, 2002.

ACRONYMS

AWI axial Ward identity

BChPT covariant baryon chiral perturbation theory

CLS Coordinated Lattice Simulations

ChPT chiral perturbation theory

EOMS extended on-mass-shell

FLAG Flavour Lattice Averaging Group

GMOR Gell-Mann–Oakes–Renner

HBChPT heavy baryon chiral perturbation theory

HMC Hybrid Monte Carlo

LECs low energy constants

LO leading order

$\overline{\textbf{MS}}$ modified minimal subtraction

NLO next-to-leading order

NNLO next-to-next-to-leading order

OZI Okubo-Zweig-Iizuka

PDFs parton distribution functions

QCD Quantum Chromo Dynamics

QED Quantum Electro Dynamics

RGI renormalization group invariant

RI′-SMOM regularization independent symmetric momentum-subtraction

SM Standard Model

ACKNOWLEDGEMENTS

I am pleased to express my gratitude to all the people who played a crucial role in this PhD project and made my work possible.

First of all I want to thank my advisor Prof. Dr. Gunnar S. Bali for giving me the opportunity to do my PhD in Lattice QCD, a field which is very fascinating to me. Likewise I want to thank PD Dr. Sara Collins who's contributions to this project were indispensable. To both I am deeply grateful for their support, guidance and advice throughout the last years. Their great expertise and patience in explaining things to me lays the cornerstone for this thesis.

Further, I want to say thank you to all the members of the research group who were always friendly and willing to help. In particular I want to thank Prof. Dr. Gunnar S. Bali, PD Dr. Sara Collins, PD Dr. Wolfgang Söldner and Dr. Thomas Wurm for their contributions to the publications this thesis is based on as well as Dr. Rudolf Rödl, Dr. Marius Löffler, Dr. Piotr Korcyl and Dr. Benjamin Gläßle for their contributions regarding the (stochastic) three-point function code. Moreover, I would like to thank my long term office mates Marius Löffler, Maximilian Schlemmer and Daniel Richtmann as well as my colleagues Andreas Rabenstein, Rudolf Rödl, Jakob Simeth, Daniel Jenkins, Thomas Wurm, Peter Georg, Philipp Wein, Wolfgang Söldner and Stefan Solbrig for all the helpful advices, endless discussions, continuous support and numerous coffee breaks. Especially I want to thank Marius who accompanied me from the first semester until today – having you around as a friend and colleague was invaluable and our joint (working) hours were always a pleasure. In addition, I also want to express my gratitude to Andreas Rabenstein for proof reading this thesis and providing valuable comments.

I would like to extend my thanks to all members of the PhD committee, namely, Prof. Dr. Jörg Wunderlich, Prof. Dr. Gunnar S. Bali, Prof. Dr. Taushif Ahmed and Prof. Dr. Andrea Donarini for their efforts.

Last but not least, I want to thank my friends and family. Thank you Tommy, Christian, Christian, Niki, Nina, Antonella, Michi, Ulli, Martin and many others for all the motivational encouragements, your priceless company and endless climbing sessions. Many thanks to my parents and my sister for the support throughout all the years and the fact that I always could rely on you. Lastly, I want the thank my beloved girlfriend Kathl. Thank you for supporting me in all possible ways, for dealing with my lately often absent mind and for trying to keep my psyche high – I am truly grateful.